Modeling urban microclimate

Development, implementation and evaluation of new and improved calculation methods for the urban microclimate model ENVI-met

Dissertation zur Erlangung des Grades

„Doktor der Naturwissenschaften“ im Promotionsfach

Geographie

am Fachbereich Chemie, Pharmazie und Geowissenschaften
der Johannes Gutenberg-Universität Mainz

Helge Simon

geb. in Koblenz

Mainz, März 2016

Dekan:

1. Berichterstatter:

2. Berichterstatter:

Tag der mündlichen Prüfung: 02. Juni 2016

D77 (Dissertation Universität Mainz)

Zusammenfassung

In der vorliegenden Dissertation werden entscheidende Neuerungen des im wissenschaftlichen Bereich etablierten Mikroklimamodells ENVI-met vorgestellt und anhand von Proof-of-Concept-Szenarien sowie mittels von Vergleichen zwischen Messungen und Modellergebnissen evaluiert.

Es wurden Verbesserungen bei der Modellierung von Pflanzen vorgenommen, die es erlauben Aussagen über den mikroklimatischen Nutzen sowie die Vitalität von Pflanzen als einheitliches Objekt / Organismus zu treffen. Evaluationen im Rahmen von Proof-of-Concept-Simulationen und Vergleiche zu Messdaten konnten zeigen, dass ENVI-met durch die Weiterentwicklungen des Vegetationsmodells im Stande ist pflanzenbasierte Parameter wie Transpirationsraten sowie Blattflächentemperaturen zuverlässig und genau zu modellieren. Weitere Verbesserungen betrafen das Chemiemodell. Auf Basis eines neu implementieren Isoprenemissionsmodells wurde ENVI-mets Chemiemodell um isopren-induzierte Reaktionen erweitert, die zu einer Veränderung der Konzentration von troposphärischem Ozon führen. Proof-of-Concept-Simulationen bestätigten die Validität des Modells. ENVI-mets Gebäudemodell wurde um weitere Berechnungsknoten erweitert, die es erlauben, Wände und Dächer aus einer Abfolge verschiedener Materialen zu erstellen. Dies ermöglicht eine exaktere Berechnung der Innenraumtemperatur sowie der Fassadentemperaturen. Proof-of-Concept-Simulationen sowie ein Vergleich mit Messdaten des Fraunhofer Instituts für Bauphysik Holzkirchen zeigten sehr hohe Übereinstimmung. Die Kopplung des größerskaligen Klimamodells MUKLIMO_3 des Deutschen Wetterdienstes mit dem mikroskaligen ENVI-met wurde verbessert. Simulationsergebnisse von gekoppelten Modellläufen in einfachen Modellgebieten zeigten sehr viel versprechende Ergebnisse. In komplexeren Modellgebieten hingegen scheint die Diskrepanz in den bodennahen Temperaturfeldern noch nicht vollends behoben.

Abstract

In this dissertation, major developments of the scientifically well-established microclimate model ENVI-met are presented. The new developments are evaluated based on proof-of-concept scenarios as well as by comparisons against measurements.

Improvements in the modeling of plants have been undertaken that allow the simulation of the microclimatic benefits and the vitality of plants as a single object / organism. Proof-of-concept simulations and a comparison with measured data showed that due to the improvements of the vegetation model ENVI-met is now capable to reliably and accurately model plant-based parameters such as transpiration and leaf area temperatures. New chemical reactions were implemented into the chemistry model. Based on the implementation of an isoprene emission model ENVI-met's chemistry model has been extended by isoprene-induced reactions, which lead to changes in the concentration of tropospheric ozone. Proof-of-concept simulations have confirmed the validity of the model. ENVI-met's wall and roof model has been extended by multiple computation nodes, which enable the construction of more complex walls and roofs consisting of different materials. This allows a more accurate calculation of the interior temperature as well as the facade temperatures. Proof-of-concept simulations as well as a comparison of modeled facade temperatures with measurement data from the Fraunhofer Institute for Building Physics Holzkirchen showed very high agreement. The coupling of the larger scale climate model MUKLIMO_3 of the German Meteorological Service with the microscale model ENVI-met has been improved. Simulation results of coupled model runs in simplified model areas showed very promising results. In more complex model areas, however, the discrepancies in the near-ground surface temperatures do not seem to be fully resolved yet.

Contents

List of figures **X**

List of tables **XI**

1 Introduction **1**

2 The microclimate model ENVI-met **7**

2.1 Introduction 7

2.2 General model properties 7

2.3 1D boundary model 9

2.3.1 Initial values 10

2.3.2 Lateral boundary conditions 10

2.3.3 Linkage 1D boundary 3D core model 11

2.4 The 3D core model 11

2.4.1 The atmosphere model 12

2.4.1.1 Wind field 12

2.4.1.2 Air temperature and humidity 13

2.4.1.3 Turbulence 13

2.4.1.4 Gas and particle dispersion model 14

2.4.1.5 Radiation 15

2.4.1.6 Ground and building surfaces 19

2.4.2 The soil model 21

2.4.3 The vegetation model 22

2.5 Conclusion 29

3 Plant vitality assessment - Introduction of the plant-as-object model **33**

3.1 Introduction 34

3.2 The plant-as-object model . . . 36
3.2.1 Integration of LAD cells to canopies . . . 37
3.2.2 Implementing a three-dimensional root model . . . 39
3.3 Proof-of-concept simulations for the plant-as-object model . . . 43
3.3.1 Proof-of-concept simulations assessing the effect of different tree geometries . . . 44
3.3.2 Proof-of-concept simulation assessing the effect of different microclimates . . . 49
3.4 Conclusion and outlook . . . 54

4 Modeling transpiration and leaf temperature of urban trees - an evaluation of the microclimate model ENVI-met using measurement data 61
4.1 Introduction . . . 62
4.2 Methods . . . 64
4.2.1 Study site . . . 64
4.2.2 Monitored parameters . . . 65
4.2.3 ENVI-met . . . 67
4.2.3.1 ENVI-met boundary conditions . . . 68
4.2.3.2 ENVI-met model area . . . 69
4.3 Results and discussion . . . 70
4.3.1 Transpiration rates . . . 71
4.3.2 Shaded leaf temperatures . . . 75
4.4 Conclusion . . . 76

5 Introduction of a BVOC model 83
5.1 Introduction . . . 84
5.2 Implementation of a BVOC model . . . 86
5.2.1 Estimation of isoprene emissions . . . 86

5.2.2 Implementation 89
5.2.2.1 Model adjustments 89
5.2.2.2 Dispersion model 91
5.2.2.3 Chemical reaction model 97
5.3 Evaluation - proof-of-concept simulations 102
5.3.1 Basic proof-of-concept simulations for the isoprene emission model 102
5.3.2 Proof-of-concept simulations assessing the effects of biological parameter alterations 115
5.3.3 Proof-of-concept simulations for the dispersion and chemistry model 119
5.3.3.1 Proof-of-concept simulations for the dispersion and chemistry model in a simplified model area 119
5.3.3.2 Proof-of-concept simulations for the dispersion and chemistry model in a complex model area 127
5.3.3.2.1 Model outputs excluding isoprene emissions and reactions 131
5.3.3.2.2 Model outputs including isoprene emissions 134
5.3.3.2.3 Model output comparison 139
5.4 Conclusion 146

6 Evaluation of ENVI-met's multiple-node model and estimation of indoor climate 152

6.1 Introduction 153
6.2 The multiple-node wall and roof model 154
6.3 Proof-of-concept simulation for the multiple-node model 159
6.3.1 Model area and boundary conditions 159
6.3.2 Model results 161

6.4 Evaluation of the multiple-node model by comparison with measurement data . . . 164
6.4.1 Study site . . . 164
6.4.2 Monitored parameters & material properties . . . 165
6.4.3 ENVI-met boundary conditions & model area . . . 166
6.4.4 Results and discussion . . . 170
6.5 Conclusion and outlook . . . 173

7 Further advancement of the coupling module of MUKLIMO_3 and ENVI-met 177
7.1 Introduction . . . 178
7.2 MUKLIMO_3 . . . 179
7.3 Coupling of the two models - full-forcing mode . . . 181
7.4 Deficits of the initial status of the coupling . . . 182
7.5 Identification of deficits in the coupling between the two models . . . 182
7.6 Interface enhancements and model adjustments . . . 185
7.6.1 Reference surface for shortwave direct radiation . . . 185
7.6.2 Extraction and transformation of physical parameters of surface, wall and roof materials and vegetation from MUKLIMO_3 to ENVI-met . . . 186
7.6.3 Soil moisture and temperature . . . 189
7.6.4 Calculation of potential temperature and specific humidity . . . 190
7.6.5 Vertical interpolation of wind speed and air temperature . . . 191
7.6.6 Wind flow calculation . . . 193
7.6.7 Time adjustment . . . 193
7.7 Calibration simulations . . . 193
7.7.1 Model area: Sealed surface . . . 194
7.7.1.1 Model run: status quo . . . 194
7.7.1.2 Model run: advanced version . . . 195

7.7.2 Model area: Meadow 201
7.7.2.1 Model run: status quo 202
7.7.2.2 Model run: version including all advancements . . . 203
7.7.3 Model area: City 205
7.8 Conclusion and outlook 207

8 Conclusion **210**

List of Figures

2.1 Model overview ENVI-met 8
2.2 Model architecture ENVI-met 9

3.1 Comparison of plants as loose conglomerate of LAD and plants as an object including three-dimensional root system 38
3.2 Dialog to create a three-dimensional root structure of a tree 41
3.3 Diurnal cycle of the air temperature and relative humidity in 2 meters height in the proof-of-concept simulations 44
3.4 Overview over the different tree geometries 46
3.5 Model area for the plant-as-object proof-of-concept simulation, effects of different tree geometries 46
3.6 Diurnal cycle of the average leaf temperature and the water access factor of the different trees 47
3.7 Diurnal cycle of the normalized latent heat flux of the different trees 48
3.8 Model area for the plant-as-object proof-of-concept simulation, effects of different microclimates 50
3.9 Effect of different microclimates on average latent heat flux 51
3.10 Effect of different microclimates on maximum leaf temperature and water access 52
3.11 Wind speed at vegetation 53
3.12 Aerodynamic resistance at vegetation 54

4.1 Monitoring and simulation site 65
4.2 Sap flow measurement 66
4.3 Diurnal variations of the forced direct (dashed lines) and diffuse (solid lines) radiation of the four simulation periods based on measurements of the meteorological station 3 km SW of the study site 69

4.4 Comparison of the measured sap flow and leaf temperature with the modeled transpiration rate and leaf temperature 73

5.1 3D-plant editing tool Albero 91
5.2 3D presentation of the isoprene flux of a tree 92
5.3 Basic tree geometry for the isoprene proof-of-concept simulation 103
5.4 Model area for the basic proof-of-concept simulations for the isoprene emission model 104
5.5 Diurnal cycle of the air temperature and relative humidity in 2 meters height in the isoprene proof-of-concept simulations 105
5.6 Isoprene emission dependence on photosynthetic active radiation 106
5.7 Isoprene emission dependence on leaf temperature 106
5.8 Local isoprene emission flux - base tree - simulation time: 09:00h, simulation date: 23.07.2003 107
5.9 Local isoprene emission flux - base tree - simulation time: 12:00h, simulation date: 23.07.2003 108
5.10 Received PAR - base tree - simulation time: 09:00h, simulation date: 23.07.2003 109
5.11 Received PAR - base tree - simulation time: 12:00h, simulation date: 23.07.2003 110
5.12 Local leaf temperature - base tree - simulation time: 09:00h, simulation date: 23.07.2003 111
5.13 Local leaf temperature - base tree - simulation time: 12:00h, simulation date: 23.07.2003 112
5.14 Diurnal cycle of the isoprene emission flux and the average stomatal resistance for the base tree as a whole - first day of simulation: 23.07.2003 . . . 113
5.15 Isoprene flux and normalized water access for the base tree over the first three simulated days: 23.-25.07.2003 115
5.16 Comparison of isoprene fluxes between high and low leaf weight scenarios and the base tree - first day of the simulation: 23.07.2003 117
5.17 Comparison of isoprene fluxes between high and low base isoprene capacity scenarios and the base tree - first day of the simulation: 23.07.2003 117

5.18 Comparison of isoprene fluxes between high and low LAD scenarios and the base tree - first day of the simulation: 23.07.2003 118
5.19 Model area for the dispersion and chemistry model proof-of-concept simulations in a simplified model area 120
5.20 Diurnal cycle of the air temperature and relative humidity in 2 meters height. Spring day and summer day scenarios 122
5.21 Graphical visualization of the different scenarios 123
5.22 Diurnal cycle of the average ozone concentration in a height of 1.8 meters - spring scenarios 125
5.23 Diurnal cycle of the average ozone concentration in a height of 1.8 meters - summer scenarios 126
5.24 Model area for the dispersion and chemistry model proof-of-concept simulations in a more complex model area 128
5.25 2D visualization of the model area including the pollution sources 129
5.26 Chemistry without isoprene: NO concentration at 11:00h in 1.8 meters height 132
5.27 Chemistry without isoprene: NO_2 concentration at 11:00h in 1.8 meters height 133
5.28 Chemistry without isoprene: O_3 reaction terms at 11:00h in 1.8 meters height 134
5.29 Chemistry without isoprene: O_3 concentration at 11:00h in 1.8 meters height 135
5.30 Chemistry without isoprene: O_3 concentration at 14:00h in 1.8 meters height 136
5.31 Chemistry including isoprene: C_5H_8 concentration at 11:00h in 1.8 meters height 137
5.32 Chemistry including isoprene: O_3 concentration at 11:00h in 1.8 meters height 138
5.33 Chemistry including isoprene: O_3 reaction terms at 11:00h in 1.8 meters height 139
5.34 Chemistry including isoprene: C_5H_8 concentration at 14:00h in 1.8 meters height 140
5.35 Chemistry including isoprene: O_3 concentration at 14:00h in 1.8 meters height 141

5.36 Diurnal cycle of the ozone concentrations with and without isoprene, average concentration in a height of 1.8 meters - Proof-of-concept-simulation in a more complex model area 142
5.37 Effect of isoprene on ozone concentration - comparison of ozone concentration with and without isoprene emission at 11:00h 143
5.38 Effect of isoprene on ozone concentration - comparison of ozone concentration with and without isoprene emission at 14:00h 144
5.39 Effect of isoprene on ozone concentration - comparison of ozone terms with and without isoprene emission at 14:00h 145

6.1 Schematics of the new wall and roof model 155
6.2 New dialog to create or alter the composition of walls / roofs 156
6.3 Visualization of different building zones. The different shades of red indicate confined spaces inside the buildings 158
6.4 Model area for the proof-of-concept simulation 159
6.5 Diurnal cycle of the boundary conditions: air temperature and humidity . . 161
6.6 Outside facade temperatures at 10:00, fourth simulation day 162
6.7 Indoor air temperature at 18:00, fourth simulation day 163
6.8 Comparison of the surface temperatures on the inside node (node 7) 164
6.9 Aerial photo of the Fraunhofer Institute for Building Physics testing site and the facade temperature measurement 165
6.10 Diurnal variations of the direct and diffuse shortwave radiation of the four simulation periods 168
6.11 Structure of the digitized uninsulated wall 169
6.12 3D visualization of the model area. The red box indicates the location of the contact thermometer 169
6.13 Comparison of the measured and modeled facade temperatures 172

7.1 Air temperature in 1.8 meters height, model area Frankfurt am Main - Status Quo 2012 183

7.2 Information memo about the converted physical parameters that need to be adjusted in the DBManager and Albero 188
7.3 Schematic visualization of the logarithmic interpolation of the wind speed between all MUKLIMO_3 height levels 192
7.4 Sealed surface: Air temperature, status quo simulation 195
7.5 Sealed surface: Air temperature, incl. all advancements but the continuous calculation of the wind flow 196
7.6 Sealed surface: Comparison of the direct shortwave radiation: MUKLIMO_3, status quo and advanced version 197
7.7 Sealed surface: Comparison of the surface temperature: MUKLIMO_3, status quo and advanced version 198
7.8 Sealed surface: Comparison of the relative wind speed change from the inflow boundary to the three-dimensional model area, incl. all advancements but the continuous calculation of the wind flow 199
7.9 Sealed surface: Comparison of the latent heat flux at the ground surface: MUKLIMO_3, advanced version excluding and including the continuous calculation of the wind flow 199
7.10 Sealed surface: Air temperature, incl. the continuous calculation of the wind flow 200
7.11 Sealed surface: Comparison of the relative wind speed change from the inflow boundary to the model area - continuous wind flow calculation . . . 201
7.12 Meadow: Air temperature, status quo simulation 203
7.13 Meadow: Air temperature, incl. all advancements 204
7.14 Meadow: Comparison of the surface temperature meadow: MUKLIMO_3, status quo and including all advancements 204
7.15 Model area City: Frankfurt am Main 205
7.16 City: Air temperature at 15:00 simulation time in 1.75 meters height in the coupled model run Frankfurt am Main 206

List of Tables

2.1 Q_{10} functions of different parameters for C_3 and C_4 plants 26

4.1 Boundary conditions of the four simulation periods 69
4.2 Model fit between the simulated and estimated (sap flow derived) transpiration rates in different cloud conditions 72
4.3 Model fit between simulated and monitored shaded leaf temperatures 76

5.1 Initial values of basic environmental and meteorological parameters 104
5.2 Different values of the altered isoprene emission regulating parameters . . . 116
5.3 Diurnal cycle of NO and NO_2 emission values for the line sources 130

6.1 Physical properties of the building materials of the three houses 160
6.2 Material properties of the components of the measured facade 166
6.3 Average meteorological conditions for the four simulation periods 167
6.4 Model fit between measured and modeled facade temperatures 170

7.1 Land use classes MUKLIMO_3 180

Index of abbreviations

AVOC	Anthropogenic Volatile Organic Compound
BVOC	Biogenic Volatile Organic Compound
IBP	Fraunhofer Institute for Building Physics Holzkirchen
LAD	Leaf Area Density
LAI	Leaf Area Index
MUKLIMO_3	Mikroskaliges urbanes Klimamodell 3-dimensionale Version
PAR	Photosynthetic Active Radiation
PET	Physiological Equivalent Temperature
PPFD	Photosynthetic Photon Flux Density
RAD	Root Area Density
SVF	Sky View Factor
UHI	Urban Heat Island
VOC	Volatile Organic Compound

1 Introduction

Urban climate and the study of the same are becoming more and more important as urban areas show significantly higher rates of population growth than rural areas. While in 1950, only around 30 percent of the world's population lived in urban areas, today already more than half of the world's population lives in urban areas. The United Nations project that by 2050 more than 66% of the world's population will live in an urban area (UN Department of Economic and Social Affairs, 2014).

This rapid urbanization not only means that more people are exposed to the effects of urban microclimate but also that the already significant environmental challenges present in urban areas will rise even further. Consequences of increased urbanization such as reduced biodiversity, growing amounts of traffic, higher demand for energy-intensive indoor cooling systems or the urban heat island effect directly affect the inhabitants' well-being and health as they are exposed to higher rates of air pollution and more intense heat waves (Güneralp and Seto, 2008; Seto et al., 2011, 2012). The negative effects of these conditions have been documented in many studies that have linked heat waves to increased circulatory issues as well as increased mortality (Basu and Samet, 2002; Clarke, 1972; Vandentorren et al., 2004). Together with the effects of climate change, which will lead to an increase of the intensity and duration of long lasting heat waves, the already high environmental stress will increase the vulnerability of urban agglomerations even further (Fujibe, 2011; Wilby, 2006).

To address these problems, urban planning strategies now incorporate not only commercial, industrial and residential interests but also take into account meso- and microclimatic considerations to cope with the effects of urban climate especially in the context of climate change and rapid urbanization. Many countries and regions have therefore implemented compulsory adaptation strategies that require vulnerability analyses and demand mitigation measures to reduce the effects of the urban

heat island as well as to control air pollution (see, e.g., KLIMZUG-program by the German Federal Ministry of Education and Research[1] or the "Mayors Adapt" program by the European Commission[2]).

Yet, for these adaptation strategies to be effective the consequences of different measures need to be appraised. Since the urban climate is characterized by a multitude of interactions between urban structure (dimensions of the buildings and the spaces between them, the street widths and street spacing), urban cover (built-up, paved, vegetated, bare soil, water), urban fabric (construction and natural materials) and the urban metabolism (heat, water and pollutants due to human activity), the effects of mitigation measures cannot easily be assessed (Oke, 2006). In evaluating different strategies and identifying the most efficient measures, microclimate models can be of great use. Climate models offer a cheap and reliable way to compare different options and evaluate and quantify the possible outcome of any adaption strategy. Furthermore they are able to simulate the effects of hypothetical scenarios or future climates at almost no costs.

Yet, given the complexity of the urban climate, any viable microclimate model needs to account for a vast number of parameters and processes. Furthermore, to understand, study and analyze the local urban microclimate as a whole, a model needs to consider all these processes and interactions with adequate accuracy. One scientifically established urban microclimate model is ENVI-met (Bruse and Fleer, 1998), which considers physical fundamentals based on the principles of fluid mechanics, thermodynamics and atmospheric physics to calculate three-dimensional wind fields, turbulence, air temperature and humidity, radiative fluxes and pollutant dispersion. The advantages of ENVI-met compared to other microclimate models like MISKAM or MITRAS (Eichhorn, 1989; Schlünzen, 1988; Schlünzen et al., 2003) lie in ENVI-met's holistic approach to simulate the complex interactions of building structures,

[1] http://www.klimzug.de/en/index.php
[2] http://climate-adapt.eea.europa.eu/mayors-adapt

atmosphere, soil, pollutant and vegetation processes in one model.

However, ENVI-met still has some limitations with regard to crucial elements that characterize the urban microclimate that will be addressed in this dissertation. Firstly, while ENVI-met is able to simulate the effects of plants onto the microclimate quite accurately, it is not capable of assessing the effects of microclimate onto plants. This is due to the way plants are digitized in ENVI-met: They are represented by loose clusters of cells that have a leaf area density, making it impossible to treat them as single organisms. Therefore, their vitality and health as well as their effects onto the microclimate and the effects of microclimates onto them as a whole cannot be assessed. Secondly, while ENVI-met's chemistry model is able to simulate the formation of tropospheric ozone by the chemical reactions of nitrogen monoxide and nitrogen dioxide, the additional effects of biogenic volatile organic compounds (BVOC) are neglected. This may result in a substantial underestimation of tropospheric ozone as BVOCs can, in the presence of higher amounts of hydroxyl radicals and nitrogen monoxide, lead to an immense additional formation of tropospheric ozone. Thirdly, more complex wall and roof structures consisting of a combination of different materials cannot be digitized. This restricts the accurate simulation of building physics such as surface temperatures and the estimation of indoor climate. Furthermore, the previously developed coupling of ENVI-met with the larger scale model MUKLIMO_3 (Huttner, 2011) shows substantial discrepancies in the near-ground surface temperatures between the two models. This is problematic because the quality of the model outputs of a microclimate model like ENVI-met, with its very limited model area, is strongly dependent on the boundary conditions driving the microclimate simulation. Hence, deficits in the coupling with a larger scale model may result in seriously distorted model results.

The aim of this dissertation is to address these limitations: After a brief introduction to ENVI-met in chapter 2, a plant-as-object model that enables the organism-based analysis of plants is introduced in chapter 3. The new implementations are

first evaluated in proof-of-concept simulations validating the general concept of the model. In a second step, the model results are evaluated against measurement data of (sap-flow derived) transpiration and leaf temperatures of urban trees (chapter 4). The potential underestimation of tropospheric ozone due to the neglection of biogenic volatile compounds is addressed in chapter 5, where an isoprene emission and chemistry model is developed. This model is subsequently evaluated in a set of proof-of-concept simulations. As a third limitation, ENVI-met's wall and roof model is approached in chapter 6: The multiple-node model is improved and enhanced so that more complex walls / roofs can now be constructed and simulated. Additionally, building zones within a building can now be defined which act as confined spaces of air volumes (rooms / flats) and allow a more accurate estimation of indoor temperatures. This estimation of indoor temperatures is evaluated in a proof-of-concept simulation, and the advanced multiple-node model is further tested against measurement data of surface temperatures of a facade. In chapter 7, the deficits in the previously developed coupling between the larger scale model MUKLIMO_3 and ENVI-met are analyzed. The problems identified in this analysis are then resolved by making various adjustments both to ENVI-met and the coupling interface. The effectiveness of these adjustments is tested in several coupled simulation runs.

Bibliography

Basu, R. and Samet, J. M. Relation between Elevated Ambient Temperature and Mortality: A Review of the Epidemiologic Evidence. *Epdidemiologic Reviews*, 21 (2):190–202, 2002.

Bruse, M. and Fleer, H. Simulating surface-plant-air interactions inside urban environments with a three dimensional numerical model. *Environment Modelling & Software*, 13(3-4):373–384, 1998.

Clarke, J. F. Some effects of the urban structure on heat mortality. *Environmental Research*, 5(1):93–104, 1972.

Eichhorn, J. *Entwicklung und Anwendung eines dreidimensionalen mikroskaligen Stadtklima-Modells.* Dissertation, Johannes Gutenberg-University Mainz, 1989.

Fujibe, F. Urban warming in Japanese cities and its relation to climate change monitoring. *International Journal of Climatology*, 31(2):162–173, 2011.

Güneralp, B. and Seto, K. C. Environmental impacts of urban growth from an integrated dynamic perspective: A case study of Shenzhen, South China. *Global Environmental Change*, 18(4):720–735, 2008.

Huttner, S. Dynamische Kopplung von MUKLIMO_3 mit dem mikroskaligen Klimamodell ENVI-met. unpublished project report, 2011.

Oke, T. Initial guidace to obtain represensatitive meteorological observations at urban sites. World Meteorological Organization: Instruments and observing methods. Report No. 81, 2006.

Schlünzen, H. *Das mesoskalige Transport- und Strömungsmodell 'METRAS' - Grundlagen, Validierung, Anwendung.* Dissertation, University of Hamburg, 1988.

Schlünzen, K. H., Hinneburg, D., Knoth, O., Lambrecht, M., Leitl, B., Lopez, S., Lüpkes, C., Panskus, H., Renner, E., Schatzmann, M., Schoenemeyer, T., Trepte, S., and Wolke, R. Flow and Transport in the Obstacle Layer: First Results of the Micro-Scale Model MITRAS. *Journal of Atmospheric Chemistry*, 44:113–130, 2003.

Seto, K. C., Fragkias, M., Güneralp, B., and Reilly, M. K. A Meta-Analysis of Global Urban Land Expansion. *plos one*, 6(8):1–9, 2011.

Seto, K. C., Güneralp, B., and Hutyra, L. R. Global forecasts of urban expansion to 2030 and direct impacts on biodiversity and carbon pools. *Proceedings of the National Academy of Sciences of the United States of America*, 104(40):16083–16088, 2012.

UN Department of Economic and Social Affairs. *World Urbanization Prospects: The 2014 Revision*. United Nations, New York, 2014.

Vandentorren, S., Suzan, F., Medina, S., Pascal, M., Maulpoix, A., Cohen, J. C., and Ledrans, M. Mortality in 13 French Cities During the August 2003 Heat Wave. *American Journal of Public Health*, 94(9):1518–1520, 2004.

Wilby, R. L. Past and projected trends in London's urban heat island. *Weather*, 58 (7):251–260, 2006.

2 The microclimate model ENVI-met

2.1 Introduction

ENVI-met is a prognostic, three-dimensional, high resolution microclimate model. With its physical fundamentals that are based on the principles of fluid mechanics, thermodynamics and the laws of atmospheric physics it is able to calculate three-dimensional wind fields, turbulence, air temperature and humidity, radiative fluxes and pollutant dispersion (Bruse, 1999).

One of the unique features of ENVI-met is the detailed modeling of vegetation. With its high spatial resolution ENVI-met allows the simulation of the individual photosynthesis rates taking into account the local solar radiation, the air temperature and humidity, the wind speed, the CO_2 concentration and many other parameters (Bruse, 2004b).

The ENVI-met model has established itself as a well recognized standard method for assessing the urban microclimate. The quality of the model is constantly evaluated by mostly independent publications and dissertations (among others, Nikolova et al., 2011; Yang et al., 2012).

2.2 General model properties

The ENVI-met model basically consists of a one-dimensional boundary model, that includes vertical profiles of different meteorological parameters up until a height of 2500 meters (approx. the height of the planetary boundary layer) and a three-dimensional core model that includes all atmosphere, soil, building and vegetation processes. A so called “nesting” area surrounds the core model. Its purpose is

to create stable lateral boundary conditions for the core model (figure 2.1) (Bruse, 1999).

Figure 2.1: Model overview ENVI-met

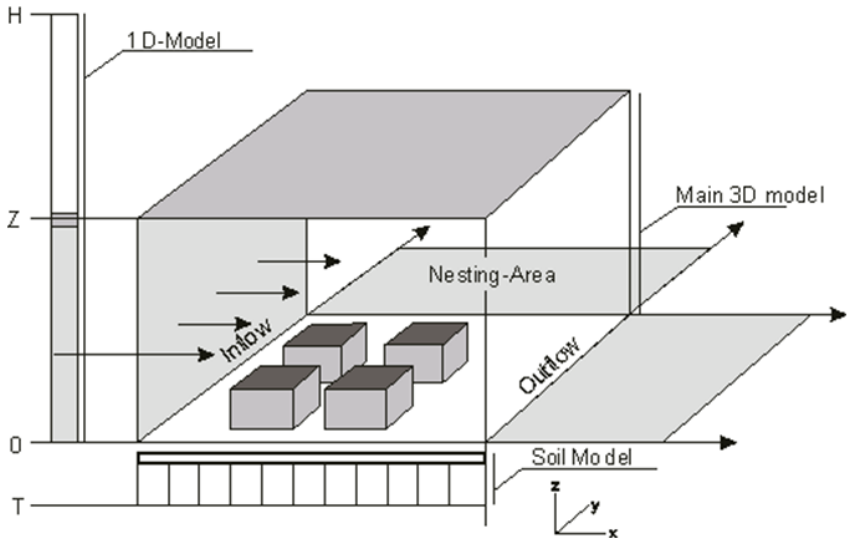

(Bruse, 1999)

The typical spatial and temporal resolution is 0.5 meters to 10 meters and 1 second to 5 seconds, the simulated time usually lies between 24 hours and 5 days (Bruse, 2015a). The size of the model areas highly depend on the spatial resolution of the model. Due to the limits in computation power and memory, 250×250 cells horizontally and 30 cells vertically are typically the maximum amount of cells used.

Due to the high resolution, objects in the urban environment such as buildings and vegetation can be modeled directly without a parametrization, whereas subscale processes are integrated through explicit parametrization (Bruse, 1999).

Figure 2.2 shows the model architecture of the core model with the main processes included in the model.

Figure 2.2: Model architecture ENVI-met

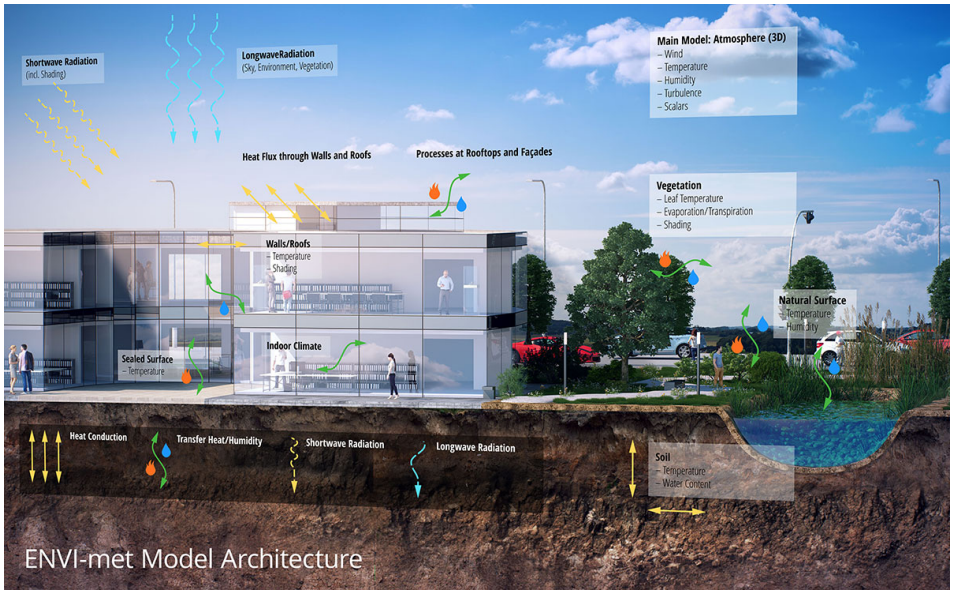

(Bruse, 2010)

2.3 1D boundary model

Due to the fact that ENVI-met only simulates part of the atmosphere, boundary conditions are required for the lateral and vertical borders of the 3D model. To provide these boundary conditions, the 1D boundary model generates one-dimensional profiles for meteorological parameters such as air temperature, specific humidity, wind vectors (horizontal), kinetic energy and turbulent exchange. To ensure stable laminar conditions the boundary model extends to an altitude of 2500 meters (average height of the planetary boundary layer). The one-dimensional boundary model with its horizontally homogeneous vertical profiles is then used to provide data on the borders of the 3D model (Bruse, 1999).

2.3.1 Initial values

The required input data to create the vertical profiles of the 1D boundary model are latitude, longitude, the date and duration of the simulation, the horizontal wind speed at 10 meters height, the roughness length, the air temperature in 2 meters height, the specific humidity in 2500 meters altitude and the relative humidity in 2 meters height. To generate realistic boundary conditions of the variables mentioned above, the one-dimensional model is integrated over time until the vertical profiles of the parameters reach a quasi-stationary state (Bruse, 1999).

2.3.2 Lateral boundary conditions

The ENVI-met model includes three different types of lateral boundary conditions (Bruse, 2015b):

- **open lateral boundary conditions:** The values of the next grid point close to the border are copied to the border each time step.
- **forced lateral boundary conditions:** The values of the one-dimensional model are copied to the border.
- **cyclic lateral boundary conditions:** The values of the downstream model border are copied to the upstream model border.

The open and the cyclic lateral boundary condition types allow to start simulations with only a few initial parameters. However, with these lateral conditions it is not possible to recreate specific scenarios, making it very difficult to compare the simulation output with a real situation. The forcing method, in contrast, allows to reconstruct real scenarios or imaginary scenarios by defining a diurnal cycle of boundary conditions for various meteorological parameters such as radiation, air temperature or humidity (obtained from, for example, measured data or data from other models).

2.3.3 Linkage 1D boundary 3D core model

In order to ensure a "smooth" transition of the horizontally homogenous border conditions of the 1D border model and the 3D core model, the atmospheric cells at the border of the 3D model should not be occupied with buildings or other non-porous objects. To adequately simulate the local microclimate, the area of interest should be located in the center of the model area (Bruse, 1999). For the upper boundary of the core model, the values of the one-dimensional boundary model are being directly transferred to the top border of the 3D model. To ensure horizontal homogeneity at the upper border of the 3D model, the vertical extent of the 3D model should be at least twice as large as the tallest structures in the model (Bruse, 1999).

2.4 The 3D core model

The three-dimensional core model consists of three orthogonal orientated axes, which generate a three-dimensional cube, the model area. The model area consists of a number of cells which represent different objects such as buildings, vegetation or atmosphere. The number of cells is dependent on the model area dimensions and its spatial resolution. Each cell is defined by its physical properties. For example, a building cell is defined by its material types, and the material type is defined by the specific heat capacity and other parameters. In combination with databases of all the different objects, this structure allows a detailed reconstruction of an urban environment. In the default settings the lowest atmospheric grid cell is vertically split into 5 smaller cells to better replicate the dynamic processes at the boundary layer close to the ground surface (Bruse, 1999).

At the bottom side, this three-dimensional atmosphere model is linked to a three-dimensional soil model which reaches down to a depth of five meters (see figure 2.2).

A vegetation model extends into both the atmosphere and the soil model.

2.4.1 The atmosphere model

In the atmosphere model the main processes on the urban climate are simulated: wind field, air temperature and humidity distribution, turbulence, gas and particle dispersion, radiation, exchange processes on ground and building surfaces.

2.4.1.1 Wind field

The spatial and temporal evolution of the wind field is calculated using the non-hydrostatic three-dimensional Navier-Stokes equation. Using the Boussinesq approximation, the density of air can be assumed to be constant and thus be eliminated from the Navier-Stokes equations, resulting in equations 2.1, 2.2 and 2.3. Since air is now - based on the Boussinesq approximation - treated as an incompressible fluid, the conservation of mass needs to be ensured (equation 2.4) (Bruse, 1999; Bruse and Fleer, 1998; Huttner, 2012).

$$\frac{\partial u}{\partial t} + u_i \frac{\partial u}{\partial x_i} = -\frac{\partial p'}{\partial x} + K_m \left(\frac{\partial^2 u}{\partial x_i^2} \right) + f(v - v_g) - S_u \tag{2.1}$$

$$\frac{\partial v}{\partial t} + u_i \frac{\partial v}{\partial x_i} = -\frac{\partial p'}{\partial y} + K_m \left(\frac{\partial^2 v}{\partial x_i^2} \right) - f(u - u_g) - S_v \tag{2.2}$$

$$\frac{\partial w}{\partial t} + u_i \frac{\partial w}{\partial x_i} = -\frac{\partial p'}{\partial z} + K_m \left(\frac{\partial^2 w}{\partial x_i^2} \right) + g \frac{\theta(z)}{\theta_{ref}(z)} - S_w \tag{2.3}$$

$$\frac{\partial u}{\partial x} + \frac{\partial v}{\partial y} + \frac{\partial w}{\partial z} = 0 \tag{2.4}$$

with p' as the local pressure perturbation, K_m as the local exchange coefficient, $\theta(z)$

as the potential temperature at height level z, f as the Coriolis parameter with the geostrophic wind components u_g and v_g (currently switched off), S_u, S_v and S_w as local source / sink terms accounting for wind speed reduction due to vegetation and u_i, x_i as the three-dimensional advection and diffusion terms written in Einstein summation ($u_i = u, v, w$; $x_i = x, y, z$) (Bruse and Fleer, 1998; Huttner, 2012).

2.4.1.2 Air temperature and humidity

The distribution of the potential temperature θ and specific humidity q is calculated using the combined advection-diffusion equation including internal sources and sinks: Q_θ and Q_q. K_θ and K_q in equations 2.5 and 2.6 describe the diffusion coefficients of heat and water vapor, whereas c_p shall be the specific heat capacity of air under the pressure p. The term $\frac{1}{c_p p}\frac{\partial Q_{lw}}{\partial z}$ accounts for the change in air temperature due to divergence of the longwave radiation. The internal sources and sinks of the equations present linkages to the vegetation model (see chapter 2.4.3) - quantifying the effects of the exchange processes of vegetation and atmosphere on the distribution of the air temperature and humidity in the atmosphere (Bruse, 1999; Bruse and Fleer, 1998; Huttner, 2012).

$$\frac{\partial \theta}{\partial t} + u_i \frac{\partial \theta}{\partial x_i} = K_\theta \left(\frac{\partial^2 \theta}{\partial x_i^2} \right) + \frac{1}{c_p p} \frac{\partial Q_{lw}}{\partial z} + Q_\theta \tag{2.5}$$

$$\frac{\partial q}{\partial t} + u_i \frac{\partial q}{\partial x_i} = K_q \left(\frac{\partial^2 q}{\partial x_i^2} \right) + Q_q \tag{2.6}$$

2.4.1.3 Turbulence

Due to the huge variations in spatial and temporal scales, the direct numerical simulation of turbulent flow conditions and exchange processes require extreme resolutions in space and time resulting in an increase of computing time. To be able

to simulate turbulences in a coarser resolution and in less computation time, closure models are used that parametrize the turbulent flows presenting mean flow characteristics. Turbulences in ENVI-met are parametrized using a E-ϵ 1.5 order closure model. The E-ϵ model basically consists out of two prognostic equations, one describing the production for turbulent energy and the other its dissipation. In contrast to first order closure models the E-ϵ model allows the simulation of advective processes in horizontally inhomogeneous environments without needing as much computation time as closure models of higher order (Ali-Toudert, 2005; Bruse, 1999).

2.4.1.4 Gas and particle dispersion model

The gas and particle dispersion model allows the simulation of emission and dispersion of various gases and particles in the model area. Apart from the dispersion and emission, ENVI-met also simulates the deposition as well as chemical reactions of the gases NO, NO_2 and O_3. The dispersion of gases and particulate matter in the atmosphere is calculated using the advection-diffusion equation (equation 2.7) with χ for the local concentration of the gas/particle (unit: mg(χ) per kg(Air)) (Bruse, 2007).

$$\begin{aligned} &\frac{\partial \chi}{\partial t} + u\frac{\partial \chi}{\partial x} + v\frac{\partial \chi}{\partial y} + w\frac{\partial \chi}{\partial z} = \\ &\frac{\partial}{\partial x}\left(K_\chi \frac{\partial \chi}{\partial x}\right) + \frac{\partial}{\partial y}\left(K_\chi \frac{\partial \chi}{\partial y}\right) + \frac{\partial}{\partial z}\left(K_\chi \frac{\partial \chi}{\partial z}\right) + \\ &Q_\chi(x,y,z) + S_\chi(x,y,z) \end{aligned} \tag{2.7}$$

Similar to the combined advection-diffusion equation of the air temperature and humidity field, sources and sinks terms (Q_χ and S_χ) are included in the equation. These terms represent sedimentation or chemical conversion processes by locally

increasing or decreasing the gas or particle concentration (Bruse, 2007). Chapter 5 presents the introduction of isoprene into the dispersion and the chemical reaction model.

2.4.1.5 Radiation

The incoming longwave and shortwave radiation on the upper border of the model domain are calculated based on "a two-stream approximation and some empirical formula" (Bruse and Fleer, 1998). To accurately calculate the incoming longwave radiation, the amount and distribution of aerosols and gases together with their wavelength dependent absorption and emission characteristics would be needed. Since this information is usually not available, ENVI-met simplifies the calculation by only taking the effects of water vapor into account - the error of this method can, due to the broad absorption band of water vapor and thus the resulting overlaps, be ignored (Bruse, 1999).

This way the incoming longwave radiation can be - as long as there are no modifications due to e.g. vegetation - approximated using the sum of absorption and emission dependent on the temperature of the overlaying atmosphere layers N (equation 2.8) (Ali-Toudert, 2005; Bruse, 1999).

$$Q_{lw}^{\downarrow} = \sum_{n=1}^{N} \sigma T^4(n)[\epsilon_n(m + \Delta m) - \epsilon_n(m)] \tag{2.8}$$

with ϵ_n as the emissivity, m as the amount of water vapor between the lower boundary of layer n and the height z and $m + \Delta m$ as the amount of water vapor between the the upper boundary of layer n and the height z.

The incoming shortwave radiation at the top of the model (equation 2.9) is calculated by integrating the radiation of the sun I_0 for the wavelengths between $\lambda = 0.29\mu$m and $\lambda = 4.0\mu$m taking into account the optical mass m as a function of the sun's

height angle, the Rayleigh scattering α_R and the Mie scattering α_M (Bruse, 1999).

$$Q^*_{sw} = \int_{0,29}^{4,0} I_0(\lambda) \exp\{-\alpha_R(\lambda)m + \alpha_M(\lambda)m\} d\lambda \tag{2.9}$$

$$Q^0_{sw,dir} = Q^*_{sw} - Q_{sw,abs} \tag{2.10}$$

The direct shortwave radiation on the upper boundary of the model $Q^0_{sw,dir}$ results from the difference of the incoming shortwave radiation Q^*_{sw} and the absorption of the shortwave radiation by water vapor $Q_{sw,abs}$ (equation 2.10). The incoming diffuse shortwave radiation $Q^0_{sw,dif}$ at the top of the model (equation 2.11) for clear sky conditions is calculated after Brown and Isfält (1974) (Bruse, 1999):

$$Q^0_{sw,dif} = Q^0_{sw,dir} \sin h \left(\frac{\Upsilon(h)}{1 - \Upsilon(h)} \right) \tag{2.11}$$

with $\Upsilon(h) = \frac{1}{1+8(\sin h)^{0.7}}$ and h as the sun's height angle. In cloudy conditions the incoming diffuse shortwave radiation $Q^0_{sw,dif,cloudy}$ is calculated after Taesler and Anderson (1984):

$$Q^0_{sw,dir,cloudy} = Q^0_{sw,dir} \left(1 - \frac{N}{8} \right)$$

$$Q^0_{sw,dif,cloudy} = \left(\frac{Q^0_{sw,dir} \sin h}{1 - \Upsilon(h)} \right) \left(\frac{a_s - 1}{a_c a_s - 1} \right) - Q^0_{sw,dir,cloudy} \sin h \tag{2.12}$$

with N as the cloud cover in eighths, a_c as the mean albedo of the clouds depending on their height level and a_s as the mean albedo of the soil.

Modification of the radiation due to objects like vegetation and buildings in the model are represented using a concept of five reduction coefficients σ, ranging from 0 (totally obstructed) to 1 (undisturbed) (Ali-Toudert, 2005; Bruse, 1999; Bruse and

Fleer, 1998). The five reduction coefficients are:

- Sky View Factor (SVF) σ_{svf}
- Effects of vegetation on the direct shortwave radiation $\sigma_{sw,dir}$
- Effects of vegetation on the diffuse shortwave radiation $\sigma_{sw,dif}$
- Effects of vegetation on the incoming longwave radiation $\sigma_{lw}^{\downarrow}$
- Effects of vegetation on the outgoing longwave radiation $\sigma_{lw}^{\uparrow}$

The sky view factor σ_{svf} indicates the amount of visible sky from the center of a grid point. It is calculated by:

$$\sigma_{svf} = \frac{1}{360} \sum_{\pi=0}^{360} \cos \omega(\pi) \tag{2.13}$$

with ω as the maximum cutoff angle in spatial direction π.

The effects of vegetation (coefficients 2 to 5 above) on radiation largely depend on the Leaf Area Index (LAI) (one-sided leaf area per area of ground surface). Equations 2.14 to 2.17 show the calculation of the reduction coefficients for the effects of vegetation on the direct shortwave radiation (2.14), the diffuse shortwave radiation (2.15), the incoming longwave radiation (2.16) and the outgoing longwave radiation (2.17) with z being the height level, z_p as height at the top of the plant and LAI* as the LAI with respect to the inclination of the sun (Bruse and Fleer, 1998).

$$\sigma_{sw,dir}(z) = \exp(F \cdot \mathrm{LAI}^*(z)) \tag{2.14}$$

$$\sigma_{sw,dif}(z) = \exp(F \cdot \mathrm{LAI}(z, z_p)) \tag{2.15}$$

$$\sigma_{lw}^{\downarrow}(z, z_p) = \exp(F \cdot \mathrm{LAI}(z, z_p)) \tag{2.16}$$

$$\sigma_{lw}^{\uparrow}(0,z) = \exp(F \cdot \mathrm{LAI}(0,z)) \tag{2.17}$$

Using the reduction coefficients the shortwave radiation budget $Q_{sw}(z)$ in height z can then be written as (Bruse and Fleer, 1998):

$$Q_{sw}(z) = \sigma_{sw,dir}(z)Q^0_{sw,dir} + \sigma_{sw,dif}(z)\sigma_{svf}(z)Q^0_{sw,dif} + (1-\sigma_{svf}(z))Q^0_{sw,dir} \cdot a_s$$

While the second term accounts for the diffuse shortwave radiation, the first and third terms account for the direct shortwave radiation. Since the diffuse radiation is assumed isotropic in the model, the reduction of diffuse radiation in the height z is approximated by the reduction of clear view of the sky using the sky view factor. Reflections of shortwave radiation between buildings are calculated using the albedo of the surfaces (a_s) (Bruse, 1999).

The downward longwave radiation $Q_{lw}^{\downarrow}(z)$ and upward longwave radiation $Q_{lw}^{\uparrow}(z)$ for a grid cell in a given height z are calculated by equations 2.18 and 2.19 (Bruse and Fleer, 1998):

$$Q_{lw}^{\downarrow}(z) = \sigma_{lw}^{\downarrow}(z,z_p)Q_{lw,0}^{\downarrow}(z) + (1-\sigma_{lw}^{\downarrow}(0,z))\epsilon_f\sigma_B\overline{T_{f+}^4} + (1-\sigma_{svf}(z))Q_{lw}^{\leftrightarrow}(z) \tag{2.18}$$

$$Q_{lw}^{\uparrow}(z) = \sigma_{lw}^{\uparrow}(0,z)\epsilon_s\sigma_B\overline{T_0^4} + (1-\sigma_{lw}^{\uparrow}(0,z))\epsilon_f\sigma_B\overline{T_{f-}^4} \tag{2.19}$$

with $Q_{lw}^{\leftrightarrow}(z)$ as the longwave radiation emitted from buildings, ϵ_f and ϵ_s as the emissivity of the leaves and the surface, $\overline{T_{f+}^4}$ and $\overline{T_{f-}^4}$ as the average foliage temperature of the overlying / underlying vegetation layer, z_p as the plant's height and T_0 as the surface temperature.

2.4.1.6 Ground and building surfaces

In contrast to the upper and lateral boundaries of the 3D model, ground and building surfaces represent actual physical boundaries (Bruse, 1999).

To calculate the ground surface temperature T_0 the energy balance of the ground surface is iteratively solved (equation 2.20).

$$0 = Q_{sw,net} + Q_{lw,net} - G_0 - H_0 - LE_0 \tag{2.20}$$

with $Q_{sw,net}$ as the net incoming shortwave radiation, $Q_{lw,net}$ as the net longwave radiation, G_0 as the soil heat flux, H_0 as the sensible heat flux and LE_0 as the latent heat flux (Bruse, 1999).

$$Q_{sw,net} = (\cos\beta^* \cdot Q_{sw,dir}(z=0) + Q_{sw,dif}(z=0)) \cdot (1 - a_s) \tag{2.21}$$

The net shortwave radiation of the ground surface ($z = 0$) is calculated taking into account the direct shortwave radiation $Q_{sw,dir}$, the diffuse shortwave radiation $Q_{sw,dif}$ and the albedo of the surface a_s (equation 2.21). For the incoming direct radiation ($Q_{sw,dir}$) Lambert's cosine law is used to estimate the actual radiation on the surface with β^* as the angle between sun height and the normal of the surface. Since the diffuse radiation is assumed isotropic, the angle of the diffuse radiation ($Q_{sw,dif}$) does not need to be taken into account. For artificial surfaces the albedo (a_s) is taken directly from the database entry and used as a constant, while the albedo for natural surfaces is calculated dynamically taking into account the sun's height angle, the soil moisture of the topmost layer and the water content at saturation after Idso et al. (1975) (Bruse, 1999).

The calculation of the net longwave radiation for equation 2.20 is calculated taking into account the unobstructed net longwave radiation ($Q_{lw,net}^{unobs}$) from the sky and

the net longwave radiation emitted by objects like buildings or vegetation ($Q^{obs}_{lw,net}$) (Bruse, 1999):

$$Q_{lw,net} = \sigma_{svf} Q^{unobs}_{lw,net} + (1 - \sigma_{svf}) Q^{obs}_{lw,net}$$

The soil heat flux G_0 is calculated by:

$$G_0 = \lambda_s (k = -1) \frac{T_0 - T_{k=-1}}{0.5 \Delta z_{k=-1}}$$

with $k = -1$ as the topmost height level of the soil model, λ_s as the heat transfer coefficient of the soil layer, T_0 as the surface temperature, $T_{k=-1}$as the temperature of the soil layer in the depth $k = -1$ and $\Delta z_{k=-1}$ as the thickness of the topmost grid cell of the soil model (Ali-Toudert, 2005; Huttner, 2012).

The turbulent sensible and latent heat fluxes H_0 and LE_0 in equation 2.20 are implemented as functions of the turbulent exchange coefficients between the ground surface and the lowest grid cell of the atmosphere (Ali-Toudert, 2005; Huttner, 2012).

Since Version 4.0 the calculation of the surface temperature of buildings is carried out using a three-node model which is based on the works of Terjung and O'Rourke (1980). Terjung and O'Rourke's multiple-node transient state model allows the calculation of facade temperatures for an infinite amount of nodes in a wall. For the first implementation of the method in ENVI-met (Huttner, 2012), three nodes were applied to a wall, allowing the calculation of the temperature on the outside, the inside and the center of the wall.

The energy balance is then calculated with the temperature of the node n at time t, the air temperature, the heat transfer coefficient and the heat conduction coefficient of the wall as well as the distance of the nodes (Huttner, 2012; Terjung and O'Rourke, 1980). For non-greened facades, the humidity at building facades is set to the humidity of the adjacent atmosphere cell.

A more detailed discussion of the node model can be found in chapter 6, where advancements in the multiple-node model are introduced and evaluated.

2.4.2 The soil model

The soil model is connected to the underside of the atmosphere model. Within the soil model hydrological and thermodynamical processes up to a depth of $z = -5\text{m}$ are calculated. The vertical extent of 5 meters guarantees constant conditions regarding the temperature and water content of the soils within the typical simulation periods of 24 hours to 5 days as well as providing enough space for roots of large plants. Since soils have a great impact on the microclimate and are typically vertically inhomogeneous ENVI-met soil are organized in layers of different soil types which each have different adjustable hydrological and thermodynamical parameters.

As the dynamics of the hydrological and thermodynamical processes decrease with increasing depth, ENVI-met's soil profiles are horizontally divided into 20 non-equidistant layers where the upper layers show finer vertical resolutions (five topmost layer thickness $\Delta z = 0.01\text{m}$) than deeper layers (bottom layer thickness $\Delta z = 0.5\text{m}$). Within natural soils heat and water exchange is simulated whereas in impermeable surfaces only heat fluxes are calculated (equations 2.22 and 2.23) (Bruse, 1999; Bruse and Fleer, 1998).

$$\frac{\partial T_s}{\partial t} = \kappa_s \frac{\partial^2 T_s}{\partial z^2} \tag{2.22}$$

$$\frac{\partial \eta}{\partial t} = D_\eta \frac{\partial^2 \eta}{\partial z^2} + \frac{\partial K_\eta}{\partial z} - S_\eta(z) \tag{2.23}$$

with T_s as the soil temperature, t as the time, η as the volumetric water content, D_η as the hydraulic diffusivity of the soil, K_η as the hydraulic conductivity of the soil and S_η as the water extraction from the soil by plants. For natural soils the thermal

diffusivity κ_s is a function of the soil moisture η, for impermeable soils κ_s is a user defined, constant parameter (Bruse, 1999; Huttner, 2012).

2.4.3 The vegetation model

Vegetation in ENVI-met is represented by clusters of cells having a leaf area density in the atmosphere model and root area density in the soil model, allowing the remodeling of the distribution and shape of roots and crowns of plants. Apart from the effects of these cell clusters on the wind field and the radiation, the modeled plants use biological control mechanisms that regulate the exchange of CO_2 and water vapor with the atmosphere. Based on the calculation of the stomatal conductance using Jacobs' $A - g_s$ model (Jacobs, 1994), vegetation in ENVI-met tries to balance the water use and CO_2 assimilation to maximize carbon gain and minimize water loss (Bruse, 2004b). With the main factors of the stomatal conductance being the photosynthesis rate and the respiration, a large number of atmospherical and biological parameters such as the carbon fixation type of the plant, the water vapor gradient between the leaf and the atmosphere, the leaf surface temperature, the photoactive radiation and the access to water are taken into account to calculate the exchange fluxes between the plants and the atmosphere (Bruse, 2004b).

The exchange of heat and moisture on the leaf surfaces are implemented as sources and sinks in the calculation of air temperature and humidity (equations 2.24 and 2.25) with z as the height, Q_θ as the potential temperature and Q_q as the specific humidity (Bruse, 2004a). The heat fluxes are divided into $J_{f,h}$ for the direct heat flux at the leaf surface, $J_{f,evapo}$ for the moisture flux at the leaf surface due to evaporation and $J_{f,trans}$ for the moisture flux at the leaf surface due to transpiration (Bruse and Fleer, 1998).

$$Q_\theta(z) = \mathrm{LAD}(z) J_{f,h} \tag{2.24}$$

$$Q_q(z) = \mathrm{LAD}(z)(J_{f,evapo} + J_{f,trans}) \tag{2.25}$$

The direct heat flux $J_{f,h}$, the moisture flux due to evaporation $J_{f,evapo}$ and $J_{f,trans}$ for the moisture flux at the leaf surface due to transpiration are calculated by equations 2.26, 2.27 and 2.28 with T_f as the leaf temperature, T_a as the air temperature, Δq as the humidity gradient between leaf and atmosphere, r_s as the stomatal resistance, r_a as the aerodynamic resistance of the leaf, f_w as the ratio of moistened leaf area and δ_c as a factor being 1 if transpiration or evaporation can occur ($\Delta q \geq 0$) and being 0 if only condensation can occur (Bruse, 2004b,c).

$$J_{f,h} = 1.1 r_a^{-1}(T_f - T_a) \tag{2.26}$$

$$J_{f,evapo} = r_a^{-1}\Delta q \delta_c f_w + r_a^{-1}(1 - \delta_c)\Delta q \tag{2.27}$$

$$J_{f,trans} = \delta_c(r_a + r_s)^{-1}(1 - f_w)\Delta q \tag{2.28}$$

The linkage of the vegetation model with the soil model via the roots of the plants enables the estimation of water loss in the soil due to the water uptake of plants. The calculation of water loss in the soil model is weighted by the local root surface area, the water content of the soil cells and the current hydraulic conductivity. Further details are shown in chapter 3.

To simulate the complex behavior of living organisms that react and interact with the microclimatic environment, the vegetation model includes a stomata model calculating the stomatal conductance based on the works of Jacobs' empirical $A - g_s$ model (Jacobs, 1994). The main hypothesis of the $A - g_s$ model is that the goal of plants is to operate the stomatal conductance in a way that while the water loss of

the plant is minimized, the CO_2 assimilation and thus the carbon gain is maximized (Bruse, 2004b; Damour et al., 2010; Jacobs, 1994).

Although there is little to no evidence of a direct causal relationship between the stomatal conductance and the photosynthesis, many models as well as Jacobs' $A-g_s$ model use the assumption above and make use of the empirically observed relations between the stomatal conductance for water g_s and the photosynthesis A by modeling the photosynthesis to directly draw conclusions onto the stomatal behavior and thus stomatal conductance (Damour et al., 2010; Jacobs, 1994). Equation 2.29 shows the relation of the net photosynthetic rate A_n and the stomatal conductance g_s. The calculation of the net photosynthetic rate together with the CO_2 concentration at the leaf's surface C_s and in the leaf itself C_i allows the prognosis of the stomatal conductance. The factor 1.6 accounts for the different diffusivities of CO_2 and H_2O (Jacobs, 1994).

$$g_s = 1.6\frac{A_n}{C_s - C_i} \tag{2.29}$$

By default Jacobs' $A - g_s$ takes into account two factors that restrict the net photosynthesis rate A_n:

1. insufficient light
2. insufficient CO_2

1) Insufficient light

Under circumstances of insufficient light A_n is calculated by equation 2.30 with ϵ as the initial quantum use efficiency, I_a as the photosynthetically active radiation (PAR) and R_d as the dark respiration (Jacobs, 1994).

$$A_n = \epsilon I_a - R_d \tag{2.30}$$

Since the PAR accounts for approximately 48 percent of the global radiation, the

incoming shortwave radiation in the height z in ENVI-met is reduced by 52 percent using equation 2.31.

$$\mathrm{PAR}(z) = 0.48 \cdot (\sin\phi Q_{sw,dir}(z) + Q_{sw,dif}(z)) \tag{2.31}$$

with $\sin\phi Q_{sw,dir}(z)$ as the direct shortwave radiation on a perpendicular surface to the sun's height ϕ and the diffuse shortwave radiation $Q_{sw,dif}$ taking into account the SVF and possible reflections of e.g. walls (Bruse, 2004b).

The initial quantum use efficiency ϵ is calculated using equation 2.32.

$$\epsilon = \epsilon_0 \frac{C_i - \Gamma}{C_i + 2\Gamma} \tag{2.32}$$

C_i represents the CO_2 concentration in the leaf, Γ the carbon compensation point and ϵ_0 is the theoretical quantum requirement of the Calvin cycle (≈ 0.025 mg J^{-1} PAR) including a loss factor depending on the carbon fixation type of the plants. For C_3 plants an ϵ_0 of 0.017 mg J^{-1} PAR and for C_4 plants an ϵ_0 of 0.014 mg J^{-1} PAR is taken. In case of C_4 plants Γ is almost zero (Bruse, 2004b; Jacobs, 1994).

2) Insufficient CO_2

In conditions of high light intensities and limiting CO_2 concentrations the photosynthetic rate at saturation of light A_m can be described by equation 2.33.

$$A_m = (C_i - \Gamma) \cdot g_m \ \ [0.001 \cdot \phi_{CO_2}] \tag{2.33}$$

with $[0.001 \cdot \phi_{CO_2}]$ being a conversion factor from ppm into mg m^{-3} and g_m as the mesophyll conductance (Bruse, 2004b).

Combining both equations (equation 2.30 and 2.33) the effects of insufficient light and insufficient CO_2 on the net photosynthetic rate A_n can be written as equation 2.34 with R_d parametrized as $R_d = A_m/9$ after van Heemst (1986).

$$A_n = (A_m + R_d) \cdot \left(1 - \exp\left(\frac{-\epsilon I_a}{A_m + R_d}\right)\right) - R_d \tag{2.34}$$

To avoid unrealistically high values for A_n in conditions where neither light nor CO_2 are limiting the photosynthesis, a maximum possible photosynthetic rate at saturation of light $A_{m,max}$ is defined using equation 2.35. Taking into account a saturation response, the equation provides a smooth transition between A_m and $A_{m,max}$.

$$A_m = A_{m,max} \cdot \left(1 - \exp\left(\frac{-\epsilon I_a}{A_m + R_d}\right)\right) - R_d \tag{2.35}$$

Some of the chemical processes of the photosynthesis are dependent on the ambient temperature. To account for this, the temperature dependencies of Γ, g_m and maximum possible photosynthetic rate at saturation of light $A_{m,max}$ are approximated using a Q_{10} function which describes the reaction velocity increase based on an increase of temperature. Table 2.1 shows the different parameters and their values at a temperature of 25°C together with the Q_{10} values and the sensitivity ranges T_1 and T_2 (Jacobs, 1994).

Table 2.1: Q_{10} functions of different parameters for C_3 and C_4 plants

	Parameter (X)	**X(@25)**	$\boldsymbol{Q_{10}}$ **value**	$\boldsymbol{T_1}$**[°C]**	$\boldsymbol{T_2}$**[°C]**
C_3	ϵ_0 [mg J^{-1} PAR]	0.017	-	-	-
	Γ [μmol mol^{-1}]	45	1.5	-	-
	g_m [mm s^{-1}]	7.0	2.0	5	28
	$A_{m,max}$ [mg m^{-2} s^{-1}]	2.2	2.0	8	38
C_4	ϵ_0 [mg J^{-1} PAR]	0.014	-	-	-
	Γ [μmol mol^{-1}]	2.8	1.5	-	-
	g_m [mm s^{-1}]	17.5	2.0	13	36
	$A_{m,max}$ [mg m^{-2} s^{-1}]	1.7	2.0	13	38

Based on Jacobs (1994)

Since the CO_2 concentration inside the leaf C_i is unknown, the concentration is parametrized by the stomatal responses to air humidity using equation 2.36.

$$\frac{C_i}{C_s} = f + (1 - f)\frac{\Gamma}{C_s} \tag{2.36}$$

Here C_s stands for the CO_2 concentration at the leaf's surface and f for a factor taking into account the stomatal response to humidity (equation 2.37). D_s as the saturation deficit between the air and the leaf's surface and D_{max} as the maximum saturation deficit (45 g kg^{-1} for crops and deciduous forests after Choudhury and Monteith, 1986). f_0 represents the value of f at $D_s = 0$ g kg^{-1} - for C_3 plants 0.85, for C_4 plants 0.5 (Bruse, 2004b; Jacobs, 1994).

$$f = f_0 \left(1 - \frac{D_s}{D_{max}}\right) + f_{min} \left(\frac{D_s}{D_{max}}\right) \tag{2.37}$$

f_{min} is calculated using the cuticular conductance g_c (set to a value of 0.25 mm s^{-1}) and g_m as the mesophyll conductance (equation 2.38).

$$f_{min} = \frac{g_c}{g_c - g_m} \tag{2.38}$$

Since the original $A - g_s$ model by Jacobs does not include the effects of water stress, the advancements of the $A - g_s$ model by Calvet et al. (1998) are implemented in ENVI-met. The implementation adds the factor ξ to the calculation of the mesophyll conductance (equation 2.39), thus reducing the conductance at low levels of soil moisture.

$$g_m = \xi \cdot g_m^{'} \tag{2.39}$$

ξ is defined as:

$$\xi = \frac{\eta - \eta_{wilt}}{\eta_{fc} - \eta_{wilt}} \tag{2.40}$$

with η as the volumetric soil moisture, η_{wilt} as the water content at wilting point and η_{fc} as the field capacity (Bruse, 2004b; Calvet et al., 1998).

Using the equations above the stomatal conductance for CO_2 $g_{s_{CO_2}}$ [mm s^{-1}] can be calculated using the following equation:

$$g_{s_{CO_2}} = \left(A_n - A_{m,min} \cdot \frac{D_s}{D_{max}} \cdot \frac{(A_n + R_d)}{(A_m + R_d)} + R_d \left(1 - \frac{(A_n + R_d)}{(A_m + R_d)} \right) \right) \frac{1}{(C_s - C_i)\phi_{CO_2}}$$

with

$$A_{m,min} = 0.001 g_m \cdot (C_{min} - \Gamma)\phi_{CO_2}$$

C_{min} being the CO_2 concentration inside the leaf (C_i) when the saturation deficit between the air and the leaf's surface (D_s) reaches the maximum saturation deficit D_{max} (after equations 2.36, 2.37 and 2.38) is calculated by:

$$C_{min} = \frac{g_c C_s + g_m \Gamma}{g_c + g_m}$$

To avoid negative values of stomatal conductances, the net photosynthetic rate A_n (calculated by equation 2.34) is limited by:

$$A_n = \max(A_{m,min}, A_n)$$

Having calculated the stomatal conductance for CO_2 $g_{s_{CO_2}}$ [mm s^{-1}] the total conductance for water vapor $g_{s,c}$ [m s^{-1}] of the leaf including stomatal and the cuticular conductances can be written as:

$$g_{s,c} = 1.6 \cdot 1000 g_{s_{CO_2}} + g_c \tag{2.41}$$

2.5 Conclusion

As could be seen above, the ENVI-met model consists of a network of complex submodels interacting with each other to adequately simulate the microclimatic conditions in urban environments. With its holistic approach a large variety of different research areas can be studied using ENVI-met, such as meteorological processes (turbulence production, wind flow etc.), processes in soil science (soil moisture fluxes), building physics (surface temperatures, heat fluxes), atmospheric chemistry (dispersion and reaction of pollutants) and botany (transpiration of plants).

However, the ENVI-met model still has some shortcomings. The following limitations will be addressed in the remainder of this dissertation: In the present state ENVI-met is able to simulate the effects of plants onto the microclimate quite accurately but is not capable of assessing the effects of microclimate onto plants since plants are represented by loose clusters of grid cells rather than a uniform object / organism. Furthermore, while the chemistry model is able to simulate the formation of tropospheric ozone by photolyzation of nitrogen dioxide and its destruction by reacting with nitrogen monoxide, the release of isoprene and its additional contribution to the formation of tropospheric ozone is disregarded as of yet. While the introduction of a multiple-node model into ENVI-met (Huttner, 2012) showed big improvements in the calculation of facade temperatures, the implementation of only three nodes limits the complexity of a wall or roof structure to only one material. More complex walls or roofs consisting of a combination of different materials such as a combination of brick, heat insulation and plaster cannot be digitized. The possibility to create coupled simulation runs between ENVI-met and the larger scale model MUKLIMO_3, where MUKLIMO_3 provides boundary conditions for ENVI-met (Huttner, 2011), shows substantial discrepancies in the near-ground surface temperatures between the two models.

Bibliography

Ali-Toudert, F. *Dependence of Outdoor Thermal Comfort on Street Design in Hot and Dry Climate.* Dissertation, Albert-Ludwigs-Universität Freiburg, 2005.

Brown, G. and Isfält, E. *Solar Irradiation and Sun Shading Devices.* Stockholm: Report R19:1974, National Swedish Council for Building Research, 1974.

Bruse, M. *Die Auswirkungen kleinskaliger Umweltgestaltung auf das Mikroklima. Entwicklung des prognostischen numerischen Modells ENVI-met zur Simulation der Wind-, Temperatur- und Feuchteverteilung in städtischen Strukturen.* Dissertation, Ruhr-Universität Bochum, 1999.

Bruse, M. ENVI-met documentation `http://www.envi-met.com/documents/Envimet30.PDF`. 16.04.2015, 2004a.

Bruse, M. ENVI-met implementation of the Jacobs $A - g_s$ Model to calculate the stomata conductance `http://envi-met.com/documents/new_a_gs.pdf`. 15.04.2015, 2004b.

Bruse, M. ENVI-met 3.0: Updated Model Overview `http://www.envi-met.com/documents/papers/overview30.pdf`. 17.04.2015, 2004c.

Bruse, M. ENVI-met implementation of the gas/ particle dispersion and deposition model PDDM `http://envi-met.com/documents/sources.PDF`. 13.04.2015, 2007.

Bruse, M. Von ENVI-met bis BOTworld. Mikroskalige Simulation des Stadtklimas in der Environmental Modelling Group Mainz. unpuplished presentation, 2010.

Bruse, M. ENVI-met `http://www.envi-met.info/hg2e/doku.php?id=intro:modelconept`. 17.04.2015, 2015a.

Bruse, M. ENVI-met LBC `http://www.envi-met.info/hg2e/doku.php?id=lbc-types`. 17.04.2015, 2015b.

Bruse, M. and Fleer, H. Simulating surface-plant-air interactions inside urban environments with a three dimensional numerical model. *Environment Modelling & Software*, 13(3-4):373–384, 1998.

Calvet, J.-C., Noilhan, J., Roujean, J.-L., Bessemoulin, P., Cabelguenne, M., Olioso, A., and Wigneron, J.-P. An interactive vegetation SVAT model tested against data from six contrasting sites. *Agricultural and Forest Meteorology*, 92(2):73–95, 1998.

Choudhury, B. J. and Monteith, J. L. Implications of stomatal response to saturation deficit for the heat balance of vegetation. *Agricultural and Forest Meteorology*, 36 (3):215–225, 1986.

Damour, G. T., Simonneau, T., Cochard, H., and Urban, L. An overview of models of stomatal conductance at the leaf level. *Plant, Cell and Environment*, 33:1419–1438, 2010.

Huttner, S. Dynamische Kopplung von MUKLIMO_3 mit dem mikroskaligen Klimamodell ENVI-met. unpublished project report, 2011.

Huttner, S. *Further development and application of the 3D microclimate simulation ENVI-met*. Dissertation, Johannes Gutenberg-University Mainz, 2012.

Idso, S. B., Jackson, R. D., Reginato, R. J., Kimball, B. A., and Nakayama, F. S. The Dependence of Bare Soil Albedo on Soil Water Content. *Journal of Applied Meteorology*, 14(1):109–113, 1975.

Jacobs, C. M. J. *Direct impact of atmospheric CO2 enrichment on regional transpiration*. Dissertation, Agricultural University Wageningen, Wageningen., 1994.

Nikolova, I., Janssen, S., Vos, P., Vranken, K., Mishra, V., and Berghmans, P. Dispersion modelling of traffic induced ultrafine particles in a street canyon in Antwerp, Belgium and comparison with observations. *Science of the Total Environment*, 412-413:336–343, 2011.

Taesler, R. and Anderson, C. A method for solar radiation computings using routine meteorological observations. *Energy and Buildings*, 7(4):341–352, 1984.

Terjung, W. and O'Rourke, P. Simulating the casual elements of urban heat islands. *Boundary-Layer Meteorologie*, 19(1):93–118, 1980.

van Heemst, H.D.J. Physiological principles. In Van Keulen, H. and Wolf, J., editors, *Modelling of agricultural production: weather, soils and crops*, pages 13–26. Pudoc Wageningen, 1986.

Yang, X., Zhao, L., Bruse, M., and Meng, Q. An integrated simulation method for building energy performance assessment in urban environments. *Energy and Buildings*, 54:243–251, 2012.

3 Plant vitality assessment - Introduction of the plant-as-object model

Helge Simon[1]

[1] Department of Geography, Johannes Gutenberg University Mainz, 55099 Mainz, Germany

3.1 Introduction

Vegetation plays a vital role in urban environments: Aside from the aesthetic benefits, trees and other vegetation help mitigate the effects of the urban heat island (UHI) by increasing the latent heat flux through evapotranspiration, resulting in lower air temperatures. They cast shade on buildings and other artificial surfaces that otherwise would heat up more and store more energy, thus reducing the total energy surplus of an urban environment (Bowler et al., 2011; Norton et al., 2015). The reduction of the surface temperature of facades also reduces the cooling demand, which again reduces the heat transfer into the atmosphere. Furthermore, "functioning" vegetation absorbs CO_2 through the processes of photosynthesis, releasing O_2 into the air, and helps reduce emissions such as particulate matter (Janhäll, 2015; Sgrigna et al., 2015; Song et al., 2015).

Given these important benefits, vegetation in all its different forms (parks, trees, facade greening etc.) is the most advised strategy to mitigate the UHI effect and to help improve the urban microclimate (Andersson-Sköld et al., 2015; Norton et al., 2015; Phelan et al., 2015; Salata et al., 2015). Vegetation, however, will only be able to deliver the benefits outlined above if its own requirements and preferences regarding location and microclimate are met. These requirements range from the right mix of sun and shade, adequate ventilation, humidity and air temperature to appropriate soil and water supply (Eppel et al., 2012; Larcher, 2004; Savi et al., 2015).

Research on the effects of vegetation onto the microclimate is vast and has been conducted for decades (e.g. Dimoudi and Nikolopoulou, 2003; Honjo and Takakura, 1990; Robitu et al., 2006; Susca et al., 2011; Vinet et al., 2000; Wilmers, 1990; Ali-Toudert and Mayer, 2007). Most of the studies show that vegetation contributes to significant reductions in air temperature as well as biometeorological indices such as the physiological equivalent temperature (PET) and thus helps alleviate urban

heat island effects. With regard to climate adaptation strategies, many authors hence advise to increase the amount of vegetation in urban environments (Lee et al., 2016; Norton et al., 2015; Oliveira et al., 2011). The vitality and sustainability of vegetation in the complex urban environments, especially with regard to the impacts of climate change, however, is mostly disregarded.

While research on climate change, drought and microclimate in general has been conducted for crops, forests and other agricultural environments (e.g. Allen et al., 2010; Challinor et al., 2009; Lindner et al., 2014; Lobell et al., 2008; Zhu et al., 2013), research about the effects of microclimate onto the health and livability of urban vegetation and especially street trees is quite scarce. Only most recently, urban tree health assessment studies have been conducted (Eppel et al., 2012; Gillner et al., 2013, 2016; May et al., 2013; Moore, 2013; Roman et al., 2014; Savi et al., 2015). These studies conclude that common urban tree species in the temperate zones (such as oak, lime, maple and plane trees) already find themselves under immense heat and drought stress during long lasting heat waves. They further indicate that the combination of the urban climate and the effects of climate change will lead to even more alarming situations which the common urban tree species of today might not be able to tolerate (Eppel et al., 2012; Savi et al., 2015). Particularly in these conditions, when the beneficial effects of trees on the microclimate would be most needed, the environmental stress not only hinders the positive effects but also detrimentally affects the health of the plant, causing increased costs for care-taking, watering etc. to preserve the plant in the unfavorable conditions. To mitigate these problems and create sustainable planning programs, urban vegetation needs to be chosen carefully, taking into account the plant's special requirements and its complex interactions with the environment.

Several studies have examined the resistance capabilities of different species in the context of urban microclimate and climate change by planting various tree species in urban environments and subsequently monitoring numerous plant physiological

parameters. However, as almost all of the current studies (such as Eppel et al., 2012) are of an empirical nature, only a limited number of combinations of locations, microclimate and plant can be investigated. An active, concrete and optimized location decision based on the plant's needs *and* characteristics of the location's microclimate as well as the interactions between plant and microclimate cannot be realized using these empirical approaches due to the enormous costs and expenditure of time. Appropriate location, microclimate and plant combinations that ensure both the health and sustainability of the plants as well as maximized climate benefits can only be found in combination with model approaches.

A first step in developing such model approaches to tree health assessment and active, optimized location decisions is undertaken in this chapter. While ENVI-met has proven itself to accurately describe the effects of plants onto the microclimate, the new implementations focus on the reverse direction: The effects of microclimate onto plants. The implementation of new analyzation methods that allow to simulate the complex microclimatic requirements and interactions of plants with the environment required the development of new techniques in ENVI-met's vegetation model. This chapter will introduce these new methods, starting with the new plant-as-object model that allows to model plants as uniform organisms. New calculation and analyzation methods are presented that allow to estimate the environmental stress of plants, to simulate the plant's behavior depending on its surroundings and to assess its health in an urban microclimate. These new methods are subsequently evaluated in two proof-of-concept simulations.

3.2 The plant-as-object model

ENVI-met allows to model vegetation in two ways. Grasses, corn, hedges and other plants that only feature a simple vertical structure, i.e. do not have overhanging canopies, are modeled as so called "simple plants". The leaf area density (LAD) of

simple plants is represented by 10 layers in the atmosphere, while the roots consist of 10 layers of root area density (RAD) in the soil model. Plants with a more complex canopy, like trees, are represented by clusters of cells that have an LAD, providing a three-dimensional shape of the plant. Because these plants are carrying their own three-dimensional geometry, they are called "3D-plants" and are managed by a special editor program called "Albero".

In previous versions of ENVI-met, the 3D-plants were loose clusters of LAD that just happened to create the shape of a tree. The root model of 3D-plants was, just like the root model of simple plants, a column of RAD cells extending vertically into the soil model. While these simplifications were accurate enough to simulate the effects of vegetation onto the microclimate, the model did not permit statements about the plants. To evaluate the reverse effects - microclimate onto vegetation -, the model needs to be adjusted to resemble plants as uniform organisms. In order to do so, an object model is created that allows to aggregate the processes calculated at the individual leaf level back to the associated plant. Additionally, a three-dimensional root model is introduced that also integrates all processes of the plant, making a 3D-plant a complete organism.

3.2.1 Integration of LAD cells to canopies

In previous versions, 3D-plants did already allow the remodeling of the distribution of LAD cells and thus the shape of a tree. The cells themselves, however, were not part of the tree but instead acted as individual leaves. With the new advancements, LAD cells are now part of a bigger object, which allows the evaluation of a plant as an organism. Figure 3.1 shows the advancement in an exaggerated form: On the left hand side, a 3D-plant was digitized as a loose conglomerate of LAD. The single cells do not belong to each other, not allowing any conclusions about the plant as such. The right hand side shows a different 3D-plant with the new plant-as-object

model. Here, the single LAD cells belong to each other, forming a bigger entity.

Figure 3.1: Comparison of plants as loose conglomerate of LAD and plants as an object including three-dimensional root system

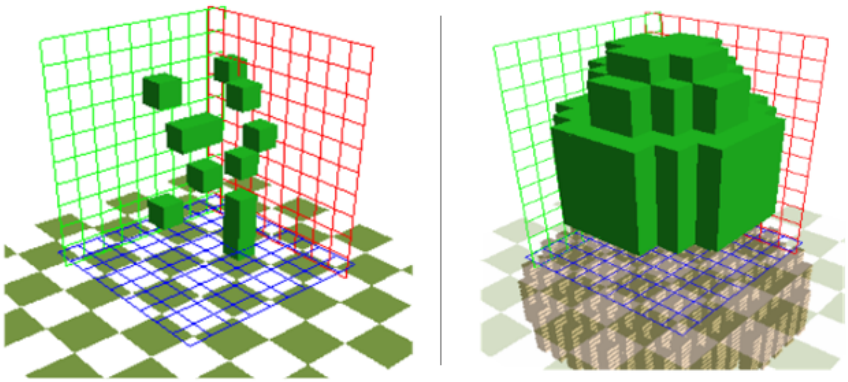

To examine the processes of trees as a whole, the calculated effects at leaf scale needed to be integrated to the plant level (Bruse and Simon, 2015):

$$J_{trans}^{sum} = \iiint_{C(X,Y,Z)} \mathrm{LAD}(x,y,z) \cdot \rho_a j_{f,trans}(x,y,z) dxdydz \tag{3.1}$$

with J_{trans}^{sum} as the total sum of transpiration of the tree canopy in [g(H_2O) s^{-1}], $C(X,Y,Z)$ as the three-dimensional space of the tree crown, LAD as the Leaf Area Density inside the crown at cell x,y,z, $j_{f,trans}$ as the local transpiration flux at leaf scale and ρ_a as the density of air.

In case tree crowns overlap with crowns of other trees, which would result in multiple occupancy of the same grid cells, the LAD cells with the higher LAD take the grid cell while still belonging to their corresponding tree. The "losing" LAD grid cells are subsequently removed from the other tree.

3.2.2 Implementing a three-dimensional root model

In ENVI-met, the amount of water uptake through the roots of a plant is determined by the transpiration of the plant. The transpired water, regulated by the $A - g_s$ stomata model (cf. chapter 2.4.3), is extracted from the soil occupied by the roots of the plant. Since the root system of a tree plays a vital role in the transpiration and many other processes of plants (water stress etc.), a three-dimensional root model was developed to calculate the object-based water access and extraction of soil water. Other than the LAD cells, the three-dimensional root structure is defined implicitly by a small set of parameters. The vertical distribution of the roots is determined by a one-dimensional profile of root area density RAD(z) reaching from the surface $z = 0$ to the lowest part of the root at $z = R_z$. To enable vertical distribution patterns, the root profile is subdivided into 10 equidistant layers representing the root area in the layers of depth $1 \cdot R_z/10, 2 \cdot R_z/10, ..., 10 \cdot R_z/10$. The horizontal extension is defined by a radius R_{xy} around the tree's definition point x_c, y_c (which normally equals the stem's location). The root's radius can be adjusted individually for each of the root's 10 vertical layers (Bruse and Simon, 2015).

Having defined the geometry of the root by the vertical extent of the root together with the radius for each layer, the actual amount of root surface area RSA in each layer is calculated by the root area density of the layer RAD(z) and its horizontal extent R_{xy}. Since absolute values of the root area density are almost impossible to acquire, the root area density of a layer represents nothing but a weighting factor to calculate the share of root surface area for each vertical layer. The extraction of water from the soil model due to transpiration at the tree's leaves depends on the share of RSA, weighted with the water availability in the soil.

The absolute RSA in a grid cell (i, j, k) in the soil model can be written as (Bruse and Simon, 2015):

$$\mathrm{RSA}(i,j,k) = \mathrm{RAD}(i,j,k)\Delta x_i \Delta y_j \Delta z_k \tag{3.2}$$

The root surface area of a tree can thus be written as (Bruse and Simon, 2015):

$$\mathrm{RSA}^{tree} = \iiint\limits_{R(X,Y,Z)} \mathrm{RAD}(x,y,z)dxdydz \tag{3.3}$$

with $R(X,Y,Z)$ as the three-dimensional root zone space occupied by the roots of the tree.

Analogously to the leaf model, soil cells cannot be occupied by roots of more than one tree. Here the tree's root cells with the higher RAD will occupy the soil cell, reducing the root model of the other tree. Artificial soil materials like asphalt or concrete also reduce the amount of root cells of a tree since it cannot extend its roots there (Bruse and Simon, 2015).

Figure 3.2 shows the dialog to create a three-dimensional root structure. The dialog offers predefined sets of root structures and shows the resulting root surface area RSA of the structure on the fly.

To calculate the object-based water access, the water distribution in the soil needs to be modeled. The loss of water in the soil due to plants depends on the fraction of root surface in the soil segment, as well as on the level of difficulty to extract water out of the soil. The transpiration model and the distribution of water extraction are handled in two processes: First, the transpiration rate of the leaves is adjusted by the last known soil water conditions. Second, the transpired water is actually extracted from the soil, resulting in a new soil water condition for the next update of the transpiration rate. This two-step iterative approach entails that in case a tree fails to extract the water it transpired, the adjustments to the new soil conditions will not be handled before the following transpiration calculation (Bruse and Simon, 2015).

Figure 3.2: Dialog to create a three-dimensional root structure of a tree

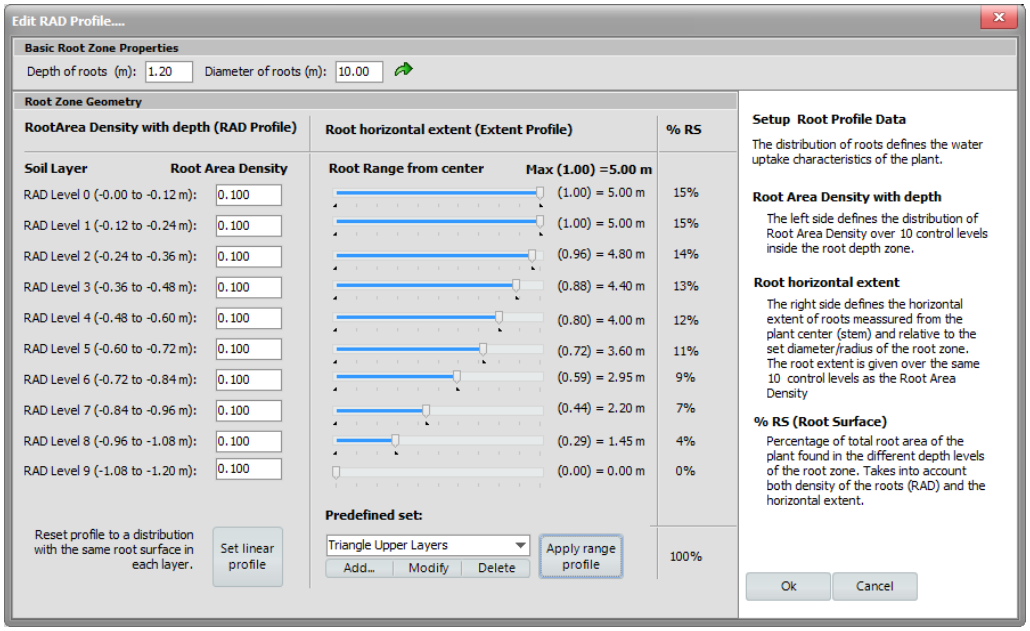

The water uptake $S_\eta(i,j,k)$ in [m^3 Water /m^3 Soil $\cdot \mathrm{s}^{-1}$] by the roots is defined as:

$$S_\eta(i,j,k) = \phi_\eta(i,j,k) \cdot \frac{1}{\rho_w} J_{trans}^{sum} \cdot (\Delta x_i \cdot \Delta y_j \cdot \Delta z_k)^{-1} \tag{3.4}$$

with ρ_w as the density of water (const. $= 998.2$ [kg/m^3]) and ϕ_η as a non-dimensional water distribution parameter calculated in equation 3.5. Taking into account the root surface area, the water availability and the current hydraulic conductivity in the respective soil layer, it manages the accessibility of water for the plant (Bruse and Simon, 2015).

The water availability of the plant is weighted by the water content of the soil cells and the current hydraulic conductivity, making soil cells where the water content approaches the wilting point (ϕ_{water}) and the hydraulic conductivity (D_η) is low harder to access.

$$\phi_\eta(i,j,k) = \frac{\phi_{water}(i,j,k) D_\eta(i,j,k) \mathrm{RAD}(i,j,k) \Delta x_i \Delta y_j \Delta z_k}{\mathrm{RSA}_w^{tree}} \tag{3.5}$$

ϕ_{water} is a water access function given by:

$$\phi_{water} = \frac{\eta - \eta_{wilt}}{\eta_{fc} - \eta_{wilt}} \tag{3.6}$$

where η is the current volumetric soil water content of the soil layer, η_{wilt} the water content at the permanent wilting point and η_{fc} the water content at field capacity. The calculation's result is the relative distance of actual water content from field capacity to the permanent wilting point, making it a good soil indicator for plant water stress. The maximum value of ϕ_{water} is set to 1 for an unrestricted water access, and the lower limit is set to 0.001 for maximum water stress.

RSA_w^{tree} [m^2] in equation 3.5 is the water availability weighted for the entire plant's root surface area. It is calculated by integrating the water access factor and the soil's hydraulic conductivity of all affected root cells taking into account their dimension (Bruse and Simon, 2015):

$$\mathrm{RSA}_w^{tree} = \iiint\limits_{R(X,Y,Z)} \phi_{water} D_\eta \mathrm{RAD}(x,y,z) dx dy dz \tag{3.7}$$

To obtain water access information for the whole tree, the average water access factor needs to be scaled up to the tree's root system ϕ_{water}^{tree} as described in the following equation 3.8:

$$\phi_{water}^{tree} = \iiint\limits_{R(X,Y,Z)} \phi_{water}(x,y,z) \frac{\mathrm{RSA}(x,y,z)}{\mathrm{RSA}^{tree}} dx dy dz \tag{3.8}$$

With these new implementations, ENVI-met's vegetation model is now able to simulate not only the effects of plants onto the microclimate but should also be able to

assess the plants' vitality and the effects of the microclimate onto this vitality.

3.3 Proof-of-concept simulations for the plant-as-object model

In the following section, two proof-of-concept simulations are conducted in order to assess the validity of the plant-as-object model. For each of the proof-of-concept simulations, the model results are checked for plausibility against theoretically derived expectations about the trees' vitality and their microclimatic performance. Both proof-of-concept simulations will analyze three aggregated tree parameters that reflect the trees' vitality and their microclimatic performance: latent heat flux, leaf temperatures and water access. In the first proof-of-concept simulation, the effect of different tree geometries onto these aggregated tree parameters is examined under uniform microclimatic conditions. In the second proof-of-concept simulation, the effects of different microclimatic environments onto the aggregated tree parameters are examined for a uniform tree geometry.

Both proof-of-concept simulations use the same meteorology, which shall resemble a warm summer day during a summer's dry spell. The diurnal cycle for the boundary conditions of the air temperature and the relative humidity in 2 meters height are displayed in figure 3.3. The wind speed in 10 meters height was set to 1.5 m s^{-1} and the wind direction to southwest.

Figure 3.3: Diurnal cycle of the air temperature and relative humidity in 2 meters height in the proof-of-concept simulations

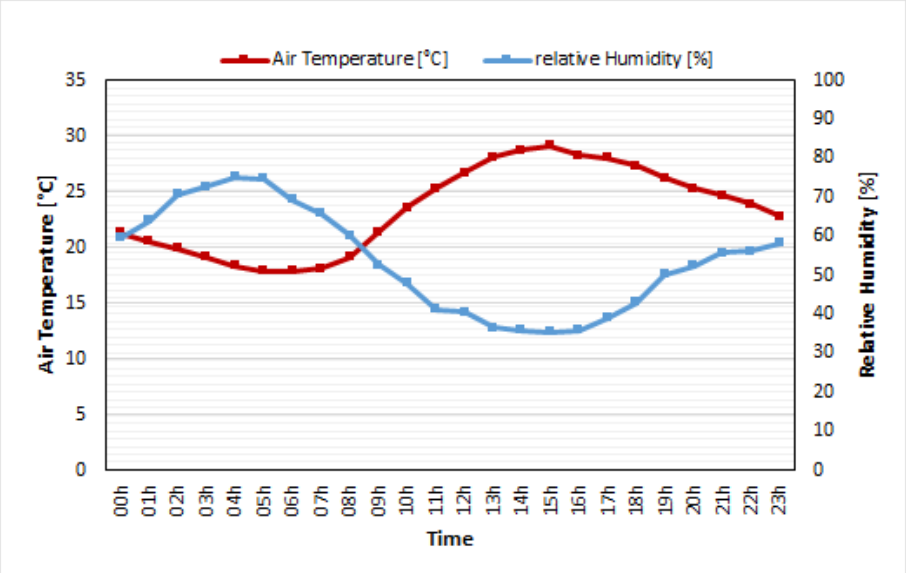

3.3.1 Proof-of-concept simulations assessing the effect of different tree geometries

To examine the effects of different canopy sizes and root volumes on the trees' vitality and microclimatic performance, three different versions of a "base" tree were generated. The versions are based on permutations in canopy sizes and root volumes that were conducted using linear scaling: While the base tree has, for example, a canopy height of 12 meters, the up-scaled tree has a canopy height of 24 meters, and the down-scaled tree has a canopy height of 6 meters. The resulting three trees are:

- Base tree: medium sized canopy, medium root volume (canopy height: 12 m, canopy width: 9 m, root depth: 1.5 m, root diameter: 7 m)
- Up-scaled tree: larger sized canopy, bigger root volume (canopy height: 24 m, canopy width: 19 m, root depth: 3 m, root diameter: 14 m)

- Down-scaled tree: smaller sized canopy, smaller root volume (canopy height: 6 m, canopy width: 5 m, root depth: 0.75 m, root diameter: 3.5 m)

With regard to the effects of these different tree geometries, the basic expectation is that bigger trees will be more resistant to heat stress than smaller trees due to their more beneficial surface-area-to-volume ratio and their bigger root systems. With their higher surface-area-to-volume ratio, smaller trees are more exposed to direct radiation as relatively more leaves are directly illuminated by the sun. This leads to higher leaf temperatures as well as to a higher photosynthesis rate, increasing transpiration and thus water loss. It is therefore assumed that an inverse relationship exists between the size of the tree's canopy and the average leaf temperatures. In addition, bigger root systems should allow larger trees to access more water, hence retaining a larger water access factor.

As far as the latent heat flux is concerned, the picture is expected to look more complex: On the one hand, the small trees' higher photosynthesis rates should initially result in increased transpiration rates and thus latent heat flux. On the other hand, as their smaller root systems provide them with less access to water, these elevated transpiration rates most likely cannot be upheld during the midday hours, when direct radiation and ambient air temperatures are especially high. In order to avoid losing too much water, the smaller trees are expected to increase their stomatal resistances, resulting in a clear midday depression in transpiration. This reduction in transpiration, however, will only lead to even higher leaf temperatures, putting the smaller trees under even more heat stress. Larger trees, in contrast, should have access to more water thanks to their bigger root systems and thus be able to uphold their transpiration rates during midday, allowing them to keep their leaf temperatures lower.

To ensure the best results for the linear scaling of the trees, the resolution for the simulation was set to 1 meter in x, y and z direction. Figure 3.4 shows the different tree geometries, from left to right: down-scaled tree, base tree and up-scaled tree.

Figure 3.4: Overview over the different tree geometries

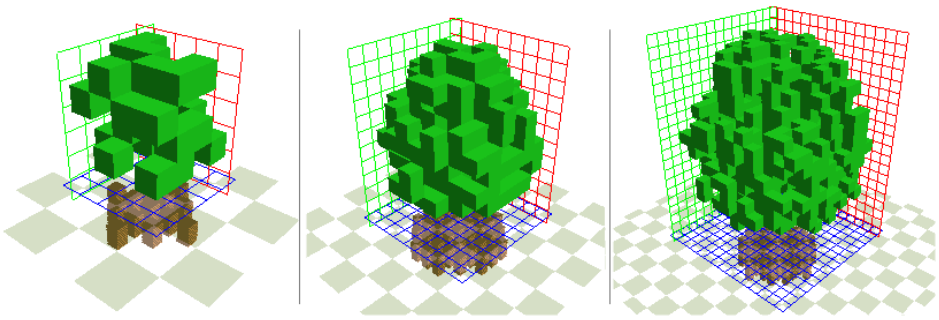

From left to right: down-scaled tree, base tree and up-scaled tree

To reduce various effects of the local microclimate on the aggregated tree parameters and enable a longer simulation period, the model area was kept small ($30 \times 30 \times 35$ grids) and very simple. Figure 3.5 shows the model area.

Figure 3.5: Model area for the plant-as-object proof-of-concept simulation, effects of different tree geometries

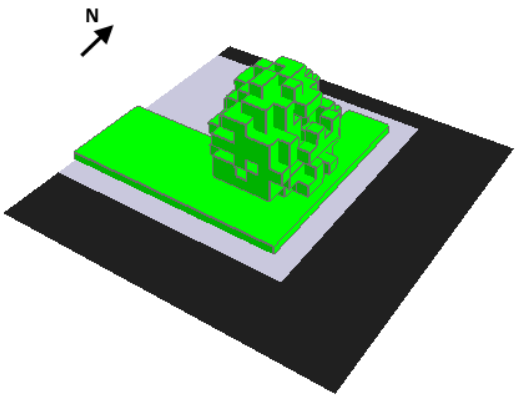

Model area dimensions: $30 \times 30 \times 35$ grids; vertical and horizontal resolution: 1 meter; location: Mainz, Germany

Figure 3.6: Diurnal cycle of the average leaf temperature and the water access factor of the different trees

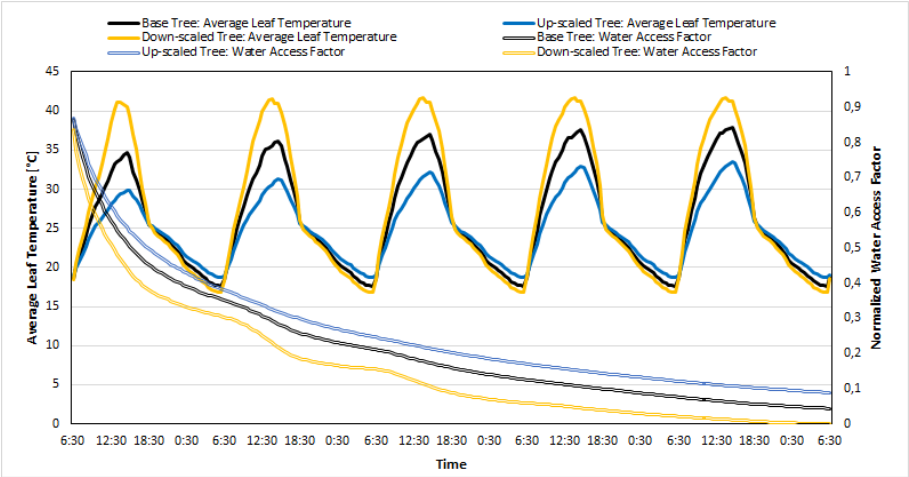

The results of these proof-of-concept simulations show that, as expected, the average leaf temperature correlates inversely with the size of the trees: the larger the tree, the lower the average leaf temperatures (see figure 3.6). The diurnal cycle of the average leaf temperatures of the different trees in figure 3.6 shows that the down-scaled tree, even when its water access factor is still relatively high, reaches average leaf temperatures of over 40°C. Leaf temperatures that high could cause damages to the leaves which could result in the death of the down-scaled tree after several days. In contrast, the average leaf temperatures of the up-scaled tree do not exceed 33°C during the course of the simulation. A comparison of the water access factors for the trees also confirms the expectations: The up-scaled tree with its bigger root system has better access to water than the smaller trees, although the water access factors for all three trees decline substantially over the course of the simulation period.

Figure 3.7 shows the normalized latent heat flux of the three trees. Since the actual heat fluxes differ very much because of the different sizes of the trees, the normalized latent heat flux is a better basis for comparing the heat fluxes between the trees. The normalized values show that, relative to the amount of leaves, the down-scaled

Figure 3.7: Diurnal cycle of the normalized latent heat flux of the different trees

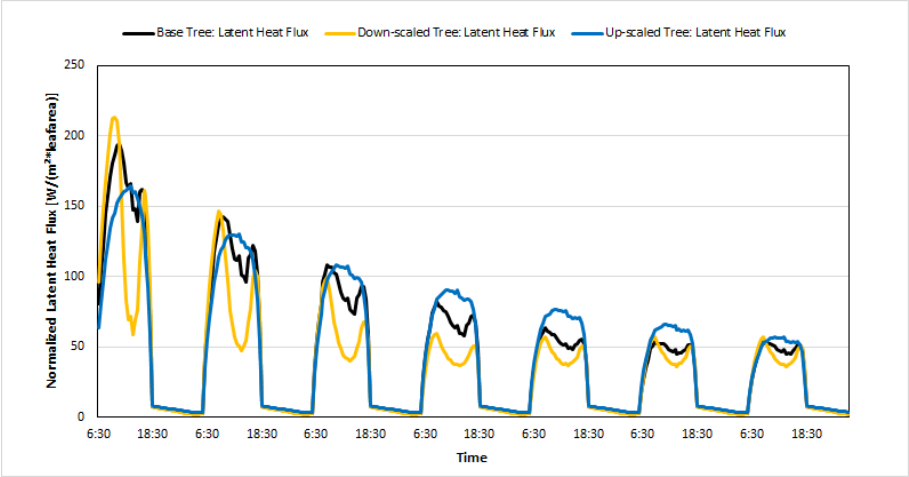

and the base tree transpire more water than the up-scaled tree in the morning hours of the first and second day. At midday, however, the normalized latent heat flux of the smaller trees shows a strong midday depression, while the normalized latent heat flux of the up-scaled tree retains a bell-shaped curve (especially in the first three days of the simulation). Again, this corroborates the theoretical assumptions and thus the quality of the new plant-as-object model. Over the course of the simulation period, a general decline of the latent heat flux for all trees is clearly visible. This is caused by the declining water access factors of the trees. After day three, the shape of the latent heat flux curve of the up-scaled tree also begins to flatten out, indicating that the up-scaled tree also increases its stomatal resistance around midday due to the increasing water shortage. The repeating patterns visible for the down-scaled tree after day four and for the base tree after day six are caused by ENVI-met which, in order to prevent instabilities, resets the soil moisture to certain values in case it drops below a minimum value.

Summing up, the simulation results show that bigger trees with their more favorable surface-area-to-volume ratio and bigger root systems are more resistant to heat and water stress, confirming the theoretically derived expectations and thus validating

the plant-as-object model. This is also true for the more detailed expectations that larger trees should be able to retain lower leaf temperatures and higher transpiration rates during midday, while smaller trees suffer from higher leaf temperatures and a marked midday depression in transpiration rates.

Moreover, the results indicate that there seems to be a dilemma: To be more likely to survive severe heat and dry spells, smaller trees would have to grow bigger to profit from more favorable surface-area-to-volume ratios and larger root volumes; however, as they are more stressed by the extreme conditions, such growth cannot easily be achieved. This implies that smaller trees need an increased amount of nurturing early in their lifetime, when they are still highly susceptible to heat and water stress; as they grow older and bigger, they should eventually require less protection from heat and dry spells.

3.3.2 Proof-of-concept simulation assessing the effect of different microclimates

In the second part of the proof-of-concept-simulations for the plant-as-object model, the effects of different microclimates onto the aggregated tree vitality parameters are examined. In order to isolate the effects of the different microclimates, the tree parameters were kept constant and the trees were digitized in a model area that features different microclimates. Figure 3.8 shows the model area. Its dimensions are $200 \times 120 \times 50$ meters in a horizontal and vertical resolution of 2 meters. The geographical location is Mainz, Germany. The model area consists of different urban structures that generate their own local microclimates. These microclimates are: the courtyard, where the trees are less exposed to direct radiation and wind and more exposed to longwave radiation from the surrounding buildings; the well ventilated south facing street, where the trees are unprotected from the incoming direct radiation and possible reflections off of nearby buildings; and the small park,

where trees are surrounded by other trees and thus partially shaded by them. Out of these microclimates, three particular trees were examined more closely: the courtyard tree ("CTgrass") whose stem area is covered with grass and whose roots are placed in sandy loam; the street tree ("STsouth") which, due to its southern exposition, is subject to high values of direct radiation as well as, due to its position on the sidewalk, subject to limited natural soil availability; the park tree ("PT") which is located in the center of the small park and partially shaded by the surrounding trees. The exact locations are marked by the signatures in figure 3.8.

Figure 3.8: Model area for the plant-as-object proof-of-concept simulation, effects of different microclimates

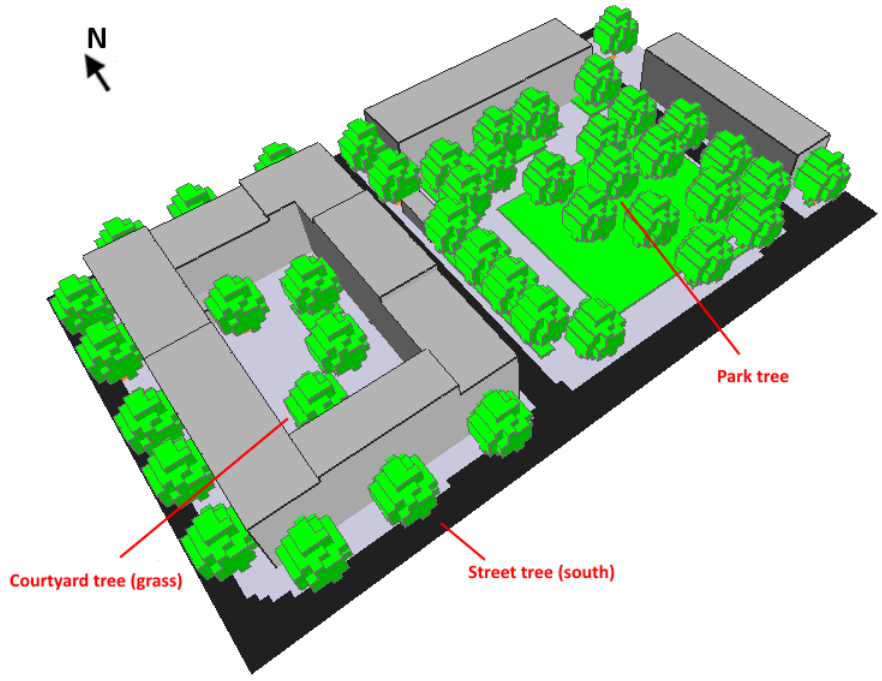

Model area dimensions: $100 \times 60 \times 25$ grids; vertical and horizontal resolution: 2 meters; location: Mainz, Germany

It is expected that the park tree shows the highest transpiration flux since it is

well ventilated, its roots can fully unfold thanks to the unsealed soil and it receives plenty of photosynthetically active radiation. Due to this high transpiration flux, the park tree should also exhibit the lowest maximum leaf temperatures as its leaves are cooled by the high transpiration activity. However, its initially high water access should decline more quickly than the other trees' water access due to its high transpiration rate. The street tree should receive the most photosynthetically active radiation as there are no obstructions to its south. Nonetheless, its latent heat flux should be slightly reduced compared to the park tree since its root system cannot unfold completely in its mostly sealed location on the sidewalk next to the southern street. This reduced heat flux should result in maximum leaf temperatures higher than the ones of the park tree. For the courtyard tree, the reduced PAR and wind speed inside the courtyard should result in reduced latent heat fluxes. Furthermore, the courtyard tree's maximum leaf temperatures should be elevated since the vapor pressure deficit of the inside of the leaf to the atmosphere is reduced due to the reduced ventilation inside the courtyard. With its reduced latent heat flux, however, the courtyard tree's water access should decrease more slowly.

Figure 3.9: Effect of different microclimates on average latent heat flux

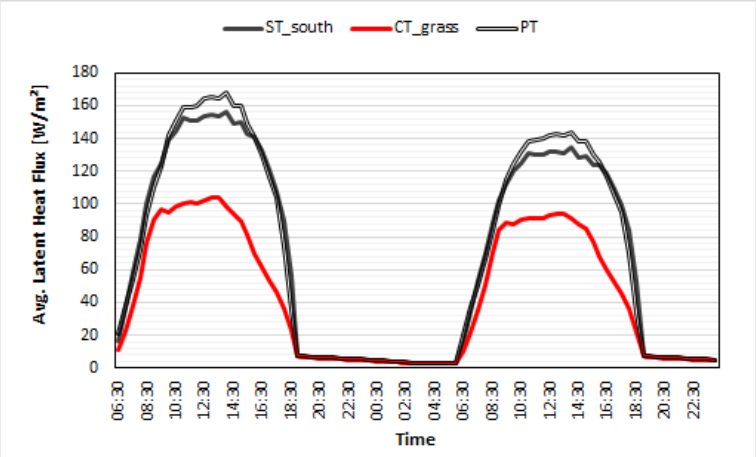

The simulation results (figures 3.9 and 3.10) show that the expected outcomes can

Figure 3.10: Effect of different microclimates on maximum leaf temperature and water access

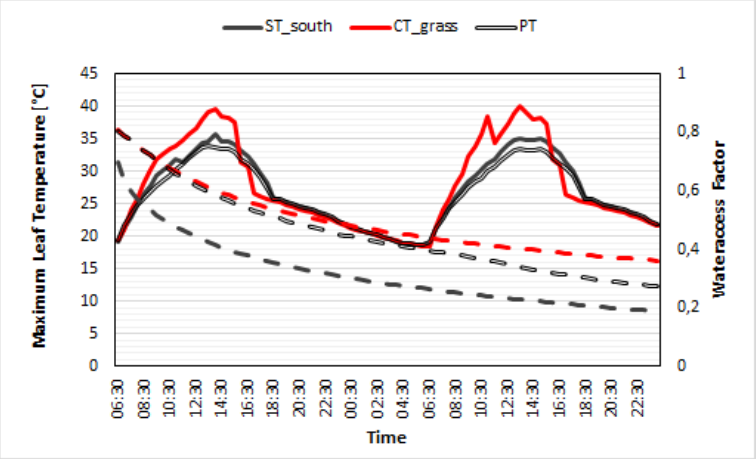

be confirmed. The latent heat fluxes of the trees (figure 3.9) match the expectations with the lowest latent heat flux being recorded for the courtyard tree: It was hypothesized that the reduced PAR and wind speed inside the courtyard should result in reduced latent heat fluxes for the courtyard tree. In combination with figure 3.11, the dependence of water vapor flux on wind speed is clearly visible. The lower wind speeds lead to increased aerodynamic resistances at the leaves that hinder the exchange of CO_2 and water vapor massively (figure 3.12), reducing the transpiration rate and thus the latent heat flux. The park tree, as expected, shows the highest latent heat flux values due to its greater water access compared to the street tree. The comparison of the latent heat fluxes of day one with day two shows that all trees have lower latent heat fluxes on the second day. The graph reveals that the decrease of the latent heat flux is particularly big for the park tree and the street tree, while the courtyard tree shows smaller declines in the latent heat fluxes from day one to day two.

The maximum leaf temperatures of the different trees vary quite considerably (figure 3.10). As was expected based on its local microclimate, the park tree shows the

Figure 3.11: Wind speed at vegetation

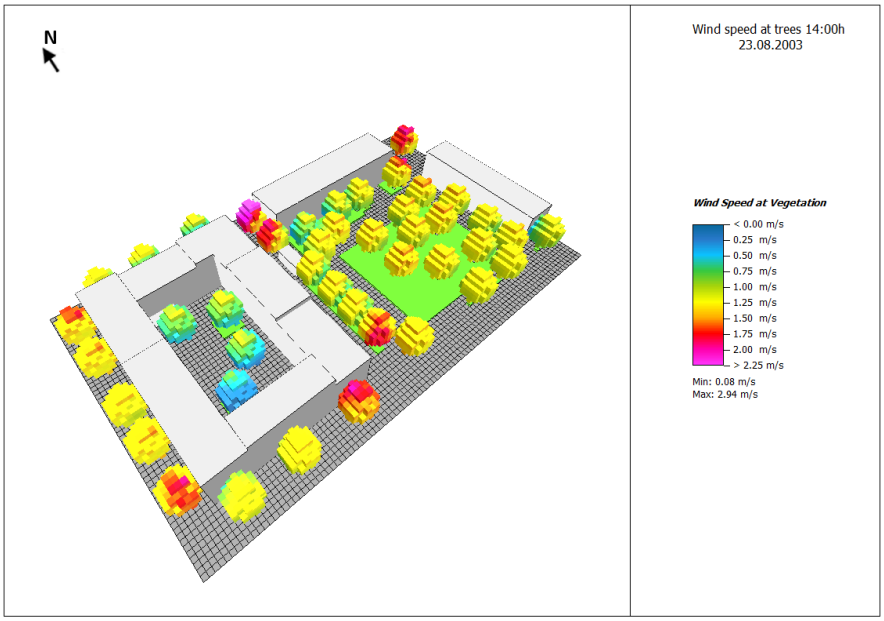

lowest maximum leaf temperatures (up to only 33°C) for the entire simulation period, while the courtyard tree clearly stands out with leaf temperatures of up to 40°C on both simulation days. Accordingly, the park tree does not show any signs of heat stress in its maximum leaf temperatures on either the first or second day, even though its water access factor does decrease quickly due to its high transpiration rate. Yet again, this matches the expectations. For the street tree, first signs of water stress can be observed as the maximum leaf temperatures rise with the declining water access on the second day. However, its maximum leaf temperatures still remain fairly close to the ones of the park tree, considerably below the 40°C reached by the courtyard tree's leaves. For the courtyard tree, water access does not decrease as quickly as for the other two trees, confirming the assumption that its reduced heat fluxes (as evidenced by figure 3.9) should result in a slowed decrease in water access. Figure 3.12 further corroborates the expectation that the lower wind speed inside the courtyard and the thereby increased aerodynamic resistances of the

Figure 3.12: Aerodynamic resistance at vegetation

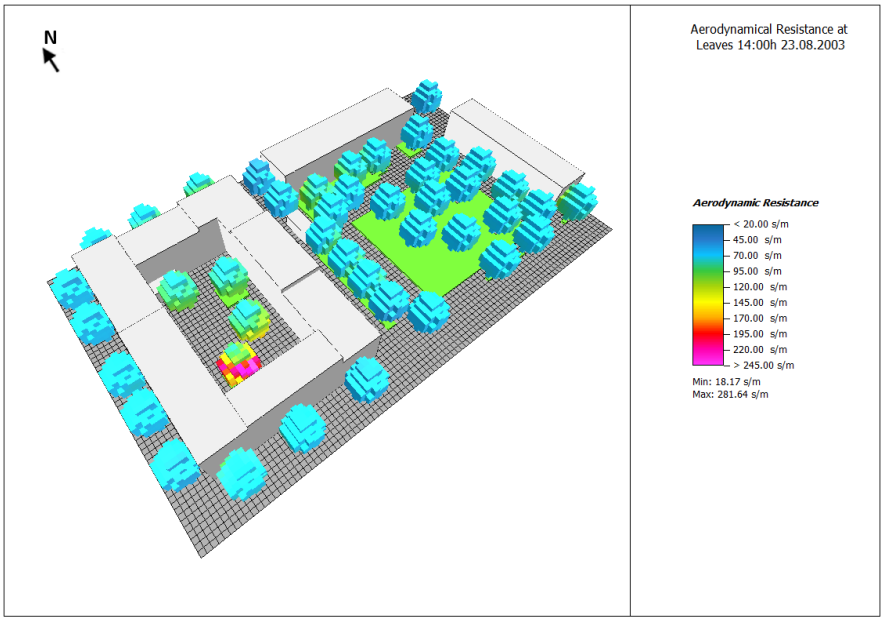

leaves are causing a reduction in transpiration and consequently result in higher leaf temperatures. In addition, the courtyard tree's uppermost leaves, while still being exposed to only very low wind speeds, are hit by direct sunlight, resulting in even higher maximum leaf temperatures.

Summing up, the anticipated effects of different microclimates onto the aggregated tree parameters latent heat flux, maximum leaf temperatures and water access could be simulated accurately. In addition, the impact of different microclimates onto these aggregated tree parameters proofed to be quite substantial.

3.4 Conclusion and outlook

The study described the introduction of plants as individual organisms in the microclimate model ENVI-met. Before the new implementations, plants in ENVI-met

consisted out of a collection of grids cells with individual leaf area densities. There was no information that linked these grid cells to a particular organism. Furthermore, no distinct root area that belonged to a plant could be digitized. It was therefore impossible to generate an object-based analysis of a plant's water access and vitality. While these simplifications were accurate enough to simulate the effects of vegetation onto the microclimate, the model did not permit any statements about the plants' vitality.

To overcome this problem, a new plant-as-object model was implemented that allows to aggregate the processes calculated at the individual leaf level back to the associated plant. Additionally, a three-dimensional root model was introduced that allows the calculation of an object-based water supply for each plant organism. Making use of these advancements, evaluations of the plant parameters as aggregated clusters of leaf area density and root area density can now be performed.

To evaluate the new plant-as-object model, two proof-of-concept simulations were conducted. The first proof-of-concept simulation examined the effects of different tree geometries onto the aggregated plant parameters. As expected, the simulations showed that larger trees with their more advantageous surface-area-to-volume ratio can withstand more environmental stress than smaller trees. The second proof-of-concept simulation examined the effects of different microclimates onto the aggregated plant parameters. The model results showed that the local microclimates have a big impact on the aggregated plant parameters and that these parameters strongly interact with each other in the same ways that would be expected on theoretical grounds.

Using the advancements of the plant-as-object model, it is therefore now possible to not only model a tree's influence on the microclimate, but also to assess the tree's vitality in different microclimates. This renders it possible to conduct tree health simulations which can help to approximate the amount of environmental stress a tree would be exposed to in a specific microclimatic location without actually having to

plant the tree in this location.

In the future, the implementation of additional defining characteristics of plant species, such as special water retention strategies, could enable tree health assessment simulations that form the basis of specific decision guidelines to designate the optimal combination of location and plant.

Bibliography

Ali-Toudert, F. and Mayer, H. Effects of asymmetry, galleries, overhanging façades and vegetation on thermal comfort in urban street canyons. *Solar Energy*, 81(6): 742–754, 2007.

Allen, C. D., Macalady, A. K., Chenchouni, H., Bachelet, D., McDowell, N., Vennetier, M., Kitzberger, T., Rigling, A., Breshears, D. D., Hogg, E. H., Gonzalez, P., Fensham, R., Zhang, Z., Castro, J., Demidova, N., Lim, J. H., Allard, G., Running, S. W., Semerci, A., and Cobb, N. A global overview of drought and heat-induced tree mortality reveals emerging climate change risks for forests. *Forest Ecology and Management*, 259(4):660–684, 2010.

Andersson-Sköld, Y., Thorsson, S., Rayner, D., Lindberg, F., Janhäll, S., Jonsson, A., Mobacke, U., Bergman, R., and Granberg, M. An integrated method for assessing climate-related risks and adaptation alternatives in urban areas. *Climate Risk Management*, 7:31–50, 2015.

Bowler, D. E., Buyung-Ali, L., Knight, T. M., and Pullin, A. S. Urban greening to cool towns and cities: A systematic review of the empirical evidence. *Landscape and Urban Planning*, 97:147–155, 2011.

Bruse, M. and Simon, H. Advanced microscale modelling of vegetation processes in urban environments: The MIcrocale Plant Simulation System MIPSS Version 2. unpublished working paper, October 2015.

Challinor, A. J., Ewert, F., Arnold, S., Simelton, E., and Fraser, E. Crops and climate change: progress, trends, and challenges in simulating impacts and informing adaptation. *Journal of Experimental Botany*, 60(10):2775–2789, 2009.

Dimoudi, A. and Nikolopoulou, M. Vegetation in the urban environment: microclimatic analysis and benefits. *Energy and Buildings*, 35(1):69–76, 2003.

Eppel, J., Sander, G., Schönfeld, P., Körber, K., and Böll, S. *Projekt Stadtgrün 2021 - Selektion, Anzucht und Verwendung von Gehölzen unter sich ändernden klimatischen Bedingungen*. Bayerische Landesanstalt für Weinbau und Gartenbau, 2012.

Gillner, S., Vogt, J., and Roloff, A. Climatic response and impacts of drought on oaks at urban and forest sites. *Urban Forestry & Urban Greening*, 12(4):597–605, 2013.

Gillner, S., Hofmann, M., Tharang, A., and Vogt, J. Development of a database for urban trees. In Roloff, A., editor, *Urban Tree Management - for a Sustainable Development of Green Cities*, pages 196–210. Wiley-VCH, 2016.

Honjo, T. and Takakura, T. Simulation of thermal effects of urban green areas on their surrounding areas. *Energy and Buildings*, 15(3-4):443–446, 1990.

Janhäll, S. Review on urban vegetation and particle air pollution - Deposition and dispersion. *Atmospheric Environment*, 105:130–137, 2015.

Larcher, W. *Physiological Plant Ecology*. Springer, 4th edition, 2004.

Lee, H., Mayer, H., and Chen, L. Contribution of trees and grasslands to the mitigation of human heat stress in a residential district of Freiburg, Southwest Germany. *Landscape and Urban Planning*, 148:37–50, 2016.

Lindner, M., Fitzgerald, J. B., Zimmermann, N. E., Reyer, C., Delzon, S., van der Maaten, E., Schelhaas, M.-J., Lasch, P., Eggers, J., van der Maaten-Theunissen, M., Suckowc, F., Psomas, A., Poulter, B., and Hanewinkel, M. Climate change and European forests: What do we know, what are the uncertainties, and what are the implications for forest management? *Journal of Environmental Management*, 146:69–83, 2014.

Lobell, D. B., Burke, M. B., Tebaldi, C., Mastrandrea, M. D., Falcon, W. P., and Naylor, R. L. Prioritizing Climate Change Adaptation Needs for Food Security in 2030. *Science*, 319(5863):607–610, 2008.

May, P. B., Livesley, S. J., and Shears, I. Managing and Monitoring Tree Health and Soil Water Status During Extreme Drought in Melbourne, Victoria. *Arboriculture & Urban Forestry*, 39:136–145, 2013.

Moore, G. M. Adaptations of Australian Tree Species Relevant to Water Scarcity in the Urban Forest. *Arboriculture & Urban Forestry*, 39(3):109–115, 2013.

Norton, B. A., Coutts, A. M., Livesley, S. J., Harris, R. J., Hunter, A. M., and Williams, N. S. G. Planning for cooler cities: A framework to prioritise green infrastructure to mitigate high temperatures in urban landscapes. *Landscape and Urban Plannin*, 134:127–138, 2015.

Oliveira, S., Andrade, H., and Vaz, T. The cooling effect of green spaces as a contribution to the mitigation of urban heat: A case study in Lisbon. *Building and Environment*, 46:2186–2194, 2011.

Phelan, P. E., Kaloush, K., Miner, M., Golden, J., Phelan, B., Silva III, H., and Taylor, R. A. Urban Heat Island: Mechanisms, Implications, and Possible Remedies. *Annual Review of Environment and Resources*, 40:285–307, 2015.

Robitu, M., Musy, M., Inard, C., and Groleau, D. Modeling the influence of vegetation and water pond on urban microclimate. *Solar Energy*, 80(4):435–447, 2006.

Roman, L. A., Battles, J. J., and McBride, J. R. The balance of planting and mortality in a street tree population. *Urban Ecosystems*, 17(2):387–404, 2014.

Salata, F., Golasi, I., de Lieto Vollaro, A., and de Lieto Vollaro, R. How high albedo and traditional buildings' materials and vegetation affect the quality of urban microclimate. A case study. *Energy and Buildings*, 99:32–49, 2015.

Savi, T. S., Bertuzzi, S., Branca, M., Tretiach, M., and Nardini, A. Drought-induced xylem cavitation and hydraulic deterioration: risk factors for urban trees under climate change? *New Phytologist*, 205:1106–1116, 2015.

Sgrigna, G., Saebo, A., Gawronski, S., R., Popek, and Calfapiet, C. Particulate Matter deposition on Quercus ilex leaves in an industrial city of central Italy. *Environmental Pollution*, 197:187–194, 2015.

Song, Y., Maher, B. A., Li, F., Wang, X., Sun, X., and Zhang, H. Particulate matter deposited on leaf of five evergreen species in Beijing, China: Source identification and size distribution. *Atmospheric Environment*, 105:53–60, 2015.

Susca, T., Gaffin, S. R., and Dell'Osso, G. R. Positive effects of vegetation: Urban heat island and green roofs. *Environmental Pollution*, 159(8-9):2219–2126, 2011.

Vinet, J., Raymond, F., and Inard, C. A simulation tool to assess the impact of vegetation on the urban microclimate. In *Proceedings of IBPC 2000 International Building Physics Conference*, pages 637–644, 2000.

Wilmers, F. Effects of vegetation on urban climate and buildings. *Energy and Buildings*, 15(3-4):507–514, 1990.

Zhu, K., Woodall, C. W., Ghosh, S., Gelfand, A. E., and Clark, J. S. Dual impacts of climate change: forest migration and turnover through life history. *Global Change Biology*, 20(1):251–264, 2013.

4 Modeling transpiration and leaf temperature of urban trees - an evaluation of the microclimate model ENVI-met using measurement data

Helge Simon[1], *Jenny Lindén*[1], *Peter Braun*[2], *David Hoffmann*[1], *Michael Bruse*[1], *Jan Esper*[1]

[1] Department of Geography, Johannes Gutenberg University Mainz, 55099 Mainz, Germany

[2] Department of Horticulture, University Geisenheim, Von-Lade-Str. 1, 65366 Geisenheim, Germany

4.1 Introduction

Strategies for reducing urban heat excess and mitigating heat stress are of great interest when planning for a warmer future climate. Studies of the ambient air temperature within cities have shown a mosaic of cooler and warmer places, in which cooler places are closely connected to increased vegetation cover (Alavipanah et al., 2015; Fan et al., 2015; Harlan et al., 2006; Lindén, 2011; Middel et al., 2012; Norton et al., 2015). Harlan et al. (2006) showed that increased urban vegetation significantly correlates to improved thermal comfort conditions, particularly during heat waves. Increasing the vegetation cover in cities is thus one of the key approaches to lower both air and radiative temperatures and improve thermal comfort through shading and transpiration (e.g. Bowler et al., 2011; Norton et al., 2015).

Quantifying the vegetation-induced air temperature cooling effect in urban areas requires reliable information about the transpiration rate of urban vegetation, which can be obtained through a number of methods. For example, measurements of leaf gas exchange provide a direct measure of transpiration, but are labor intense and expensive. In natural environments, such type of data is typically restricted to short time periods and to only a few leaves, which are assumed to represent the whole canopy (e.g. Bowden and Bauerle, 2008; Konarska et al., 2016). Another way to estimate transpiration is through the measurement of sap flowing up the stem, which is directly related to the amount of transpired water (e.g. Forster, 2014; Granier, 1987; Green et al., 2003). Sap flow can be measured and quantified in-situ continuously and over longer periods, but instrumentation is often expensive. In addition, the scarcity of suitable locations in urban areas where the risk of vandalism is acceptable, often limits measurements to a few trees. Alternative possibilities to estimate the transpiration of urban vegetation are therefore greatly needed.

Apart from transpiration, leaf temperatures and tree vitality are also crucial when trying to assess the microclimatic effects of urban vegetation since only healthy,

unstressed plants can fully provide their beneficial effects on the microclimate. In conditions where water supply is limited and heat is increased, the plants endure severe drought and heat stress. Under these conditions the plants reduce their transpiration rate in order to prevent excessive water loss, which in turn increases leaf temperature and reduces positive microclimatic effects (May et al., 2013; Savi et al., 2015). The increased leaf temperatures can, when exceeding a plant-specific threshold, lead to irreversible damage to plant growth and development (Feller and Vaseva, 2014; Haldimann and Feller, 2004). One way to assess leaf temperatures and tree vitality as well as transpiration is via simulation methods using microclimate models.

A frequently used urban microclimate model is ENVI-met (Bruse, 1999), which considers physical fundamentals based on the principles of fluid mechanics, thermodynamics and atmospheric physics, to calculate three-dimensional wind fields, turbulence, air temperature and humidity, radiative fluxes, and pollutant dispersion. The advantage of ENVI-met lies in its holistic approach to simulate the complex interactions of building structures, atmosphere, soil and vegetation processes in one model. The particularly sophisticated vegetation model in ENVI-met allows accurate modeling of the plant-atmosphere interactions through a stomata behavior model at the leaf level (Bruse, 2004). The calculation of stomatal behavior using Jacobs' A - g_s model (Jacobs, 1994) together with the introduction of object-based assessments of plant parameters (see chapter 3) allows the simulation of the effects of plants on the microclimate as well as the simulation of effects of microclimates on the vitality of plants.

In this paper, the vegetation model of ENVI-met is evaluated based on a comparison of modeled transpiration rates and leaf temperatures with monitored sap flow and leaf temperature measurements under four different meteorological conditions in a complex urban environment.

Continuous measurements of meteorological parameters, leaf temperatures and sap

flow measurements have been conducted on two different trees in a confined courtyard in an urban environment in Mainz, Germany. Four different periods were extracted from the measurement data to test the modeled results against the measurements in different conditions. Each period covered two to three days that featured different levels of cloud cover and air temperatures since the photosynthetic active radiation (PAR) and the air temperature are assumed to have the biggest impact on transpiration and leaf temperature.

4.2 Methods

4.2.1 Study site

The study has been performed in the city of Mainz, Germany (50.0°N, 8.3°E, elevation 100 m a.s.l.). Mainz is an inland city with approximately 200,000 inhabitants, located in a landscape of gently rolling hills along the Rhine river. The climate is temperate with an annual average temperature of 10.7°C and precipitation of 620 mm (Koeppen Cfb). The summers are warm and humid (June to August: 19.2°C and 175 mm, from 1981-2010, www.dwd.de). The urban architecture is of compact midrise structure (Stewart and Oke, 2012) with smaller parks, grassy areas, and streets with scattered trees.

The examined location is a courtyard located in the sparsely vegetated urban center, approximately 500 m away and 7 m above the Rhine River. The courtyard is 43 × 48 m and completely enclosed by buildings 10-16 m tall (figure 4.1). The ground is covered with lightly colored gravel and the vegetation consists of five mature Platanus × acerifolia reaching heights of 10-17 m, and a 10 × 10 m drip irrigated herb garden. The trees are not irrigated. Soil conditions at the study site are likely variable and disturbed since the buildings were destroyed in the Second World War and new structures built on top of the rubble.

Figure 4.1: Monitoring and simulation site

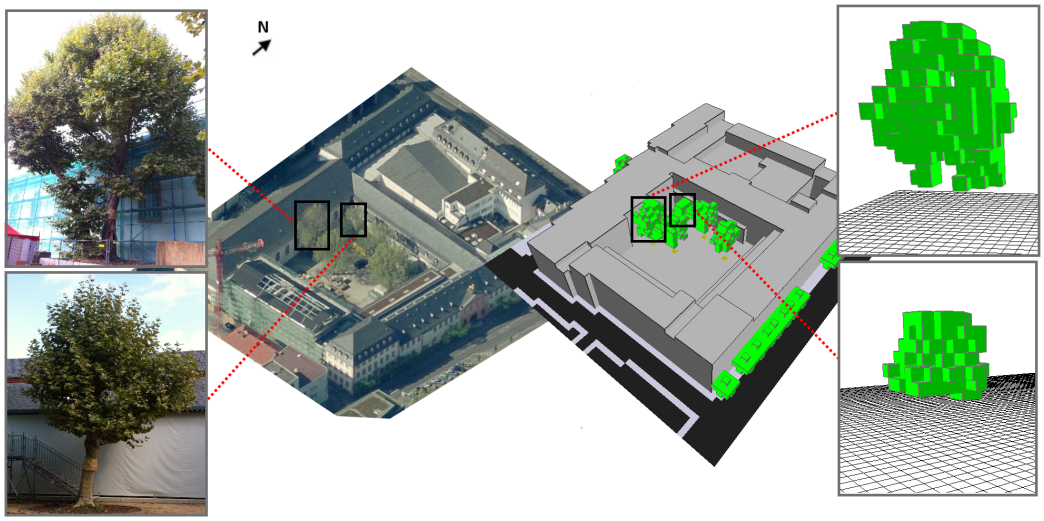

Aerial photo of the courtyard monitoring site together with photos of a large (top left) and small tree (bottom). Digitized model area and trees are shown on the right

4.2.2 Monitored parameters

Meteorological parameters

Air temperature and relative air humidity were monitored using HOBO U23-001 Pro v2 data loggers placed in RS1 solar radiation shields (Onset, Bourne, MA, USA) (da Cunha, 2015), at a height of 3 m in the courtyard as well as directly outside in a southwest-northeast oriented street. Prior to installation, a comparison among the sensors located in a well ventilated rooftop for a period of 22 days (with T_A ranging from -4°C to 18°C and HR from 30 to 100%) showed agreement with an average difference in $T_A < \pm 0.08$ K ($< 2\%$ exceeding $\pm$ 0.2 K), and in HR $< 0.2\%$ ($< 2\%$ exceeding 1%). These measurements were used to derive specific humidity. Precipitation, wind and solar radiation were obtained from a meteorological station run by the Institute of Atmospheric Physics at Johannes Gutenberg University 3 km southwest of the study area. This location is more open than the urban locations and thus only used to define the general daily meteorological conditions.

Tree sap flow

Sap flow velocity was monitored on two of the courtyard trees at 30-minute intervals using the compensation heat pulse method, sensor type HP4TC (Tranzflo NZ Ltd, New Zealand) connected to Campbell data loggers (CR 1000). With the compensation heat pulse method two temperature probes are placed above and below a heater probe into the sap wood of a tree stem (see figure 4.2). In periodic intervals the heater probe sends a heat pulse into the tree stem. The time delay until both temperature sensors show an equally large temperature rise is then used to trace the sap flow velocity (Green et al., 2003). The sensors were installed in four directions around the stem with a 90° angle between them and at a height of approximately 2 m above ground, but well below the first branches. Sap flow velocity was measured at four depths reaching a maximum of 6 cm into the sapwood in each direction. Total flux was calculated according to Swanson and Whitfield (1981) and Green et al. (2003). The sap flow velocity data were compared against modeled transpiration rates of entire trees.

Figure 4.2: Sap flow measurement

Photo of the two temperature probes placed above and below a heater probe into the sap wood (before insulation)

Leaf temperature

Leaf temperatures were measured using a self-built low cost infrared thermometer based on an Arduino microcontroller. An infrared sensor manufactured by Melexis was used to measure thermal radiation within a five degrees field of view and estimate the leaf temperature with an emissivity factor of 0.97 (Idso et al., 1969). Measurements of leaf temperature were obtained several times a second, and the mean values of these measurements were integrated over five-minute intervals. The instrument was mounted on a branch in five meters height and oriented towards a dense leaf cluster three meters below. Since the measured area of approximately 540 cm^2 was positioned in the large tree (see figure 4.1), it remained shaded most of the day. As these leaves constitute only a small sample, they were not compared with the model data of the entire tree, but only with a single leaf grid cell situated close to the measurement point.

4.2.3 ENVI-met

ENVI-met is a high resolution, three-dimensional prognostic microclimate model. With its holistic approach it models the wind field, air temperature and humidity, turbulence, radiative fluxes, building physics as well as soil and vegetation processes in urban environments (Bruse and Fleer, 1998). A key component is the detailed modeling of vegetation. With the newly developed plant-as-object model, plants in ENVI-met are no longer treated as loose grid cells of leaf area density (LAD), but can be regarded as aggregated objects or organisms that react to their immediate environmental conditions (see chapter 3). With its high resolution, ENVI-met is able to model the exchange of CO_2 and water vapor at the leaf level using an adaptation of Jacobs' A - g_s stomata model (Bruse, 2004). The A - g_s model is used to estimate stomatal behavior of single leaves considering the microclimatic conditions of the whole plant. The main assumption of the model is that plants operate stomatal conductance in a way that maximizes CO_2 gain while the associated water loss is

minimized (Jacobs, 1994). As an empirical model, the A - g_s model links stomatal conductance (water loss) with photosynthesis (CO_2 gain), although there is little evidence of a direct causal relation. Empirical observation, however, showed that there is a strong correlation between the stomatal conductance of water (g_s) and photosynthesis (A) (Damour et al., 2010; Jacobs, 1994).

Using this relation, the calculation of net photosynthesis rates allows the model to draw conclusions about the stomatal behavior of the plant. Among other parameters, ENVI-met's stomatal behavior model takes into account the following factors limiting net photosynthesis and thus stomatal conductance:

- Insufficient photosynthetic active radiation
- Insufficient CO_2
- Insufficient water access

The prognostic output parameters of the model are, among others: transpiration rate, leaf surface temperature, root water access, received photosynthetic active radiation and aerodynamical resistance. With the plant-as-object model, the model results of single plant grid cells of leaf area density are aggregated to form an integrated organism - a tree - that allows conclusions about the physiological and climatic parameters at the plant level instead of a grid cell level.

4.2.3.1 ENVI-met boundary conditions

Based on the meteorological observational data, four simulations of two to three consecutive days were run using ENVI-met 4 Expert. Since PAR is expected to have the biggest impact on plant transpiration, four periods with different cloud covers were chosen to evaluate model performance in different PAR conditions.

Using the meteorological measurements different diurnal cycles of wind speed, radiation, air temperature and humidity were created as boundary conditions for the

model. The four simulation periods feature different meteorological conditions (table 4.1, figure 4.3). The differences in the absolute amounts as well as in the ratio of direct and diffuse shortwave radiation are clearly visible.

Table 4.1: Boundary conditions of the four simulation periods

Condition	**Parameter (average)**		
	air temperature	vapor pressure deficit	wind speed
Clear sky (02.-03.08.2015)	25.6°	2.1 kPa	1.3 m/s
Slightly cloudy (06.-07.08.2015)	29.3°	2.3 kPa	0.9 m/s
Mostly cloudy (11.-14.08.2015)	26.7°	1.4 kPa	1.4 m/s
Fully cloudy (16.-17.08.2015)	16.8°	0.3 kPa	1.8 m/s

Figure 4.3: Diurnal variations of the forced direct (dashed lines) and diffuse (solid lines) radiation of the four simulation periods based on measurements of the meteorological station 3 km SW of the study site

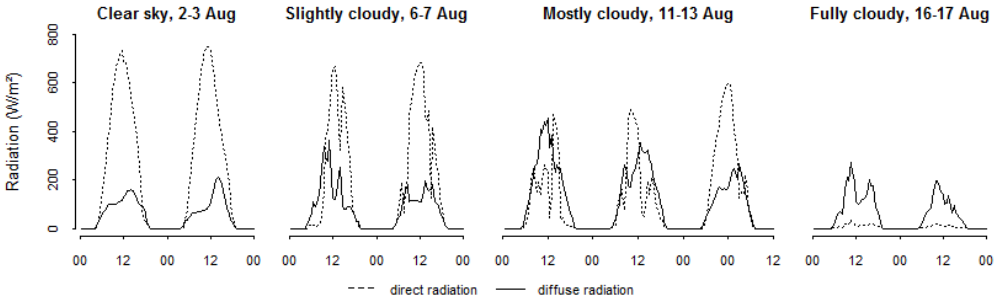

4.2.3.2 ENVI-met model area

The model area covers 140 × 116 × 40 m and was digitized in a resolution of 2 m so that the different tree geometries could be replicated accurately. This is particularly important in the context of this study, which aims to evaluate the vegetation model of ENVI-met based on transpiration flux and leaf temperature. Previous test runs showed that a close representation of a tree's geometry and leaf area density are

of utmost importance for the estimation of the actual transpiration flux for a tree. Figure 4.1 shows the two trees in their real environment as well as their represented geometry in the digitized model area.

The height of the larger tree was set to 16 m; the height of the smaller tree to 10 m. Since leaf area density was not directly measured, this parameter was approximated based on empirical studies. Hipps et al. (2014) and Van der Zande et al. (2008) found that Platanus × acerifolia feature LADs ranging from 0.5 m^2 m^{-3} to 0.7 m^2 m^{-3}. The individual leaf grid cells were thus set to an LAD of 0.6 m^2 m^{-3} for both trees in this study.

4.3 Results and discussion

The vegetation model of ENVI-met will be evaluated in two steps. In a first step the measured sap flow is compared against the modeled transpiration flux of the two trees. In a second step the measured leaf temperatures of shaded leaves are compared against modeled leaf temperatures of a single leaf grid cell situated close to the measurement point. As measures of overall model fit, R^2 and RMSE will be calculated. While R^2 provides information on how much of the variability in the actual values is explained by the model, i.e. on how well the shapes of the curves match, it does not give any indication about the fit of the absolute values. For example, a model predicting exactly half the values actually measured would still return a perfect model fit of $R^2 = 1.0$. To also capture the differences in absolute values between the modeled and measured data, the root-mean-square error RMSE is used. Since values of RMSE are dependent on the absolute values and can thus not be readily compared across meteorological conditions and trees, RMSE values are normalized by dividing by the range of measured values (NRMSE). This allows a direct comparison between the different conditions and a comparative assessment of overall model fit. In addition to these measures of overall model fit, the diurnal

variations of modeled and measured data are examined in detail to test whether the model is able to also capture short-term variations in transpiration and leaf temperatures.

4.3.1 Transpiration rates

To evaluate the vegetation model of ENVI-met, first the transpiration as obtained through sap flow measurements on the two trees was compared against the modeled transpiration (table 4.2, figure 4.4). Very high agreement for both the shape of the curves (R^2 between 0.88 and 0.95) as well as the absolute values (NRMSE between 0.09 and 0.16) was found between the modeled and measured (sap-flow derived) transpiration for the three examined periods where PAR plays an important role: clear sky, slightly cloudy and mostly cloudy (table 4.2). The model fit was lower during the fully cloudy period (R^2 between 0.38 and 0.48; NRMSE between 0.25 and 0.37) where PAR was very low and other parameters such as wind speed and water vapor deficit might become dominating factors impacting transpiration. As wind speed (and radiation) were measured approximately 3 km southwest of the trees actual location, the values driving the transpiration model likely differ from the actual conditions at the trees' location. While radiation can - apart from temporary distortions due to passing clouds (see below) - be assumed to be similar between the sites, the wind conditions might differ considerably. With the low PAR in the fully cloudy period, the inevitable error caused by the discrepancy between actual and measured (off-site) wind speeds might become a substantial bias affecting the transpiration comparison. Furthermore, the measurement of sap flow shows larger uncertainties in conditions of low sap flow (low PAR or at night), making a validation of the model harder in these conditions (Green et al., 2003).

Despite the discrepancies under low PAR conditions, the comparison of diurnal variations between the modeled transpiration rate and measured sap flow of the two

Table 4.2: Model fit between the simulated and estimated (sap flow derived) transpiration rates in different cloud conditions

Condition	R^2		RMSE [l/30min]		NRMSE	
	Small tree	Large tree	Small tree	Large tree	Small tree	Large tree
Clear sky	0.88	0.92	2.08	4.08	0.13	0.15
Slightly cloudy	0.88	0.90	2.40	4.71	0.14	0.16
Mostly cloudy	0.95	0.91	1.39	4.34	0.09	0.16
Fully cloudy	0.45	0.38	0.84	3.09	0.25	0.37

trees shows a remarkable agreement between the simulations and measurements over all four periods (figure 4.4). The model accurately simulates even the short-term variations of tree transpiration in cloudy, slightly cloudy, mostly cloudy and fully cloudy situations.

The differences between the small and large tree are well captured in the model. In both, the empirical and simulation data, the maximum transpiration rate for the larger tree is almost twice as high as the rate of the smaller tree (note the differing Y-axis scales in figure 4.4). With the exception of the heat-stress related midday depression on the second day of the clear sky and slightly cloudy situations (see below), the modeled and measured transpiration rates match better for the small tree, compared to the large tree. The disparity of the larger tree is probably caused by its more complex geometry. While the geometry of the small tree, with its dense and compact crown, can be represented easily in ENVI-met, the geometry of the larger tree, with its very heterogeneous crown, is very difficult to digitize correctly. Additionally, the trunk of the larger tree splits right at the base of the trunk (see figure 4.1). While the second trunk (to the left in figure 4.1) is disregarded in the sap flow measurements as well as the transpiration modeling, it does cast a shade onto the first tree and further complicates the already complex structure of the larger tree.

Figure 4.4: Comparison of the measured sap flow and leaf temperature with the modeled transpiration rate and leaf temperature

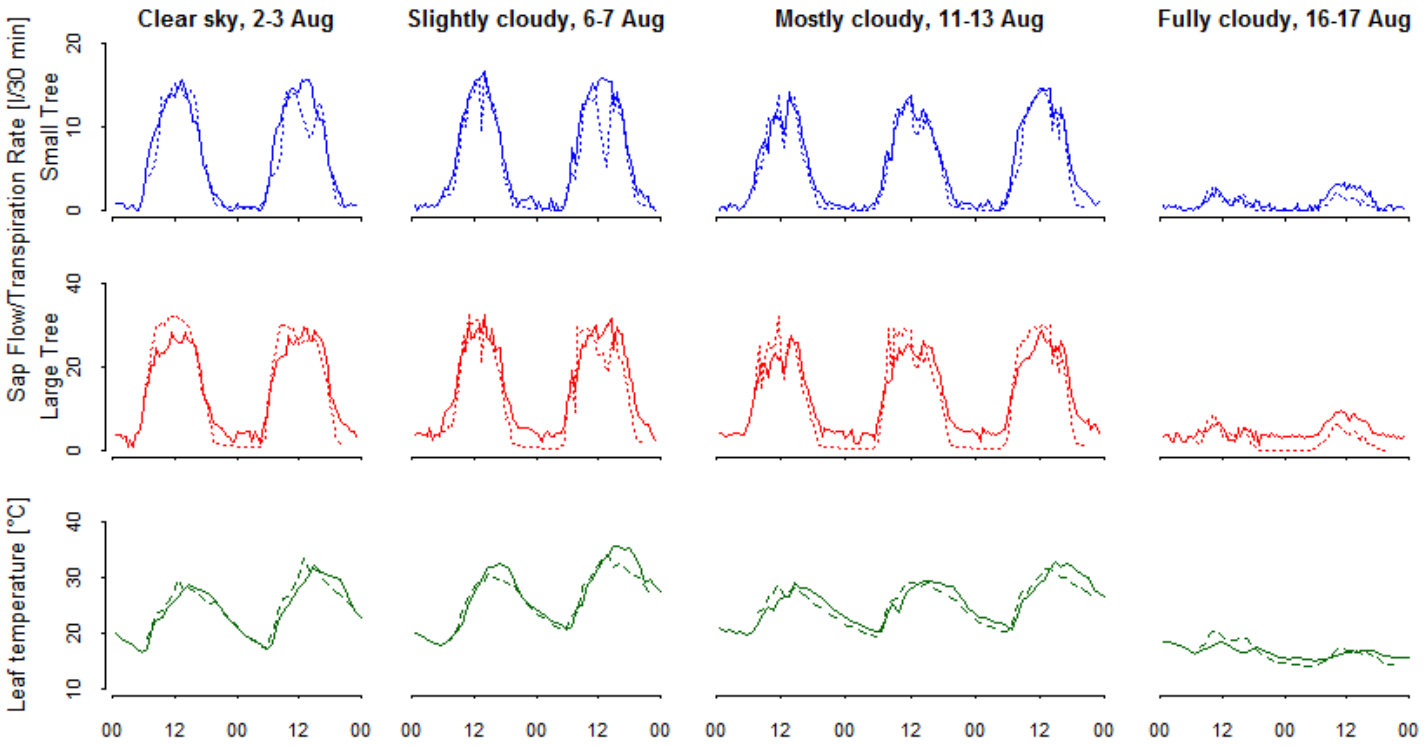

Comparison of the measured (solid lines) sap flow and leaf temperatures with the modeled (dashed lines) transpiration rates and leaf temperatures of a small (blue) and large tree (red). The bottom panel shows measured temperatures of shaded leaves (green solid lines) compared with modeled temperatures (dashed lines) of leaves close to the measurement point

A distinct discrepancy between modeled and empirical data is the reduced transpiration in the simulations after midday on the second day of the clear and slightly cloudy situations. A midday depression in transpiration in response to stress is a common water saving adaptation, which has been reported in both tropical and temperate trees (Brodribb and Holbrook, 2004; Gindaba et al., 2004; Kamakura et al., 2012; Kosugi et al., 2009). This water saving strategy is reflected in ENVI-met's vegetation model: In the A - g_s model, trees try to optimize their carbon gain in relation to water loss. In the clear sky and slightly cloudy situations, the model assumes this relation to be less beneficial and induces higher stomatal resistance to save water after midday (Bruse, 2004). The observational data, however, do not show reduced values in the sap flow, pointing to an underestimation of available soil water and an overestimation of the heat stress in the model.

During the first slightly cloudy day, a similar discrepancy between modeled and measured data is visible. However, this is not caused by an overestimation of heat stress in the model but rather by a difference in radiative conditions between the trees' location and the met station site 3 km southwest of the tree location. Figure 4.3 shows a drop in the direct shortwave radiation around 13:00, caused by a passing cloud temporarily blocking the sun at the met station site, thus reducing the modeled transpiration. At the same time, the measured tree sap flow shows no reaction indicating that the cloud did not pass over the monitoring site.

The stronger reduction in modeled transpiration at sunset, and negligible transpiration throughout the night is based on the ceased availability of PAR after sunset. The measurements show a slower decline and continued sap flow throughout the night, particularly in the larger tree. Sap flow has been found to generally continue at night, amounting to on average around 12% compared to daytime (e.g. Forster, 2014; Lindén et al., 2015; Zeppel et al., 2014). Although nocturnal sap flow is partly used for embolism refilling and recharge of capacitance, studies have shown that 50-95% of this nocturnal flow is lost through transpiration from the canopy

(Alvarado-Barrientos et al., 2015; Moore et al., 2008; Zeppel et al., 2010). While these processes seem generally to be captured by the model, the nocturnal transpiration may still be underestimated in the simulations. Although limited in comparison to daytime levels, the cooling induced by nocturnal transpiration has been found to be more important for urban climates as it reduces atmospheric mixing at this time (Konarska et al., 2016). Quantifying the stored versus transpired fractions of measured nocturnal sap flow, and exploring the possibility to adjust modeled evening and night transpiration was not addressed at this stage. However, due to the potential impact on the nocturnal urban climate, this issue needs to be examined in future research.

4.3.2 Shaded leaf temperatures

In addition to the transpiration rate, the leaf temperatures measured on a single branch were compared with modeled leaf temperatures of the corresponding single grid cell. Very high overall agreement for both the shape of the curves (R^2 between 0.81 and 0.90) as well as the absolute values (NRMSE between 0.10 and 0.12) was again found between the modeled and measured data for the clear sky, slightly cloudy and mostly cloudy periods, which are characterized by a dominant role of PAR (table 4.3). The reduced model fit of $R^2 = 0.71$ and NRSME = 0.38 respectively for the fully cloudy situation can again be explained by the more dominant role of other microclimatic parameters in situations where PAR is low. Since wind speed and wind direction were not measured at the exact location of the trees, the effects of advective cooling might not be captured correctly by the model resulting in a higher deviation of modeled leaf temperatures for the fully cloudy situation.

The comparison of diurnal variations in simulated and measured leaf temperatures (figure 4.4 bottom panel) demonstrates that the model is capable of predicting the short-term variations in leaf temperatures accurately as well. Only in the evening

Table 4.3: Model fit between simulated and monitored shaded leaf temperatures

Condition	R^2	RMSE [K]	NRMSE
Clear sky	0.87	1.55	0.10
Slightly cloudy	0.90	1.85	0.11
Mostly cloudy	0.81	1.59	0.12
Fully cloudy	0.71	1.25	0.38

hours, the model seems to underestimate the measured leaf temperatures slightly, reaching a maximum difference of 3K.

4.4 Conclusion

In this paper, the vegetation and plant-as-object models of the microclimate model ENVI-met were evaluated by comparing monitored and simulated transpiration fluxes and leaf temperatures of urban trees. The monitored transpiration rates were derived from sap flux measurements. To test the modeled transpiration under different conditions, four different synoptic situations including clear sky, slightly cloudy, mostly cloudy and fully periods extending over two to three days each were chosen. Different cloud covers were considered as the availability of photosynthetic active radiation is key to plant transpiration. To replicate the different situations, the model was run in a full-forcing mode allowing the definition of diurnal variations as boundary conditions for the measured meteorological parameters: air temperature and humidity, wind speed and direction and radiation (shortwave direct, diffuse and longwave). To accurately simulate the transpiration rate of the trees, the model area and particularly the replication of tree geometry in the model proved to be substantial.

The comparison of the simulation results with the measurement data showed very high agreement. ENVI-met's vegetation model is capable of not only capturing the

magnitude but also the short-term variations in the transpiration that were caused by minor environmental changes such as local cloud cover. For the smaller tree on the warmer days, however, the model predicted a midday depression in stomatal conductance leading to reduced transpiration. Even though the microclimatic conditions were quite hot and dry, the measured data showed no such depression. In addition, the modeled data did not closely fit the measured data in the fully cloudy simulation. This discrepancy is partly explained by uncertainties of the measurement method with transpiration rates derived from very low sap flow rates as well as by discrepancies between the actual and measured (off-site) wind speeds acting as boundary conditions for the model. An underestimation of modeled transpiration was also found in the evening and during night, but as the connection between nocturnal sap flow and transpiration was not determined at this stage, this discrepancy could not be addressed yet. Due to the potentially strong influence of nocturnal transpiration cooling on the nocturnal urban climate (Lindén 2011; Lindén et al. 2015), this issue requires further research. The comparison of simulated and monitored shaded leaf temperatures confirmed the high agreement between the model and measurements. Both the diurnal variations as well as the absolute values matched very well.

The study showed that the microclimate model ENVI-met is able to accurately simulate the transpiration rate and the changes of leaf temperatures of trees in complex urban environments. It confirmed that ENVI-met is a viable tool to assess the effects of trees on the urban microclimate (transpirational cooling effects) as well as to simulate tree vitality parameters in specific microclimate conditions.

Bibliography

Alavipanah, S., Wegmann, M., Qureshi, S., Weng, Q., and Koellner, T. The Role of Vegetation in Mitigating Urban Land Surface Temperatures: A Case Study of Munich, Germany during the Warm Season. *Sustainability*, 7(4):4689–4706, 2015.

Alvarado-Barrientos, M. S., Holwerda, F., Geissert, D. R., Muñoz-Villers, L. E., Gotsch, S. G., Asbjornsen, H., and Dawson, T. E. Nighttime transpiration in a seasonally dry tropical montane cloud forest environment. *Trees*, 29(1):259–274, 2015.

Bowden, J. D. and Bauerle, W. L. Measuring and modeling the variation in species-specific transpiration in temperate deciduous hardwoods. *Tree Physiology*, 28: 1675–1683, 2008.

Bowler, D. E., Buyung-Ali, L., Knight, T. M., and Pullin, A. S. Urban greening to cool towns and cities: A systematic review of the empirical evidence. *Landscape and Urban Planning*, 97:147–155, 2011.

Brodribb, T. J. and Holbrook, N. M. Diurnal depression of leaf hydraulic conductance in a tropical tree species. *Plant Cell and Environment*, 27:820–827, 2004.

Bruse, M. *Die Auswirkungen kleinskaliger Umweltgestaltung auf das Mikroklima. Entwicklung des prognostischen numerischen Modells ENVI-met zur Simulation der Wind-, Temperatur- und Feuchteverteilung in städtischen Strukturen.* Dissertation, Ruhr-Universität Bochum, 1999.

Bruse, M. ENVI-met implementation of the Jacobs $A - g_s$ Model to calculate the stomata conductance `http://envi-met.com/documents/new_a_gs.pdf`. 15.04.2015, 2004.

Bruse, M. and Fleer, H. Simulating surface-plant-air interactions inside urban envi-

ronments with a three dimensional numerical model. *Environment Modelling & Software*, 13(3-4):373–384, 1998.

da Cunha, A. R. Evaluation of measurement errors of temperature and relative humidity from HOBO data logger under different conditions of exposure to solar radiation. *Environmental Monitoring and Assessment*, 187:1–11, 2015.

Damour, G. T., Simonneau, T., Cochard, H., and Urban, L. An overview of models of stomatal conductance at the leaf level. *Plant, Cell and Environment*, 33:1419–1438, 2010.

Fan, C., Myint, S. W., and Zheng, B. Measuring the spatial arrangement of urban vegetation and its impacts on seasonal surface temperatures. *Progress in Physical Geography*, 39(2):199–219, 2015.

Feller, U. and Vaseva, I. Extreme climatic events: impacts of drought and high temperature on physiological processes in agronomically important plants. *frontiers in Environmental Science*, 2:1–17, 2014.

Forster, M. A. How significant is nocturnal sap flow? *Tree Physiology*, 34:757–765, 2014.

Gindaba, J., Rozanov, A., and Negash, L. Response of seedlings of two Eucalyptus and three deciduous tree species from Ethiopia to severe water stress. *Forest Ecology and Management*, 201:121–131, 2004.

Granier, A. Sap flow measurements in douglas-fir tree trunks by means of a new thermal method. *Annales Des Sciences Forestieres*, 44:1–14, 1987.

Green, S., Clothier, B., and Jardine, B. Theory and practical application of heat pulse to measure sap flow. *Agronomy Journal*, 95:1371–1379, 2003.

Haldimann, P. and Feller, U. Inhibition of photosynthesis by high temperature in oak (Quercus pubescens L.) leaves grown under natural conditions closely correlates

with a reversible heat-dependent reduction of the activation state of ribulose-1,5-bisphosphate carboxylase/oxygenase. *Plant, Cell & Environment*, 27(9):1169–1183, 2004.

Harlan, S. L., Brazel, A. J., Prashad, L., Stefanov, W. L., and Larsen, L. Neighborhood microclimates and vulnerability to heat stress. *Social Science & Medicine*, 63:2847–2863, 2006.

Hipps, N. A., Davies, M. J., Dunn, J. M., Griffiths, H., and Atkinson, C. J. Effects of two contrasting canopy manipulations on growth and water use of London plane (Platanus x acerifolia) trees. *Plant Soil*, 382:61–74, 2014.

Idso, S. B., Jackson, R. D., Ehrler, W. L., and Mitchell, S. T. A Method for Determination of Infrared Emittance of Leaves. *Ecology*, 50:899–902, 1969.

Jacobs, C. M. J. *Direct impact of atmospheric CO2 enrichment on regional transpiration*. Dissertation, Agricultural University Wageningen, Wageningen., 1994.

Kamakura, M., Kosugi, Y., Takanashi, S., Tobita, H., Uemura, A., and Utsugi, H. Observation of the scale of patchy stomatal behavior in leaves of Quercus crispula using an Imaging-PAM chlorophyll fluorometer. *Tree Physiology*, 32:839–846, 2012.

Konarska, J., Uddling, J., Holmer, B., Lutz, M., Lindberg, F., Pleijel, H., and Thorsson, S. Transpiration of urban trees and its cooling effect in a high latitude city. *International Journal of Biometeorology*, 60:159–172, 2016.

Kosugi, Y., Takanashi, S., Matsuo, N., and Nik, A. R. Midday depression of leaf CO2 exchange within the crown of Dipterocarpus sublamellatus in a lowland dipterocarp forest in Peninsular Malaysia. *Tree Physiology*, 29:505–515, 2009.

Lindén, J. Nocturnal Cool Island in the Sahelian city of Ouagadougou, Burkina Faso. *International Journal of Climatology*, 31:605–620, 2011.

Lindén, J., Simon, H., Fonti, P., Esper, J., and Bruse, M. Observed and modeled transpiration cooling from urban trees in Mainz, Germany. International Conference on Urban Climate 9, 2015.

May, P. B., Livesley, S. J., and Shears, I. Managing and Monitoring Tree Health and Soil Water Status During Extreme Drought in Melbourne, Victoria. *Arboriculture & Urban Forestry*, 39:136–145, 2013.

Middel, A., Brazel, A.J., Gober, P., Myint, S. W., Chang, H., and Duh, J.-D. Land cover, climate, and the summer surface energy balance in Phoenix, AZ, and Portland, OR. *International Journal of Climatology*, 32:2020–2032, 2012.

Moore, G.W., Cleverly, J. R., and Owens, M. K. Nocturnal transpiration in riparian Tamarix thickets authenticated by sap flux, eddy covariance and leaf gas exchange measurements. *Tree Physiology*, 28:521–528, 2008.

Norton, B. A., Coutts, A. M., Livesley, S. J., Harris, R. J., Hunter, A. M., and Williams, N. S. G. Planning for cooler cities: A framework to prioritise green infrastructure to mitigate high temperatures in urban landscapes. *Landscape and Urban Plannin*, 134:127–138, 2015.

Savi, T. S., Bertuzzi, S., Branca, M., Tretiach, M., and Nardini, A. Drought-induced xylem cavitation and hydraulic deterioration: risk factors for urban trees under climate change? *New Phytologist*, 205:1106–1116, 2015.

Stewart, I. D. and Oke, T. R. local climate zones for urban temperature studies. *Bulletin of the American Meteorological Society*, 93:1879–1900, 2012.

Swanson, R. H. and Whitfield, D. W. A. A numerical-anaysis of heat pulse velocity theory and practice. *Journal of Experimental Botany*, 32:221–239, 1981.

Van der Zande, D., Jonckheere, I., Stuckens, J., Verstraeten, W. W., and Coppin, P. Sampling design of ground-based lidar measurements of forest canopy structure

and its effect on shadowing. *Canadian Journal of Remote Sensing*, 34:526–538, 2008.

Zeppel, M. J. B., Tissue, D., Taylor, D., Macinnis-Ng, C., and Eamus, D. Rates of nocturnal transpiration in two evergreen temperate woodland species with differing water-use strategies. *Tree Physiology*, 30:988–1000, 2010.

Zeppel, M. J. B., Lewis, J. D., Phillips, N. G., and Tissue, D. T. Consequences of nocturnal water loss: a synthesis of regulating factors and implications for capacitance, embolism and use in models. *Tree Physiology*, 34:1047–1055, 2014.

5 Introduction of a BVOC model

Helge Simon[1]

[1] Department of Geography, Johannes Gutenberg University Mainz, 55099 Mainz, Germany

5.1 Introduction

In addition to the urban heat island, the urban microclimate is also characterized by levels of air pollution that are considerably higher than in rural areas (Cohen et al., 2004). In summer, when the ambient air temperature is high, many cities record heightened levels of tropospheric ozone. A multitude of studies have shown that extensive exposure to tropospheric ozone can lead to eye and throat irritation, coughing, asthma attacks, other respiratory symptoms and even an increased mortality (Bell et al., 2004, 2007; Gryparis et al., 2004; Ito et al., 2005; Mudway and Kelly, 2000).

Ozone is not a primary pollutant in the troposphere, meaning that - other than nitrogen monoxide and nitrogen dioxide - it is not directly emitted into the atmosphere but rather formed by photochemical reactions in the troposphere. The formation of ozone in the troposphere primarily stems from the photolyzation of nitrogen dioxide, which has mainly anthropogenic sources: combustion processes. In the absence of volatile organic compounds (VOCs), the ozone concentration forms a photochemical equilibrium with the concentrations of nitrogen monoxide and nitrogen dioxide, where the ozone concentration depends on the ratio of NO_2 and NO (Fischer et al., 2011):

$$O_3 \approx \frac{NO_2}{NO}$$

In the presence of volatile organic compounds, however, the oxidation of nitrogen monoxide is drastically increased, leading to a surplus of NO_2 which destroys the equilibrium and, via photolyzation, leads to higher ozone concentrations. Depending on the type of volatile organic compound, one molecule of a VOC can contribute to the formation of more than one nitrogen dioxide and thus ozone molecule (Carter, 1994; Fischer et al., 2011). This makes VOCs an important factor in the formation

of tropospheric ozone.

Volatile organic compounds can be distinguished by their origin: Firstly, the anthropogenic volatile organic compounds (AVOCs) that are mainly produced by combustion processes. The main AVOCs in urban areas are aliphatic and aromatic hydrocarbons. Secondly, the biogenic volatile organic compounds (BVOCs) that are released by plants due to e.g. heat stress (Calfapietra et al., 2013).

Among the biogenic volatile organic compounds, isoprene plays a central role: Compared to other BVOCs, it forms higher quantities of reactive oxygen compounds which in turn can directly lead to higher ozone concentrations. Calfapietra et al. (2013) state that the reactivity factor / the ozone-forming potential of isoprene is 9.1, meaning that 9.1 grams of ozone can be formed per gram of isoprene. Together with the fact that isoprene is the most abundant volatile organic compound emitted by plants, the emission of isoprene and the isoprene-induced reactions play a key role in the formation of tropospheric ozone (Guenther et al., 2006; Sharkey et al., 2008).

The isoprene emission of plants strongly depends on high levels of photosynthetically active radiation and high leaf temperatures. The studies of Guenther et al. (1993), Guenther et al. (1995) and Guenther et al. (1999) have shown that the isoprene emission strongly increases with leaf temperatures up until around 312 Kelvin. This relation means that urban areas with their higher ambient air temperatures encourage an increased emission of isoprene into the atmosphere. Together with the higher concentrations of nitrogen monoxide in the urban areas, the formation of ozone is thus drastically increased compared to rural sites.

In order to examine the effects of isoprene onto the formation of tropospheric ozone on a microscale level, both the plant-based emissions of isoprene and the chemical reactions induced by this isoprene need to be incorporated into the microclimate model, ENVI-met. Therefore, in a first step, the isoprene-emission model of Guen-

ther et al. (1993) is implemented into ENVI-met. In a second step, a simplified isoprene-oxidation scheme is developed and introduced into ENVI-met's chemistry model, including the reactions leading to an increase of tropospheric ozone due to the emission of isoprene. The validity of the implementations is then evaluated in several proof-of-concept simulations that examine the isoprene-emission model as well as the advancements in the chemistry model under different chemical and meteorological conditions.

5.2 Implementation of a BVOC model

In order to account for the isoprene emission of plants and its effects onto the formation of tropospheric ozone, a model to estimate the emissions of isoprene (C_5H_8) was first developed based on the works of Guenther et al. (1993) and the advancements in Guenther et al. (1999) and Guenther et al. (2006). This model was then implemented into the microclimate model ENVI-met. Additionally, the dispersion of isoprene into the atmosphere and its chemical reactions with other gases leading to tropospheric ozone were introduced into ENVI-met's dispersion and chemistry model.

5.2.1 Estimation of isoprene emissions

To calculate the diurnal isoprene emissions the processes described in equation 5.1 were implemented.

$$E[\mu g\ \mathrm{C}\ g^{-1}h^{-1}] = [\epsilon][D_P D_T][\gamma_P \gamma_T \gamma_A \gamma_{SM}][\rho] \tag{5.1}$$

ϵ is the ecosystem / plant dependent mass-based emission capacity [μg C g^{-1} h^{-1}] at a photosynthetically active photon flux density (PPFD) of 1000 μmol m^{-2} s^{-1}

and at a leaf temperature of 303.15K. D_P is the annual peak foliar density [kg (dry matter) m^{-2}] and D_T the current fraction of the same. γ_P, γ_T, γ_A and γ_{SM} represent dimensionless adjustment factors accounting for the influence of PPFD, leaf temperature, the leaf age and situations of severe drought on the emission activity (see equations 5.2, 5.5 and 5.10), while ρ accounts for the amount of isoprene that is released into the above-canopy atmosphere (Guenther et al., 1999, 2006).

The adjustment factor for the influence of PPFD is defined as follows:

$$\gamma_P = \frac{\alpha C_L Q}{\sqrt{1 + \alpha^2 + Q^2}} \tag{5.2}$$

α and C_L are empirical coefficients, altered by the cumulative Leaf Area Index (LAI) above the observed leaves (equations 5.3 and 5.4) taking into account the shading effects of the plant's canopy. Q as the current photosynthetic photon flux density PPFD [μmol m^{-2} s^{-1}].

$$\alpha = 0.001 + 0.00085 \text{ LAI} \tag{5.3}$$

$$C_L = 1.42 \exp(-0.3 \text{ LAI}) \tag{5.4}$$

The temperature dependency γ_T of the emission activity in equation 5.1 is described as follows:

$$\gamma_T = E_{opt} \left(\frac{C_{T2} \ \exp(C_{T1} x)}{C_{T2} - C_{T1}(1 - \exp(C_{T2} x))} \right) \tag{5.5}$$

with E_{opt} as the maximum normalized emission capacity and T_{opt} as the temperature at which E_{opt} is reached. $C_{T1} = 95$ and $C_{T2} = 230$ are empirical coefficients representing the energy of activation and deactivation (Guenther et al., 1999).

x is defined as:

$$x = \left(\frac{1}{T_{opt}} - \frac{1}{T} \right) / R \tag{5.6}$$

with T as the current leaf temperature and R as the universal gas constant (= 0.00831 [kJ mol^{-1} K^{-1}]).

The values for T_{opt} and E_{opt} can either be set constant to 312.5K and 1.9 respectively, neglecting the effects of temperature that the leaf has been exposed to in the past days/weeks (see Sharkey et al. 1999). Alternatively, both coefficients can be adjusted taking into account the mean temperature T_d of the past 15 days (see equations 5.7 and 5.8).

$$T_{opt} = 312.5 + 0.5(T_d - 301) \tag{5.7}$$

$$E_{opt} = 1.9 \exp\left(0.125(T_d - 301)\right) \tag{5.8}$$

Severe drought influences the isoprene emission rate in multiple ways: Aside from indirect effects such as higher stomatal resistances which hinder the plant's transpirational flux leading to higher leaf temperatures (the temperature influence γ_T), the direct effect of extreme drought on metabolic processes leads to a significant reduction of isoprene emissions. The drought factor γ_{SM} used in equation 5.1 introduces a linear scaling factor reducing the isoprene emission in the case the actual volumetric water content θ [m^3 m^{-3}] almost reaches the wilting point θ_W (equations 5.9, 5.10, 5.11).

In case: $\theta > \theta_1$:

$$\gamma_{SM} = 1 \tag{5.9}$$

In case: $\theta_W < \theta < \theta_1$

$$\gamma_{SM} = \frac{(\theta - \theta_W)}{\Delta\theta_1} \tag{5.10}$$

In case: $\theta < \theta_W$

$$\gamma_{SM} = 0 \tag{5.11}$$

with $\Delta\theta_1$ as an empirically determined constant ($= 0.06$) and θ_1 defined as:

$$\theta_1 = \theta_W + \Delta\theta_1 \tag{5.12}$$

5.2.2 Implementation

5.2.2.1 Model adjustments

Since the majority of applications of the isoprene emission model of Guenther et al. (1993) are used in the field of remote sensing (see Guenther et al. 2006 and Wong et al. 2013), a number of input parameters are adjusted to larger scales in time and space. The coarser resolution in space together with the analytical (GIS-) models lead to more parametrizations in the calculation of variables, while the larger scales in time enable the modeling of changes in the plant's canopy such as leaf age and the leaf shedding of deciduous trees.

However, as ENVI-met operates on the microscale level some of the parametrizations in the original model can instead be simulated directly. This is especially the case for the calculation of dissipation of the incoming PAR. Contrary to GIS / remote sensing approaches, ENVI-met is able to model the radiation fluxes in the canopy (see chapter 2.4.1.5), producing much more sophisticated results than the parametrizations of PPFD dissipation caused by shade casting leaves in equations 5.3 and 5.4 can account for. Since the effects of shade casting leaves on α and C_L are directly simulated with ENVI-met's radiation model, the coefficients α and C_L

can be set constant to the suggested values (Guenther et al. 1995): $\alpha = 0.0027$ and $C_L = 1.066$. The constants are calibrated so that an incoming PPFD of 1000 μmol m^{-2} s^{-1} (the same amount as in ϵ) would result in a γ_P of 1, thus radiation would have no influence on the actual emission rate.

To model the influence of PAR onto the basal isoprene emission capacity, the calculated PAR in ENVI-met [W m^{-2}] had to be converted to quantum units [μmol m^{-2} s^{-1}] using the following approximation:

$$\text{PPFD} \approx \text{PAR} \cdot 4.57$$

The effects of leaf age γ_A, leaf shedding of deciduous trees and the release of isoprene into the atmosphere above the canopy ρ do not need to be implemented using the coefficients in equation 5.1: Due to the comparatively short period of simulated time the effects of changing leaf age γ_A can be set constant for the model run. The effects of leaf shedding can be accounted for by reduced values of LAD either from the model start or by reducing it to given values in the course of the simulation run. The release of isoprene into the atmosphere above the canopy can directly be modeled by introducing isoprene into the dispersion and chemistry model (see chapter 5.2.2.2).

Since ENVI-met's trees did not have properties for leaf weight and isoprene emission capacity, these properties were included into *Albero*, the three-dimensional plant editing tool; figure 5.1 shows the new edit fields. The leaf weight is, due to comparison and compatibility reasons that allow an easier adaptation to LAD, expected to be entered in grams of leaf per square meter leaf surface (one-sided) [g_{leaf} m^{-2}]. The isoprene emission capacity field expects the emission capacity [μg C g^{-1} h^{-1}] at standard conditions: At a leaf temperature of 303.15K and a PPFD of 1000 μmol m^{-2} s^{-1}. If no further adjustment is undertaken the default values are 12 [μg C g^{-1} h^{-1}] for the isoprene emission capacity and 100 [g_{leaf} m^{-2}] for the leaf weight per

m^2 leaf surface.

Figure 5.1: 3D-plant editing tool Albero

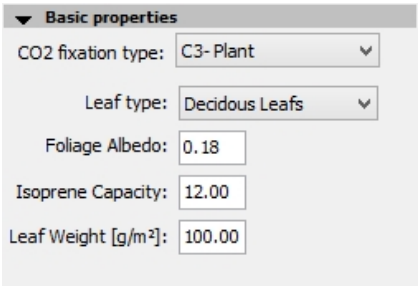

Given these properties the total leaf weight in one grid cell Λ_{abs} can then be calculated using the LAD of the grid cell and the dimensions $\Delta x_i \Delta y_j \Delta z_k$:

$$\Lambda_{abs} = \Lambda \cdot \mathrm{LAD}(i, j, k) \cdot \Delta x_i \Delta y_j \Delta z_k$$

Using equation 5.1 together with the implementation adjustments shown above, the hourly isoprene emission rate can be calculated for every plant cell. Figure 5.2 shows a simulation result of the isoprene emissions of a single tree on a hot summer day at noon. The high resolution of the ENVI-met model enables the simulation of differences in the emissions for every cell, allowing the reproduction of e.g. vertical distribution patterns of emission with higher levels at the top of the crown and lower ones at the bottom due to the differences of incoming radiation.

5.2.2.2 Dispersion model

Apart from the isoprene emission of plants, the dispersion of isoprene in the atmosphere and its chemical reactions with other gases are also implemented. The dispersion of isoprene is directly simulated by extending ENVI-met's gas and particle dispersion and deposition model (Bruse, 2007). This makes the original factor in equation 5.1, accounting for the release of isoprene into the atmosphere above the

Figure 5.2: 3D presentation of the isoprene flux of a tree

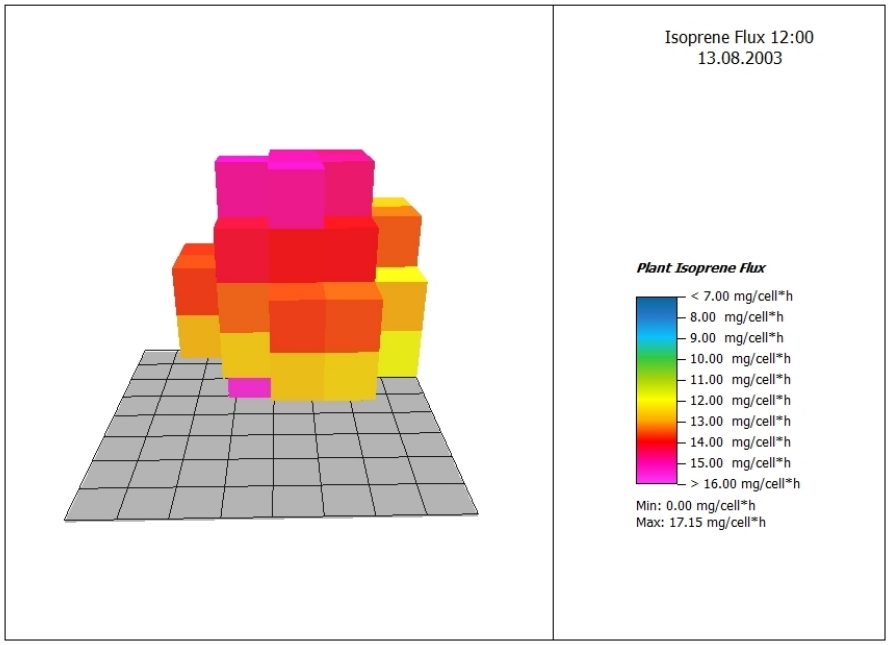

canopy, ρ, obsolete ($\rho_{const} = 1$). The dispersion of isoprene is being calculated analogously to e.g. NO_x using the advection-diffusion equation of the gas and particle model:

$$\begin{aligned} &\frac{\partial \chi}{\partial t} + u\frac{\partial \chi}{\partial x} + v\frac{\partial \chi}{\partial y} + w\frac{\partial \chi}{\partial z} = \\ &\frac{\partial}{\partial x}\left(K_\chi \frac{\partial \chi}{\partial x}\right) + \frac{\partial}{\partial y}\left(K_\chi \frac{\partial \chi}{\partial y}\right) + \frac{\partial}{\partial z}\left(K_\chi \frac{\partial \chi}{\partial z}\right) + \\ &Q_\chi(x,y,z) + S_\chi(x,y,z) \end{aligned} \tag{5.13}$$

with χ as the local concentration of the compound in [μg χ kg^{-1} Air] and Q_χ and S_χ both in [μg Compound s^{-1}] as source and sink terms leading to a local increase or decrease in concentration (Bruse, 2007).

The source term Q_χ [μg s^{-1}] in equation 5.13 needed to be implemented differently to other emitters in the gas and particle dispersion and deposition model: Since isoprene is released by existing objects (trees) and thus by sources that are already included in the model, no additional sources need to be digitized specificly. Also the diurnal cycle of the emission rates is calculated prognosticly using equation 5.14 so no predefined emission pattern is needed.

When the isoprene extension is enabled, the new BVOC model calculates the emission of every plant grid cell taking into account the specific leaf weight per square meter leaf Λ [g_{leaf} m^{-2}], the emission capacity at standard conditions ϵ [μg_{iso} g_{leaf}^{-1} h^{-1}], the LAD [m^2 m^{-3}], the grid size [m^3] and the influences of soil moisture γ_{SM}, radiation γ_P and leaf temperature γ_T:

$$\epsilon_{abs}\left[\frac{\mu\text{g}}{\Delta x\Delta y\Delta z[\text{m}^3]\cdot\text{s}}\right] = \frac{\epsilon\cdot\text{LAD}(i,j,k)\cdot\Lambda\cdot\Delta x\Delta y\Delta z\cdot\gamma_P\cdot\gamma_T\cdot\gamma_{SM}}{3600} \tag{5.14}$$

Since the source term expects the release of compound mass based in [μg Compound kg^1 Air s^{-1}], the volume based isoprene emission ϵ_{abs} [μg Compound m^{-3} volume grid s^{-1}] needs to be transformed using ρ, the density of air [kg m^{-3}] at 20°C, and $\Delta x\Delta y\Delta z$ as the grid dimensions:

$$Q_\chi = \epsilon_{abs}\cdot\frac{1}{\Delta x\Delta y\Delta z\cdot\rho}$$

The sink term S_χ [μg s^{-1}] in equation 5.13 influences the concentration of isoprene in two ways: First, via deposition on solid surfaces, plant leaves, water bodies etc. due to aerodynamic resistance, molecular diffusivity and absorption, and second, via chemical transformation which leads to a reduction of the concentration of two or more compounds and an increase of other compounds.

The deposition on various surfaces can be added as an additional advective com-

ponent using deposition velocities υ_d as relevant transportation velocities (Bruse, 2007):

$$\frac{\partial \chi}{\partial t} = \upsilon_d \frac{\partial \chi}{\partial z}$$

The deposition velocity υ_d can be expressed as the inverted sum of the resistances r_a, the aerodynamic resistance, r_b, the sublayer resistance, and r_t, the surface resistance.

$$\upsilon_d = \frac{1}{r_a + r_b + r_t}$$

The aerodynamic resistance r_a at ground surfaces of walls is derived from the turbulent exchange coefficient for heat at the ground surface or at walls $K_{h,0}^{(\omega)}$ using (Bruse, 2007):

$$r_a = \frac{\Delta\omega}{K_{h,0}^{(\omega)}} \tag{5.15}$$

The aerodynamic resistance r_a at plants is calculated after Braden (1982) with equation 5.16 (Bruse, 2007):

$$r_a = A\sqrt{\frac{D^*}{\max(u, 0.05)}} \tag{5.16}$$

with u as the wind speed at the leaf surface and A and D^* as plant specific constants - $A = 87\sqrt{\text{s}}\ \text{m}^{-1}$ for deciduous trees and grass and $A = 200\sqrt{\text{s}}\ \text{m}^{-1}$ for conifers. D^* accounts for the leaf diameter, 0.15 m for deciduous trees and 0.02 m for conifers and grass in the model (Bruse, 2007).

The sublayer resistance r_b represents resistances caused by the quasi-laminar layer adjacent to the surface. Here, the transfer velocities depend on the molecular properties of the compound and the surface. The sublayer resistance is calculated (see

equation 5.17) using friction velocity u_* and the Schmidt-Number which is defined as the ratio of the kinematic viscosity of air ν ($\nu = 1.5 \cdot 10^{-5}$ at 298K) and the molecular diffusivity D_χ of the compound in air - here isoprene: $D_{\chi iso} = 0.110$ cm^2 s^{-1} (Leng et al., 2013).

$$S_c = \frac{\nu}{D_\chi}$$

$$r_b = \frac{1}{u_*} \cdot 5Sc^{2/3} \tag{5.17}$$

The surface resistance r_t accounts for solubility processes of the compound with various surfaces. It is dependent on chemical properties of both the gas and the surface type. ENVI-met differentiates between four different surfaces (Bruse, 2007):

- bare soil $r_{t,Soil}$
- sealed/artificial surfaces incl. walls and roofs $r_{t,Sealed}$
- water surfaces $r_{t,Water}$
- plant leaves $r_{t,Plant}$

The surface resistance for bare soil is calculated using the resistances of SO_2 and O_3 as reference points for reactive (SO_2) and non-reactive (O_3) species. The resistance for SO_2 and O_3 are set to $r_{t,SO_2} = 1000$ and $r_{t,O_3} = 400$. The resistance for other gases is then calculated by (Bruse, 2007):

$$r_{t,Soil} = \left(\frac{10^{-5} \cdot H_i^*}{r_{t,SO_2}} + \frac{f_0^i}{r_{t,O_3}} \right)$$

with H_i^* as the effective Henry's law constant of the gas and f_0^i as the normalized reactivity. For isoprene, $H_i^* = 2.8 \cdot 10^{-2}$ mol L^{-1} atm^{-1} for the solubility of isoprene and $f_0^i = 0.1$ (Leng et al., 2013).

Since sealed surfaces do not absorb gases, the resistance for sealed/artificial surfaces incl. walls and roofs $r_{t,Sealed}$ is set to 9999 making the absorption of gases practically impossible (Bruse, 2007).

For the resistance of water surfaces ENVI-met uses the approach presented by Sehmel (1980):

$$r_{t,Water} = \frac{2.54 \cdot 10^4}{H_i^* \cdot T_0 \cdot u_*}$$

with T_0 as the local surface temperature and u_* as the friction velocity (Bruse, 2007).

To calculate the resistance of plant leaves $r_{t,Plant}$, the stomatal resistance, the mesophyll resistance and the effects of dew that might cover a plant's leaves are taken into account. The resistance is then calculated by:

$$r_{t,Plant} = (1 - f_w) r_s^* + f_w r_{t,Water}$$

with f_w as the fraction of leaf that is covered by water (e.g. dew) and r_s^* as the combined resistance of the stomata and mesophyll. To correctly describe the stomatal resistance for the compound, the resistance r_s is multiplied with the ratio of molecular diffusivity of water and the compound D_{H_2O}/D_χ (Bruse, 2007):

$$r_s^* = r_s (D_{H_2O}/D_\chi) + r_{meso}$$

The mesophyll resistance r_{meso} is calculated after Seinfeld and Pandis (1998) using the Henry's law constant (H_i^*) and the normalized reactivity of the compound (f_0^i) (Bruse, 2007):

$$r_{meso} = \left(3.3 \cdot 10^{-4} H_i^* + 100 \cdot f_0^i\right)^{-1}$$

5.2.2.3 Chemical reaction model

Apart from the deposition of isoprene due to the various resistances mentioned above, a chemical reaction model reducing the concentration of isoprene and increasing the concentrations of the reaction products was developed. The main focus of the chemical reaction model is the estimation of the influence of isoprene on the production of tropospheric ozone. Since the biochemical reactions of isoprene are very complex and depend to a great extent on the environmental conditions, only the most important reaction processes leading to a change in ozone concentrations have been implemented as of yet.

Tropospheric ozone is mainly formed under the influence of NO_x. In absence of VOCs, nitrogen oxide, nitrogen dioxide and ozone form a chemical equilibrium in which the ozone concentration can be expressed as a linear relation of NO and NO_2:

$$O_3 \approx \frac{NO_2}{NO}$$

The dominant processes in this chemical equilibrium are:

$$O_3 + NO \longrightarrow NO_2 + O_2 \tag{5.18}$$

$$NO_2 + h\nu \longrightarrow NO + O \tag{5.19}$$

$$O + O_2 + M \longrightarrow O_3 + M \tag{5.20}$$

At nighttime the oxidation of NO with O_3 (reaction 5.18) will lead to an increase of NO_2 until all O_3 is used up. The reaction runs fast and takes only a few minutes, depending on concentration and ambient temperature. During the daytime and in

presence of sunlight the destruction of NO_2 due to photolysis is predominant (see equation 5.19). Reaction 5.20 then rapidly leads to the formation of ozone (Atkinson, 2000).

In the presence of VOCs such as isoprene, however, complex oxidation processes can disrupt the equilibrium and increase the formation of NO_2 leading to more potential compound that can form tropospheric ozone via reactions 5.19 and 5.20. The most important of these processes, primary oxidation with hydroxyles (OH) and secondary oxidation of hydroperoxides (RO_2) with NO, are implemented in ENVI-met to yield the ozone-building potential of the BVOC isoprene.

In addition to the reactions above, the following (simplified) NO_2 forming and therefore ozone-increasing isoprene related reactions after Paulot et al. (2009) and Sander et al. (2011) are implemented[1]:

$$\mathrm{C_5H_8 + OH \longrightarrow RO_2 + O_2} \tag{5.21}$$
$$k^1_{C5H8+OH} = 3.1 \cdot 10^{-11} \exp\left(\frac{350}{T}\right)$$

$$\mathrm{RO_2 + NO \longrightarrow 0.883NO_2 + 0.803HO_2 + x} \tag{5.22}$$
$$k^2_{RO2+NO} = 2.7 \cdot 10^{-12} \exp\left(\frac{350}{T}\right)$$

[1]The indices for the reaction constants k [cm^3 $molecule^{-1}$ s^{-1}] indicate their source:
1: Sander et al. (2011)
2: Paulot et al. (2009)
3: Saunders et al. (2003)
4: IUPAC (2015)

$$\mathrm{HO_2 + NO \longrightarrow OH + NO_2} \tag{5.23}$$
$$k^1_{HO2+NO} = 3.3 \cdot 10^{-12} \exp\left(\frac{270}{T}\right)$$

with RO_2 as the isoprene oxidation product ($HOCH_2C(OO)(CH_3)CH{=}CH_2$) and x as compounds resulting from reactions that are not implemented in the model.

Besides these implicit ozone-forming reactions the following reactions reducing the amount of either potential precursor compounds to ozone or the ozone concentration itself were implemented:

$$\mathrm{HO_2 + HO_2 \longrightarrow H_2O_2 + O_2} \tag{5.24}$$
$$k^1_{HO2+HO2} = 2.2 \cdot 10^{-13} \exp\left(\frac{600}{T}\right)$$

$$\mathrm{RO_2 + HO_2 \longrightarrow x} \tag{5.25}$$
$$k^3_{RO2+HO2} = 2.91 \cdot 10^{-13} \exp\left(\frac{1300}{T}\right) \cdot (1 - \exp(-0.245 \cdot n_C))$$

$$\mathrm{HO_2 + O_3 \longrightarrow OH + 2O_2} \tag{5.26}$$
$$k^4_{HO2+O3} = 2.03 \cdot 10^{-16} \left(\frac{T}{300}\right)^{4.57} \cdot \exp\left(\frac{693}{T}\right)$$

$$\mathrm{OH} + \mathrm{O_3} \longrightarrow \mathrm{HO_2} + \mathrm{O_2} \tag{5.27}$$
$$k^4_{OH+O3} = 1.7 \cdot 10^{-12} \exp\left(\frac{-940}{T}\right)$$

$$\mathrm{OH} + \mathrm{NO_2} \longrightarrow \mathrm{HNO_3} \tag{5.28}$$
$$k^4_{OH+NO2} = 3.5 \cdot 10^{-11}$$

with n_C as the carbon number of the compound, here 5.

Before the overall concentrations of the different compounds can be calculated using the rate equation scheme of the OSPM model (Berkowicz et al. 2011), the concentration of the isoprene emission of a plant-gridcell in $[\mu g_{iso}\ kg^{-1}_{Air}]$ has to be converted into $\frac{\text{molecules}}{\text{cm}^3_{Air}}$:

$$\mathrm{C_5H_8}\left[\frac{\text{molecules}}{\text{cm}^3_{\text{Air}}}\right] = \rho\left[\frac{\text{kg}_{\text{Air}}}{\text{m}^3}\right] \cdot \mathrm{N_A}\left[\frac{\text{molecules}}{\text{mol}}\right] \cdot \mathrm{M^{-1}_{iso}}\left[\frac{\text{mol}}{\text{g}}\right] \cdot \mathrm{C_5H_8}\left[\frac{\mu\text{g}_{\text{iso}}}{\text{kg}_{\text{Air}}}\right] \cdot 1^{-12}$$

with ρ as the density of air (1.29kg m^{-3} at 20°C), $\mathrm{N_A}$ as the Avogadro constant ($\approx 6.022 \cdot 10^{23}\mathrm{mol}^{-1}$) and $\mathrm{M_{iso}}$ as the molecular mass of isoprene (68.12 g mol^{-1}).

The rate equations handle the increases and decreases of local concentration of the various compound due to the reactions 5.18 to 5.28:

$$\frac{\mathrm{d}\,[\mathrm{C_5H_8}]}{\mathrm{dt}} = -k_{C5H8+OH}[\mathrm{C_5H_8}]\,[\mathrm{OH}]$$

$$\frac{\mathrm{d}\,[\mathrm{RO_2}]}{\mathrm{dt}} = k_{C5H8+OH}[\mathrm{C_5H_8}]\,[\mathrm{OH}] - k_{RO2+NO}[\mathrm{RO_2}]\,[\mathrm{NO}] - k_{RO2+HO2}[\mathrm{RO_2}]\,[\mathrm{HO_2}]$$

$$\begin{aligned}\frac{\mathrm{d}\,[\mathrm{HO_2}]}{\mathrm{dt}} =& k_{RO2+NO}[\mathrm{RO_2}]\,[\mathrm{NO}] - k_{RO2+HO2}[\mathrm{RO_2}]\,[\mathrm{HO_2}] - k_{HO2+NO}[\mathrm{HO_2}]\,[\mathrm{NO}] \\ &+ k_{OH+O3}[\mathrm{OH}]\,[\mathrm{O_3}] - k_{HO2+O3}[\mathrm{HO_2}]\,[\mathrm{O_3}] - k_{HO2+HO2}[\mathrm{HO_2}]\,[\mathrm{HO_2}]\end{aligned}$$

$$\frac{\mathrm{d}\,[\mathrm{NO}]}{\mathrm{dt}} = -k_{NO+O3}[\mathrm{NO}]\,[\mathrm{O_3}] + \mathrm{J}\,[\mathrm{NO_2}] - k_{RO2+NO}[\mathrm{RO_2}]\,[\mathrm{NO}] - k_{HO2+NO}[\mathrm{HO_2}]\,[\mathrm{NO}]$$

$$\begin{aligned}\frac{\mathrm{d}\,[\mathrm{NO_2}]}{\mathrm{dt}} =& k_{NO+O3}[\mathrm{NO}]\,[\mathrm{O_3}] - \mathrm{J}\,[\mathrm{NO_2}] + k_{RO2+NO}[\mathrm{RO_2}]\,[\mathrm{NO}] \\ &+ k_{HO2+NO}[\mathrm{HO_2}]\,[\mathrm{NO}] - k_{OH+NO2}[\mathrm{OH}]\,[\mathrm{NO_2}]\end{aligned}$$

$$\begin{aligned}\frac{\mathrm{d}\,[\mathrm{O_3}]}{\mathrm{dt}} =& -k_{NO+O3}[\mathrm{NO}]\,[\mathrm{O_3}] + \mathrm{J}\,[\mathrm{NO_2}] - k_{OH+O3}[\mathrm{OH}]\,[\mathrm{O_3}] \\ &- k_{HO2+O3}[\mathrm{HO_2}]\,[\mathrm{O_3}]\end{aligned}$$

Due to the high reaction velocity of reaction 5.20 the term $\mathrm{J}\,[\mathrm{NO_2}]$ includes both the photolysis of NO_2 (reaction 5.19) and implicitly the formation of ozone (reaction 5.20) (Berkowicz et al., 2011).

5.3 Evaluation - proof-of-concept simulations

In the following chapter, the different elements of the BVOC model (isoprene emission model, dispersion model, chemical reaction model) will be evaluated using proof-of-concept simulations. For the evaluation of the isoprene emission model, two different sets of proof-of-concept simulations are conducted: First, the general plausibility of the resulting isoprene emissions will be tested within a simple model, examining both the local isoprene emission patterns within a tree canopy as well as the aggregated isoprene emissions for the entire tree. Second, the isoprene emission model is subjected to further validity tests by assessing the effects of different biological parameters on the resulting actual isoprene emissions. For the evaluation of the dispersion and chemical reaction models, two more sets of proof-of-concept simulations were conducted: In the first set, the additional effect of isoprene on the formation of tropospheric ozone is examined in a simple model area. To evaluate the causal relations and the impact of isoprene on the ozone formation, the influence of different meteorologies and different combinations of other compounds were assessed and compared against simulations excluding the emission of isoprene. In the second set of simulations, the dispersion and the ozone-building potential of isoprene were analyzed in a realistic case scenario in a larger model area. To evaluate the additional ozone formation due to the release of isoprene in the more realistic scenario, the simulation results of the isoprene-including scenario are again compared against a simulation where the isoprene emissions are excluded.

5.3.1 Basic proof-of-concept simulations for the isoprene emission model

In order to assess the general validity of the results obtained from the isoprene emission model, a simple model area containing a single mid-sized tree was created, and actual isoprene emissions were simulated over a period of ten days. These actual

isoprene emissions were then examined regarding both their local distributional patterns as well as the aggregated values for the entire tree. For the local distributional patterns, plausibility criteria were derived from theoretical expectations, and the aggregated values were compared to empirical values obtained from the literature to test their validity. Furthermore, the aggregated values were evaluated with regard to their reaction to varying leaf temperatures, received PAR and drought stress.

To start off, a basic tree geometry was defined (figure 5.3). The height of the tree is 15 meters, its crown diameter extends up to 13 meters. The roots are digitized in a cylindrical form with a vertical dimension of 2.5 meters and a diameter of up to 8.75 meters.

Figure 5.3: Basic tree geometry for the isoprene proof-of-concept simulation

The base isoprene emission capacity of the tree was set to 10 μg_{iso} g_{leaf}^{-1} h^{-1}, the dry leaf weight to 100 g_{leaf} m^{-2} and the leaf area density (LAD) to 1 m^2 m^{-3}. The base isoprene emission capacity per grid cell is thus 1 mg_{iso} $gridcell^{-1}$ h^{-1}. The tree was then placed into a simple model area with dimensions of 30 × 30 × 35 grids and a horizontal and vertical resolution of 1 meter. The area is kept very simple, containing no other objects but the tree itself, to avoid any complex influences of

the local microclimate (figure 5.4). Its geographical location is Mainz, Germany.

Figure 5.4: Model area for the basic proof-of-concept simulations for the isoprene emission model

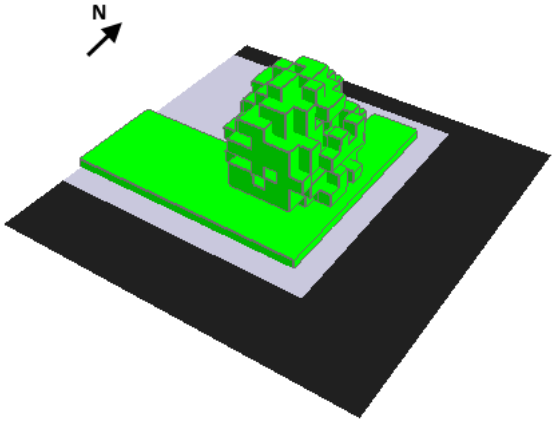

Model area dimensions: $30 \times 30 \times 35$ grids; vertical and horizontal resolution: 1 meter; location: Mainz, Germany

The initial values of basic parameters of the simulation are displayed in table 5.1, and the diurnal cycle of the boundary conditions for the air temperature and relative humidity is plotted in figure 5.5.

Table 5.1: Initial values of basic environmental and meteorological parameters

parameter	**value**
simulation start date	23th July 2003
simulation start time	06:00:00
total simulation time	240 h
wind speed in 10 m height	1.3 m/s
wind direction	225 deg
maximum air temperature	304.79K
minimum air temperature	293.33K

Since actual isoprene emissions are directly affected by the amount of received PAR and the leaf temperature (equation 5.1), several distinct patterns should emerge

Figure 5.5: Diurnal cycle of the air temperature and relative humidity in 2 meters height in the isoprene proof-of-concept simulations

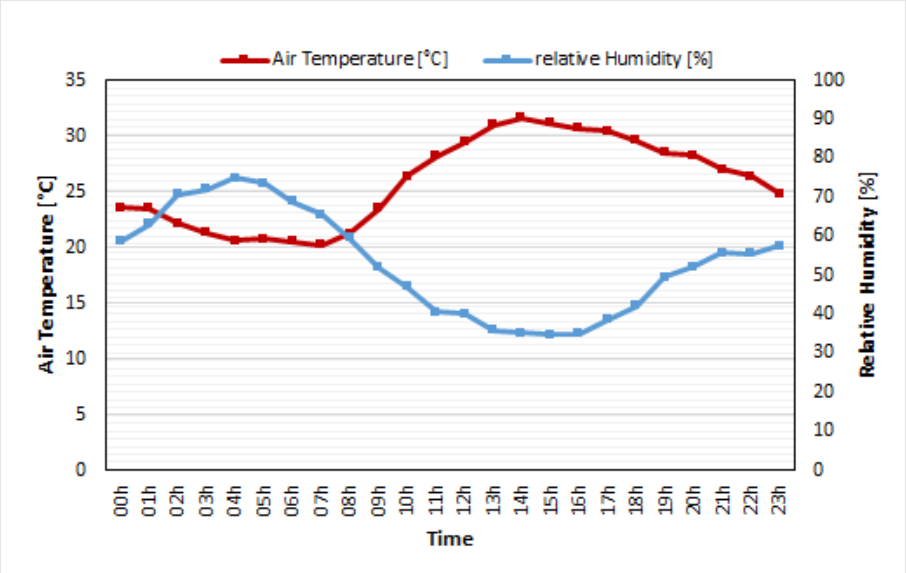

when examining the simulation results for local isoprene emissions inside the tree canopy: First of all, as grid cells receive different amounts of PAR and are subject to different leaf temperatures, local differences in actual isoprene emissions should be observable between these grid cells. Furthermore, actual isoprene emissions should generally increase with increasing exposure to PAR due to the monotonically increasing effect of photosynthetic active radiation on isoprene emission (see figure 5.6). However, because of the bell-shaped relationship between leaf temperature and isoprene emission depicted in figure 5.7 and described above (equation 5.5), expectations are different for the effect of leaf temperature. Here, too, an increase of actual isoprene emissions is expected but only until $T_{opt} = 312.5K$ is reached; for leaf temperatures above this optimum temperature, a decrease of actual isoprene emissions should be visible in the simulation results.

Figure 5.8 and 5.9 depict the local isoprene emission fluxes for every grid cell in mg_{iso} gridcell^{-1} h^{-1}. The white signatures resemble values near the base emission

Figure 5.6: Isoprene emission dependence on photosynthetic active radiation

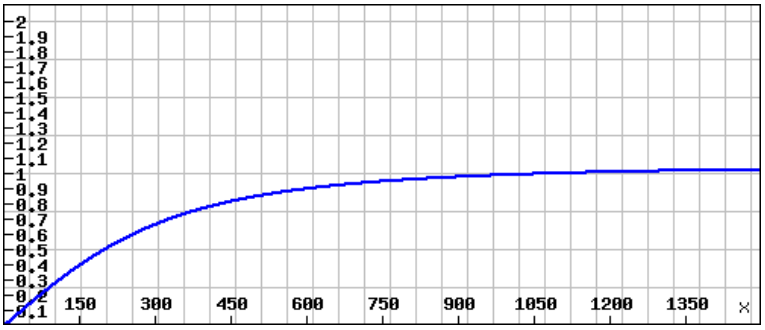

x-Axis: photosynthetic active radiation in μmol m^{-2} s^{-1}, y-Axis: normalized isoprene emission rate

Figure 5.7: Isoprene emission dependence on leaf temperature

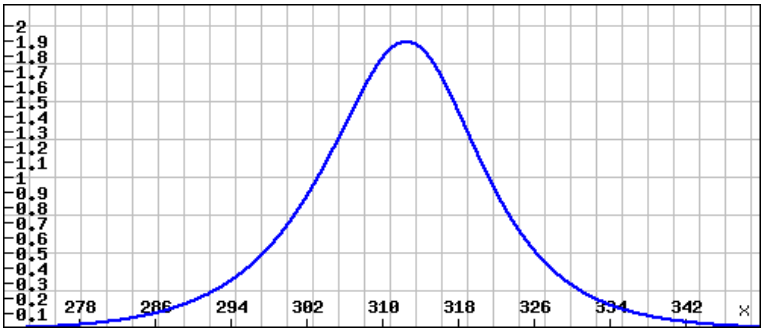

x-Axis: leaf temperature in Kelvin, y-Axis: normalized isoprene emission rate

capacity of 1 mg_{iso} $gridcell^{-1}$ h^{-1}, while green to blue colors indicate a reduced flux, and yellow to pink colors represent increased isoprene emission rates. Thanks to the high resolution of the microscale model ENVI-met, the local differences in the actual isoprene emission are clearly visible in the simulation results at both 09:00 (figure 5.8) and 12:00 (figure 5.9) of the first simulation day. Both figures show a great variation of the isoprene emission flux within the crown canopy, with emission rates varying between 0.45 mg_{iso} $gridcell^{-1}$ h^{-1} and 1.69 mg_{iso} $gridcell^{-1}$ h^{-1} in the morning (figure 5.8) and 0.36 mg_{iso} $gridcell^{-1}$ h^{-1} and 1.78 mg_{iso} $gridcell^{-1}$ h^{-1} at noon.

Figure 5.8: Local isoprene emission flux - base tree - simulation time: 09:00h, simulation date: 23.07.2003

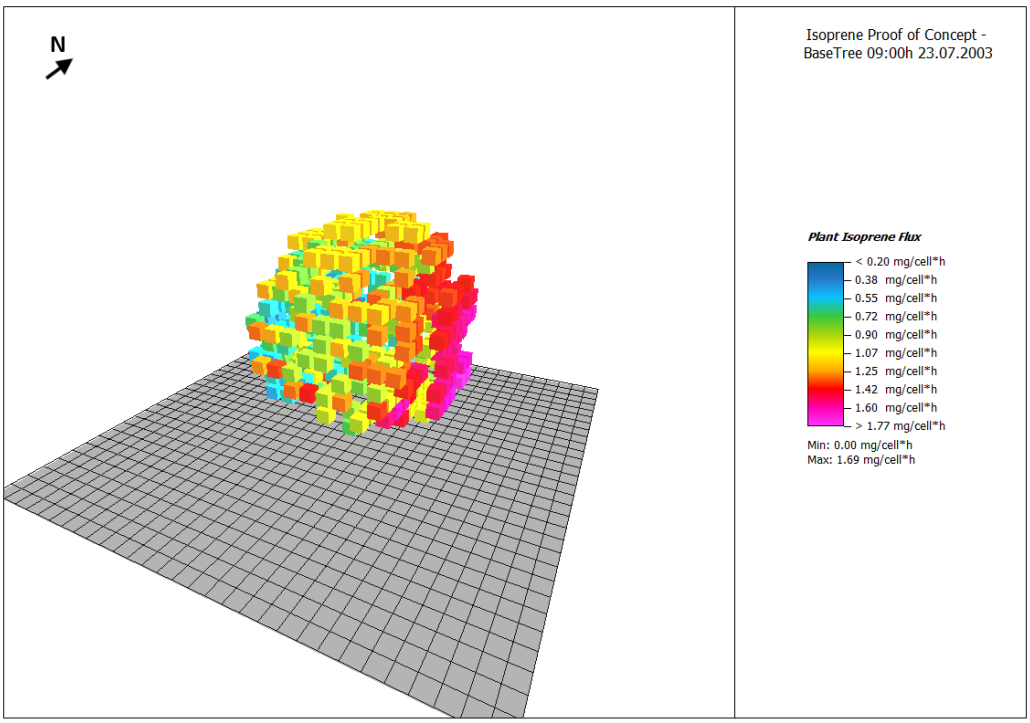

In order to test for the second proposition - that actual isoprene emissions are dependent on the amount of received PAR -, the local distributions of received PAR (figure 5.10, figure 5.11) and isoprene emissions (figure 5.8, figure 5.9) are compared. At 09:00, the highest values for both received PAR and actual isoprene emissions are reached at the East-facing side of the tree (figure 5.8), substantiating the suitability of the model. For the 12:00 simulation results, no such similarity of patterns can be observed. Here, received PAR is highest for the top- and South-facing grid cells at the outside of the canopy (figure 5.11), while isoprene emissions are highest for grid cells further inside the canopy (figure 5.9).

However, this does not indicate a bad fit of the isoprene emission model, but rather simply suggests a dominant influence of the leaf temperature: As can be observed

Figure 5.9: Local isoprene emission flux - base tree - simulation time: 12:00h, simulation date: 23.07.2003

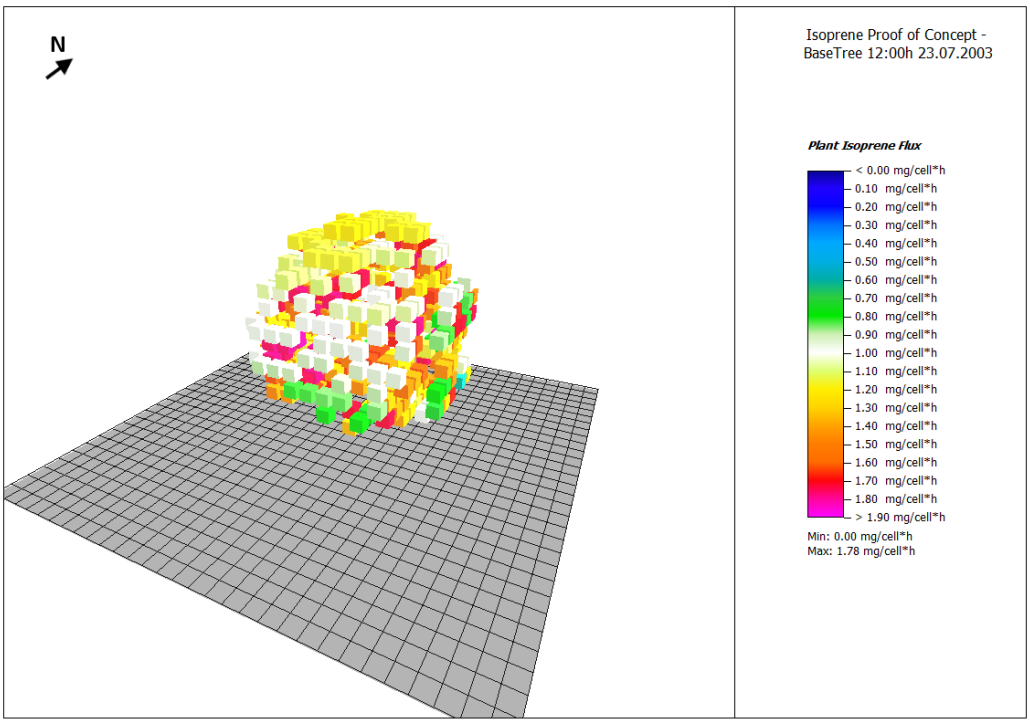

from figure 5.13, leaf temperatures for the grid cells at the outside of the canopy exceed the optimum temperature T_{opt} = 312.5K or 39.35°C, resulting in a sharp reduction of isoprene emissions (see figure 5.7). Due to the asymptotic gradient at high levels of photosynthetic active radiation (see figure 5.6), this reductive effect cannot be compensated for by the higher amount of PAR received by these grid cells, explaining the lack of fit between figure 5.11 (received PAR) and figure 5.9 (actual isoprene emission). Comparing finally the local distributional patterns for leaf temperatures (figure 5.12, figure 5.13) and actual isoprene emissions (figure 5.8, figure 5.9), the expected effects emerge: For leaf temperatures below the optimum temperature, higher leaf temperatures result in higher isoprene emissions, clearly visible at 09:00 (figure 5.8, figure 5.12); and for leaf temperatures exceeding the

Figure 5.10: Received PAR - base tree - simulation time: 09:00h, simulation date: 23.07.2003

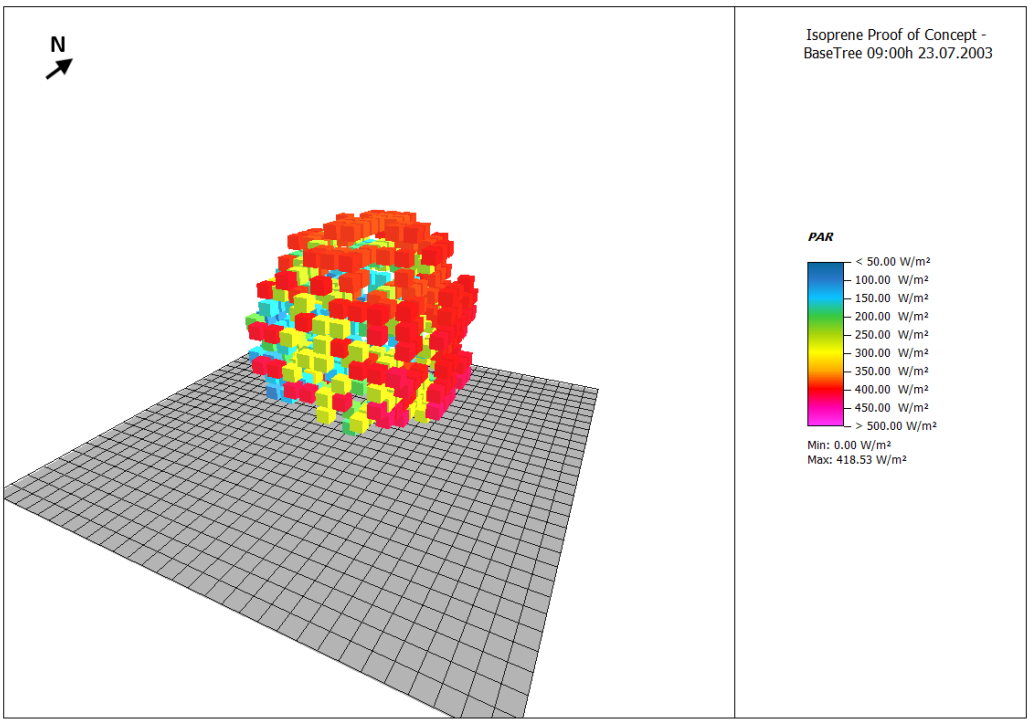

optimum temperature, isoprene emissions decrease, clearly visible for the grid cells at the outside of the canopy at 12:00 (figure 5.9, figure 5.13).

Summing up, the analysis of the local distributional patterns of actual isoprene emissions yielded promising results with regard to the accuracy of the isoprene emission model: Subject to changing amounts of PAR and varying leaf temperatures, isoprene emission fluxes varied between different grid cells within the tree canopy, confirming the expectations derived from the theoretical model.

Moving away from the in-depth analysis of local variations in actual isoprene emissions, the following section aims to validate the model results on the aggregate level. In order to do so, the model results are compared to empirical values obtained from the literature, and the aggregate effects of diurnal variations in received PAR

Figure 5.11: Received PAR - base tree - simulation time: 12:00h, simulation date: 23.07.2003

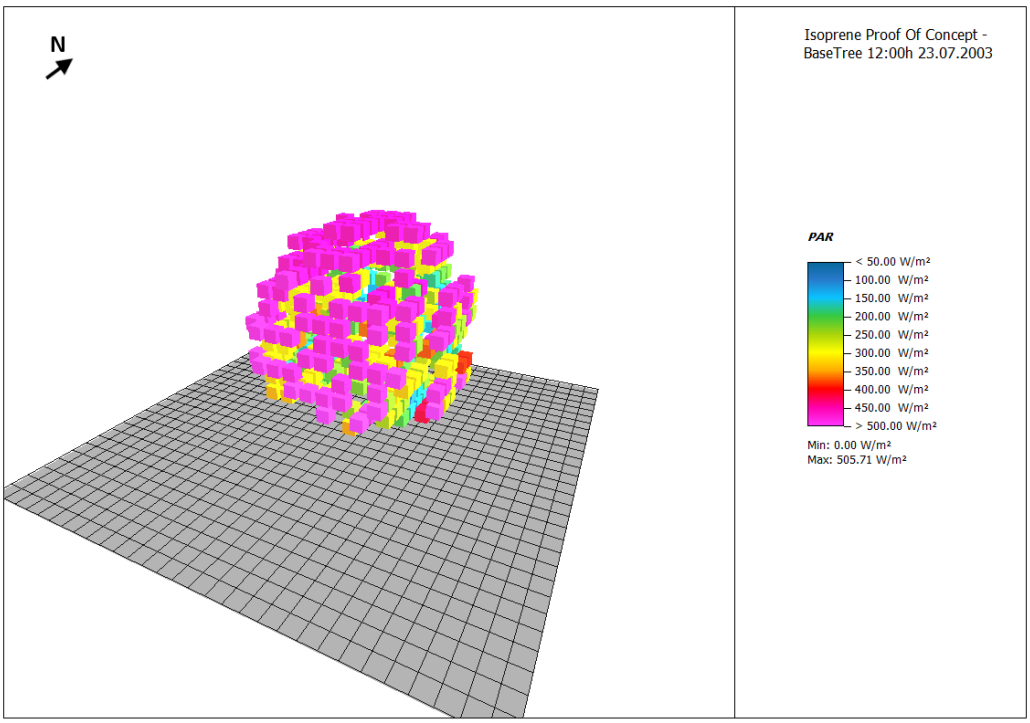

and leaf temperature as well as the effects of drought stress on the actual isoprene emissions are assessed and judged against theoretical expectations.

To obtain aggregate-level isoprene emission values for the tree as a whole, the isoprene emission values of the individual grid cells were aggregated based on the advancements of the plant-as-object model (see chapter 3). It is, however, quite challenging to find appropriate benchmark values due to the lack of empirical measurement data. The only suitable data were obtained by Benjamin and Winer (1998), who try to upscale emission data to a tree scale using biomass factors to estimate the ozone-forming potential of urban trees and shrubs. In their study, the authors used databases of emission rates of isoprene found in the literature and calculated hourly emission rates for a representative summer day in Southern California. The

Figure 5.12: Local leaf temperature - base tree - simulation time: 09:00h, simulation date: 23.07.2003

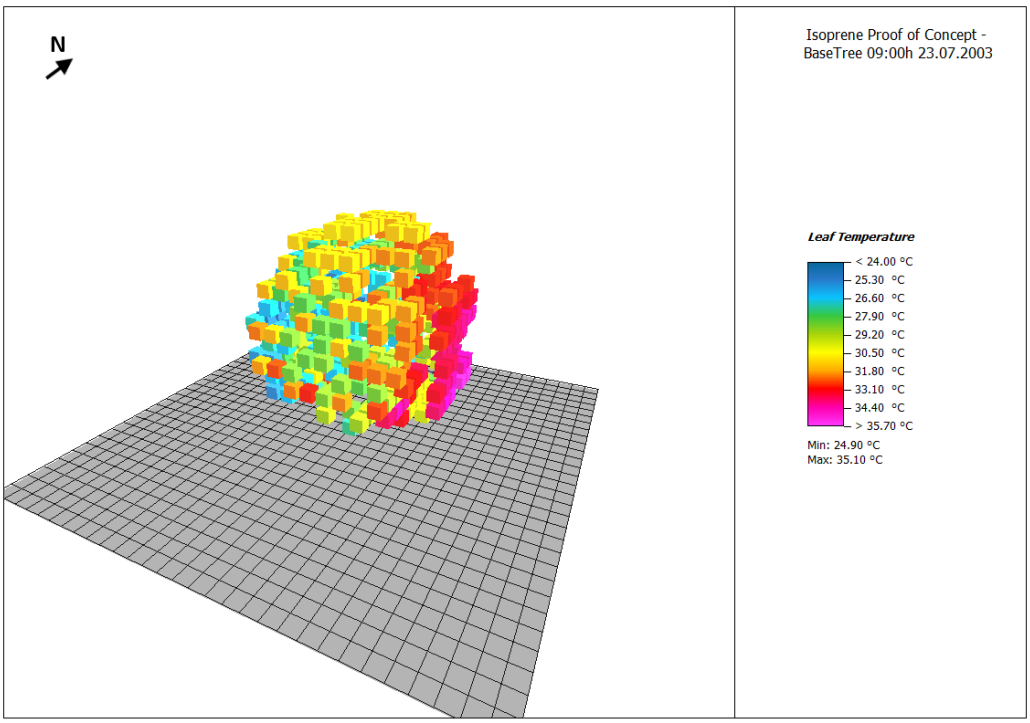

diurnal cycle of air temperature and light intensity for this representative summer day was created using averaged hourly values of air temperature and light intensity for several measurement sites and over a period of three months, July to September. Even though neither the averaged input data not the averaged location are strictly comparable to the ENVI-met model outputs used here, the dimensions of the daily isoprene emission for a tree with a similar base isoprene emission rate and leaf weight should match. One of the trees examined by Benjamin and Winer (1998) is Quercus agrifolia (Coast Live Oak), which has a biomass of 46.5 $kg_{dryleaf}$. As the proof-of-concept base tree has an LAD of 1, a dry leaf weight of 100 $g_{leafdry}$ m^2 and consists of 451 leaf grid cells, its biomass is 45.1 $kg_{dryleaf}$, constituting almost a perfect match. Consequently, the actual isoprene emissions should be within the

Figure 5.13: Local leaf temperature - base tree - simulation time: 12:00h, simulation date: 23.07.2003

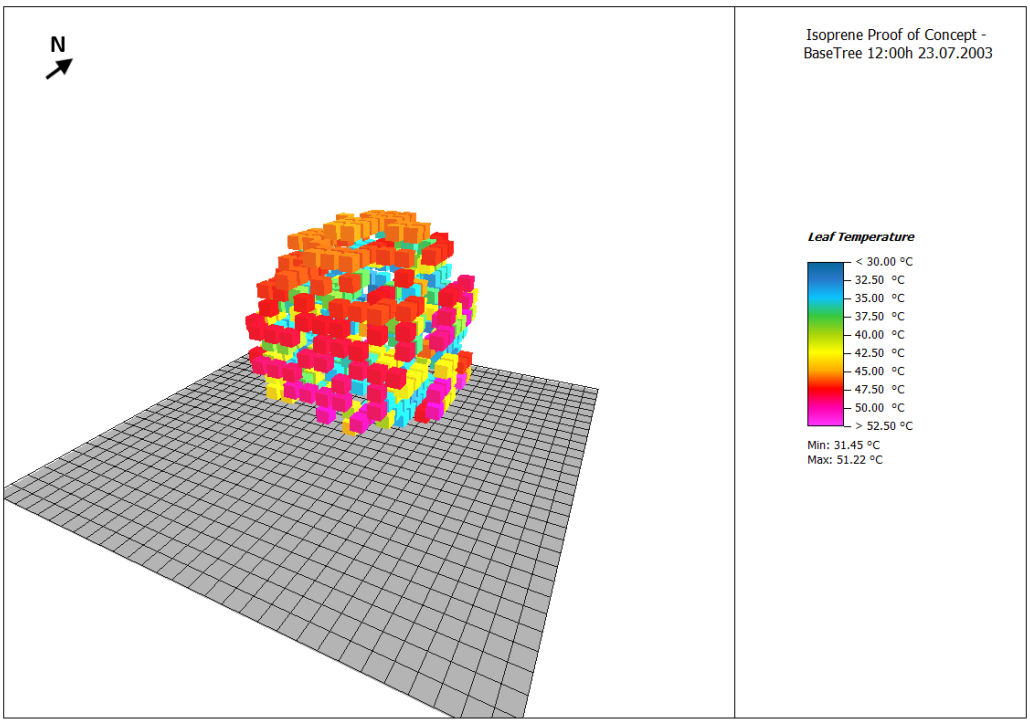

same range for both trees. The study of Benjamin and Winer (1998) estimates 12.6 g_{iso} tree^{-1} d^{-1}, while the ENVI-met model calculates 12.3 g_{iso} tree^{-1} d^{-1}. Certainly, this does not give a direct indication of the validity of the model on a tree scale, but the fact that similar input values result in similar output values definitely shows that the model does indeed estimate the actual isoprene emission in the right dimensions.

Further validity checks focus on the aggregate effects of diurnal variations in received PAR and leaf temperature. Here, the same effects should be at work as on the local level of individual grid cells: While an increase in received PAR should monotonously increase actual isoprene emissions, the positive effect of leaf temperature on isoprene emissions should be reversed once the optimum temperature $T_{opt} = 312.5$K is reached, likely suppressing the continued positive effect of received

PAR due to the shallower gradient for this factor (see figures 5.6, 5.7). In addition, as soon as received PAR reaches zero - i.e., between sunset and sunrise - isoprene emissions should also cease entirely, as can be inferred from equation 5.1.

The simulation results in figure 5.14 confirm that the isoprene emissions for the tree as a whole follow a diurnal cycle and drop to zero right after sunset around 19:30, only starting to rise again after sunrise the next day, around 05:30, reflecting the lack of PAR during the night. During the day, the non-linear effect of leaf temperature is represented in a marked midday depression of isoprene emissions caused by leaf temperatures exceeding the optimum temperature due to high stomatal resistance values. Apart from this depression, isoprene emissions steadily increase with increasing received PAR and leaf temperatures (up until around 11:00, when leaf temperatures reach T_{opt}), and decrease with ceasing sunlight and dropping temperatures (after around 17:00).

Figure 5.14: Diurnal cycle of the isoprene emission flux and the average stomatal resistance for the base tree as a whole - first day of simulation: 23.07.2003

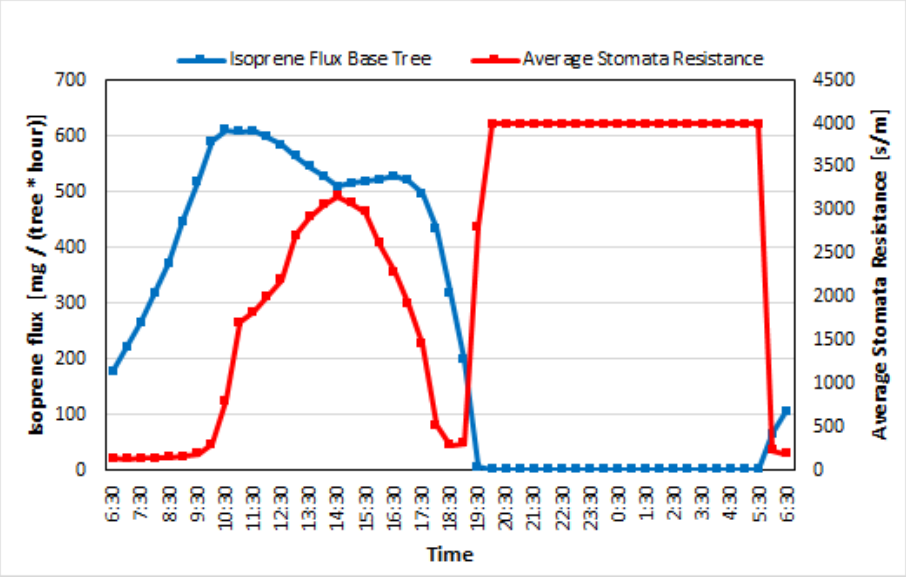

For a final validity check, the effects of drought stress were examined by running the

proof-of-concept simulation for multiple days. Since no precipitation is implemented in the ENVI-met model, transpiration of the plant as well as evaporation reduce the soil moisture over the time of the simulation, leading to drought stress for the base tree. As equations 5.10 and 5.11 demonstrate, the isoprene emission rate is reduced in situations of such drought stress; accordingly, the simulation results should show a continuous decline in isoprene emissions from day to day.

Figure 5.15 plots the isoprene emission flux together with the normalized water access factor (as defined in equation 3.6 in chapter 3) for the base tree during the first three days of the simulation. The expected effects of drought stress are clearly visible as the isoprene emission fluxes are reduced day after day, reflecting the decreasing water access. While isoprene emissions remain fairly constant during the early morning and late afternoon hours, reductions are very prominent during midday, when around 40 percent of the peak values are lost from day one to day two, and another 20 percent from day two to day three. Again, this phenomenon is related to the leaf temperatures: With reduced water access, the plant closes its stomata more and more to avoid further loss of water, thereby increasing leaf temperatures. As long as leaf temperatures exceed the optimum temperature T_{opt}, such an increase causes a yet further reduction of isoprene emissions (see figure 5.7), resulting in a more pronounced drop in isoprene emissions during midday.

Summing up, the analysis of the aggregate isoprene emissions further confirmed the suitability of the isoprene emission model: Isoprene emission values obtained from the model for the entire tree match empirical values found in the literature; diurnal variations in aggregate isoprene emissions follow the patterns expected on theoretical grounds; and isoprene emissions under drought stress behave according to the expectations derived from theoretical considerations.

Figure 5.15: Isoprene flux and normalized water access for the base tree over the first three simulated days: 23.-25.07.2003

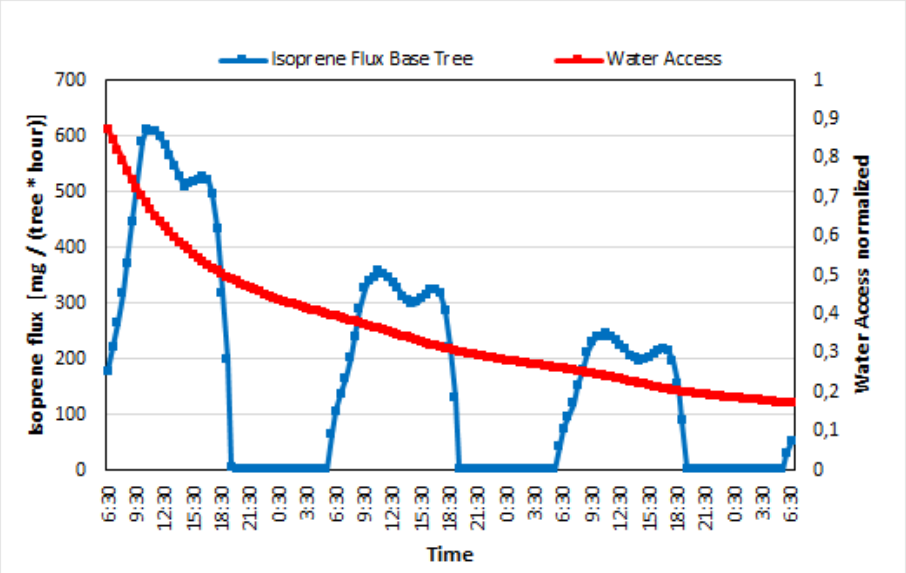

5.3.2 Proof-of-concept simulations assessing the effects of biological parameter alterations

In the second part of the isoprene emission model proof-of-concept simulations, the focus lies on assessing the plausibility of the effects of different biological parameters - dry leaf weight, base isoprene emission capacity and LAD - of trees onto the actual isoprene emissions. In order to isolate these effects, all related proof-of-concept simulations were run using the same model area and meteorology, which is identical to the conditions in the first part of the isoprene emission model proof-of-concept simulations (chapter 5.3.1). Based on equation 5.1, a linear effect of both dry leaf weight and base isoprene emission capacity on the resulting actual isoprene flux is expected. However, for the third biological parameter, LAD, no such linear effect should emerge as LAD also affects shade casting and wind speeds inside the canopy

crown, thus modifying actual isoprene emissions in a more complex way.[1] To verify that equation 5.1 has been implemented into ENVI-met correctly and that the model correctly adjusts to differences in the biological parameters of trees, simulations were conducted for low (factor 0.5), medium (base tree, factor 1.0) and high (factor 2.0) values of all three biological parameters while keeping all other parameters constant. Table 5.2 shows the exact parameter values used in the respective simulations.

Table 5.2: Different values of the altered isoprene emission regulating parameters

	base isoprene emission capacity [$\mu g_{iso}\ g_{leaf}^{-1}\ h^{-1}$]	**dry leaf weight per sqm** [$g_{Leaf}\ m^{-2}$]	**LAD** [$m^2\ m^{-3}$]
base tree	10	100	1
high leaf weight	10	*200*	1
low leaf weight	10	*50*	1
high base emission	*20*	100	1
low base emission	*5*	100	1
high LAD	10	100	*2*
low LAD	10	100	*0.5*

For all three biological parameters, based on equation 5.1, higher values should then result in higher actual isoprene emissions. This relationship could be confirmed as demonstrated in figures 5.16, 5.17 and 5.18: For all three biological parameters, higher values lead to consistently higher actual isoprene emissions in the simulation results; and lower parameter values lead to consistently lower actual isoprene emissions. In addition, the results for different parameter values of dry leaf weight and

[1] The effect of LAD on actual isoprene emissions is three-fold: First, as an increase in LAD linearly increases the actual leaf area in a grid and thus the dry leaf weight, it also affects the actual isoprene emissions directly and linearly, just as dry leaf weight and base isoprene emission capacity. Second, however, an increase in LAD also affects the microclimate within the crown canopy due to increased shadow casting, causing differences in the amount of shortwave radiation individual leaves receive. This latter effect has two implications for the actual isoprene emissions: On the one hand, an alteration of the amount of received shortwave radiation directly influences the actual isoprene emissions via γ_P in equation 5.1. On the other hand, it also triggers changes in leaf temperatures and thus γ_T, surrounding air temperature and transpirational activity, which again influence the actual isoprene emissions. Third, alterations in LAD also affect the wind speed, which in turn affects the transpirational activity, which then affects leaf temperatures - and as changes in leaf temperatures lead to changes in γ_T, actual isoprene emissions are eventually affected as well.

base isoprene emission capacity are identical. This demonstrates that the expected linear effect of dry leaf weight and base isoprene emission capacity, respectively, on actual isoprene emissions is represented accurately in the model.

Figure 5.16: Comparison of isoprene fluxes between high and low leaf weight scenarios and the base tree - first day of the simulation: 23.07.2003

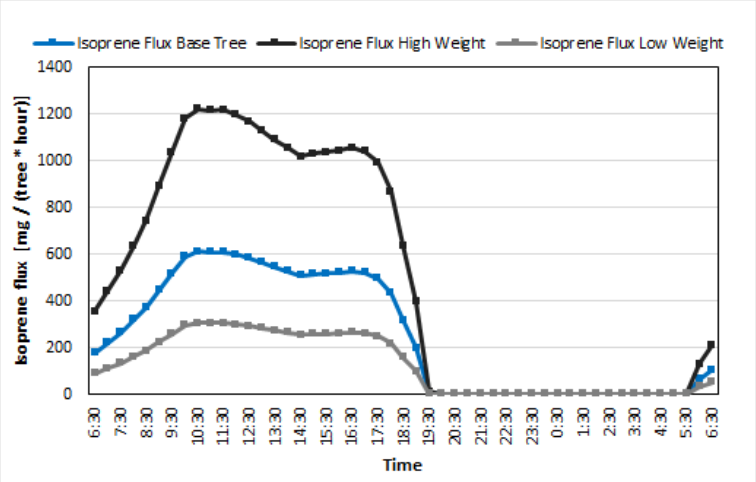

Figure 5.17: Comparison of isoprene fluxes between high and low base isoprene capacity scenarios and the base tree - first day of the simulation: 23.07.2003

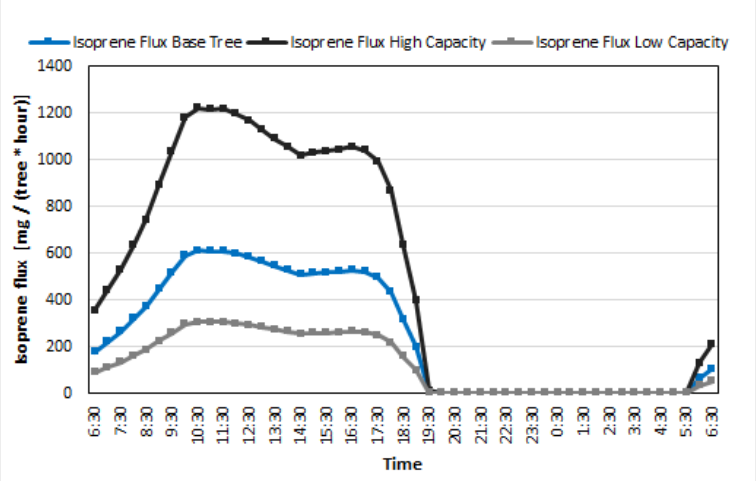

Figure 5.18: Comparison of isoprene fluxes between high and low LAD scenarios and the base tree - first day of the simulation: 23.07.2003

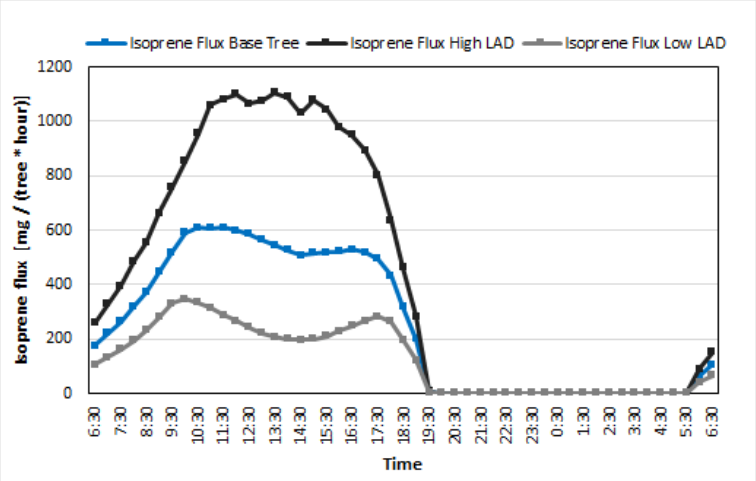

A comparison with figure 5.18 also clearly shows the expected non-linear effect of LAD on actual isoprene emissions: While actual isoprene emissions are rather similar to the ones in figures 5.16 and 5.17 for conditions of low and medium LAD, the curve looks decidedly different for high parameter values of LAD, indicating a more complex pattern of effects. More precisely, the results implicate a distinct shading effect: In conditions of high LAD, the shading effects caused by a higher density of leaves in the canopy crown lead to lower leaf temperatures around midday and thus a decreased depression of the actual isoprene emissions, which is clearly visible in the topmost curve of figure 5.18. In conditions of low LAD, this effect is reversed as shading is reduced, resulting in higher leaf temperatures and consequently a more pronounced midday depression of actual isoprene emissions, visible in the bottommost curve of figure 5.18.

Summing up, the simulation results of the isoprene emission model proof-of-concept-simulations with varying biological parameters show that the model correctly reproduces the linear effects of altered dry leaf weight and base isoprene emissions as well as the non-linear effect of changes in the LAD. This adds further weight to the

adequacy of the model.

5.3.3 Proof-of-concept simulations for the dispersion and chemistry model

Based on the results of the proof-of-concept simulations shown above, further proof-of-concept simulations were run in order to evaluate the implementations into the dispersion and chemical reaction model. This evaluation follows a basic logic, comparing the simulation results obtained using the basic dispersion and chemistry model - excluding the isoprene reactions - to the results obtained using the advanced dispersion and chemistry model which include the isoprene reactions (see chapters 2.1, 2.2). In doing so, the contribution of isoprene to the formation of tropospheric ozone can be identified and verified against theoretical expectations. The proof-of-concept simulations are split into two parts: In a first step, the effects of isoprene on the formation of tropospheric ozone are studied within a simplified model area and in different meteorological conditions and for different concentrations of the other reactants (NO, NO_2). In a second step, this impact of isoprene is examined within a larger model area, under more realistic conditions.

5.3.3.1 Proof-of-concept simulations for the dispersion and chemistry model in a simplified model area

In the first set of proof-of-concept simulations, the model area was kept small (45 x 50 x 25 grids in a 2 meter resolution) and fairly simple (figure 5.19). Its geographical location is Frankfurt am Main, Germany. To simulate the chemical processes leading to the formation and dissipation of tropospheric ozone, nitrogen monoxide and nitrogen dioxide sources had to be digitized. Since internal combustion engines are the main producers of these reactants, the sources were placed onto the streets of the model area in a height of 0.5 meters above the surface. All lanes were digitized

using line sources. Figure 5.19 displays the model area including the line sources for nitrogen monoxide and nitrogen dioxide (red dashed lines).

Figure 5.19: Model area for the dispersion and chemistry model proof-of-concept simulations in a simplified model area

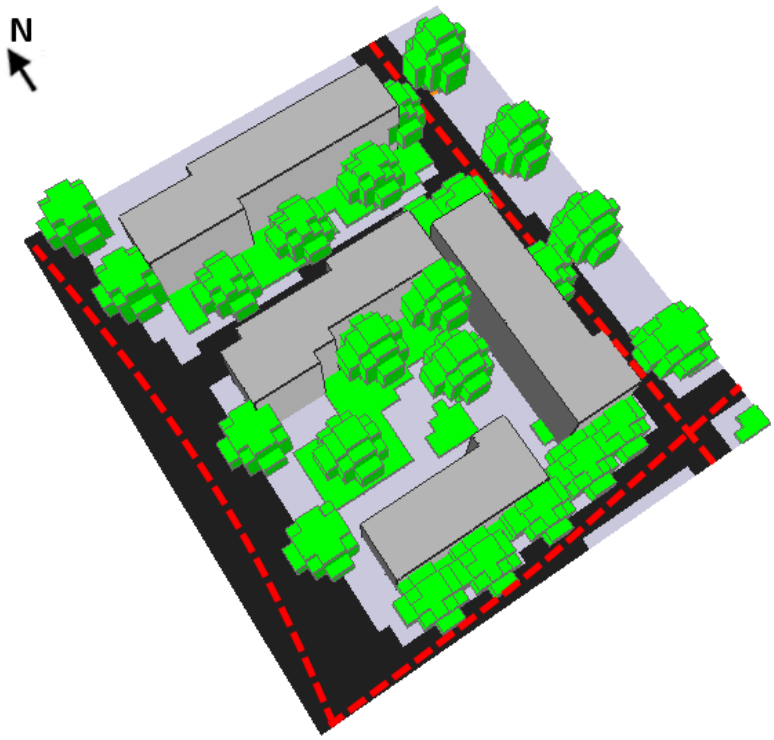

Model area dimensions: $45 \times 50 \times 25$ grids; vertical and horizontal resolution: 2 meters; location: Frankfurt am Main, Germany

In a realistic scenario, NO and NO_2 emissions would be subject to diurnal variations due to for example commuting traffic. However, in order to be able to examine the impact of isoprene on ozone formation as clearly as possible, this diurnal cycle was neglected and emission rates for both NO and NO_2 were kept constant throughout the simulation period. The absolute values were based on hypothetical amounts of traffic in the streets and on the ratio of gasoline-engined cars versus heavy load

traffic and diesel-engined cars.

Other than nitrogen monoxide and nitrogen dioxide, isoprene is produced by the LAD grids of the trees and thus had not to be digitized explicitly. All trees in the model area feature the same base isoprene emission capacity of 16 μg_{iso} g_{leaf}^{-1} h^{-1} and a leaf weight of 120 g_{Leaf} m^{-2}. The height and width of the crowns ranges from 12 meters to 17 meters in height and from 9 meters to 11 meters in width. The root volume is linearly adjusted to the crown sizes of the trees. To isolate the ozone-forming potential of isoprene, no additional background concentrations of O_3, NO and NO_2 were used.

The following evaluation of the dispersion and chemical models is conducted following the same logic as before: First, expectations about the effect of isoprene on the formation of tropospheric ozone are formulated based on theoretical considerations, then the results of different proof-of-concept simulations are validated against these expectations.

To examine the behavior of the model in different meteorological conditions, two meteorological scenarios were created. The first scenario features an average, mildly warm spring day with air temperatures around 18°C in 2 meters height. The simulation date was set to April 13th. The second scenario features a warm to hot summer day with maximum air temperatures of up to 32°C in 2 meters height. The simulation date was set to August 13th. Other boundary conditions - wind speed, leaf area density - were kept constant for both scenarios: Wind speed was set to 1.3 m s^{-1} in 10 meters height and LAD to 1 m^2 m^{-3}, neglecting leaf growth between the two scenarios. Figure 5.20 displays the diurnal cycles of air temperature and relative humidity for the two scenarios.

Apart from these different meteorological conditions, the behavior of the model was examined under two different chemical parameter constellations: In the first chemical parameter constellation, the line sources predominantly emit nitrogen monoxide,

Figure 5.20: Diurnal cycle of the air temperature and relative humidity in 2 meters height. Spring day and summer day scenarios

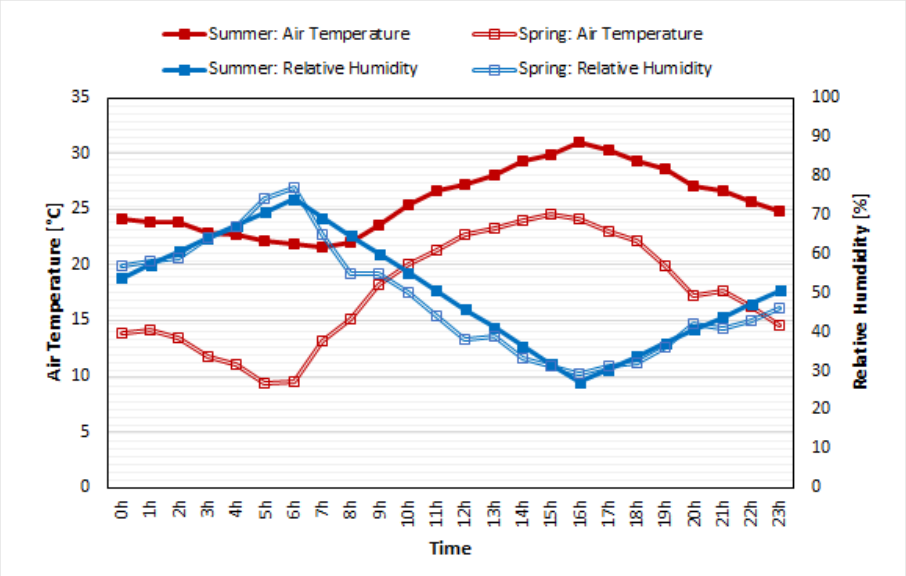

resulting in NO-dominant scenarios. This resembles a situation with a majority of gasoline-engined traffic. For these scenarios, all line sources were set to emit 20 μg s^{-1} m^{-1} of NO and 10 μg s^{-1} m^{-1} of NO_2. In the second chemical parameter constellation, the line sources in contrast predominantly emit nitrogen dioxide, resulting in NO_2-dominant scenarios. This resembles a situation with a majority of heavy load and diesel-engined traffic. For these scenarios, all line sources were set to emit 10 μg s^{-1} m^{-1} of NO and 20 μg s^{-1} m^{-1} of NO_2.

For all combinations of these conditions, two simulation results are compared in order to identify the contribution of isoprene to the formation of tropospheric ozone and verify that it conforms to the theoretical expectations: The first simulation ("isoprene-exluding scenario") only includes the chemical reactants nitrogen monoxide, nitrogen dioxide and ozone as they had been implemented into the basic dispersion and chemistry model; the second simulation ("isoprene-including scenario") additionally includes all newly implemented isoprene reactions as they have been

described above (chapters 5.2.1, 5.2.2).

The changes in the meteorology, in the ratio of NO and NO_2 and in the emissions of isoprene lead to 8 different simulation scenarios. Figure 5.21 shows the different scenarios in a graphical visualization.

Figure 5.21: Graphical visualization of the different scenarios

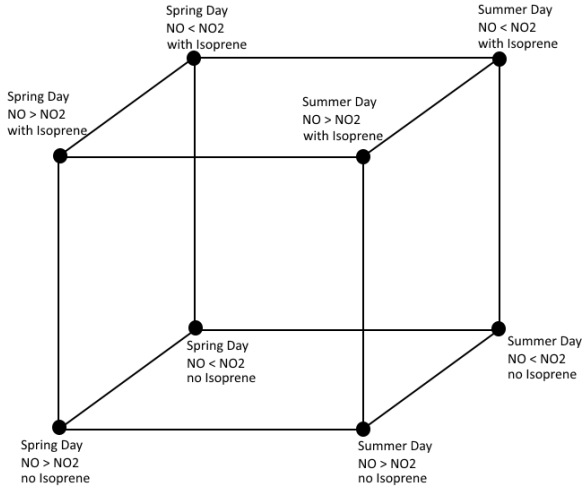

As far as the differences between the isoprene-including and isoprene-excluding scenarios are concerned, the most basic expectation is that the inclusion of isoprene in the dispersion and chemical reaction model will result in an increased formation of ozone due to the following isoprene-related reactions:

$$RO_2 + NO \longrightarrow 0.883NO_2 + 0.803HO_2 + x \tag{5.29}$$

$$HO_2 + NO \longrightarrow OH + NO_2 \tag{5.30}$$

These reactions increase the NO_2 concentration, which in turn leads to higher ozone values as described in equations 5.19 and 5.20. Furthermore, specific diurnal effects can be expected: While under conditions of sufficient solar radiation, the NO_2 resulting from the isoprene-induced reactions described above (reactions 5.29 and 5.30) is partially destroyed via photolyzation processes, these photolyzation processes are not strong enough to counter the NO_2-forming effects of isoprene under conditions of low solar radiation. These conditions are mainly present during the morning hours, when the already higher concentrations of NO_2 that accumulated overnight together with the starting isoprene production and thus its NO_2-forming effects are already quite strong, while photolyzation processes are still weak. The most drastic impact of isoprene on the formation of tropospheric ozone should thus occur during these morning hours, before the NO_2-forming effects of isoprene are countered by increasing photolyzation during the later hours of the day. On the other hand, no differences in ozone levels between the isoprene-including and isoprene-excluding scenarios should be visible during nighttime, as isoprene emissions drop to zero as soon as there is no more direct solar radiation, consequently reducing its ozone-forming effects to zero as well.

In addition to these general expectations, the effect of isoprene on the formation of tropospheric ozone should be stronger in the summer scenarios compared to the spring scenarios. This is caused by the higher radiation and ambient air temperatures which should lead to increased isoprene emissions of the trees. Furthermore, the impact of isoprene on the formation of tropospheric ozone should be much stronger in NO-dominant scenarios compared to the NO_2-dominant scenarios. While the higher NO_2 concentration in the NO_2-dominant scenarios already leads to higher ozone concentrations, NO_2 in the NO-dominant scenarios is not plentifully available for the photolyzation. With the high concentration of NO in the NO-dominant scenarios, the destruction of RO_2 and HO_2 by reacting with NO is much stronger than in the NO_2-dominant scenario. Thus the emission of isoprene into the NO-dominant

atmosphere leads to an increased reaction of RO_2 and HO_2 with NO, resulting in additional NO_2 that can be photolyzed to ozone.

Figures 5.22 and 5.23 display the diurnal cycles of the ozone concentrations for the spring and summer scenarios. The absolute levels of tropospheric ozone are very low for all scenarios (around 0.75 to 2.75 μg cm^{-3}). This is simply due to the fact that all simulations were conducted without any background concentrations of NO, NO_2 and O_3 in order to isolate the effects of isoprene.

Figure 5.22: Diurnal cycle of the average ozone concentration in a height of 1.8 meters - spring scenarios

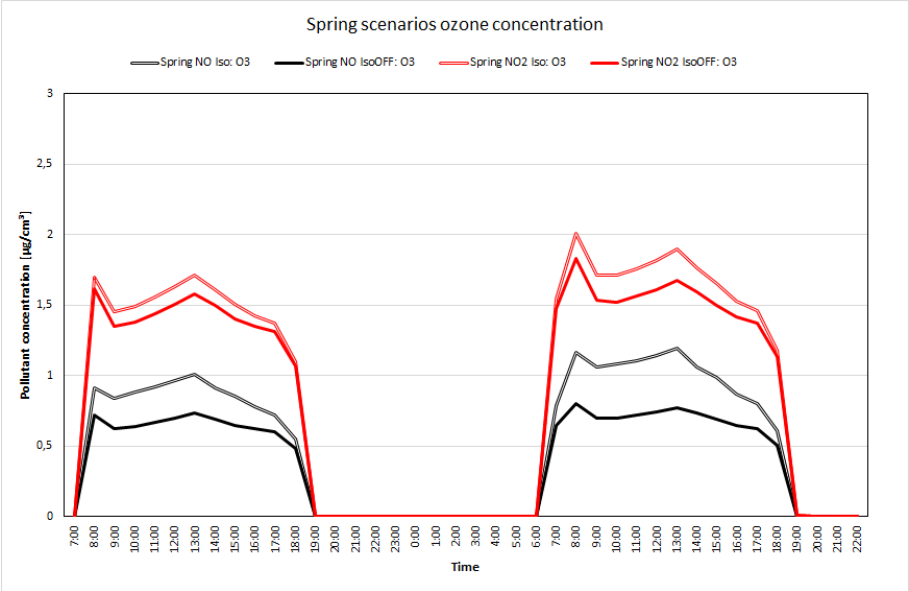

With regard to these effects of isoprene, figures 5.22 and 5.23 confirm the expected patterns: For the isoprene-including scenario, the concentration of tropospheric ozone is generally higher than for the isoprene-excluding scenario. Furthermore, the differences in ozone concentrations are largest during the morning hours (up until around 12:00) and decrease during the afternoon, when the NO_2 concentration is more and more reduced due to the ongoing photolyzation. Also, during nighttime, ozone concentration levels are zero in all scenarios, confirming the expectations and

corroborating the validity of the advanced dispersion and chemistry model.

Figure 5.23: Diurnal cycle of the average ozone concentration in a height of 1.8 meters - summer scenarios

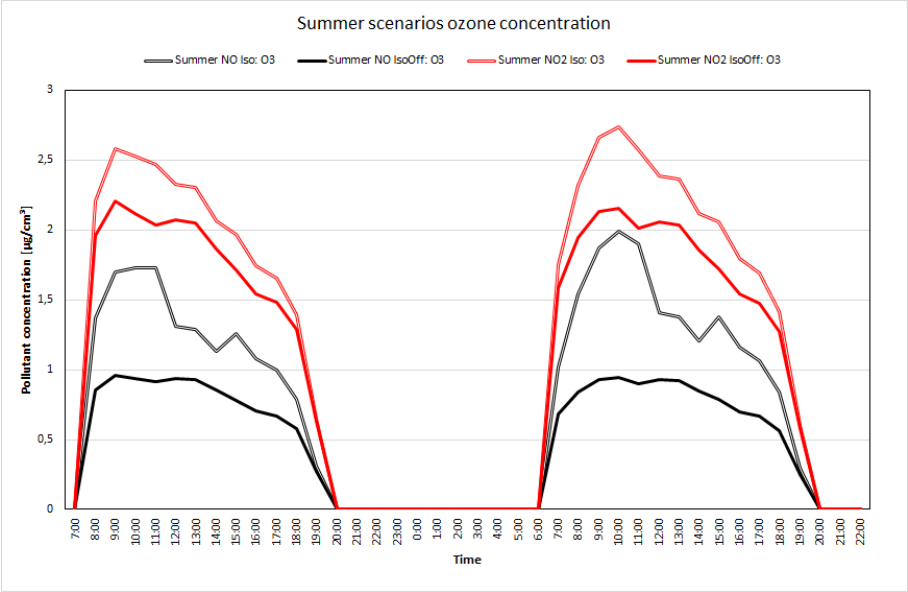

Figures 5.22 and 5.23 also confirm that the effect of isoprene on the ozone formation is generally higher in the summer scenarios than in the spring scenarios. The results also meet the expectations about the dependence of the increase of the ozone formation on the NO- and NO_2-dominant scenarios. Both figures show that the isoprene emissions in the NO-dominant scenarios lead to a higher increase of tropospheric ozone compared to the respective simulations in the NO_2-dominant scenarios.

Summing up, the proof-of-concept simulations in a simplified model area showed that the model handles the contributions of different meteorologies and different concentrations of the reactants on the building potential of tropospheric ozone quite well. It was shown that the increased amounts of nitrogen dioxide that are produced in the course of reactions with isoprene lead to increased concentrations of ozone. The emission of isoprene had positive impacts on the ozone-forming potential in all scenarios. This is especially the case for the NO-dominant scenarios, where due to

the lack of nitrogen dioxide from traffic sources the additional NO_2 from the isoprene reactions increases the ozone concentration more drastically. The impact of different meteorologies was also plausibly reflected in the model results: With the higher ambient air temperatures as well as the surplus of radiation in the summer, the ozone formation is increased in both cases with or without isoprene. In the isoprene-including summer scenarios, however, higher leaf temperatures and a greater amount of PAR also lead to an increased emission of isoprene, resulting in even higher concentrations of tropospheric ozone.

5.3.3.2 Proof-of-concept simulations for the dispersion and chemistry model in a complex model area

In the second set of proof-of-concept simulations, the local isoprene distribution and the additional impact of isoprene onto the formation of tropospheric ozone are examined in a bigger, more complex area using realistic traffic data. Again, two scenario runs are compared: While the first scenario only accounts for the reactions of NO, NO_2 and O_3 as they had been implemented in the basic dispersion and chemistry model, excluding all isoprene-induced reactions, the second scenario also accounts for the isoprene-induced reactions as they have been implemented in the advanced dispersion and chemistry model. To facilitate interpretation and isolate the effects of the isoprene, both scenarios were run without any background concentrations of any of the compounds. The absolute values for all compound concentrations shall therefore not be interpreted. Instead, local distribution patterns and concentration differences between the scenarios are used to identify the isoprene's ozone-forming potential and examine the plausibility of these results.

To evaluate the impact of isoprene under more realistic conditions than in the previous proof-of-concept simulations, a larger, more diverse model area was created. The northeastern part of this larger model area equals the model area of the first proof-of-concept simulations. Figure 5.24 shows the model area. The horizontal

and vertical resolution was set to 2 meters, the horizontal size is 300 meters × 300 meters, vertically it reaches up until 50 meters. The location of the model area is Frankfurt am Main, Germany.

Figure 5.24: Model area for the dispersion and chemistry model proof-of-concept simulations in a more complex model area

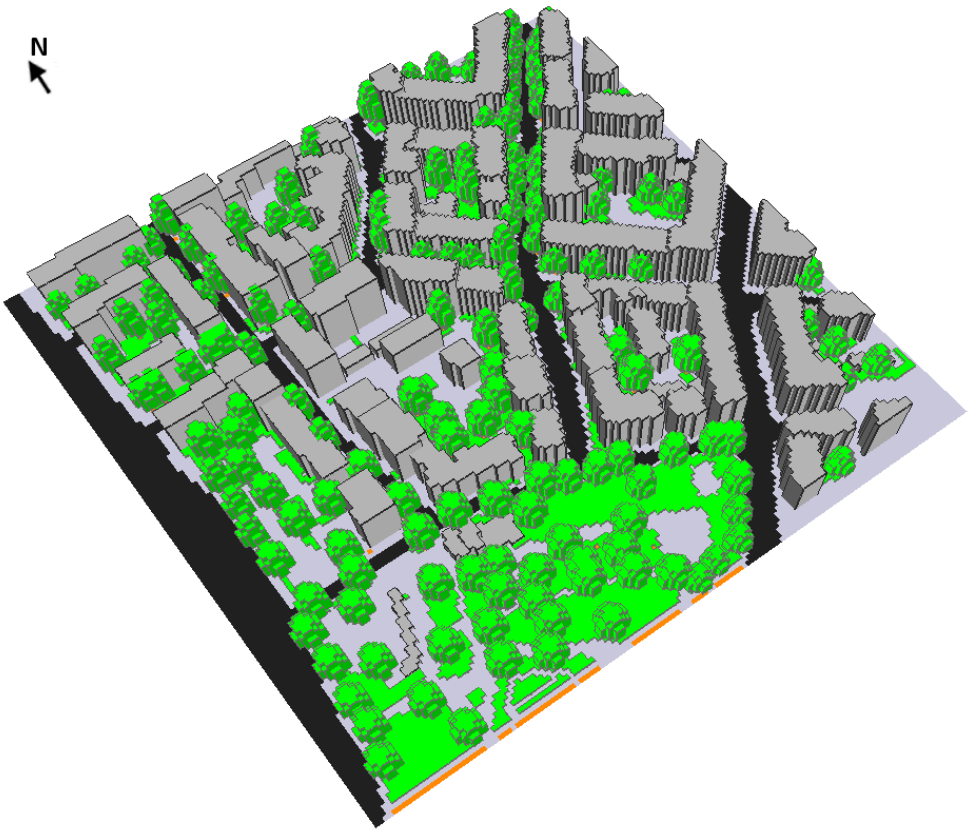

Model area dimensions: 150 × 150 × 25 grids; vertical and horizontal resolution: 2 meters; location: Frankfurt am Main, Germany

The simulation date was set to August 13th. The meteorology of the summer scenarios in the previous proof-of-concept-simulations were used: Maximum air temperatures of up to 32°C in 2 meters height and low wind speeds of around 1.3 m s^{-1} in 10 meters height were set as boundary conditions. The diurnal cycle of the air temperature and the relative humidity in 2 meters height are plotted in figure 5.20.

Figure 5.25: 2D visualization of the model area including the pollution sources

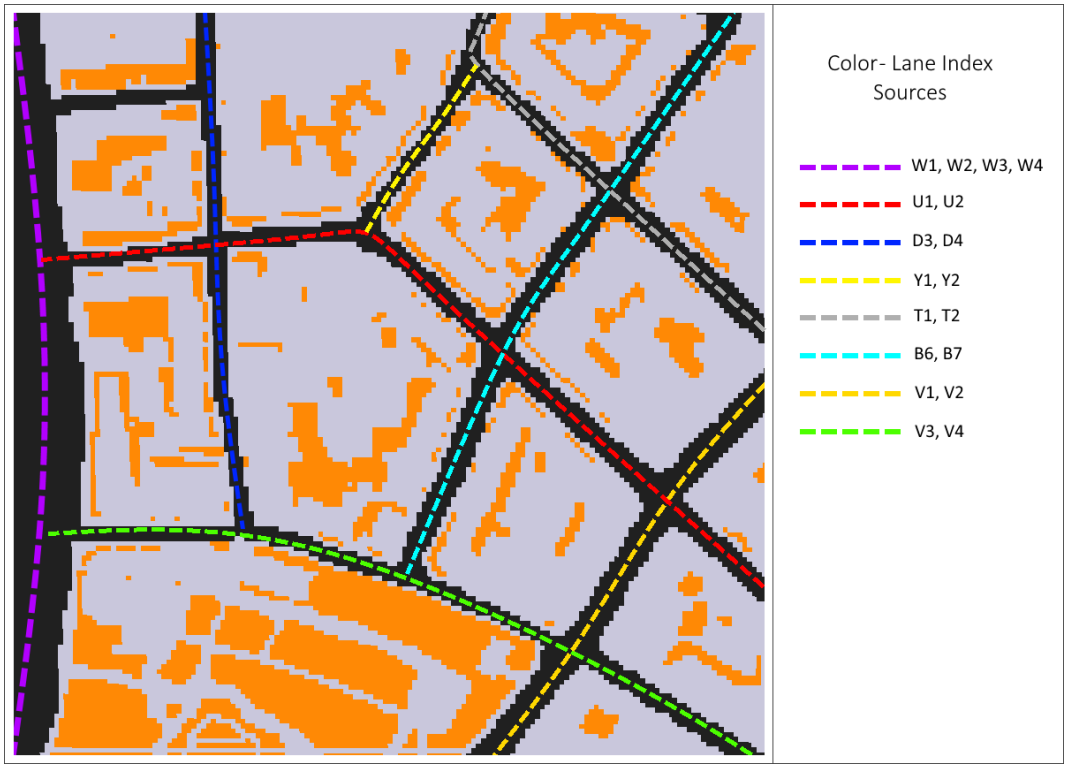

Just as in the previous simulations, nitrogen monoxide and nitrogen dioxide sources were digitized. Since the NO-dominant scenarios in the proof-of-concept simulations above showed the biggest impact of isoprene, a more NO-dominant release was chosen, resembling predominantly gasoline-engined rather than diesel-engined traffic. Other than in the previous simulations, realistic diurnal variations for the release of NO and NO_2 were created. The diurnal variations of the emission data show peaks in the early morning and late afternoon, accounting for commuting traffic. Figure 5.25 shows the arrangement of the line sources in the model area. The colored lines represent the aggregated lanes shown in the legend of the figure. Table 5.3 shows the diurnal emission cycle for NO and NO_2 for every lane in $\mu g\ s^{-1}\ m^{-1}$.

The isoprene sources are implicitly digitized by the LAD cells of the trees in the model area. Four different tree geometries were used in the model, varying in size.

Table 5.3: Diurnal cycle of NO and NO_2 emission values for the line sources

Source ID	**Time**																							
	0	1	2	3	4	5	6	7	8	9	10	11	12	13	14	15	16	17	18	19	20	21	22	23
NO B6/B7	1	1	1	3	3	10	18	20	18	19	20	19	18	18	19	21	22	20	19	15	11	7	5	4
NO_2 B6/B7	0	0	0	0	1	3	6	6	6	6	6	6	6	6	6	6	6	7	6	5	3	2	1	1
NO D3/D4	2	2	2	2	5	17	32	35	31	33	34	33	32	32	33	38	39	35	34	26	20	13	8	7
NO_2 D3/D4	1	1	1	1	1	5	10	11	10	10	11	10	10	10	10	12	12	11	10	8	6	4	2	2
NO T1/T2	0	0	0	1	1	4	7	7	7	7	7	7	7	7	7	8	8	8	8	6	4	3	2	1
NO_2 T1/T2	0	0	0	0	0	1	3	3	3	3	3	3	3	3	3	3	3	3	3	3	2	1	1	1
NO U1/U2	2	1	1	2	4	14	26	28	25	27	28	27	26	26	27	30	31	29	27	21	16	10	6	6
NO_2 U1/U2	0	0	0	0	1	3	6	7	6	7	7	7	6	6	7	8	8	7	7	6	4	3	2	1
NO V1-V4	2	2	2	3	5	19	34	37	34	35	37	36	34	34	36	40	42	38	36	28	21	14	8	7
NO_2 V1-V4	1	0	0	1	1	5	8	9	8	9	9	9	8	8	9	10	10	9	9	7	5	3	2	2
NO W1-W4	4	3	3	4	7	28	52	56	51	53	57	54	52	52	54	61	63	57	54	42	32	21	13	11
NO_2 W1-W4	1	1	1	1	2	7	13	14	13	13	14	13	13	13	13	15	15	14	13	10	8	5	3	3
NO Y1/Y2	0	0	0	1	1	4	7	7	7	7	7	7	7	7	7	8	8	8	7	6	4	3	2	1
NO_2 Y1/Y2	0	0	0	0	0	1	2	2	2	2	2	2	2	2	2	3	3	2	2	2	1	1	1	0

All values in μ g s^{-1} m^{-1}, rounded integers, sources emit in a height of 0.5 cm

The height and width of the crowns ranges from 12 meters to 17 meters in height and from 9 meters to 11 meters in width. The root volumes are linearly adjusted to the crown sizes of the trees. The same base isoprene emission capacity of 16 μg C g^{-1} h^{-1} and leaf weight of 120 g m^{-2} are shared by all trees.

It is to be expected that, just like in the abstract scenarios of the first proof-of-concept simulations, the emission of isoprene should generally lead to an increase in the concentration of tropospheric ozone. With the larger and more complex model area, the local distribution of ozone should vary as the local microclimate and the concentrations of the other compounds vary in the model area as well.

Due to the vast amount of simulation data, the following model output analysis primarily focuses on the simulation times of 11:00 and 14:00. While the ozone concentration is at peak values at 11:00 due to the combination of still high NO_2 emissions from traffic and already high radiation values, the ozone concentration

reaches a (temporary) low in both scenarios at 14:00 (see figure 5.36).

5.3.3.2.1 Model outputs excluding isoprene emissions and reactions

In the absence of VOCs, the ozone concentration reaches a more or less stable equilibrium based on the relation of NO and NO_2:

$$O_3 \approx \frac{NO_2}{NO}$$

The reactions forming this equilibrium are discussed more thoroughly in section 5.2.2.3, they are:

$$O_3 + NO \longrightarrow NO_2 + O_2$$

$$NO_2 + h\nu \longrightarrow NO + O$$

$$O + O_2 + M \longrightarrow O_3 + M$$

The concentrations of NO and NO_2 at 11:00 are shown in figures 5.26 and 5.27. Due to the much higher emissions of NO, the nitrogen monoxide concentrations show roughly three to four times higher values than the NO_2 concentrations. Additionally, the photodissociation of nitrogen dioxide increases the concentration of NO over NO_2. With the low concentrations of ozone (see figure 5.29), the destruction of nitrogen dioxide cannot be compensated by the reaction of ozone with NO. This results in a general net gain of ozone.

The reaction terms for O_3 in figure 5.28 show the net formation of ozone. The influence of the direct radiation on the photodissociation of nitrogen dioxide is clearly visible as there is only very little photodissociation in the shadows of the trees and

Figure 5.26: Chemistry without isoprene: NO concentration at 11:00h in 1.8 meters height

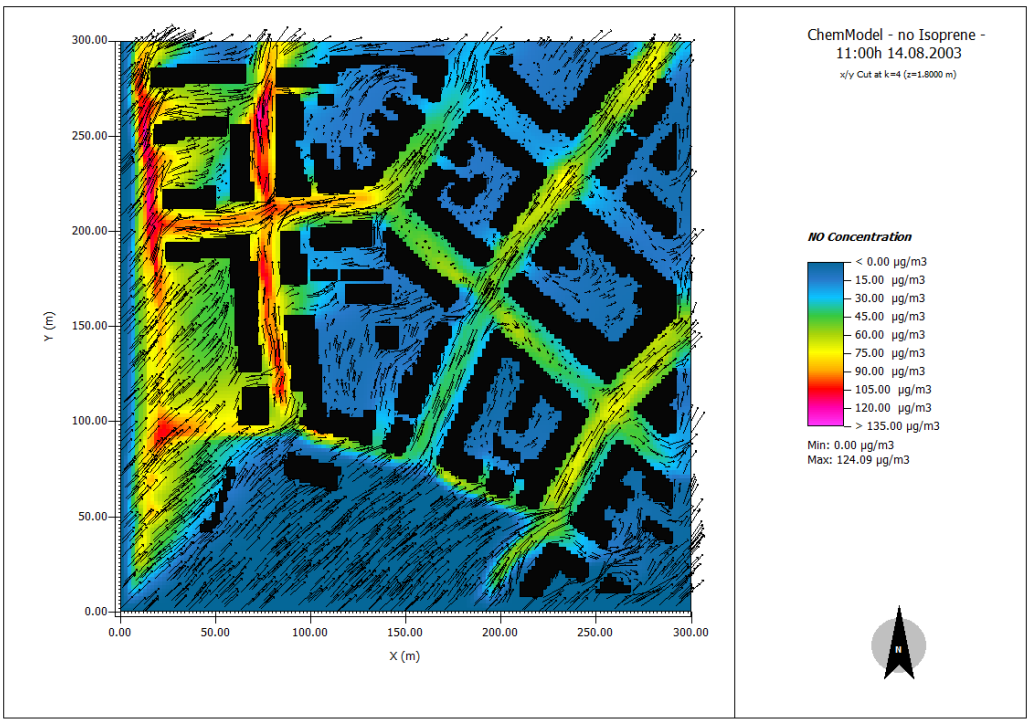

buildings. In locations that feature shade as well as a high NO concentrations, such as the junction at around X = 85m Y = 200m, a destruction of O_3 can be seen due to the reaction of O_3 with the locally highly concentrated NO. Since the reactions of NO, NO_2 and O_3 in the absence of BVOCs form an equilibrium, the ozone and nitrogen monoxide concentrations are increasing in when the NO_2 concentration is reduced. The comparison of the ozone reaction terms with the local ozone concentration in figure 5.29 shows that local peaks of the concentration are not necessarily in the same locations as the highest values of the reaction terms. The discrepancy is biggest close to the four-lane streets in the west of the model area. The discrepancies are mainly caused by locally high concentrations of nitrogen monoxide which reacts very quickly with the just formed ozone to create NO_2 and O_2. Therefore, streets with a lower

Figure 5.27: Chemistry without isoprene: NO_2 concentration at 11:00h in 1.8 meters height

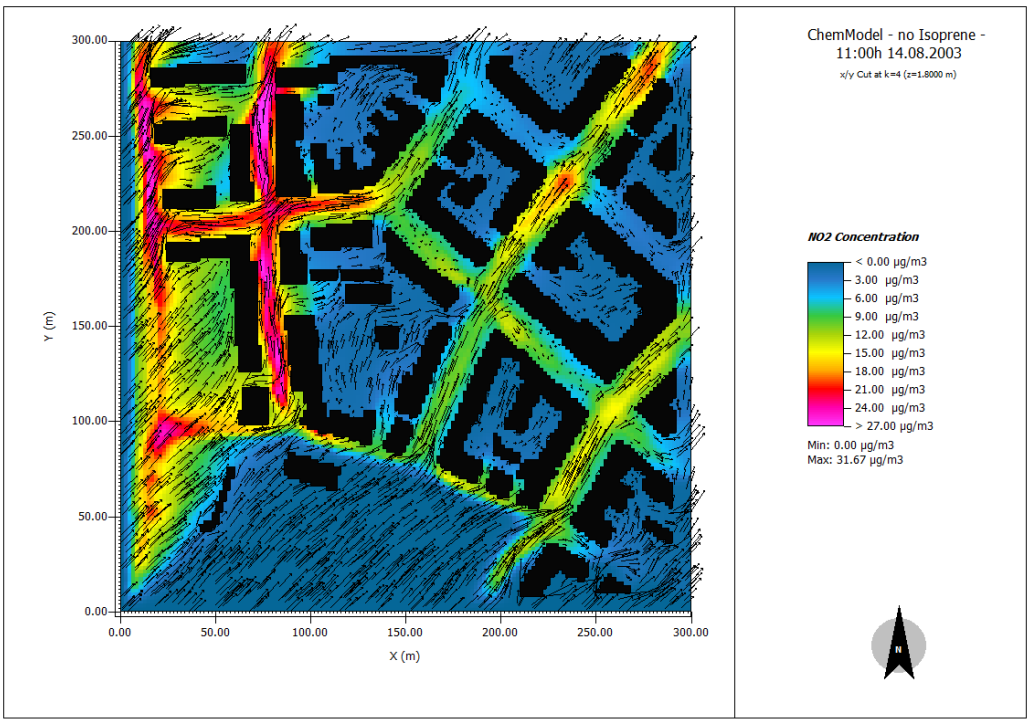

NO concentration such as the blue line sources in figure 5.25 show the highest values of O_3. In addition, the discrepancies are increased further by the dispersion of the compounds due to wind.

The same aspects apply for the ozone concentration at 14:00 simulation time (figure 5.30). However, the ozone concentration at that time is lower due to the reduced emission rates of the traffic. Figure 5.30 shows the ozone concentration in the model at 14:00 in 1.8 meters height. Even though the absolute values of the ozone concentration are lower, the local distribution pattern at 14:00 does not significantly differ from the one at 11:00.

Figure 5.28: Chemistry without isoprene: O_3 reaction terms at 11:00h in 1.8 meters height

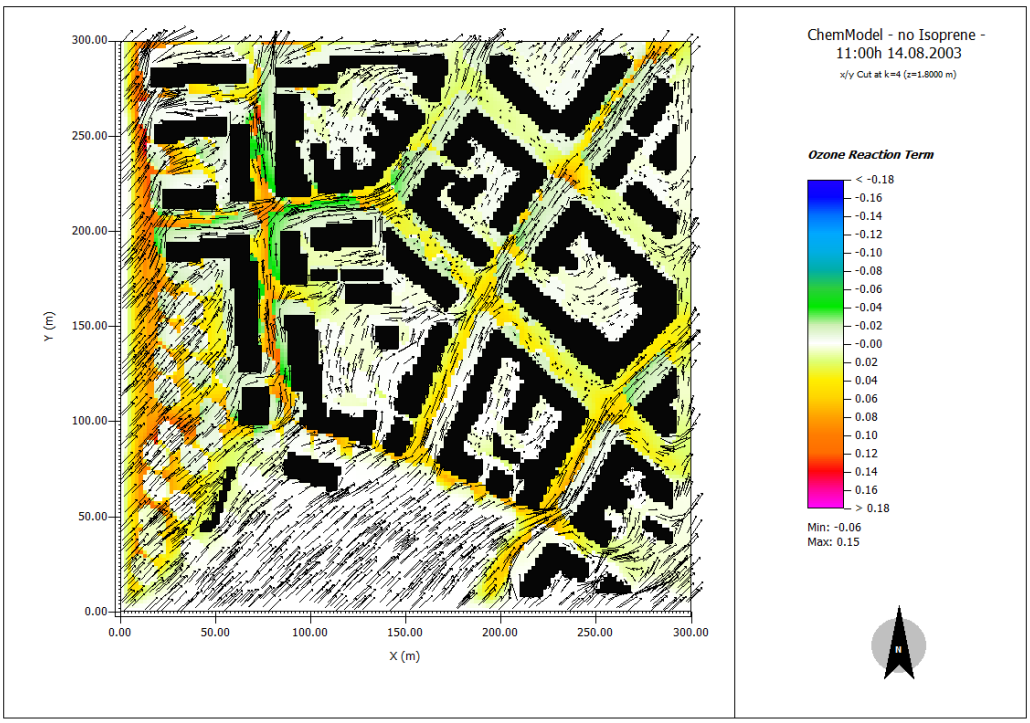

5.3.3.2.2 Model outputs including isoprene emissions

The simulation including the emission and the chemical reactions of isoprene was run using the same initial and boundary conditions as the simulation discussed before. Figure 5.31 shows the distribution of isoprene in the model area at 11:00 simulation time and in a height of 1.8 meters. The local concentration of isoprene strongly correlates with the distance to the emitting trees and the wind conditions. As expected, the concentration reaches higher values closer to the trees as well as in locations with lower wind speeds where the compound gets dispersed less. The higher concentrations can be seen in locations of lower wind speed such as the courtyard and the northeast - southwest orientated street in the center of the model. Since the figure shows the isoprene concentration in a height of 1.8 meters, the

Figure 5.29: Chemistry without isoprene: O_3 concentration at 11:00h in 1.8 meters height

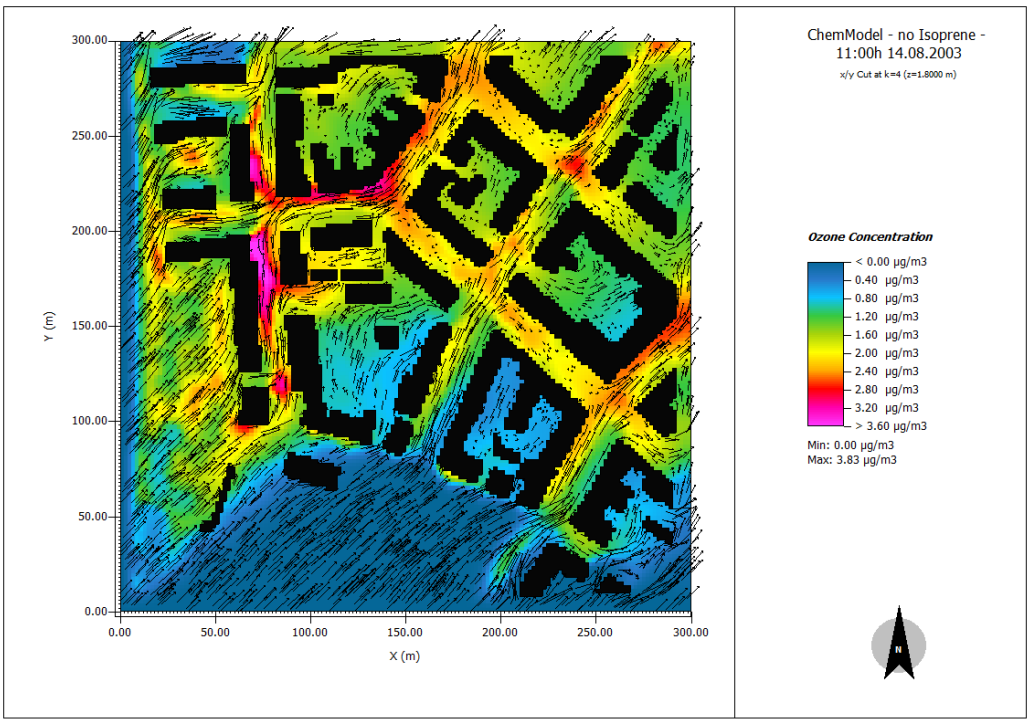

smaller trees which extend their leaves closer to the ground produce higher isoprene concentrations in that height. That way, the lower trees in the northeast corner of the model area lead to higher values in the local isoprene concentration in 1.8 meters height.

Even though the concentrations of isoprene show the highest values in the less windy courtyards, the generally higher concentration of ozone in the whole model area does show relatively low values in these locations (see figure 5.32). This has to do with the locally very low concentrations of nitrogen monoxide which is needed in the immediate processes following the destruction of isoprene (see equations 5.29 and 5.30) that lead to an increase of NO_2.

In the absence of nitrogen monoxide, the isoprene oxidation product, RO_2, will

Figure 5.30: Chemistry without isoprene: O_3 concentration at 14:00h in 1.8 meters height

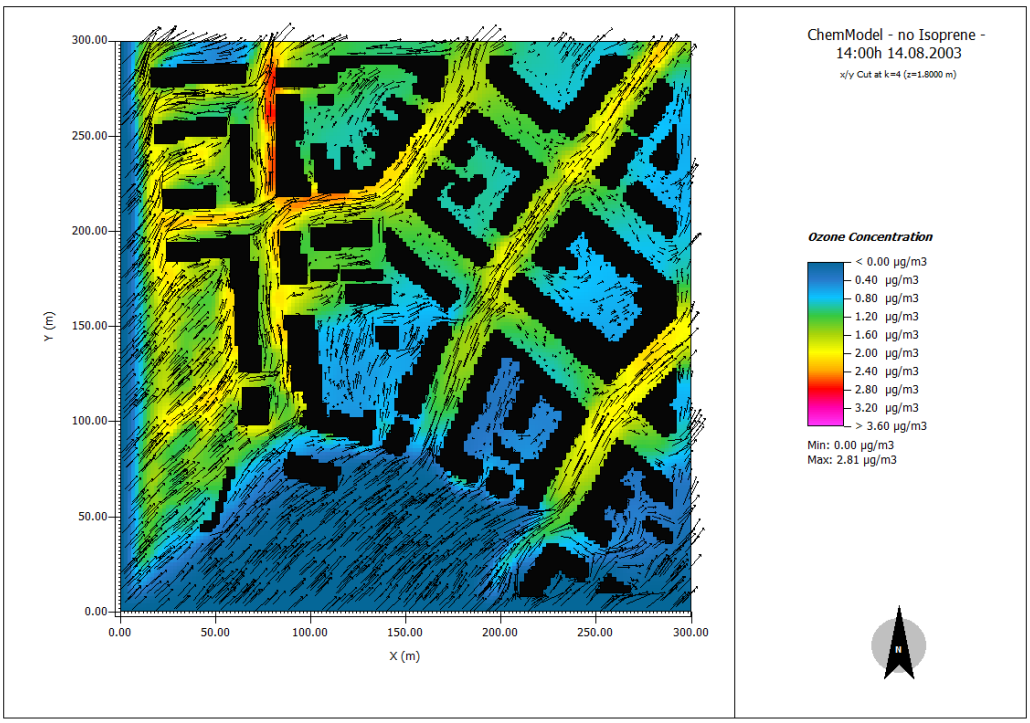

not react to nitrogen dioxide and hydroperoxyl which would fuel the production of tropospheric ozone. Because of this, the distribution of ozone in figure 5.32 shows more of less the same pattern as figure 5.29 with the highest ozone concentrations close to the emitters. Just like in the isoprene-excluding scenario above, the highest ozone concentrations are reached in the north-south orientated street at around X = 85 meters.

The reaction terms of ozone in figure 5.33 confirm the situation described above. Despite the higher isoprene levels in the courtyards, the ozone reaction terms show the highest values in the streets close to the nitrogen monoxide emitters. The effect of shade on the ozone reaction terms is again clearly visible. The north-south orientated streets, especially the one at around X = 85 meters, show the highest production

Figure 5.31: Chemistry including isoprene: C_5H_8 concentration at 11:00h in 1.8 meters height

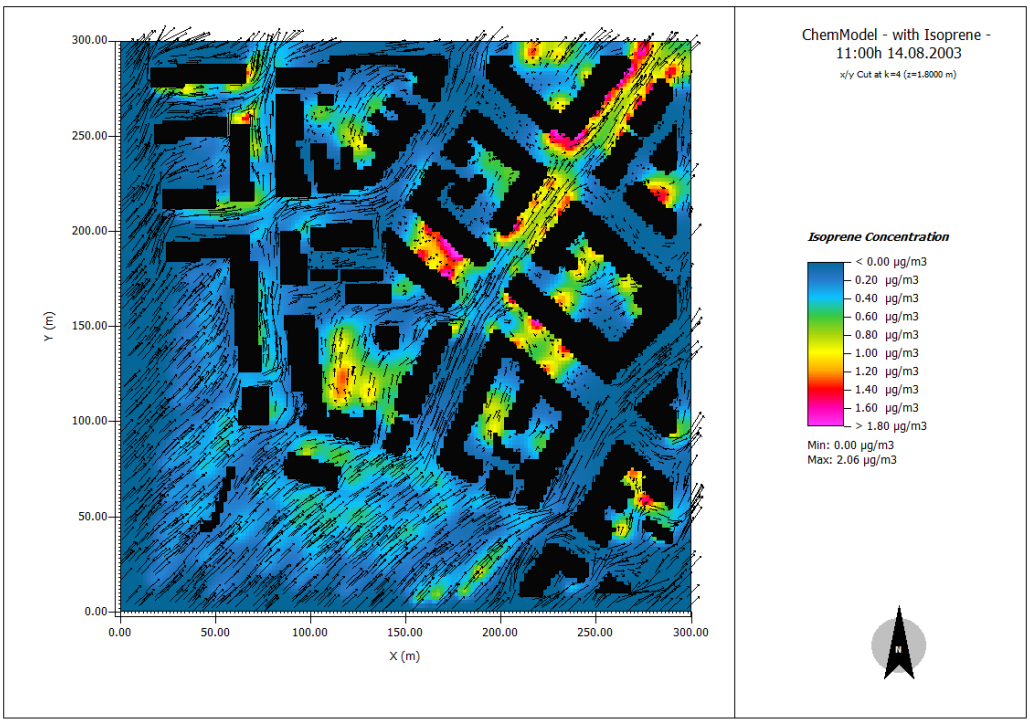

rates of O_3 due to the low amount of shading of the buildings around noon. Close to the junction at X = 85 meters and Y = 200 meters, the ozone reaction rates drop below zero, representing a net loss of ozone in these locations. The reason lies in the lack of direct radiation as well as in the locally high concentrations of NO: The buildings surrounding the junction cast a shadow which reduces the photolyzation of NO_2. The lower ozone production rate caused by the lower photolyzation rates of NO_2 cannot compensate the loss of O_3 by reacting with NO, OH and HO_2. Similar to the north-south orientated street, the most southerly located street also shows high values of the ozone reaction terms. These values tend to be overestimated by the model, since there are no adjacent buildings outside the model domain that can cast shadows onto the area.

Figure 5.32: Chemistry including isoprene: O_3 concentration at 11:00h in 1.8 meters height

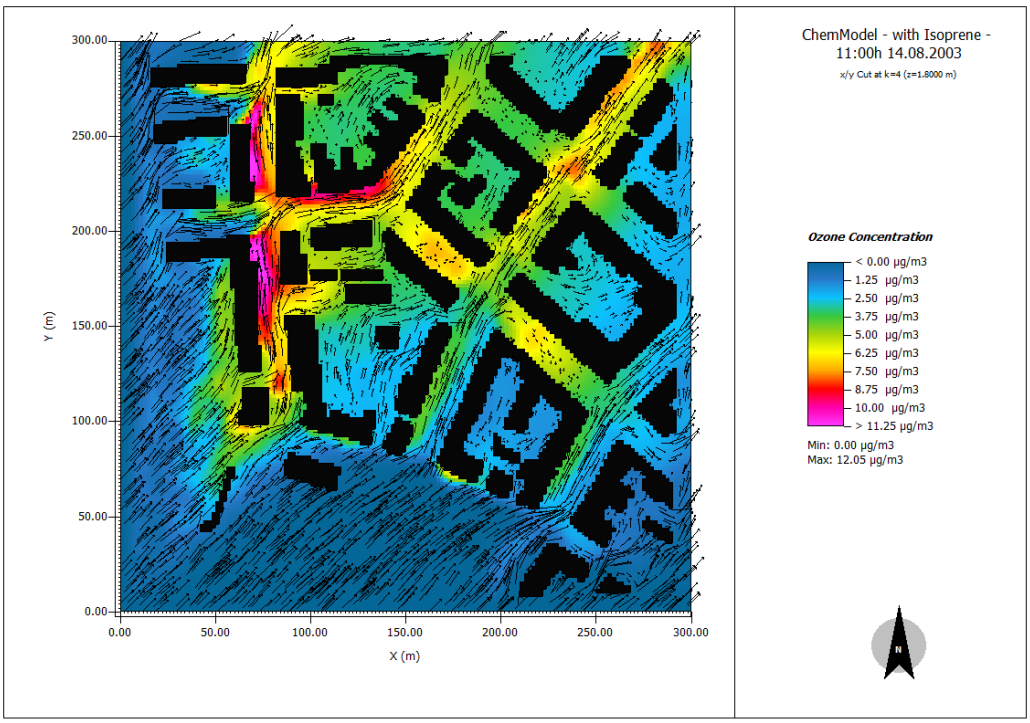

The isoprene concentrations at 14:00 simulation time (see figure 5.34) show, as the leaf temperatures come closer to the optimum of the isoprene emission rate, slightly increased values compared to the 11:00 situation. Again, the concentration of isoprene shows higher values in locations of lower wind speeds and underneath smaller trees.

As far as the concentration of ozone is concerned (see figure 5.35), however, values are significantly lower rather than higher at 14:00 than they were at 11:00. This is related to the very drastic reduction in the NO concentration due to reduced traffic. Under the lack of nitrogen monoxide, the isoprene-induced reactions of RO_2 and HO_2 with NO are hindered. Therefore, the additional amount of isoprene that is released at 14:00 cannot lead to an increase of tropospheric ozone. Additionally,

Figure 5.33: Chemistry including isoprene: O_3 reaction terms at 11:00h in 1.8 meters height

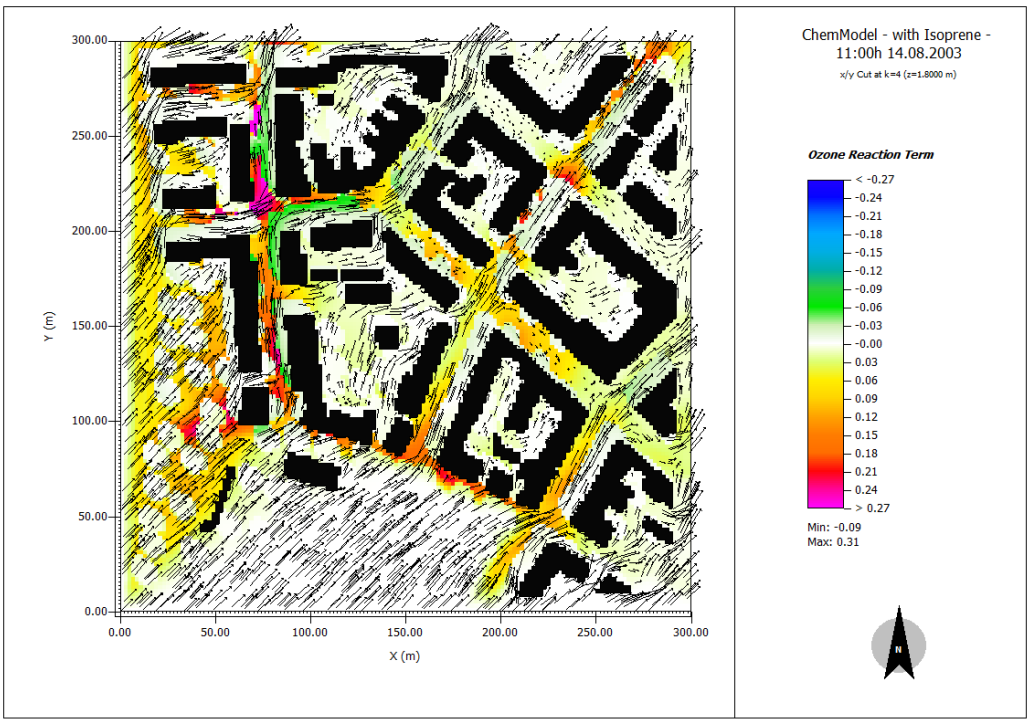

the higher rates of photolyzation and higher ambient air temperatures increase the reaction velocity of the destruction of NO_2 and O_3. In combination, these effects lead to decreased levels of nitrogen dioxide and ozone concentrations at 14:00 compared to 11:00.

5.3.3.2.3 Model output comparison

The model outputs of the simulations excluding and including isoprene showed that the additional release of isoprene leads to an increase of tropospheric ozone. In the following part, quantitative and qualitative comparisons of the chemical conditions of the two scenarios will be conducted.

The diurnal cycles of the average ozone concentration in a height of 1.8 meters

Figure 5.34: Chemistry including isoprene: C_5H_8 concentration at 14:00h in 1.8 meters height

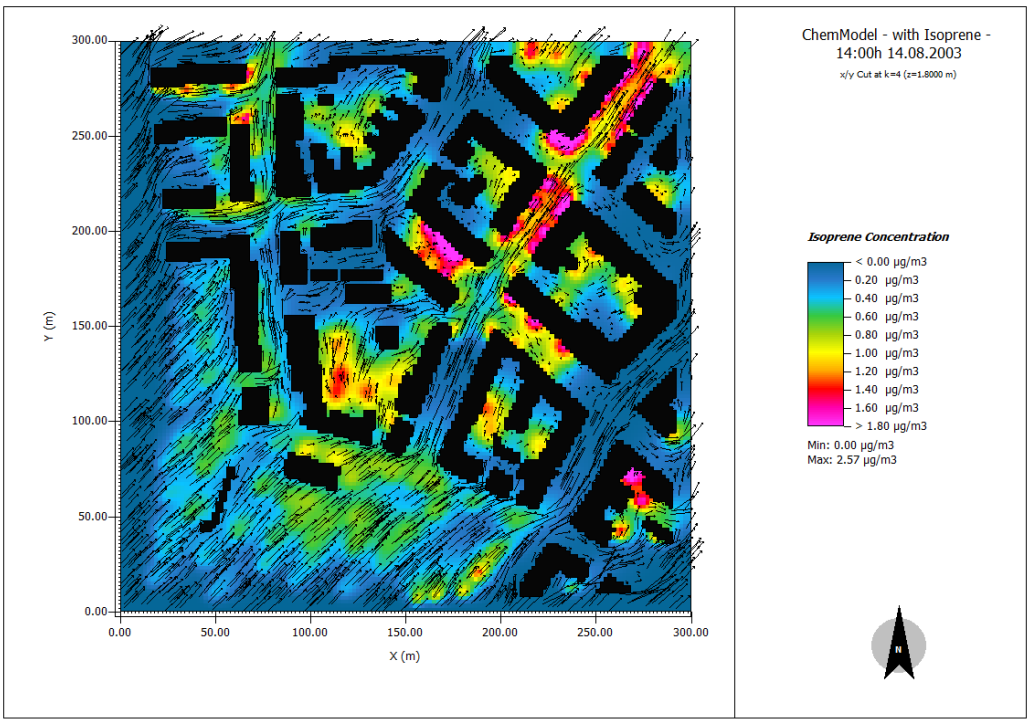

for both scenarios can be seen in figure 5.36. Initially, both curves show a similar increase of the ozone concentration. After 8:00 in the morning, however, the increase of the ozone concentration in the simulation without isoprene starts to slow down, while the ozone concentration in the isoprene-including scenario continues to rise almost unchanged. Both concentrations reach their maxima - 1.2μg m^{-3} for the isoprene-excluding scenario and around 2μg m^{-3} for the isoprene-including scenario - at 11:00. From there on, the ozone concentration in the isoprene-including scenario starts to drop until it reaches its daytime low of around 1.3μg m^{-3} at 14:00. The isoprene-excluding scenario shows a similar trend, although the amplitudes are much lower. At 15:00, the ozone concentration in the isoprene-including scenario reaches a second peak with around 1.5 μg m^{-3} before it starts to decline to 0μg m^{-3} at

Figure 5.35: Chemistry including isoprene: O_3 concentration at 14:00h in 1.8 meters height

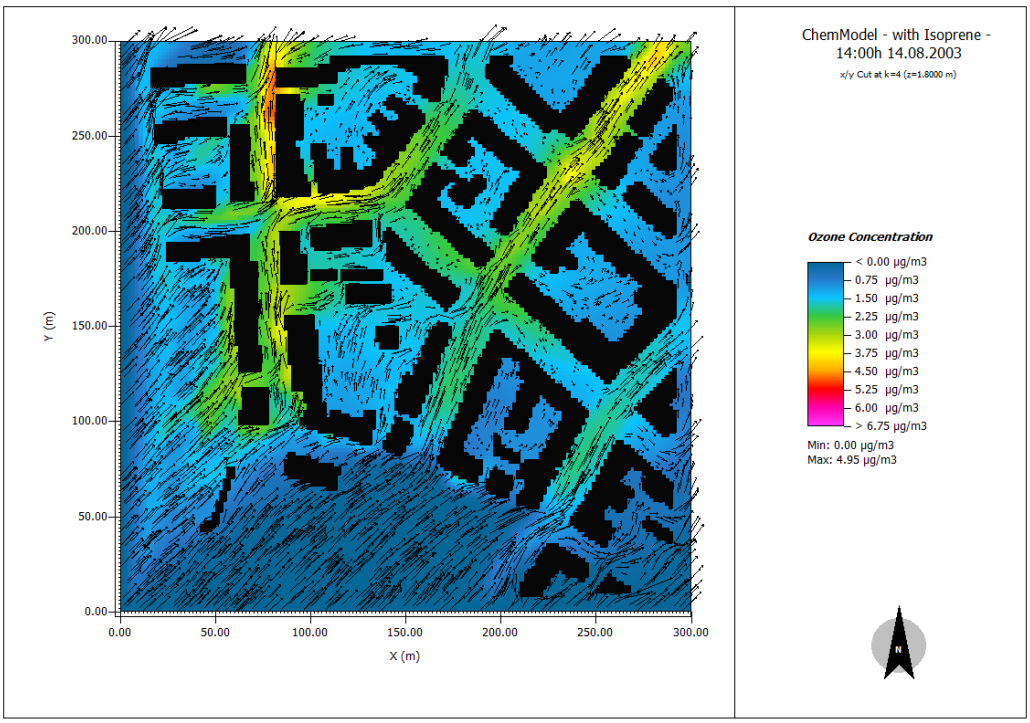

20:00 simulation time.

The expectation that the isoprene-including scenario should generally show higher ozone values than the simulation excluding isoprene can be confirmed. Furthermore, the general trend of the curves between the two scenarios matches quite nicely. In the morning, the isoprene induces a more constant rise of the ozone concentration leading to higher peak values at 11:00. With the higher peak values, the drop in the ozone concentration at midday is significantly bigger in the isoprene-including scenario.

Figures 5.37 and 5.38 show the differences in the ozone concentration between the two scenarios at 11:00 and 14:00. The comparison of the local ozone concentration levels at both times clearly shows that isoprene has a positive impact on the for-

Figure 5.36: Diurnal cycle of the ozone concentrations with and without isoprene, average concentration in a height of 1.8 meters - Proof-of-concept-simulation in a more complex model area

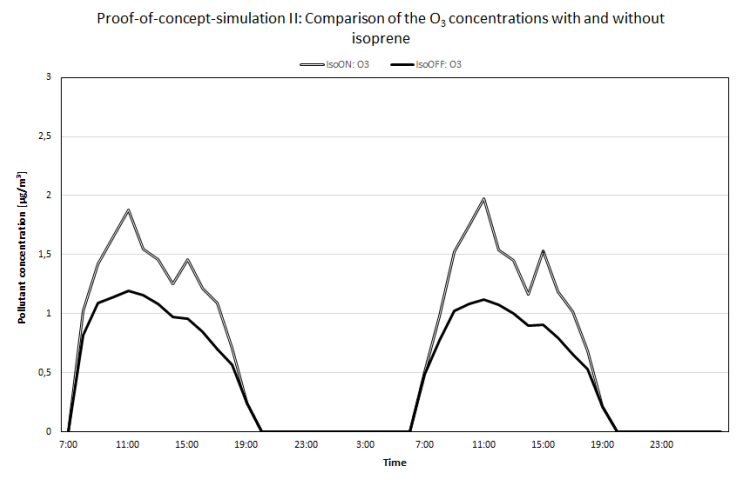

mation of ozone in almost all locations in the model area. The bigger impact of isoprene at 11:00, which was shown in figure 5.36, is clearly visible as the differences in the local ozone concentrations reach higher values at 11:00 than at 14:00.

At both times, the southern and the western parts of the model area show only slight differences in the ozone concentrations between the isoprene-including and the isoprene-excluding scenario. In the southern area, due to the absence of nitrogen monoxide sources upstream of the small park, the isoprene emissions of the trees cannot directly contribute to the formation of ozone. Only further downstream, where the isoprene products RO_2 and HO_2 of the park mix with nitrogen monoxide, the release of isoprene in the park contributes to the generally higher levels of ozone in the isoprene-including scenarios. For the four-lane street, the absence of isoprene upstream together with the newly implemented reaction of ozone with OH leads to slightly lower ozone concentrations in the isoprene-including scenario as compared to the isoprene-excluding scenario.

The general pattern of the differences shows that the positive effect of isoprene

Figure 5.37: Effect of isoprene on ozone concentration - comparison of ozone concentration with and without isoprene emission at 11:00h

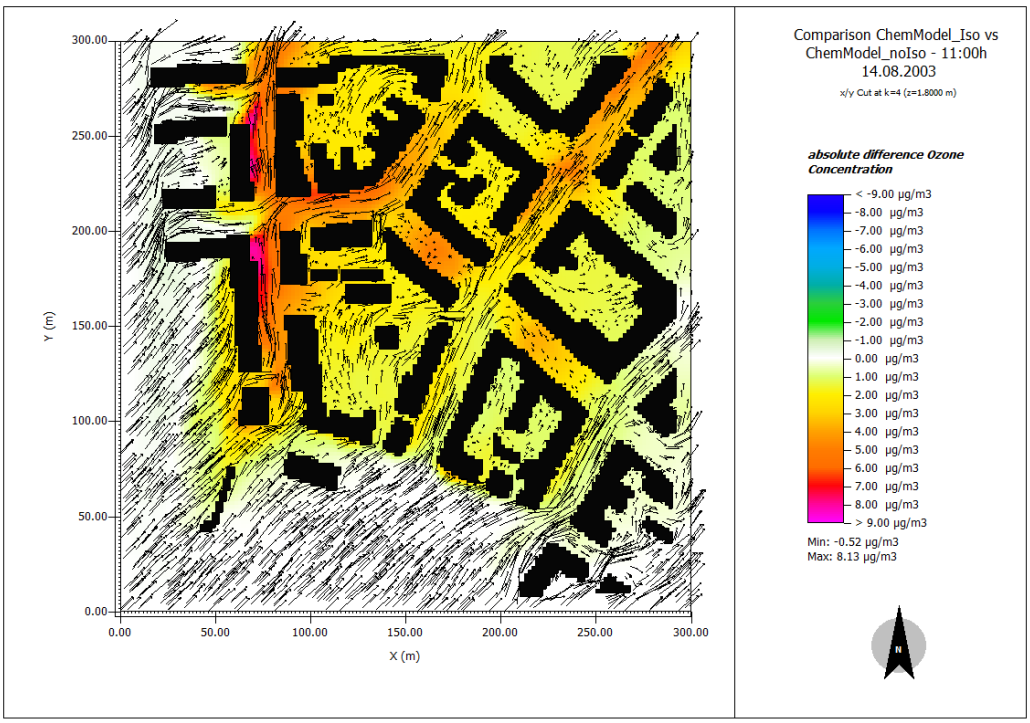

on the formation of ozone is bigger where higher concentrations of isoprene (figure 5.31) together with higher concentrations of nitrogen monoxide are found. Locations where only the isoprene emissions are increased but the nitrogen monoxide levels are low, such as in the backyards at around X = 125, Y = 125 meters, do not show particularly big increases of the ozone concentration due to the release of isoprene.

The north-south orientated street at around X = 85 meters that showed the highest absolute values of ozone in both scenarios also shows the highest values in the comparison of the ozone concentration between the two scenarios. This indicates that the positive effect of isoprene on the formation of ozone is especially big in this area (around 7μg m^{-3} at 11:00 and 2μg m^{-3} at 14:00). Even though the isoprene concentration is not particularly high in this location, the very high concentration

Figure 5.38: Effect of isoprene on ozone concentration - comparison of ozone concentration with and without isoprene emission at 14:00h

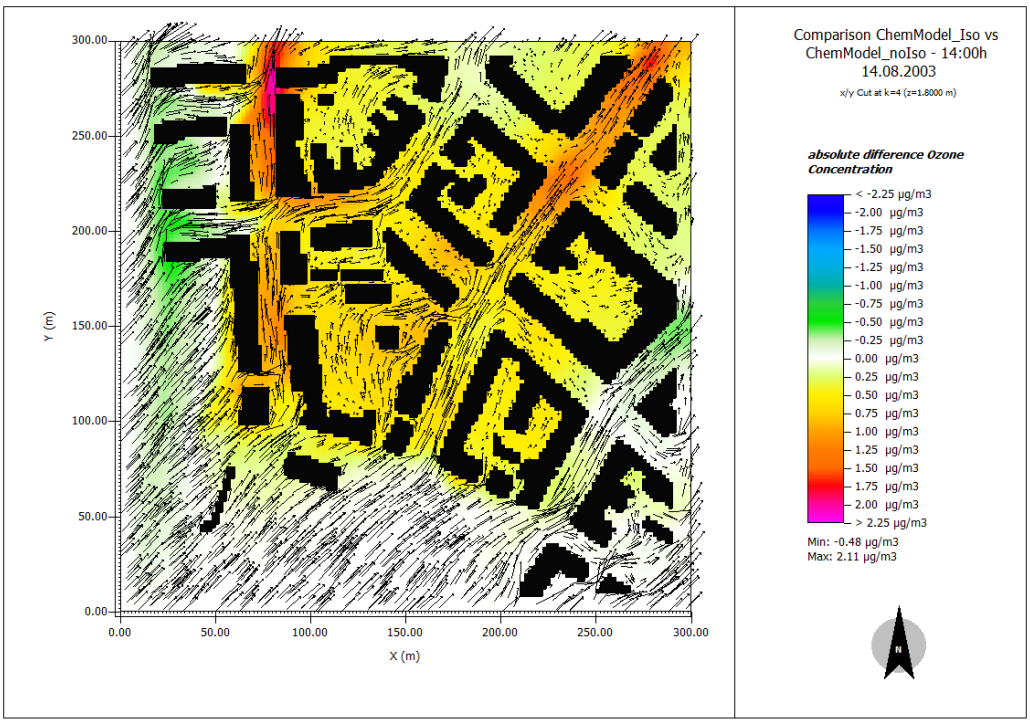

of NO caused by the line sources leads to a large increase of ozone. The local differences of the peak values between the 11:00 and the 14:00 comparisons mainly stem from the differences in the sun's elevation angle. At 11:00, the western side of the street is shaded by the adjacent buildings, resulting in reduced photolyzation rates of the additional NO_2 that is formed by the reactions of RO_2 and HO_2 with nitrogen monoxide, while at 14:00, the eastern side of the street is shaded.

Figure 5.39 confirms the analysis above. The comparison of the ozone reaction terms shows the local differences in the ozone formation and destruction between the isoprene-including and isoprene-excluding scenario. The negative values close to the four-lane street in the west and in the street around X = 275 and Y = 125 meters indicate that the newly introduced reaction of ozone with hydroxyl radicals leads

Figure 5.39: Effect of isoprene on ozone concentration - comparison of ozone terms with and without isoprene emission at 14:00h

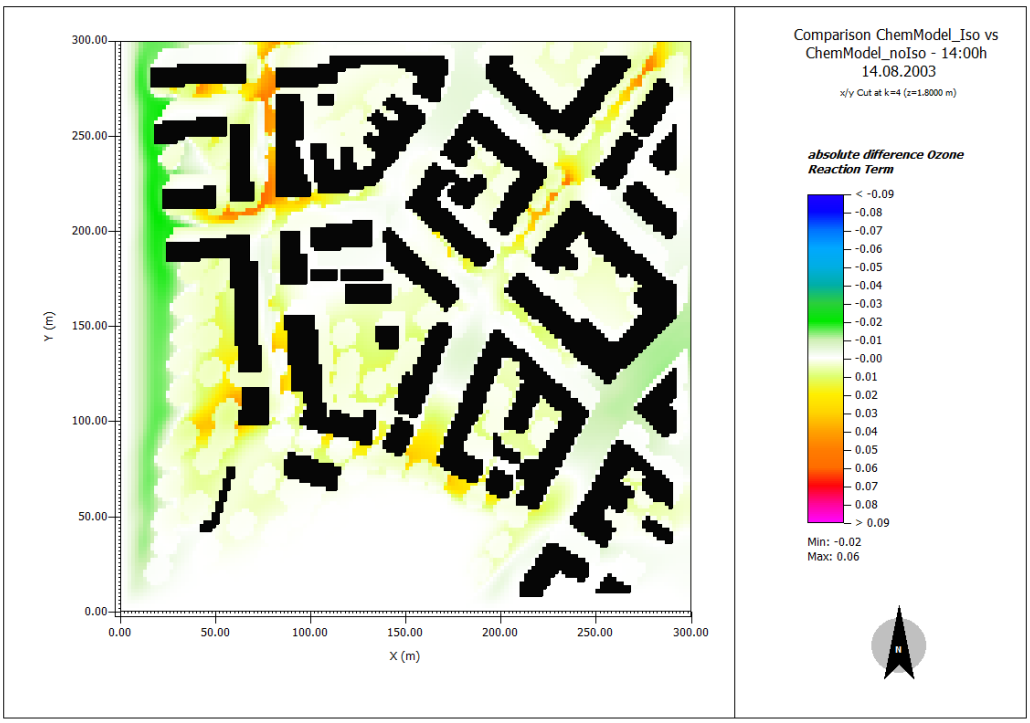

to reduced ozone-formation rates in locations where the isoprene products RO_2 and HO_2 are only sparsely available. Sunlit locations close to the isoprene-emitting trees and to nitrogen monoxide sources, however, show higher ozone reaction terms in the isoprene-including scenario compared to the isoprene-excluding scenario, leading to higher absolute concentrations of tropospheric ozone.

The comparison of the simulation results with and without isoprene showed that, just like in the first set of proof-of-concept simulations, the release of isoprene leads to overall higher concentrations of tropospheric ozone. In the larger model area, local differences in the isoprene concentration due to dispersion could be detected. All in all, the impact of isoprene onto the formation of tropospheric ozone proofed to be quite substantial. Based on the results of the first proof-of-concept simulations it

is to be expected that the impact of isoprene in a more nitrogen dioxide-dominant scenario and in a cooler (or much hotter) meteorology would have been less pronounced.

5.4 Conclusion

The aim of this study was to introduce an isoprene emission and chemistry model to approximate the impact of isoprene on the formation of tropospheric ozone in the microclimate model ENVI-met. First, a model to estimate the emissions of isoprene was developed based on the isoprene emission model of Guenther et al. (1993) and the advancements in Guenther et al. (1999) and Guenther et al. (2006). In order to implement this model into the microclimate model ENVI-met, various advancements and new properties had to be included. To validate the implementation, several proof-of-concept simulations were conducted and the resulting isoprene emission patterns were analyzed. For the local distributional patterns of actual isoprene emissions, simulation results proved to be very plausible, accurately reflecting variations in the amount of received PAR and leaf temperatures. On the aggregated level, analyses of the isoprene emissions for an entire tree further corroborated the validity of the isoprene emission model: Isoprene emission values obtained from the model match empirical values found in the literature; diurnal variations in isoprene emissions follow the patterns expected on theoretical grounds; and isoprene emissions under drought stress behave according to the expectations derived from theoretical considerations. In addition, the effects of different biological variations - dry leaf weight, base isoprene emission capacity and LAD - are correctly reproduced by the isoprene emission model, adding further weight to its adequacy.

Second, the chemical reactions of isoprene that lead to the formation of tropospheric ozone were introduced into ENVI-met's chemistry model. Since higher concentrations of isoprene do not immediately increase the ozone formation, a number of

intermediate reactions also had to be implemented. The validity of the advancements of the chemistry model was tested in several proof-of-concept simulations that compared the results of simulations based on the advanced dispersion and chemistry model - including the isoprene-induced reactions - to those of simulations based on the initial dispersion and chemistry model - including only the reactions of NO, NO_2 and O_3. A number of simulations demonstrated that the most general effect of isoprene, an increase in the concentration of ozone, is reproduced reliably by the new chemistry model. Since the amount of isoprene emissions as well as the chemical reactions depend on the local microclimate and the concentrations of other pollutants, the impact of isoprene on the formation of ozone was also examined under different meteorological and chemical conditions. To extract causal relations between the microclimate, the concentrations of the other compounds and the emission of isoprene on the formation of ozone, smaller proof-of-concept simulations with specific chemical and meteorological conditions were conducted. The comparison of the simulation results showed that the model indeed handles the contributions of different meteorologies and different chemical conditions on the building potential of tropospheric ozone well. In the last part of the study, the impact of isoprene on the formation of tropospheric ozone was examined under more realistic conditions in a bigger and more complex model area. Diurnal cycles of the release of nitrogen monoxide and nitrogen dioxide were created to account for variations in traffic. Here, too, the comparison of the isoprene-including and the isoprene-excluding scenarios yielded results conforming to the theoretical expectations, validating the model advancements.

All together, the implementation of the isoprene emission and chemistry model into ENVI-met thus proved to be a sizable advancement in the assessment of the urban microclimate. Additional validation could be achieved by comparing the model output to empirical data.

Bibliography

Atkinson, R. Atmospheric chemistry of VOCs and NOx. *Atmospheric Environment*, 34:2063–2101, 2000.

Bell, M. L., McDermott, A., Zeger, S. L., Samet, J. M., and Dominici, F. Ozone and mortality in 95 US urban communities. *Journal of the American Medical Association*, 292(19):2372–2378, 2004.

Bell, M. L., Goldberg, R., Hogrefe, C., Kinney, P. L., Knowlton, K., Lynn, B., Rosenthal, J., Rosenzweig, C, and Patz, J. A. Climate change, ambient ozone, and health in 50 US cities. *Climatic Change*, 82(1):61–76, 2007.

Benjamin, M. T. and Winer, A. M. Estimating the Ozone-Forming Potential of Urban Trees and Shrubs. *Atmospheric Environment*, 32(1):53–68, 1998.

Berkowicz, R., Ketzel, M., Lofstrom, P., and Rordam-Olesen, H. NO2 chemistry scheme in OSPM and other Danish models `http://www2.dmu.dk/AtmosphericEnvironment/Docs/NO2scheme.pdf`. 23.07.2015, 2011.

Braden, H. *Simulationsmodell für den Wasser-, Energie- und Stoffhaushalt in Pflanzenbeständen*. PhD thesis, Institut für Meteorologie und Klimatologie der Universität Hannover, 1982.

Bruse, M. ENVI-met implementation of the gas/ particle dispersion and deposition model PDDM `http://envi-met.com/documents/sources.PDF`. 13.04.2015, 2007.

Calfapietra, C., Fares, S., Manes, F., Morani, A., Sgringa, G., and Loreto, F. Role of Biogenic Volatile Organic Compounds (BVOC) emitted by urban trees on ozone concentration in cities: A review. *Environmental Pollution*, 183:71–80, 2013.

Carter, W. P. L. Development of ozone reactivity scales for volatile organic compounds. *Journal of the Air and Waste Management Association*, 44:881–899, 1994.

Cohen, A. J., Anderson, H. R., Ostro, B., Pandey, K. D., Krzyzanowski, M., Künzli, N., Gutschmidt, K., Pope, C. A., Romieu, I., Samet, J. M., and Smith, K. R. Urban Air Pollution. In Ezzati, M., Lopez, A. D., Rodgers, A., and Murray, C. J. L., editors, *Global and Regional Burden of Diseases Attributable to Selected Major Risk Factors*, chapter 17, pages 1354–1434. World Health Organisation, 2004.

Fischer, H., Bozem, H., and Lelieveld, J. Die photochemische Produktion von Ozon in der Troposphäre. *Forschungsbericht 2011 - Max-Planck-Institut für Chemie*, 1: 1–6, 2011.

Gryparis, A., Forsberg, B., Katsouyanni, K., Analitis, A., Touloumi, G., Schwartz, J., Samoli, E., Medina, S., Anderson, H. R., Niciu, E. M., Wichmann, H. E., Kriz, B., Kosnik, M., Skorkovsky, J., Vonk, J. M., and Dortbudak, Z. Acute effects of ozone on mortality from the air pollution and health: a European approach project. *American Journal of Respiratory and Critical Care Medicine*, 170(10): 1080–1087, 2004.

Guenther, A., Baugh, B., Brasseur, G., Greenberg, J., Harley, P., Klinger, L., Serca, D., and Vierling, L. Isoprene emission estimates and uncertainties for the central African EXPRESSO study domain. *Journal of Geophysical Research*, 104(23): 30625–30639, 1999.

Guenther, A., Karl, T., Harley, P., Wiedinmeyer, C., Palmer, P. I., and Geron, C. Estimates of global terrestrial isoprene emissions using MEGAN (Model of Emission of Gases and Aerosols from Nature). *Atmospheric Chemistry and Physics*, 6: 3181–3210, 2006.

Guenther, A. B., Zimmermann, P. R., and Harley, P. C. Isoprene and Monoterpene Emission Rate Variability: Model Evaluations and Sensitivity Analyses. *Journal of Geophysical Research*, 98(7):12609–12617, 1993.

Guenther, A. B., Hewitt, N. C., Erickson, D., Fall, R., Geron, C., Graedel, T., Harley, P., Klinger, L., Lerdau, M., McKay, W. A., Pierce, T., Scholes, B., Steinbrecher, R., Tallamraju, R., Taylor, J., and Zimmermann, P. A global model of natural volatile organic compound emissions. *Journal of Geophysical Research*, 100(5): 8873–8892, 1995.

Ito, K., De Leon, S. F., and Lippmann, M. Associations between Ozone and Daily Mortality: Analysis and Meta-Analysis. *Epidemiology*, 16(4):446–457, 2005.

IUPAC. IUPAC Task Group on Atmospheric Chemical Kinetic Data Evaluation `http://iupac.pole-ether.fr`. 10.08.2015, 2015.

Leng, C., Kish, J. D., Kelley, J., Mach, M., Hiltner, J., Zhang, Y., and Liu, Y. Temperature-Dependent Henry's Law Constants of Atmospheric Organics of Biogenic Origin. *The Journal of Physical Chemistry*, 117:10359–10367, 2013.

Mudway, I. S. and Kelly, F. J. Ozone and the lung: a sensitive issue. *Molecular Aspects of Medicine*, 21(1-2):1–48, 2000.

Paulot, F., Crounse, J. D., Kjaergaard, H. G., Kroll, J. H., Seinfeld, J. H., and Wennberg, P. O. Isoprene photooxidation: new insights into the production of acids and organic nitrates. *Atmospheric Chemistry and Physics*, 9:1479–1501, 2009.

Sander, S. P., Friedl, R. R., Abbatt, J. P. D., Barker, J. R., Burkholder, J. B., Golden, D. M., Kolb, C. E., Kurylo, M. J., Moortgar, G. K., Wine, P. H., Huie, R. E., and Orkin, V. L. *Chemical Kinetics and Photochemical Data for Use in Atmospheric Studies, Evaluation No. 17.* JPL Publication 10-6, 2011.

Saunders, S. M., Jenkin, M. E., Derwent, R. G., and Pilling, M. J. Protocol for the development of the master chemical mechanism, mcm v3 (part a): tropospheric degradation of non-aromatic volatile organic compounds. *Atmospheric Chemistry and Physics*, 3:161–180, 2003.

Sehmel, G. A. Particle and Gas Deposition. A review. *Atmospheric Environment*, 14(9):983–1011, 1980.

Seinfeld, J. H. and Pandis, S. N. *Atmospheric Chemistry and Physics*. John Wiley & Sons, Inc., 1998.

Sharkey, T., Singsaas, E. L., Lerdau, M. T., and Geron, C. D. Weather effects on isoprene emission capacity and applications in emission algorithms. *Ecological Society of America*, 9(4):1132–1137, 1999.

Sharkey, T. D., Wiberly, A. E., and Donohue, A. R. Isoprene emission from plants: why and how. *Annals of Botany*, 101:5–18, 2008.

Wong, M. S., Sarker, L. R., Nichol, J., Lee, S.-C., Chen, H., Wan, Y., and Chan, P.W. Modeling bvoc isoprene emissions on a gis and remote sensing database. *International Journal of Applied Earth Observation and Geoinformation*, 21:66–77, 2013.

6 Evaluation of ENVI-met's multiple-node model and estimation of indoor climate

Helge Simon[1], *Lukas Kissel*[1], *Michael Bruse*[1]

[1] Department of Geography, Johannes Gutenberg University Mainz, 55099 Mainz, Germany

6.1 Introduction

Urban areas as well as their local microclimates are predominantly characterized by their buildings' structures. Buildings shape the microclimate in various ways: They modify the wind flow, cast shade and alter the radiation and energy budget due to processes like heat storage, reflection or reduction of sky view (Arnfield, 1990; Blocken and Carmeliet, 2004; Chudnovsky et al., 2004). But not only the microclimate is influenced by buildings, the indoor climate and the need to regulate the same (heating and cooling demands) strongly depend on the outside microclimate (Kolokotroni et al., 2006; van Hooff et al., 2016). The important role of buildings has been studied for decades (Oke, 1988a,b); in the face of climate change and energy saving, however, the need for detailed analyses of the interactions of the physical properties of the building materials, building geometry and outdoor and indoor climate requires accurate modeling techniques that capture the energy exchange between facades, the interiors and the atmosphere.

This section will present an advancement of ENVI-met's wall and roof model that allows detailed analyses of building physics. With the new implementation, walls and roofs can now consist out of up to three layers which can vary in width and materials. Every material can have its own physical properties such as absorption, transmission, emissivity, thermal conductivity or density. This allows a much more accurate simulation of the facade outdoor and indoor interactions. In combination with another advancement, the implementation of building zones that allow the definition of confined air volumes inside buildings, ENVI-met is now also able to estimate the indoor air temperatures for separated indoor air volumes.

To evaluate the new implementations, a proof-of-concept simulation is first conducted that examines the evolution of the indoor air temperatures in different buildings and building zones. Subsequently, modeled surface temperatures are compared against measurement data from the Fraunhofer Institute for Building Physics

Holzkirchen under different meteorological and indoor climate conditions.

6.2 The multiple-node wall and roof model

Based on the work of Terjung and O'Rourke, ENVI-met uses a multiple transient state model to calculate the surface temperatures of walls and roofs (Huttner, 2012; Terjung and O'Rourke, 1980).

In the implementation of Huttner (2012), a wall (or roof) was treated as a uniform structure built out of one homogenous material that featured physical properties such as heat capacity, thermal conductivity, absorption or emissivity. To calculate the outside surface temperature, the inside material temperature and to approximate the indoor air temperature, the wall layer featured three calculation nodes, one on the inside and outside surface and one in its center. Compared to the previously used steady-state approach the advanced wall and roof model using the three-node model yielded much better results in the approximation of surface temperatures (Huttner, 2012). However, due to the restriction to only three nodes and thus one wall material, more complex structures where a wall consists out of layers of different materials could not be replicated without parametrizations of the individual material properties.

To solve this issue, the three-node model was extended to a dynamic multiple-node model. Where the former wall and roof model only allowed to build structures out of one material, the multiple-node model now allows the construction of much more complex structures consisting of layers of different materials (Bruse and Simon, 2015).

In its current state, the model features seven nodes, which allows the construction of up to three different layers which can vary in width and materials used. Every material can have its own physical properties (absorption, transmission, reflection,

emissivity, specific heat capacity, thermal conductivity and density). The nodes are placed in the center and at the horizontal borders of each material; a wall with three materials thus consists of seven nodes. Figure 6.1 shows a schematic of the new wall and roof model. The red dots symbolize the different nodes, located at the center and the lateral borders of each material (Bruse and Simon, 2015).

Figure 6.1: Schematics of the new wall and roof model

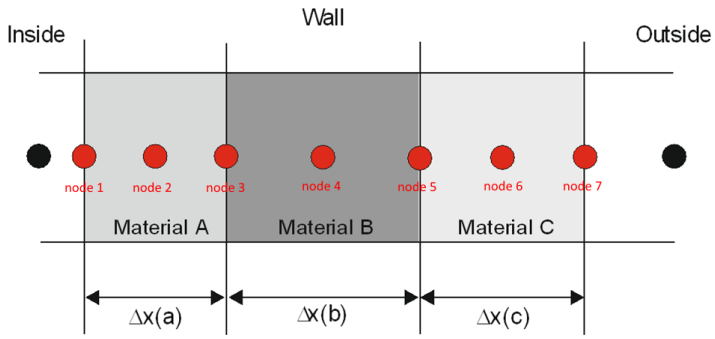

Modified from: Bruse and Simon (2015)

The database has been updated accordingly. The materials section allows to create new materials or edit material parameters including absorption, transmission, reflection, emissivity, specific heat capacity, thermal conductivity and density. The wall section allows to manually create or edit walls that now consist out of three different materials. The thickness and type of materials can be adjusted freely (see figure 6.2).

The outside surface temperature (node 1) is calculated by the facade's energy budget. It is iteratively adjusted until the balance of the energy budget equals zero.

$$EB = Q^{abs}_{sw,net} + \epsilon \cdot (Q_{lw} - \sigma T_1^4) - H_w - LE_w - G_w \cong 0$$

with $Q^{abs}_{sw,net}$ as the net shortwave radiation absorbed by the facade surface, ϵ as the emissivity of the facade, σ as the Stefan-Boltzmann Constant, $\epsilon \cdot Q_{lw} - \epsilon\sigma T_1^4$ as

Figure 6.2: New dialog to create or alter the composition of walls / roofs

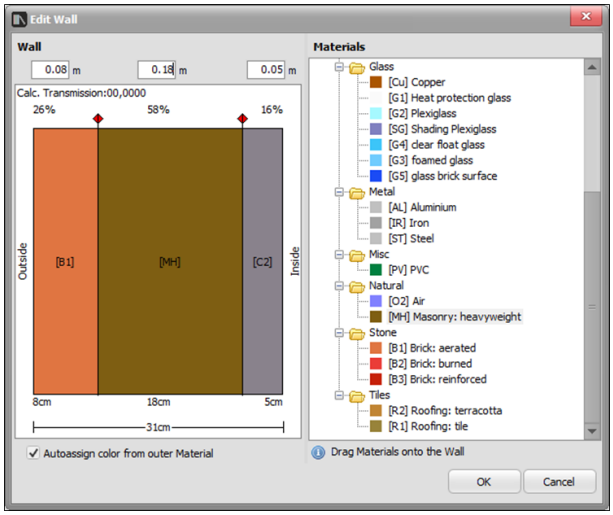

the longwave radiation balance depending on the surface temperature of the outside node T_1 and the incoming longwave radiation Q_{lw}, H_w as the sensible heat flux into the atmosphere, LE_w as the latent heat flux into the atmosphere due to evaporation or condensation of water at the outside facade surface and G_w as the conduction heat flux from or to the adjacent node inside the wall / roof (Bruse and Simon, 2015).

The surface temperature on the inside of the building (node 7 in figure 6.1) is calculated by the energy balance of the inside node:

$$EB = G_w - H_w \cong 0$$

$$G_w = \frac{\lambda(C)}{0.5\Delta(C)}(T_6 - T_7)$$

$$H_w = h_{c,w}(T_7 - T_i) \tag{6.1}$$

with G_w as the conduction heat flux between node 6 and the inner wall surface node 7, H_w as the sensible heat transfer between the inner wall surface and the indoor air, λ as the heat conductivity of the material C, Δ as the distance between the calculation nodes, $h_{c,w}$ is taken constant for the inner wall with 7.7 [W m^{-2} K^{-1}] (according to DIN 6946) and T_i as the indoor temperature (Bruse and Simon, 2015).

As the equation above shows, this simplified method does not account for reflection of shortwave radiation inside the building and radiative transfers between inner walls. The inside volumes of the buildings are, to reduce the complexity of the model, treated as an empty volume filled with air. With these simplifications, the net absorbed shortwave radiation at the inside node can be ignored and due to the isothermal indoor environment the longwave radiation budget can be assumed as equal to zero (Bruse and Simon, 2015). This simplified method allows a rough estimation of the indoor air temperature as a prognostic variable (see equation 6.1).

The calculation of the temperatures of the inner nodes (2 to 6) are carried out by using the one-dimensional Fourier Equation:

$$\frac{\partial T_i}{\partial t} = \kappa_i \frac{\partial^2 T}{\partial \Delta^2} \tag{6.2}$$

with κ_i as the thermal diffusivity [m^2 s^{-1}] at node i and Δ as the distance between the nodes. The Fourier Equation is then discretized (see equation 6.3) for the finite difference scheme and implicitly solved in the model.

$$\frac{T_i^* - T_i}{\Delta t} = \frac{1}{\Delta_{ic}} \left[\kappa_{i-} \left(\frac{T_{i-1}^* - T_i^*}{\Delta_{i-}} \right) - \kappa_{i+} \left(\frac{T_i^* - T_{i+1}^*}{\Delta_{i+}} \right) \right] \tag{6.3}$$

with T_i^* as the temperature of the node i in the future time step $t^* = t + \Delta t$, T_i as the temperature of the node i for the current time t, κ_i as the thermal diffusivity [m^2 s^{-1}] at node i and Δ_{ic}, Δ_{i-}, Δ_{i+} as the center, left and right differences between the nodes (Bruse and Simon, 2015).

For the calculation of the indoor air temperature, the indoor air volume must be known. Therefore, the model will automatically divide buildings into separate air volumes. Alternatively, the user can manually define horizontally and vertically separated building zones within a building that represent confined spaces inside the building (e.g., rooms / flats). The model then uses the respective inside air volumes in these zones to calculate the indoor air temperatures (see figure 6.3). The energy fluxes into the zones are sensible heat transfer from the indoor wall and the transmission of direct radiation through transparent wall elements such as windows. The incoming and outgoing fluxes are balanced according to the indoor air volume enclosed in the building zones. The lack or gain of energy through the walls or roofs results in a change of the indoor temperature (Bruse and Simon, 2015). Since heat transfer between adjacent building zones and heat storage of indoor walls are neglected as of yet the calculation of the indoor temperature must still be regarded as only a rough estimation.

Figure 6.3: Visualization of different building zones. The different shades of red indicate confined spaces inside the buildings

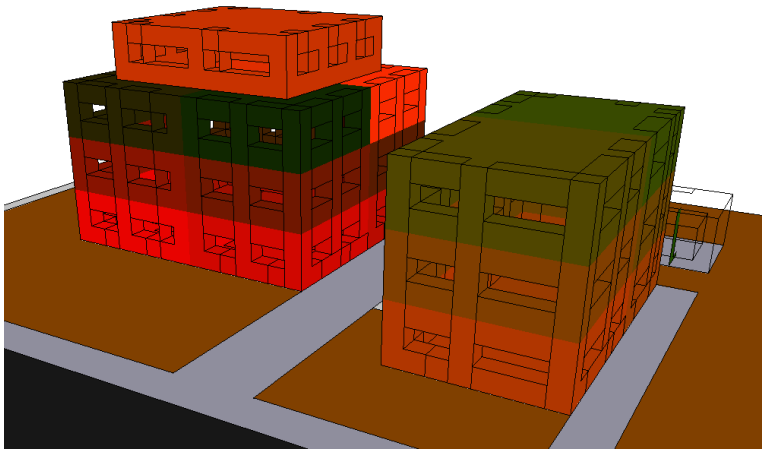

6.3 Proof-of-concept simulation for the multiple-node model

To test the capabilities of the new implementations regarding the simulation of facade surface temperatures and the estimation of indoor air temperatures, a small proof-of-concept study was conducted. In a fictional scenario, two larger residential houses built out of lightweight and heavyweight concrete and a greenhouse were modeled in a suburban environment.

6.3.1 Model area and boundary conditions

The location of the model area was set to Mainz, Germany. The model area can be seen in figure 6.4. Its dimensions are 50 meters × 50 meters × 30 meters in a resolution of 1 meter.

Figure 6.4: Model area for the proof-of-concept simulation

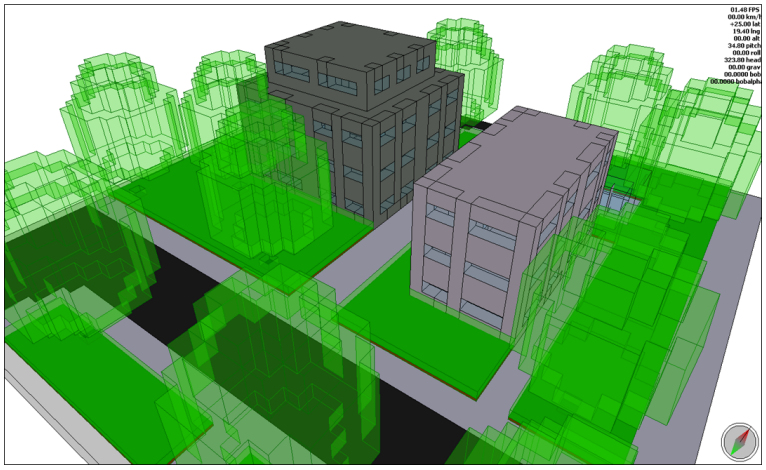

The walls and the roof of the left hand side building consist of dense concrete, whereas the right hand side building is built out of lightweight hollow concrete. In the back, a greenhouse was modeled. The insides of the buildings are separated into building zones creating individual air volumes for the calculation of the indoor air temperatures

The building in the foreground was constructed out of lightweight hollow concrete, the building material for the walls and roof of the building in the background is dense concrete. In the backyard of the buildings, a small glasshouse was digitized. The different physical parameters of the building materials are displayed in table 6.1. Both residential buildings are subdivided into building zones that define confined air volumes inside the buildings, indicated by the different shades of red in figure 6.3.

Table 6.1: Physical properties of the building materials of the three houses

Physical property	**Material**		
	lightweight concrete	dense concrete	glass
Thickness [m]	0.3	0.3	0.03
Absorption	0.7	0.7	0.05
Transmission	0	0	0.9
Reflection	0.3	0.3	0.05
Emissivity	0.9	0.9	0.9
Specific Heat Capacity [$\mathbf{J\ kg^{-1}\ K^{-1}}$]	840	840	750
Thermal Conductivity [$\mathbf{W\ m^{-1}\ K^{-1}}$]	0.2	1.9	1.05
Density [$\mathbf{kg\ m^{-3}}$]	620	2500	2500

Since heat conduction through walls / roofs is a rather slow process, the simulation duration was set to 10 days. A simple forcing was used meaning that the diurnal cycles of air temperature and humidity were the same for all 10 days. The diurnal cycle can be seen in figure 6.5. The simulation started on August 12th.

Based on the properties of the buildings materials, the glasshouse should show the lowest surface temperatures due to the high transmission. While the lightweight and dense concrete buildings have identical properties with regard to absorption, transmission, reflection and specific heat capacity, the lower density and thermal conductivity of the lightweight concrete building should lead to higher surface temperatures compared to the dense concrete building. With regard to the indoor air

temperature, the glasshouse's high transmission should result in the highest indoor temperature of all three buildings. As far as the lightweight and dense concrete buildings are concerned, the indoor temperature of the lightweight concrete building should increase, but also decrease more quickly than for the dense concrete building because its lower density results in lower heat storage.

Figure 6.5: Diurnal cycle of the boundary conditions: air temperature and humidity

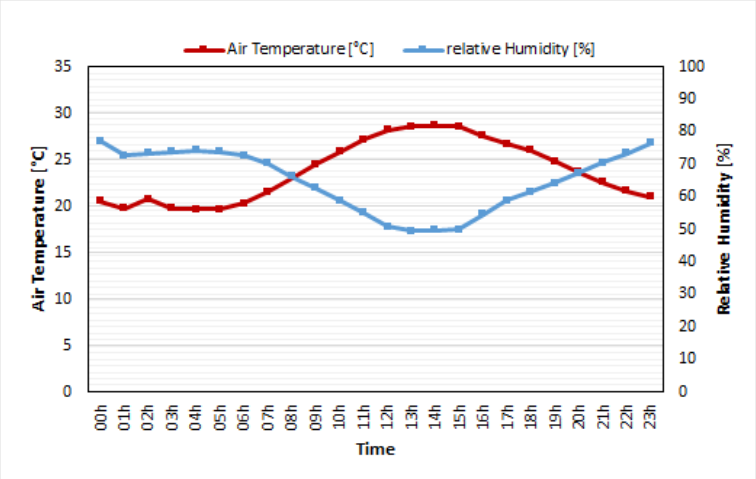

6.3.2 Model results

Figure 6.6 confirms the expectations formulated above with regard to the differences in the surface temperatures of the three buildings: While the glasshouse only reaches a surface temperature of around 25°C at 10:00, the lightweight concrete building exhibits surface temperatures of up to 55°C. The dense concrete building lies in the middle of these two with surface temperatures of up to around 35°C. In addition, the figure shows that with ENVI-met's high resolution, the influences of shadow-casting objects like trees on the outside surface temperature of the buildings can be realistically modeled. The shade cast by the tree in front of the right hand side building leads to lower outside surface temperatures for the shaded part of the facade.

The windows with their lower temperatures caused by the higher transmission are also clearly visible, corroborating the accuracy of ENVI-met's wall and roof model.

Figure 6.6: Outside facade temperatures at 10:00, fourth simulation day

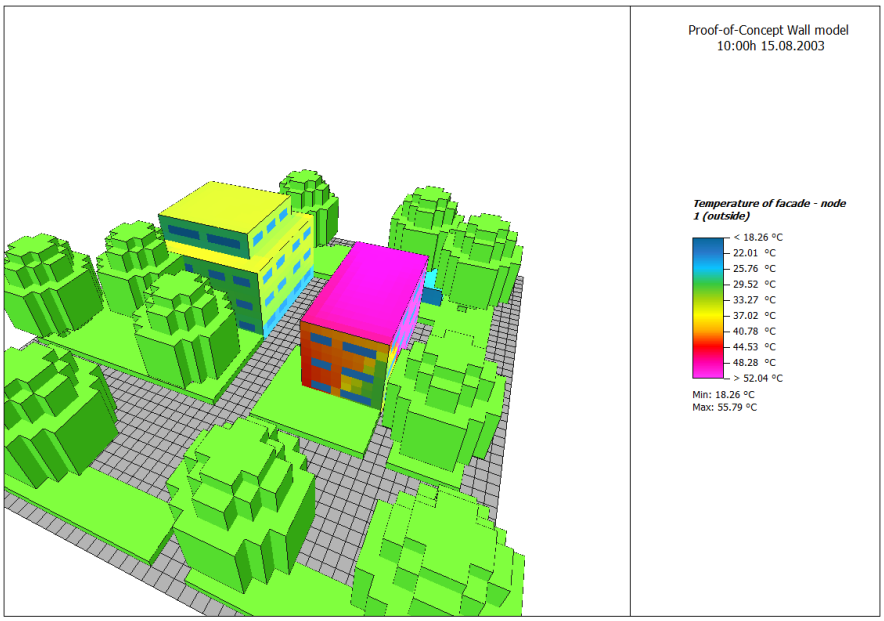

Figure 6.7 shows the different estimated indoor air temperatures in the confined air volumes at 18:00 on the fourth simulation day. Because of their exposition, the south facing building zones in the lightweight building show higher indoor air temperatures than the north facing building zones in the same building. Confirming the expectations, the dense concrete building shows generally lower indoor air temperatures as the density of its building material is almost five times higher than the lightweight concrete. This results in a significantly lower absolute heat capacity of the dense concrete building. During daytime, the glasshouse with its high transmission shows by far the absolute highest indoor air temperatures.

Figure 6.7: Indoor air temperature at 18:00, fourth simulation day

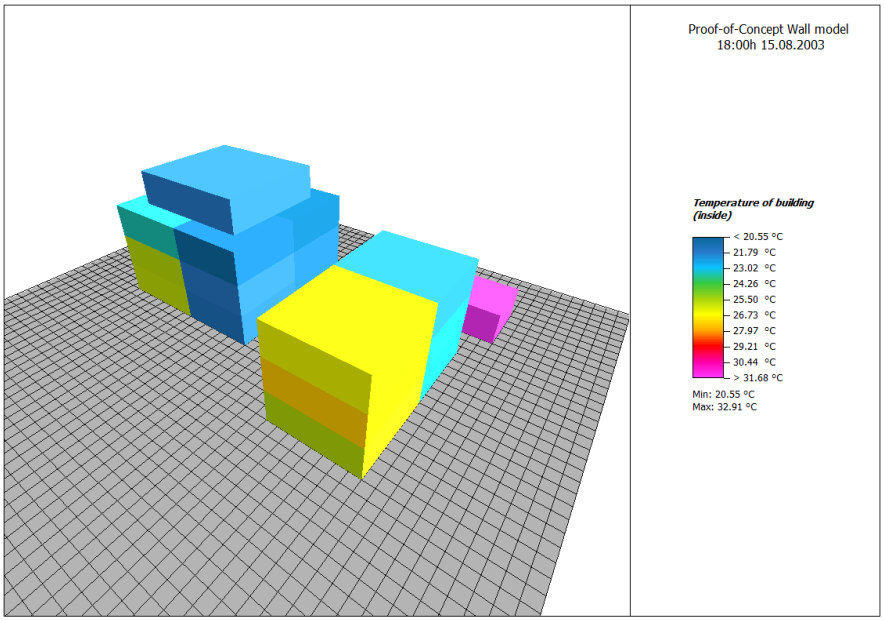

The comparison of the inside surface (node 7) temperature evolution of all buildings (figure 6.8) shows high amplitudes for the glass and the lightweight walls, as was expected. Both show a small gradual increase during the simulation period as they store more heat. They reach a state of equilibrium already after around four days. As expected, the inside node of the dense wall shows only very little diurnal variations due to the high density of the material. The gradual increase of heat, however, is greater for the dense wall than for the other walls due to the combination of high density and relatively high specific heat capacity.

Figure 6.8: Comparison of the surface temperatures on the inside node (node 7)

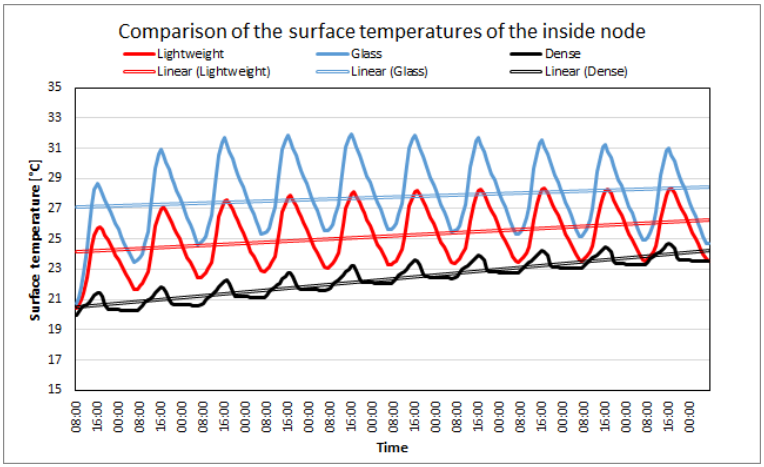

Summing up, the proof-of-concept simulation demonstrated that the advanced multiple-node model is capable of producing plausible results for both facade surface temperatures as well as indoor air temperatures.

6.4 Evaluation of the multiple-node model by comparison with measurement data

6.4.1 Study site

To further validate the new implementations, evaluation simulations were conducted and compared against measurement data. In collaboration with the Fraunhofer Institute for Building Physics in Holzkirchen (IBP), the evolution of the surface temperature of a facade was compared against ENVI-met's model results. The IBP operates a building testing site where different building materials are measured in controlled environments (see figure 6.9). The testing site is located in Holzkirchen, Germany (47.87°N, 11.73°E, elevation 680 m a.s.l.).

Figure 6.9: Aerial photo of the Fraunhofer Institute for Building Physics testing site and the facade temperature measurement

The red boxes indicate the measurement building (underlying picture, Source: Google Earth) / the location of the contact thermometer (top picture)

The facade for the comparison of the measured surface temperatures against the modeled surface temperatures can be seen in figure 6.9. The flat roof test building is 4 meters high, and 6 by 42 meters in width and length. In the lower part of the building, up until a height of 2 meters, the wall is uninsulated, while in the upper part the wall is insulated.

6.4.2 Monitored parameters & material properties

The surface temperature is continuously measured with a PT100 contact resistance thermometer on a south facing uninsulated part of the wall at a height of 0.6 meters

(see figure 6.9). In the temperature range between 0°C and +100°C the measurement accuracy of the PT100 contact thermometer should lie at ±0.3 Kelvin (Temperature Controls Pty Ltd, 2016).

All structural information such as the material composition of the walls as well as the physical parameters of components were provided by the IBP (table 6.2).

Table 6.2: Material properties of the components of the measured facade

	Wall component		
	exterior plaster	brickwork	interior plaster
Material	exterior plaster system	brick	lime plaster
Thickness [m]	0.02	0.505	0.015
Thermal conductivity [W m^{-1} K^{-1}]	0.87	0.21	0.70
Density [kg m^3]	1310	700	1600
Specific heat capacity [J kg^{-1} K^{-1}]	850	1000	850

Additionally, meteorological data were measured on the testing site and provided by the IBP. The measured parameters - air temperature and humidity, wind speed, wind direction, shortwave radiation (direct and diffuse) and longwave radiation - were used as boundary conditions for ENVI-met.

6.4.3 ENVI-met boundary conditions & model area

Based on the meteorological measurement data and ENVI-met's full-forcing method, four simulation periods of several consecutive days were selected to provide boundary conditions for the microclimate model ENVI-met. To test the model under significantly different meteorological conditions and with and without a regulation of indoor air temperatures, the first two simulation periods were chosen to be in spring while the second two simulation periods covered several consecutive days in summer. During the spring periods the building was heated to an indoor air tem-

perature of 20°C, while in the summer periods the building's indoor air temperature was not regulated. The combination of different meteorologies and the differences in the regulation of the indoor air temperature lead to a sophisticated test for the new multiple-node model.

To account for the heating during the spring periods, the indoor air temperature was set constant to 20°C for the spring simulations. In the summer simulations the indoor air temperature was prognosticly modeled using the approach shown above.

Table 6.3 shows the average meteorological conditions of the four simulation periods; figure 6.10 shows the diurnal variations of the direct and diffuse shortwave radiation for the four simulation periods.

Table 6.3: Average meteorological conditions for the four simulation periods

	Parameter (average in 10 meters above ground)		
	air temperature	specific humidity	wind speed
Spring01 (19.-25.04.2015)	9.3°C	4.4 g kg^{-1}	2.6 m/s
Spring02 (09.-15.05.2015)	14.5°C	7.5 g kg^{-1}	2.7 m/s
Summer01 (03.-09.07.2014)	17.1°C	9.0 g kg^{-1}	3.4 m/s
Summer02 (14.-20.07.2014)	19.9°C	9.7 g kg^{-1}	1.9 m/s

Figure 6.10: Diurnal variations of the direct and diffuse shortwave radiation of the four simulation periods

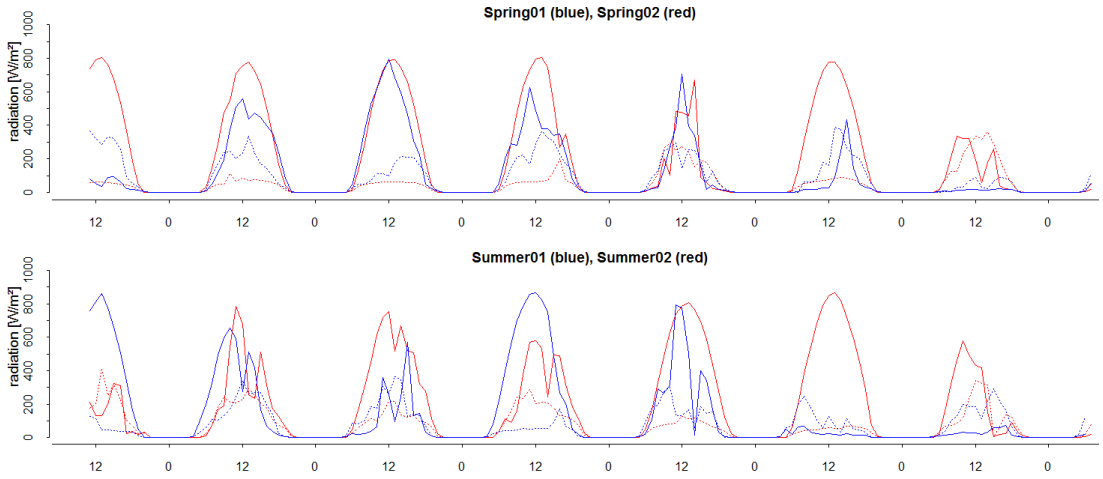

Solid lines: direct shortwave radiation, dotted lines: diffuse shortwave radiation

Utilizing the material properties of the components of the measured facade and ENVI-met's advanced multiple-node model, the material properties and wall structure were reconstructed (figure 6.11). Since the multiple-node model now features seven nodes, all three of the wall's components could be digitized without parametrization (see figure 6.11). The albedo of the exterior plaster was set to 0.6, the emissivity to 0.9 based on the data of Haug (2013) and Mayerlen (2014).

Figure 6.11: Structure of the digitized uninsulated wall

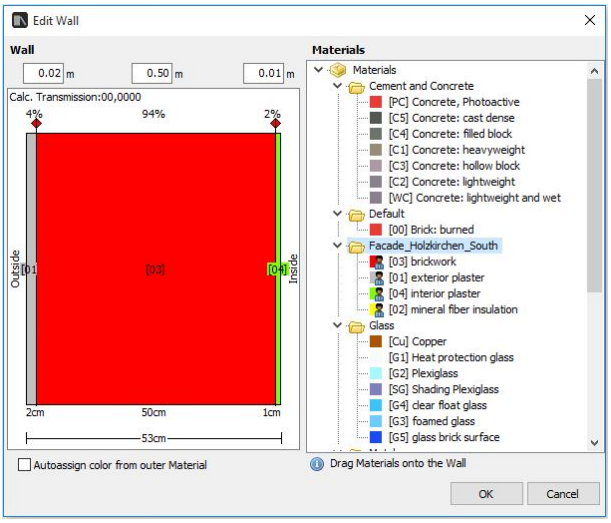

The model area covered 80 meters × 60 meters × 40 meters, its horizontal and vertical resolution was set to 2 meters (figure 6.12).

Figure 6.12: 3D visualization of the model area. The red box indicates the location of the contact thermometer

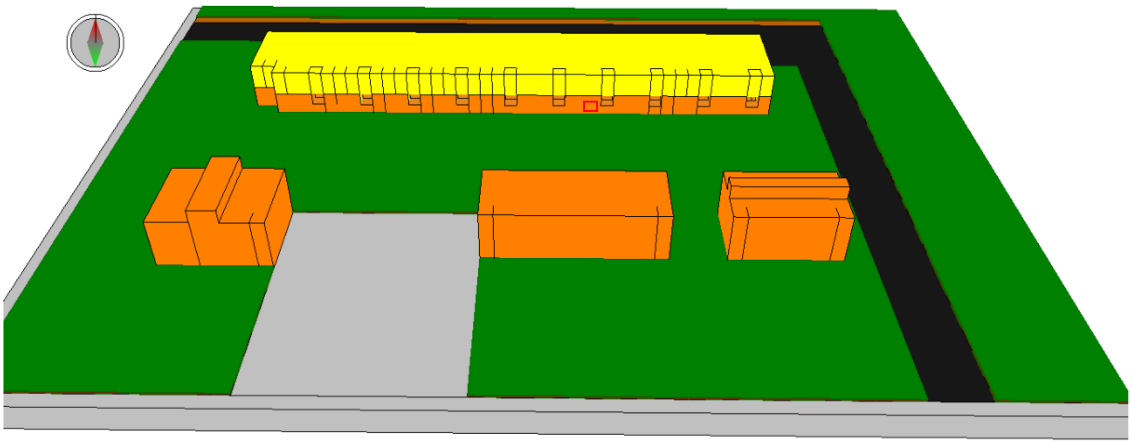

Model area dimensions: 40 × 30 × 20 grids; vertical and horizontal resolution: 2 meters; location: Holzkirchen, Germany

6.4.4 Results and discussion

The comparison of the measured and the modeled facade temperatures shows a very high overall model fit for all simulation periods: $R^2 = 0.98$ for the Spring01 period, $R^2 = 0.96$ for the Spring02 period and $R^2 = 0.98$ and $R^2 = 0.99$ for the Summer01 and the Summer02 periods, respectively (see table 6.4). The high R^2 values indicate that a very high percentage (96% to 99%) of the variation of the measured surface temperature can be explained by the model, i.e. that the shapes of the curves are remarkably similar.

Table 6.4: Model fit between measured and modeled facade temperatures

	model fit		
	R^2	RMSE [K]	NRMSE
Spring01 (19.-25.04.2015)	0.98	2.13	0.07
Spring02 (09.-15.05.2015)	0.96	1.71	0.06
Summer01 (03.-09.07.2014)	0.98	1.03	0.03
Summer02 (14.-20.07.2014)	0.99	1.25	0.05

Since high R^2 values do not automatically mean that the absolute values are closely matched between the model and the measurement, a second indicator, the root mean square error (RMSE) was calculated (see table 6.4). The RMSE accounts for the absolute differences between the simulated and the observed facade temperatures. However, it is dependent on the absolute values and can thus not be readily compared across the meteorological conditions. Therefore, a normalized RMSE (NRMSE) is calculated by dividing the RMSE by the range of measured values. This allows a direct comparison between the different meteorological conditions. The comparison of the RMSE of the measured and modeled facade temperatures for all simulation periods (table 6.4) shows a large agreement in all meteorological conditions. The generally very low RMSE - mostly below 2 Kelvin - in all four simulation periods, which feature significantly different outdoor and indoor conditions, corroborates the

high accuracy of ENVI-met's multiple-node model. Comparing the NRMSE across the meteorological conditions reveals that simulation results are even more accurate in the two summer periods than in the two spring periods. This is probably due to the spring periods being more complex because of the indoor temperature regulation to 20°C.

Figure 6.13 shows a comparison of the diurnal variations of the measured and modeled surface temperatures as well as the delta between the two for all four simulation periods. For all simulation periods the measured and the modeled temperature curves demonstrate remarkable agreement between the modeled and the measured data. ENVI-met matches the daily variations of the surface temperatures very well, even slight variations are represented by the model.

The comparison of the diurnal variations corroborates the findings based on the NRMSE reported above and shows that the agreement between the modeled and measured facade temperatures in the summer periods is significantly better than in the spring periods. The general tendency to slightly underestimate the facade temperatures compared to the measurement values is larger in both spring periods where the absolute facade temperatures are lower and the indoor temperature is regulated to 20°C. The highest discrepancies are found at around 14:00 where both the simulation and the measurement show the highest facade temperatures. Only on the second to last and the last day of the Summer01 period the model slightly overestimates the facade temperatures. This is most likely caused by small amounts of precipitation on these days. Since precipitation is not included in the model a latent heat flux reducing the surface temperature of the facade cannot be replicated in the model.

Figure 6.13: Comparison of the measured and modeled facade temperatures

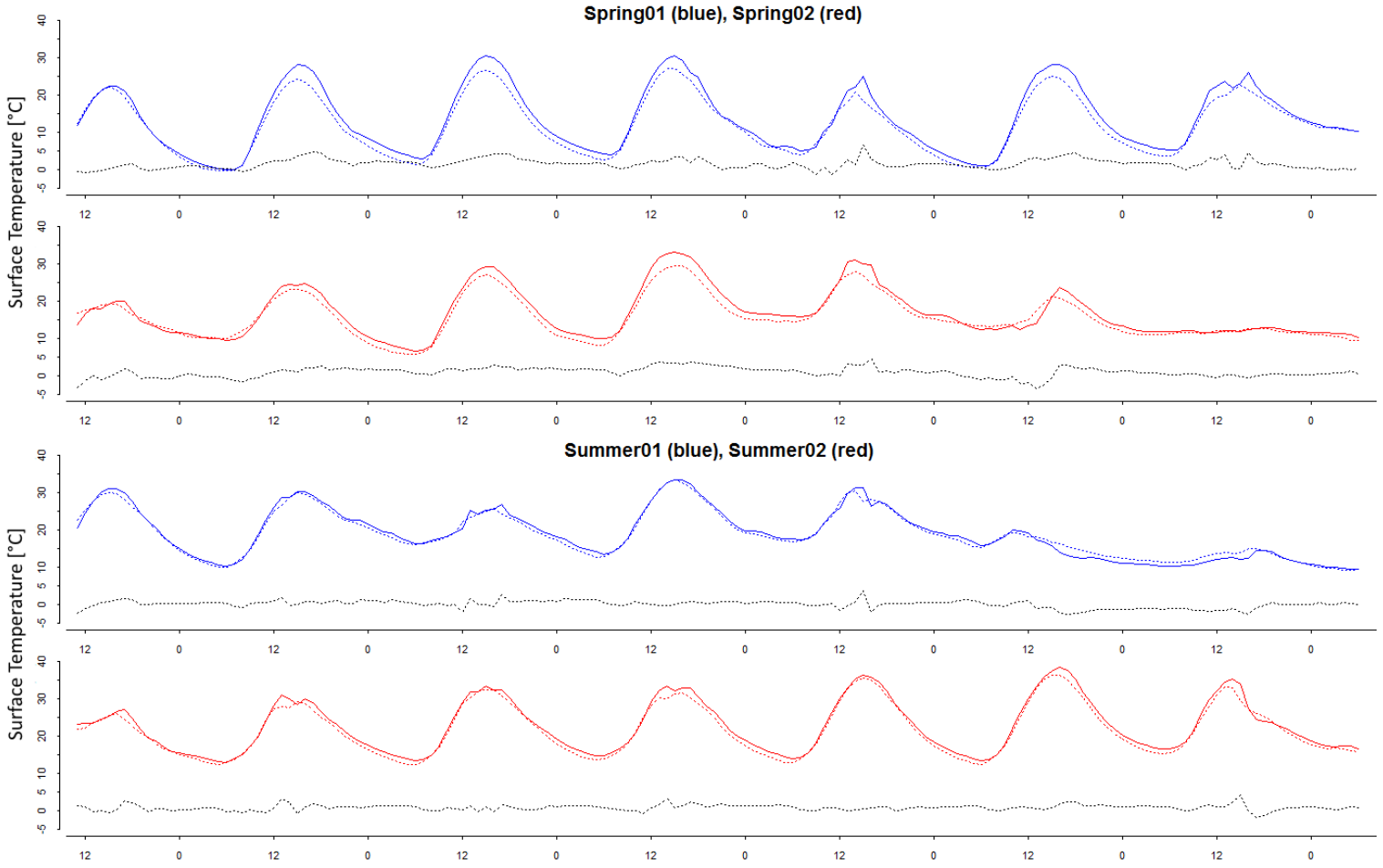

Solid lines: measured data, dotted lines: modeled data, gray dotted line: difference between measured and modeled data values

6.5 Conclusion and outlook

In this study ENVI-met's advanced multiple-node wall and roof model was presented. The new implementation of the model now allows the digitization of more complex walls or roofs consisting of up to three different materials. Together with the full 3D mode in which every building cell can be assigned different wall and roof materials, ENVI-met offers detailed analyses of building physics in complex urban environments. The possibility to divide buildings into separate building zones (rooms / flats) that are treated as confined spaces of air volumes allows a rough estimation of the indoor temperature.

In a proof-of-concept simulation the capabilities of the new implementations regarding the simulation of wall and roof temperatures and the estimation of indoor temperatures were demonstrated. The proof-of-concept simulations showed that ENVI-met produces plausible results for the effects of different wall materials on the indoor air temperature. It could furthermore be shown that the effects of the outdoor environment such as trees or other objects on the facade temperatures are reliably captured by the model.

In a comparison of the measured and modeled facade temperatures, the new implementations were evaluated against measurement data provided by the Fraunhofer Institute for Building Physics Holzkirchen. To test the model under significantly different meteorological conditions, four different periods of several consecutive days were chosen to be simulated and compared against the measurement data. The first two periods were chosen to be in summer where the indoor air temperature of the building was not regulated, the second two in spring where the indoor air temperature was heated to 20°C. The evaluation of the simulated facade temperatures against the measured facade temperatures showed extraordinarily high agreement between the modeled and the measured data for all simulation periods, which in total covered 24 days. The very good results corroborate the high accuracy of ENVI-met's

wall and roof model. Overall, the results demonstrate that, with the advancements of the multiple-node model, ENVI-met is capable of simulating building physics processes in complex environments.

Bibliography

Arnfield, A. J. Street design and urban canyon solar access. *Energy and Buildings*, 14(2):117–131, 1990.

Blocken, B. and Carmeliet, J. Pedestrian wind environment around buildings: Literature review and practical examples. *Journal of Thermal Envelope and Building Science*, 28(2):107–159, 2004.

Bruse, M. and Simon, H. Development and implementation of a high-resolution dynamical wall and roof model for ENVI-met. unpublished working paper, April 2015.

Chudnovsky, A., Ben-Dor, E., and Saaroni, H. Diurnal thermal behavior of selected urban objects using remote sensing measurements. *Energy and Buildings*, 36(11): 1063–1074, 2004.

Haug, M. Ermittlung geeigneter Wärmeübergangskoeffizienten zur Abbildung von zwei- und dreidimensionalen Ecken einer monolithischen Außenwand in WUFI Pro. Study Project, Technische Universität München, 2013.

Huttner, S. *Further development and application of the 3D microclimate simulation ENVI-met.* Dissertation, Johannes Gutenberg-University Mainz, 2012.

Kolokotroni, M., Giannitsaris, I., and Watkins, R. The effect of the London urban heat island on building summer cooling demand and night ventilation strategies. *Solar Energy*, 80(4):383–392, 2006.

Mayerlen, S. Voruntersuchungen zur Ermittlung detaillierter Wärmeübergangskoeffizienten für Fensterlaibungen. Bachelor Thesis, Technische Universität München, 2014.

Oke, T. R. *Boundary Layer Climates.* London, New York: Routledge, 2. edition, 1988a.

Oke, T. R. The urban energy balance. *Progress in Physical Geography*, 12(4):471–508, 1988b.

Temperature Controls Pty Ltd. RTD accuracy `http://www.temperature.com.au/Support/RTDSensors/RTDaccuracyClassAClassB13DIN110DIN.aspx`. 17.02.2016, 2016.

Terjung, W. and O'Rourke, P. Simulating the casual elements of urban heat islands. *Boundary-Layer Meteorologie*, 19(1):93–118, 1980.

van Hooff, T., Blocken, B., Timmermans, H. J. P., and M., Hensen J. L. Analysis of the predicted effect of passive climate adaptation measures on energy demand for cooling and heating in a residential building. *Energy*, 94:811–820, 2016.

7 Further advancement of the coupling module of MUKLIMO_3 and ENVI-met

Helge Simon[1]

[1] Department of Geography, Johannes Gutenberg University Mainz, 55099 Mainz, Germany

7.1 Introduction

Microclimate models like ENVI-met have the advantage that, thanks to their high resolutions, very little parametrization is needed to represent objects of the urban environment: Trees, building materials and complex structures can be directly reproduced within the model. However, this high resolution comes at a disadvantage as well: With increasing spatial resolutions, the differential equations guiding the model have to be solved with smaller timesteps (Courant-Friedrichs-Lewy Condition). This drastically increases the time needed to run the simulations and limits the size of the model area that can be simulated within a reasonable frame of time. Based on the processing and memory capacities of current computers, model areas are limited to approximately $250 \times 250 \times 30$ grids. Given a typical horizontal and vertical resolution of 2 meters, the model areas are usually only about $500 \times 500 \times 60$ meters in size. With such small model areas, the boundary conditions driving the microclimate simulation play a crucial role in determining the outcome and quality of the simulation. To include realistic boundary conditions, ENVI-met offers the so called "forcing" method which allows the definition of diurnal variations of various meteorological parameters as boundary conditions for the microclimate model (Huttner, 2012). Using this forcing method, the effects of larger scale processes can be simulated on a microscale level in ENVI-met.

To obtain the meteorological values for these boundary conditions, both measurement data as well as outputs from other models can be used. One of these mesoscale models is "MUKLIMO_3", which can be coupled with the microscale model ENVI-met using an offline dynamic down-scaling method developed by Huttner (2011). While the general coupling function works, evaluations of the coupled model outputs found some discrepancies between the two models with respect to the near-surface air temperatures (Bruse, 2013; Simon, 2012). This contribution tries to identify the causes of these discrepancies and applies several modifications to improve the

coupling process and consequently the agreement between the two models.

7.2 MUKLIMO_3

MUKLIMO_3 (acronym for **m**ikroskaliges **u**rbanes **Kli**ma**mo**dell, **3**-dimensionale Version - microscale urban climate model, 3-dimensional version) is a non-hydrostatic climate model. As a urban climate model it was developed to simulate the near-surface meteorology of urban areas. The model is based on a two-dimensional atmosphere model by Sievers and Zdunkowski (1986). The adaptation of the stream-function-vorticity method to three dimensions by Sievers (1995) allows the simulation of the atmospheric temperature, humidity and wind field on a three-dimensional model grid. Cloud processes as well as precipitation are, just like in ENVI-met, not considered in the model (Deutschländer et al., 2008; DWD, 2015).

The spatial resolution of the model can vary greatly, from a few meters with resolved buildings to several hundred meters with parametrized building environments. Typical simulation periods are several hours to a few days, typical spatial dimensions are up to 25 kilometers in width and length and 750 meters in height, with horizontal resolutions of around 100 meters (Früh et al., 2011b). With such coarse resolutions and such large model areas, MUKLIMO_3 can be considered a mesoscale model, inside whose model area a microclimate model like ENVI-met can be nested (on nesting, see von Storch et al., 1999).

Since the digitization of individual building structures is no longer reasonably possible when using a horizontal resolution in the range of several tens of meters, MUKLIMO_3 offers the possibility to simulate building structures horizontally unresolved using parametrizations (DWD, 2015). Based on the following statistical parameters, buildings are parametrized in the model:

- the built-up area in the grid volume

- the wall area per grid volume
- the mean height
- the ratio of sealed surfaces of the non built-up area

Using these parameters, the air flow between buildings is modeled as an air flow within a porous medium. In built-up areas the radiative fluxes are moved from the surface toward the walls and roofs of the buildings taking into account heat storage and the physical parameters of the building structures (DWD, 2015; Früh et al., 2011b). Based on these parameters, MUKLIMO_3 categorizes different built-up area types. By default, MUKLIMO_3 offers nine distinct classes which are based on urban structure classes provided by the German Federal Ministry of Regional Planning, Building and Urban Development (Früh et al., 2011a). The classes range from sparsely dense built-up areas over industrial sites to high-rise dense inner cities.

Apart from the built-up area types, MUKLIMO_3 offers several other land use classes to categorize the elements in the model area. Table 7.1 shows some of the different land use classes with their physical properties: ratio of surface area building type 1 (VG_1), wall area index type 1 (WAI_1), building height type 1 (h_1), ratio of sealed surfaces (vs), roughness length (z_0), leaf area index (LAI), height of vegetation canopy (hca), surface cover vegetation (σ_a)

Table 7.1: Land use classes MUKLIMO_3

Name	VG_1 (0-1)	WAI_1 (0-1)	h_1 (m)	vs (0-1)	z_0 (m)	LAI (m^2/m^2)	hca (m)	σ_a (0-1)
residential (high density)	0.3	2.7	15	0.8	0.2	1	0.5	0.7
open area	0.0	0.0	0.0	0.0	0.03	1	0.3	0.8
sealed area	0.0	0.0	0.0	1.0	0.01	1	0.0	0.0
meadow	0.0	0.0	0.0	0.0	0.03	2	0.3	1.0

Based on DWD (2015)

7.3 Coupling of the two models - full-forcing mode

Since MUKLIMO_3 is able to simulate very large model areas in adequate time but only in a coarser resolution, and ENVI-met on the other hand is able to simulate the microclimate in a high resolution with very little parametrization but only for smaller model areas, a one-way offline coupling of the two models was developed to combine the advantages of both models (Huttner, 2011). In the coupling, the ENVI-met model area is nested inside the larger MUKLIMO_3 model area. Based on the MUKLIMO_3 model outputs, diurnal profiles of different meteorological parameters are created that are used as initial and boundary conditions for the microclimate model ENVI-met.

To provide ENVI-met with one-dimensional profiles of different meteorological parameters, the coupling makes use of ENVI-met's full-forcing mode (Huttner, 2012). In the full-forcing mode, the user can provide diurnal cycles of one-dimensional profiles for the potential temperature, the specific humidity, the wind speed and the wind direction at ENVI-met's inflow borders as well as for the longwave and the direct and diffuse shortwave radiation at the top of the model area (Huttner, 2012).

As part of the previous research project (Huttner 2011), an interactive user interface was developed that allows the extraction of boundary and initial conditions from MUKLIMO_3 model outputs. The extracted data is then converted to the forcing file format so that it can be used in ENVI-met's one-dimensional boundary model. From there the values of the different parameters are being directly transferred to the boundary cells at the inflow border. A nudging, where the MUKLIMO_3 values would be forced onto the grid cells in ENVI-met's three-dimensional model array, is not implemented. Since the height levels of model outputs of MUKLIMO_3 do not necessarily match the vertical gridding of ENVI-met, the values of the different parameters are interpolated to fit the ENVI-met grid. The potential temperature and the specific humidity are interpolated linearly; the wind speed is interpolated

logarithmically. To prevent instabilities, the wind direction is kept constant for all height levels for each timestep. Temporally, all parameters were interpolated linearly (Huttner, 2011).

7.4 Deficits of the initial status of the coupling

Applications of the coupling revealed unsatisfactory differences in the near-surface air temperatures between the two models (Bruse, 2013; Simon, 2012). Due to these large differences in the prognostic air temperatures, the ENVI-met outputs of the air temperatures showed no differentiation within the nested model areas. Instead, the air temperature was decreasing or increasing consistently depending on whether the air temperatures extracted from the MUKLIMO_3 outputs were too hot or too cool for ENVI-met.

Figure 7.1 shows the air temperature in 1.8 meters height at 13:00 in an ENVI-met model area for a coupled simulation run in Frankfurt am Main, Germany. The inflow boundary is located in the southwest of the model area. The figure shows that the air temperatures that enter the ENVI-met model area are significantly higher than in the rest of the model. Since the forced air temperatures are substantially too high, all local differences in the air temperatures in the ENVI-met domain are superimposed by the steady decrease of the too hot air temperatures that are forced into the model area.

7.5 Identification of deficits in the coupling between the two models

In-depth analyses aimed at finding the cause(s) of these discrepancies revealed essential shortcomings and flaws in the parameter handling of the interface as well as

Figure 7.1: Air temperature in 1.8 meters height, model area Frankfurt am Main - Status Quo 2012

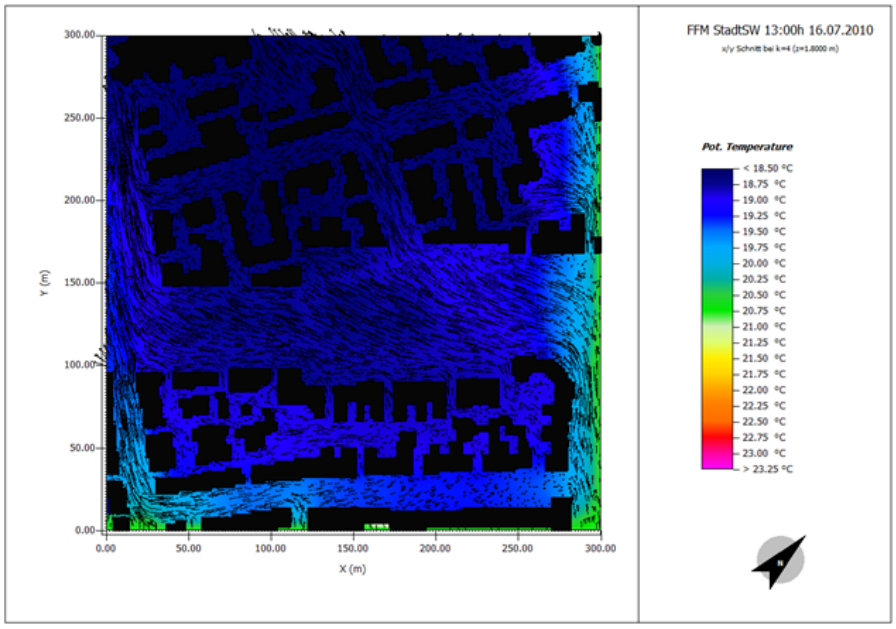

in the data handling between the two models:

While ENVI-met calculates the direct shortwave radiation on a reference surface that is orientated perpendicularly to the incoming radiation (see chapter 2.4.1.5 on page 15), the reference surface of the shortwave radiation in MUKLIMO_3 is orientated parallelly to the ground surface. In the interface software that converts the MUKLIMO_3 output data into forcing data for ENVI-met, the radiation outputs of MUKLIMO_3 are directly extracted from the output data and then used as the incoming radiation on the top of ENVI-met's 3D model area without any conversion. The differences in the reference surface orientation lead to drastic differences in the radiation budget, especially during the early morning and late evening hours when the sun's height angle is low.

The absence of a database reconciliation between the two models turned out to be another deficit in the coupling. The interface software did not extract the phys-

ical parameters of the surfaces, walls, roofs or vegetation that were used in the MUKLIMO_3 model run nor were these parameters transferred into ENVI-met's database.

The extraction of the soil moisture and the subsequent conversion for ENVI-met was flawed as well: The initial soil moisture conditions in ENVI-met need to be entered as a percentage of the useable field capacity. The soil moisture output data of MUKLIMO_3, however, is given as the volumetric water content of the soil. For the conversion of the absolute volumetric water content into the useable field capacity, the wilting point as well as the field capacity need to be known and adjustable. Yet, the software interface did not allow for any adjustments. This could result in too high or too low soil moisture values in the ENVI-met model. Moreover, the calculation of the initial soil temperatures did not account for the ratio of unsealed and sealed surfaces of the selected MUKLIMO_3 forcing cells. The calculating always used mean soil temperatures of the unsealed and sealed surface temperature outputs of MUKLIMO_3 irrespective of the actual ratio of unsealed and sealed surfaces.

In full-forcing mode, ENVI-met needs boundary conditions of the potential air temperature and the specific humidity. Even though MUKLIMO_3 internally uses the potential air temperature and the specific humidity as well, its model output only includes the absolute air temperature as well as the relative humidity. While a recalculation of these parameters was in fact done in the interface software, it proved not to be exactly the same as in MUKLIMO_3.

With MUKLIMO_3's coarser spatial resolution, the output fields refer to larger grids. To fit ENVI-met's higher resolution, interpolations of the MUKLIMO_3 outputs are needed. To fit ENVI-met's vertical resolution, MUKLIMO_3's air temperature values are interpolated linearly starting from the first atmosphere cell. The wind speed is interpolated logarithmically between all MUKLIMO_3 height levels. Since the boundary model of ENVI-met expects air temperature values for the boundary surface close to the ground, the air temperature values of the first MUKLIMO_3

atmosphere cell were also used for ENVI-met's ground level air temperature. This very unrealistic approach leads to a forcing where the air temperature is assumed to be constant from ENVI-met's ground level up to the first MUKLIMO_3 height level of around 5 meters.

Coupled simulation runs where MUKLIMO_3 provided higher wind speed conditions showed larger differences in the near-surface air temperatures between the two models. Studies showed that when ENVI-met is run in the standard configuration where the wind flow is updated in regular time intervals until a quasi-steady state is reached, the wind speed conditions that are provided by MUKLIMO_3 do not enter the ENVI-met model area. Instead, wind speeds are massively reduced.

Another, smaller, discrepancy was found in the models' timings: While MUKLIMO_3 output timing includes daylight-saving time, ENVI-met always uses the standard local time.

7.6 Interface enhancements and model adjustments

In order to rectify the shortcomings outlined above, several adjustments were made to the interface software and the ENVI-met model.

7.6.1 Reference surface for shortwave direct radiation

To correct for the differences in the reference surface, the incoming direct shortwave radiation values of MUKLIMO_3 which - other than those of ENVI-met - refer to a reference surface parallel to the ground surface, were converted using Lambert's cosine law:

$$Q^*_{sw,EN} = \frac{Q^*_{sw,MU}}{|\cos(90 - h)|}$$

with $Q^*_{sw,EN}$ as the incoming direct shortwave radiation on a surface that is orientated perpendicularly to the incoming radiation, $Q^*_{sw,MU}$ as incoming direct shortwave radiation on a surface oriented parallelly to the ground and h as the sun's height angle.

Since the diffuse and the longwave radiation are assumed to be anisotropic in ENVI-met, a conversion of the MUKLIMO_3 values is not needed.

To ensure the correct interpretation of the parameter values, the forcing file that is used for the coupled simulation runs was extended by the tag:

<surfaceOrientationRad>*horizontal*</surfaceOrientationRad>

which gives an indication on the reference surface of the incoming direct shortwave radiation.

7.6.2 Extraction and transformation of physical parameters of surface, wall and roof materials and vegetation from MUKLIMO_3 to ENVI-met

In the current state of the coupling, no physical properties of surface, wall and roof materials or vegetation were extracted from the MUKLIMO_3 model outputs and transferred to ENVI-met. The following adjustments were therefore made to the interface software:

Physical parameters: Ground surfaces

ENVI-met provides the possibility to adjust a number of physical parameters for ground surfaces: emissivity, albedo, roughness length, volumetric heat capacity and the heat conduction. While emissivity, albedo, roughness length and heat conduction can be directly extracted from MUKLIMO_3, the volumetric heat capacity had to

be recalculated: Since MUKLIMO_3 files only include information on the thermal diffusivity, the volumetric heat capacity of the ground surfaces had to be calculated by:

$$c_p = \frac{\lambda}{\kappa}$$

with c_p as the volumetric heat capacity [J m^{-3} K^{-1}], λ as the thermal diffusivity [W m^{-2} s^{-1}] and κ as the thermal conductivity [W m^{-1} K^{-1}].

Physical parameters: Wall and roof materials

For the import of the physical properties of the wall and roof surfaces of the MUKLIMO_3 simulations into ENVI-met's database, some conversion calculations needed to be applied. While the albedo, the emissivity and the thickness of the wall and roofs could directly be imported, the K-Value and the heat capacity per area had to be converted into ENVI-met's heat conduction, volumetric mass density and specific heat capacity. Thus the following conversions were implemented in the coupling interface software:

$$c = \frac{c_a}{\rho \cdot d}$$

with c as the specific heat capacity of the wall / roof [J kg^{-1} K^{-1}], c_a as MUKLIMO_3's heat capacity per area [J m^{-2} K^{-1}], ρ as the volumetric mass density [kg m^{-3}] (here set constant to 930 kg m^{-3}) and d the thickness of the wall or roofs in MUKLIMO_3 [m].

$$\lambda = \mathrm{K} \cdot d$$

with λ as the heat conductivity [W m^{-1} K^{-1}] and K as the K-Value [W m^{-2} K^{-1}] in MUKLIMO_3.

Physical parameters: Vegetation

While ENVI-met uses the leaf area density (LAD) to parametrize vegetation, MUKLIMO_3 uses the leaf area index (LAI). To convert the LAI into the LAD the following equation is used:

$$\mathrm{LAD} = \frac{\mathrm{LAI}}{h}$$

with LAD as the leaf area density in ENVI-met, LAI the leaf area index in MUKLIMO_3 and h as the height of the plants in MUKLIMO_3.

Since the physical parameters of the ground surfaces, the walls and roofs and the vegetation in ENVI-met are managed by the programs *DBManager* and *Albero*, the interface software does not automatically import the parameter values into ENVI-met's database. Instead, the parameter values that need to be adjusted in order to fit the MUKLIMO_3 data are converted and presented in the interface software for the user to adjust in the respective ENVI-met programs (see Figure 7.2).

Figure 7.2: Information memo about the converted physical parameters that need to be adjusted in the DBManager and Albero

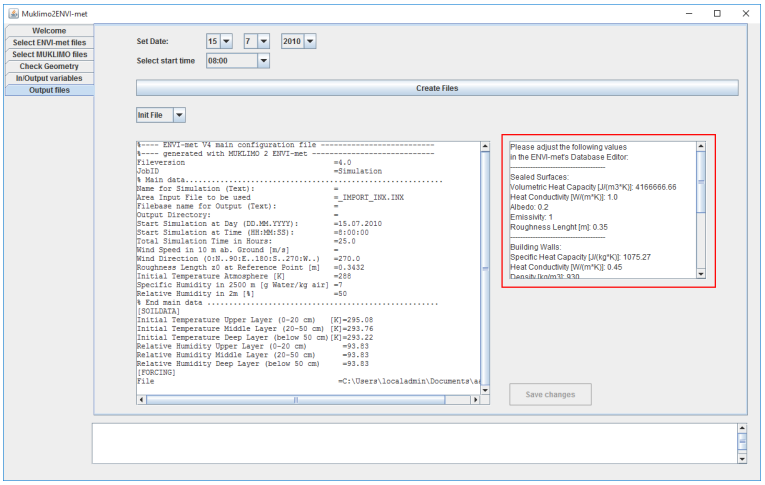

7.6.3 Soil moisture and temperature

Furthermore, the soil temperature and soil moisture values, which are used as initial parameters in ENVI-met, were not correctly converted by the interface software. As described above, the initial soil moisture conditions in ENVI-met need to be entered as a percentage of the useable field capacity. The soil moisture output data of MUKLIMO_3 is given as the volumetric water content of the soil. For the conversion of the absolute volumetric water content into the percentage of useable field capacity, the user has to insert the wilting point and the field capacity of the soil type that is used into the interface. Based on these values, the interface software calculates the initial soil moisture conditions (ξ_{Init}) for the ENVI-met simulation as follows:

$$\xi_{Init} = \frac{\eta_{MU} - \eta_{Wilt,EN}}{\eta_{FC,EN} - \eta_{Wilt,EN}} \cdot 100$$

with η_{MU} as the volumetric soil water content from the MUKLIMO_3 output, $\eta_{Wilt,EN}$ as the wilting point and $\eta_{FC,EN}$ as the field capacity of the ENVI-met soil type. In case of an over-saturation where the volumetric water content exceeds the field capacity of the soil type, the soil moisture values are being reset to 100% of the useable field capacity.

In addition, the initial state of the coupling interface did not account for the ratio of unsealed and sealed surfaces when recalculating the soil temperatures of the selected MUKLIMO_3 forcing cells into the initial soil temperatures for the ENVI-met model run. Instead, it simply assumed a ratio of 50-50 by using the mean of sealed and unsealed soil temperatures. In the improved interface software, the initial soil temperature is calculated as the *weighted* mean of the sealed and unsealed soil temperatures, with weights being based on the actual ratio of sealed and unsealed surfaces in the selected MUKLIMO_3 forcing cells.

7.6.4 Calculation of potential temperature and specific humidity

The former conversions of MUKLIMO_3's absolute air temperature and relative humidity into the potential temperature and the specific humidity for the boundary conditions for ENVI-met have been reworked.

In the initial coupling interface, the potential temperature was calculated using the hydrostatic approximation. In the new version of the interface, the potential temperature is now calculated in compliance with the internal MUKLIMO_3 approach, where a constant adiabatic air temperature gradient is assumed: 0.0098 K m^{-1}. Thus the potential temperature θ is now calculated by:

$$\theta(h) = T(h) + h \cdot \varsigma$$

with $T(h)$ as the actual air temperature T in the height h and ς as the adiabatic air temperature gradient (const 0.0098 K m^{-1}).

For the conversion of the relative humidity into the specific humidity, MUKLIMO_3's internally used August-Roche-Magnus formula was implemented into the interface:

$$e_{sat} = 6.107 \cdot \exp\left(\frac{17.15 \cdot (T - 273.15)}{T - 38.33}\right)$$

$$q = 0.62198 \cdot \left(\frac{e_{sat}}{p - 0.37802 \cdot e_{sat}}\right)$$

with e_{sat} as the saturation vapor pressure, T as the air temperature, q as the specific humidity and p as the barometric pressure.

Even though there are only very small differences between the former and the current conversion of the relative humidity into the specific humidity, the new conversion methods were implemented for conformity reasons.

7.6.5 Vertical interpolation of wind speed and air temperature

Since ENVI-met's one-dimensional boundary model features a higher resolution than MUKLIMO_3's model outputs, the extracted parameters need to be interpolated to fit ENVI-met's vertical grid structure. In the former version, the potential temperature was interpolated linearly starting from MUKLIMO_3's first atmospheric height level. For ENVI-met grid cells that are located below the first MUKLIMO_3 model output height (usually 5 meters to 10 meters above ground) the potential temperature was set to the same value as MUKLIMO_3's first atmospheric value. This resulted in a very unrealistic profile of the potential temperature where the forcing of the potential temperature for all near-surface grids up until the height of the first MUKLIMO_3 height level showed constant values.

In the new approach, the profile of the near-surface potential temperature is interpolated differently: The MUKLIMO_3 model outputs of the surface temperature are interpreted as potential temperatures for ENVI-met's lowest one-dimensional boundary model grid cell (0 meters above ground). Based on these values at ground level, a logarithmic interpolation using the roughness length of the surface is conducted until the first MUKLIMO_3 grid height is reached:

$$\theta(z) = T_s + \theta_{MU} - T_s \cdot \left(\ln\left(\frac{z}{z_0}\right)\right) / \left(\ln\left(\frac{z_{MU}}{z_0}\right)\right)$$

with $\theta(z)$ as the potential temperature in the height z, T_s as the weighted mean surface temperature of the selected MUKLIMO_3 forcing cells, θ_{MU} as the converted potential temperature output of the first MUKLIMO_3 atmosphere grid cell, z_0 as the weighted mean roughness length of the selected MUKLIMO_3 forcing cells and z_{MU} as the height of the first MUKLIMO_3 atmosphere grid cell.

The new approach leads to much more realistic potential temperature profiles at the near-ground surface level. Above the height of the first MUKLIMO_3 model output,

the interpolation is conducted linearly.

The spatial interpolation of the wind speed was simplified. In the former version, the wind speed was interpolated logarithmically between all MUKLIMO_3 height levels. This led to undesired wavelike wind profiles (see figure 7.3).

Figure 7.3: Schematic visualization of the logarithmic interpolation of the wind speed between all MUKLIMO_3 height levels

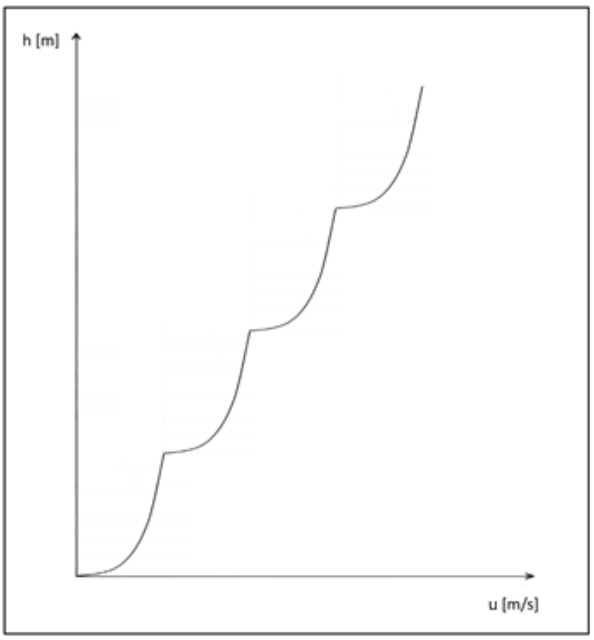

In the new version, the vertical interpolation of the wind speed is implemented analogously to the potential temperature: Only the interpolation between the ground level (wind speed = 0 m s^{-1}) and the first MUKLIMO_3 level is conducted logarithmically; and the interpolation for the ENVI-met height levels above is conducted linearly between the MUKLIMO_3 outputs.

7.6.6 Wind flow calculation

In ENVI-met's standard settings, the wind flow is updated in regular time intervals until a quasi-steady state is reached. Test simulations showed that in simulation runs where MUKLIMO_3 provided higher wind speeds, the forced wind speeds did not advance far into the ENVI-met model - the wind speed was reduced rapidly after entering the model area. When ENVI-met was operated with a prognostic, continuous calculation of the wind flow, the simulation results showed much better results: The effect of reducing wind speeds were no longer an issue. The operation of ENVI-met with a continuous calculation of the wind flow, however, drastically increases the simulation time. An alternative approach to solve both problems could be the implementation of nudging, where instead of the parameter values in ENVI-met's one-dimensional boundary model the values in the three-dimensional core model are altered according to the larger scaled model's forcing values.

7.6.7 Time adjustment

A smaller adjustment concerns the local simulation time: While ENVI-met uses the standard local time for all its inputs and outputs, MUKLIMO_3 adjusts its outputs to the daylight saving time. To correct this, the interface now adjusts the local simulation time to fit ENVI-met's standard local time for the forcing.

7.7 Calibration simulations

To further understand the discrepancies between the models and to evaluate the effects of the advancements outlined above, several test simulations were run. First, very simple model areas that feature homogenous surface covers and no buildings were used for the coupled simulation runs in order to facilitate analyzing the effects of the advancements. Based on these calibration simulations, further coupled

simulations were run in more complex model areas.

7.7.1 Model area: Sealed surface

The first model area was chosen to be a completely homogenous sealed model area with no buildings. The MUKLIMO_3 model area covered an area of 5.5 km × 5 km × 700 m in a horizontal resolution of 50 meters. The vertical resolution changed with height, the near-surface grids had a resolution of 10 meters. The model area was homogenously digitized using MUKLIMO_3's land use class "sealed area" (see table 7.1).

Since the model area featured no buildings or other objects, the nested ENVI-met model area was digitized in a coarse horizontal resolution of 30 meters. To be able to examine the effects of the discrepancies in the near-surface air temperature, a high vertical resolution of 2 meters was chosen. The dimensions of the ENVI-met model area are: 50 × 50 grids horizontally and 25 grids vertically, resulting in a model area of 1500 meters × 1500 meters × 50 meters.

In the following, the simulation results based on the initial coupling interface ("status quo") are compared to the simulation results including all interface and model advancements to show the effects of these advancements.

7.7.1.1 Model run: status quo

Figure 7.4 shows the air temperature in the ENVI-met model area in a height of 1.8 meters at 15:00 simulation time. The coupled simulation was run without any of the adjustments discussed above. The simulation output clearly shows the large discrepancies in the near-surface air temperature described in chapter 7.4. In this simulation, the forcing provided by MUKLIMO_3 results in temperatures at the inflow boundary that are around 3 Kelvin higher than the air temperatures 100 meters downstream in the ENVI-met model area.

Figure 7.4: Sealed surface: Air temperature, status quo simulation

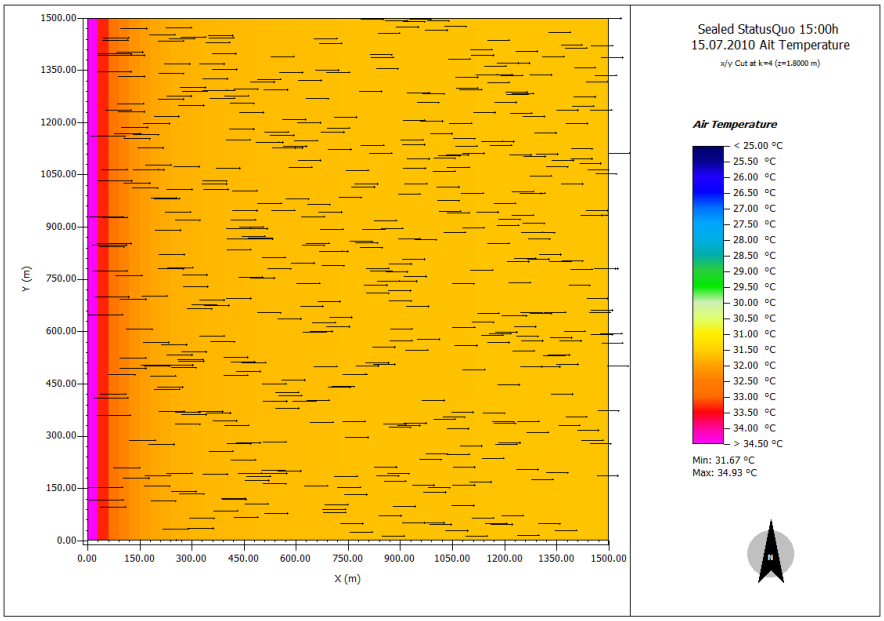

7.7.1.2 Model run: advanced version

Figure 7.5 shows the air temperature in the ENVI-met model area in a height of 1.8 meters at 15:00 simulation time. The coupled simulation was run using all advancements except for the continuous calculation of the wind flow. As the figure shows, the agreement between the two models is already very high thanks to the different adjustments. The differences between the air temperature at the inflow boundary and the air temperatures inside the ENVI-met model area are reduced from 3 K (figure 7.4) to only 0.5 K.

Figure 7.5: Sealed surface: Air temperature, incl. all advancements but the continuous calculation of the wind flow

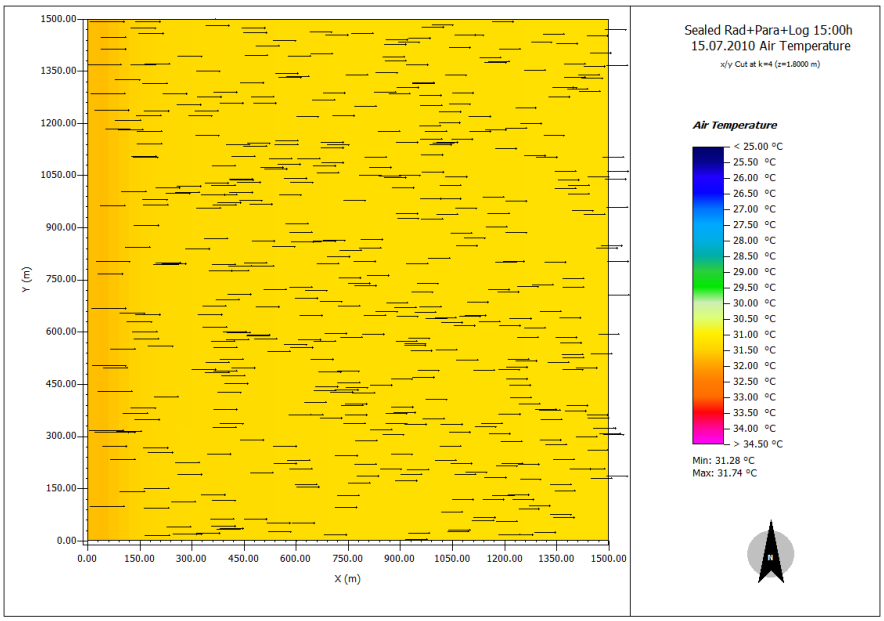

The successful adjustment of the recalculation of the direct shortwave radiation can be seen in figure 7.6. As the figure shows, direct shortwave radiation in the status quo version was constantly below values provided by the MUKLIMO_3 model output. With the recalculation of the reference surface, however, the incoming direct shortwave radiation is now correctly forced into ENVI-met.

Figure 7.6: Sealed surface: Comparison of the direct shortwave radiation: MUKLIMO_3, status quo and advanced version

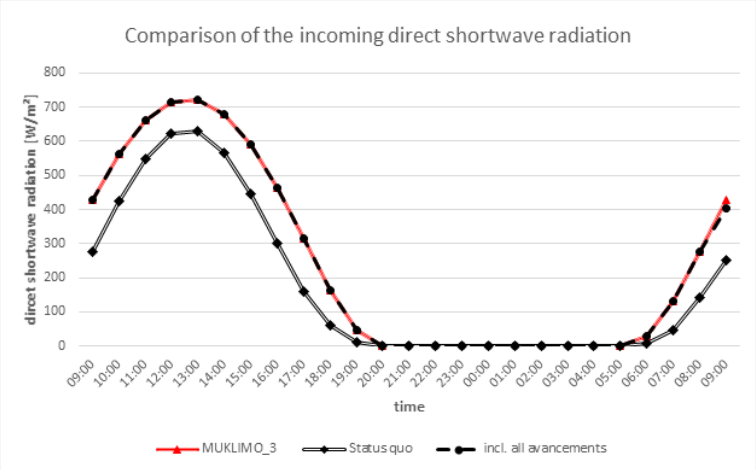

The comparison of the surface temperatures between MUKLIMO_3, the status quo and the advanced version (figure 7.7) confirms the correct implementation not only of the direct radiation but also of the physical properties of the surface materials. During daytime, the surface temperatures in the advanced version match the surface temperatures in MUKLIMO_3 very nicely. During nighttime, the agreement is less strong.

Figure 7.7: Sealed surface: Comparison of the surface temperature: MUKLIMO_3, status quo and advanced version

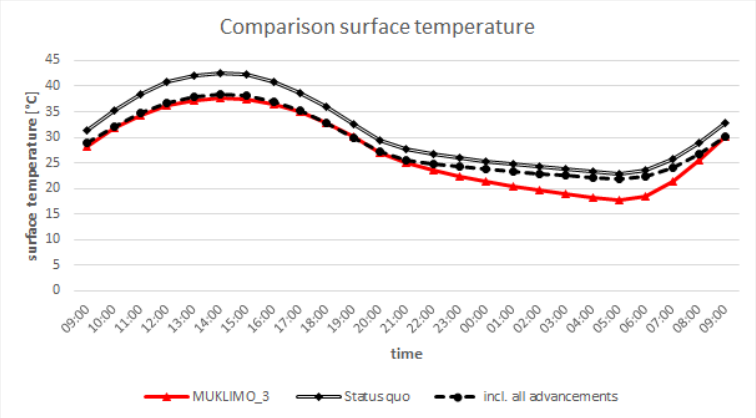

The comparison of the relative wind speed change from the inflow boundary to the three-dimensional model area (figure 7.8) as well as the comparison of the latent heat flux at the ground surface (graph updated wind flow in figure 7.9) confirms that even though there is a high agreement in the air temperatures between the two models, there are still fundamental differences regarding the wind flow and thus the sensible heat exchange.

Figure 7.8: Sealed surface: Comparison of the relative wind speed change from the inflow boundary to the three-dimensional model area, incl. all advancements but the continuous calculation of the wind flow

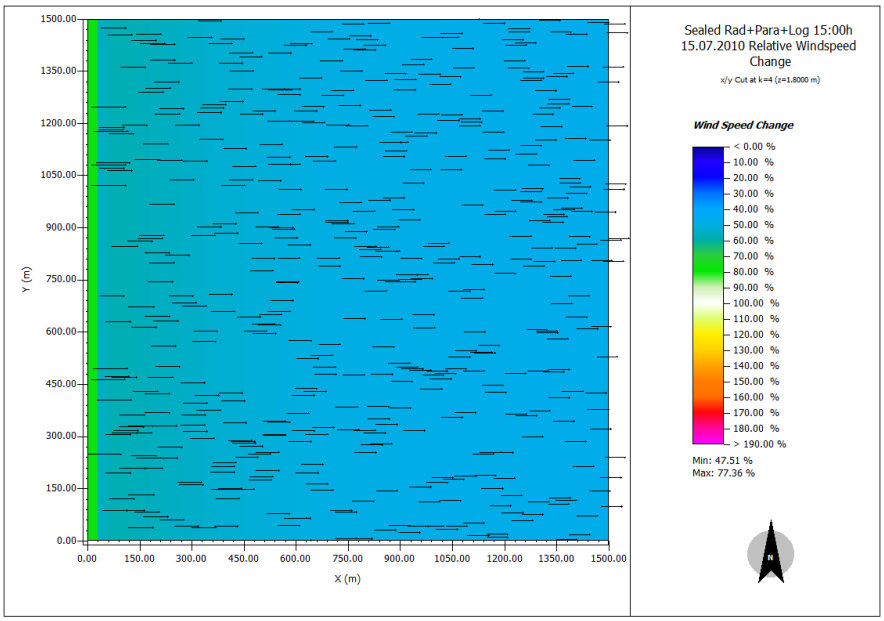

Figure 7.9: Sealed surface: Comparison of the latent heat flux at the ground surface: MUKLIMO_3, advanced version excluding and including the continuous calculation of the wind flow

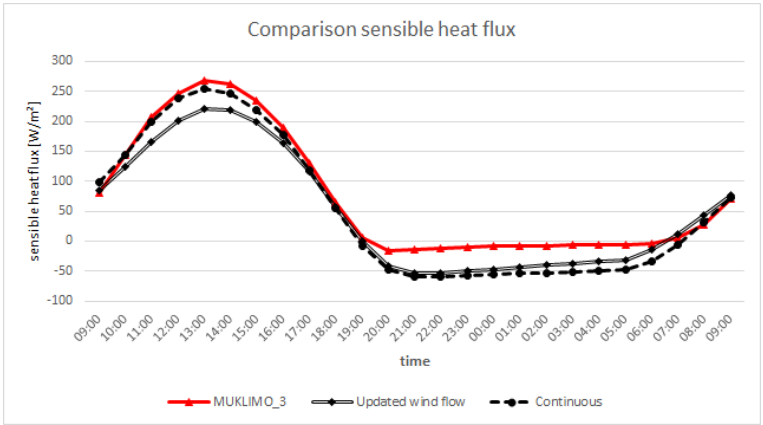

The strong wind speed reduction in the ENVI-met model area was caused by ENVI-met's standard settings for the calculation of the wind flow. In the standard settings, the wind field is updated in regular time intervals until a quasi-steady state is reached. ENVI-met was then run with a prognostic, continuous calculation of the wind flow. This yielded much better results as figures 7.10 and 7.11 show. The already high agreement regarding the air temperatures could be further improved and, more importantly, the wind speed provided by MUKLIMO_3 could be retained in the ENVI-met model area.

Figure 7.10: Sealed surface: Air temperature, incl. the continuous calculation of the wind flow

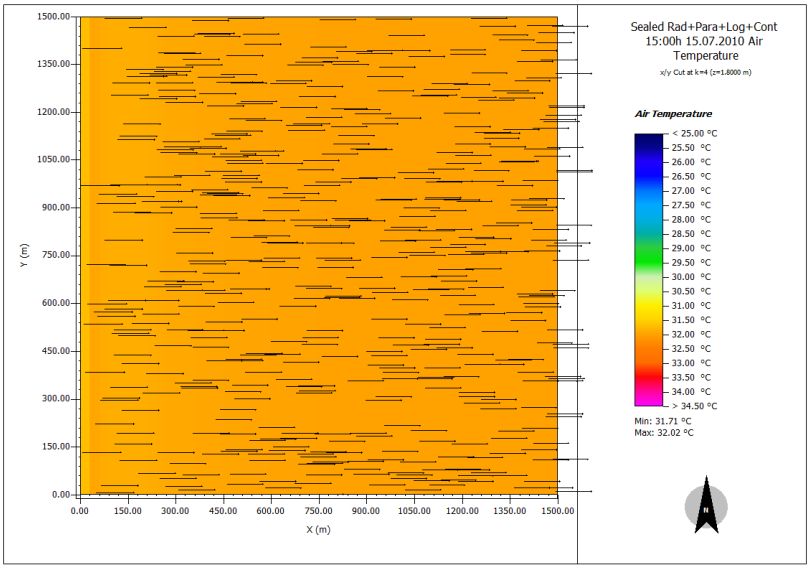

Figure 7.11: Sealed surface: Comparison of the relative wind speed change from the inflow boundary to the model area - continuous wind flow calculation

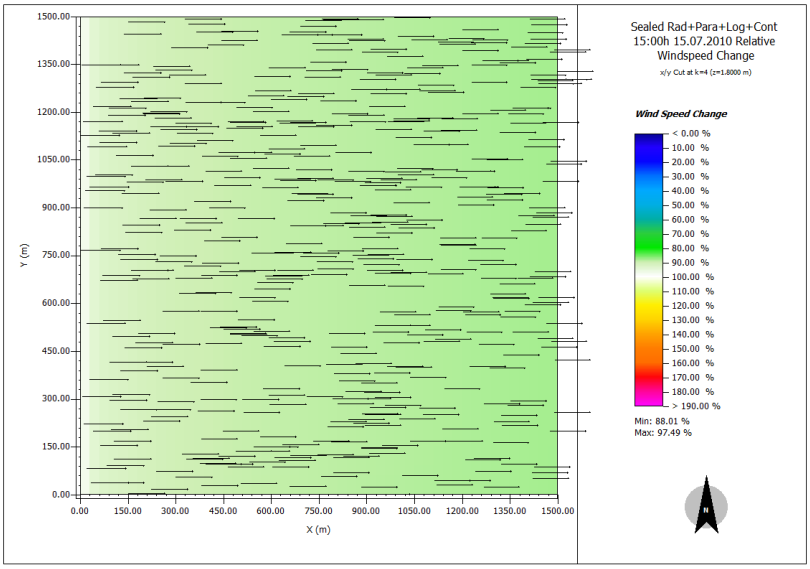

The continuous calculation of the wind flow also led to a much better agreement regarding the sensible heat flux (figure 7.9). During daytime, the sensible heat fluxes between MUKLIMO_3 and ENVI-met fit very well. During nighttime, however, the differences in the sensible heat flux increase. In MUKLIMO_3, the gradient of the air temperature and the ground surface is very small, resulting in only a very small negative sensible heat flux. The analysis of the three-dimensional soil model outputs showed that the soil temperature in MUKLIMO_3 in the upper part of the soil is first constant and then rapidly drops after a few centimeters depths.

7.7.2 Model area: Meadow

To test the advancements further, a slightly more complex model area was used. Again, the whole model area did not feature any buildings; this time, however, instead of the sealed soil a natural soil ("sandy loam") was chosen for the ground

surface (MUKLIMO_3 land use type “meadown” in table 7.1). The sandy loam was covered with a low layer of vegetation, grass. The grass was 0.3 meters high, its LAI was 2 m^2 m^{-2}. The resolution and the sizes of the model areas of both MUKLIMO_3 and ENVI-met were kept constant.

7.7.2.1 Model run: status quo

Figure 7.12 shows the air temperature in the ENVI-met model area in a height of 1.8 meters at 15:00 simulation time, based on the coupled meadow simulation run without any adjustments. It becomes apparent that, even in the status quo model run, the differences between the air temperatures at the inflow boundary and the model area downstream are smaller than in the sealed model area. The air temperature is only reduced by around 0.9 K in the first hundred meters in the ENVI-met model area, indicating a higher agreement between the models even in the status quo model run.

Figure 7.12: Meadow: Air temperature, status quo simulation

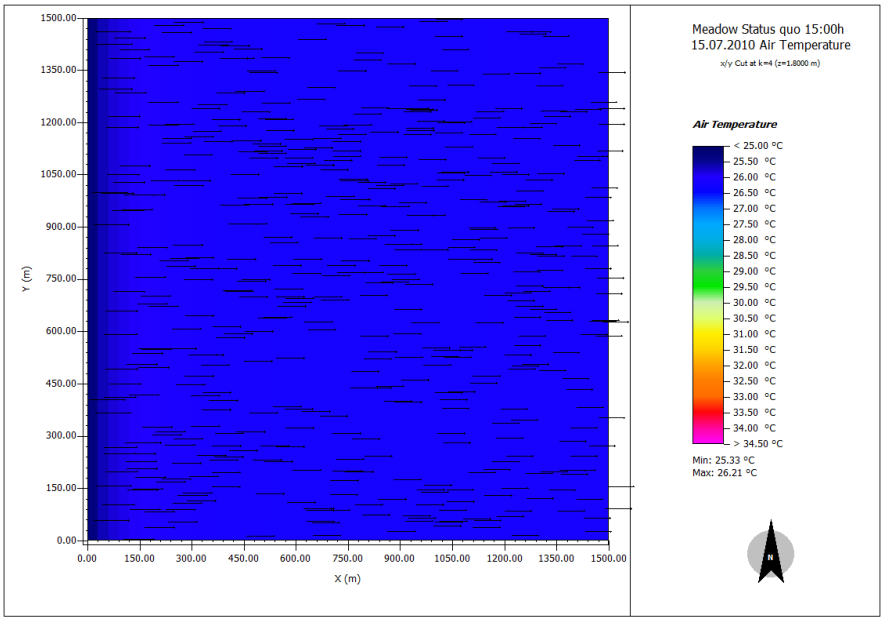

7.7.2.2 Model run: version including all advancements

The compared to the sealed model area already better agreement between the models in the meadow model area could further be improved by the advancements of the coupling. Figure 7.13 shows the air temperature in the ENVI-met model area in a height of 1.8 meters at 15:00 simulation time, based on the coupled meadow simulation run using all advancements, including the continuous calculation of the wind speed. The figure clearly shows the very high agreement regarding the air temperature between inflow boundary and three-dimensional model area. The comparison of the surface temperatures for the meadow model area (figure 7.14) confirms the very good model fit: For the entire simulation period, the surface temperatures for both models show very similar values.

Figure 7.13: Meadow: Air temperature, incl. all advancements

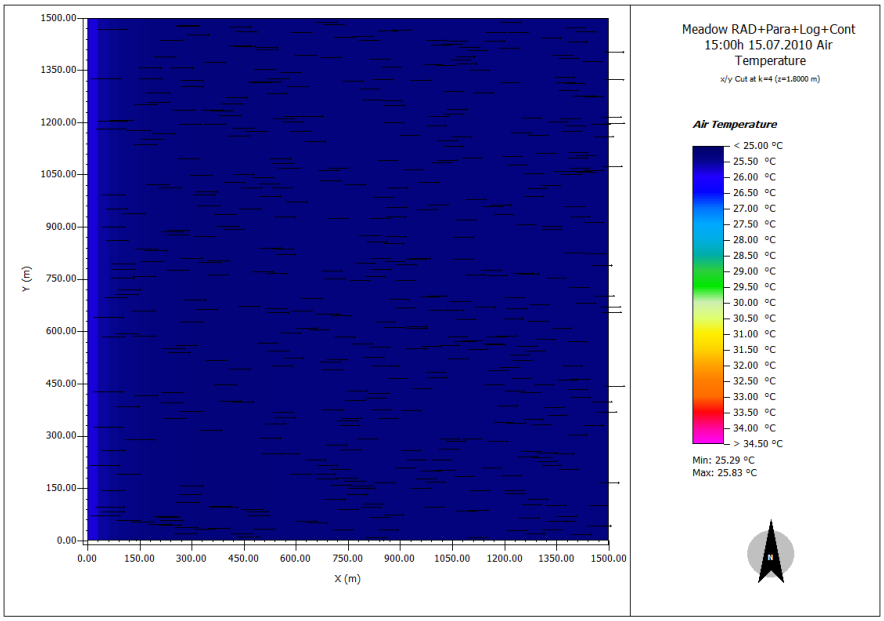

Figure 7.14: Meadow: Comparison of the surface temperature meadow: MUKLIMO_3, status quo and including all advancements

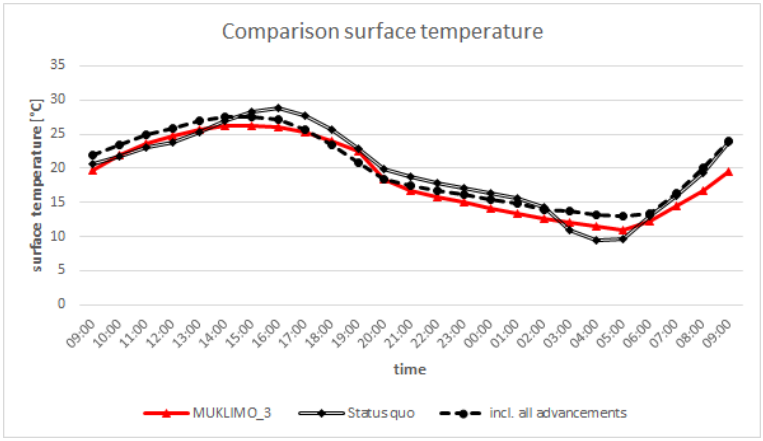

7.7.3 Model area: City

Using all advancements except for the continuous wind flow calculation, coupled simulation runs in a more complex model area with higher forced wind speed conditions were conducted. A simulation including the continuous wind flow calculation would have resulted in an enormous simulation time since a prognostic calculation of the wind flow demands exceptionally high computation power. The forcing was extracted from MUKLIMO_3 model runs of Frankfurt am Main, Germany. The size of ENVI-met's model area was 500 meters × 500 meters × 50 meters in a horizontal resolution of 5 meters and a vertical resolution of 2.5 meters. The model area is located in the inner city of Frankfurt am Main. Figure 7.15 shows an areal photo of the model area.

Figure 7.15: Model area City: Frankfurt am Main

Model area dimensions: 100 × 100 × 25 grids; vertical resolution: 2.5 meters; horizontal resolution: 5 meters; location: Frankfurt am Main, Germany (Source: Google Earth)

Figure 7.16 shows the air temperature in the ENVI-met model area in a height of 1.75 meters at 15:00. Although the advancements outlined above resulted in a good agreement between the two models in both simplified model areas, the coupled simulation run of the complex model area without the prognostic calculation of the wind flow still shows large discrepancies in the near-ground surface air temperatures. Again the forced wind speed provided by MUKLIMO_3 does not enter the ENVI-met model area. While a simulation with the continuous calculation of the wind speed might produce better results, such a solution had to be disregarded because of the enormous simulation times resulting from theses calculations.

Figure 7.16: City: Air temperature at 15:00 simulation time in 1.75 meters height in the coupled model run Frankfurt am Main

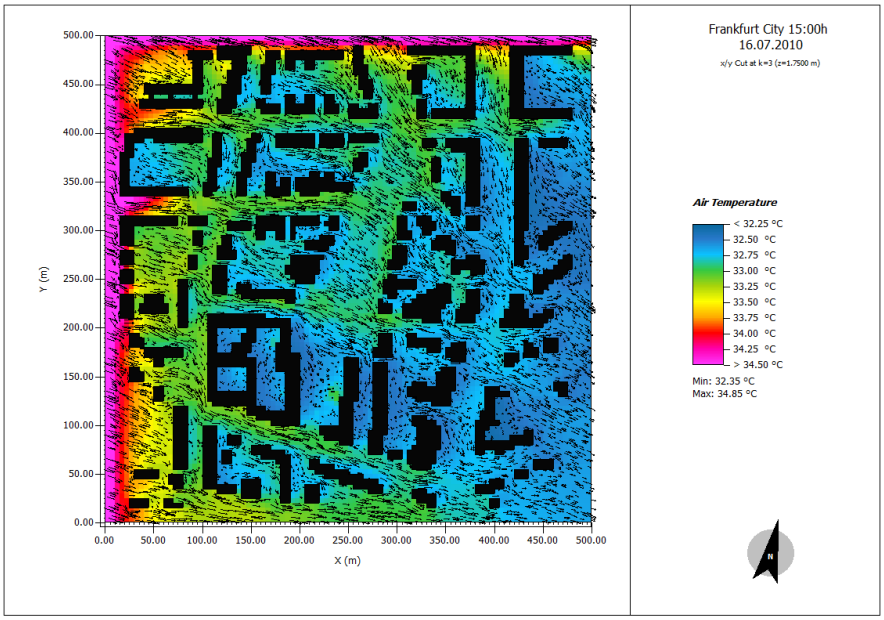

7.8 Conclusion and outlook

The analysis of the causes for the discrepancies of the near-ground surface air temperatures between the two models revealed a number of deficits in the coupling interface. Several improvements could be made to the coupling interface as well as the ENVI-met model that addressed these deficits. Calibrations showed that with the advancements, the discrepancies between the two models could be largely resolved.

In the simplified model areas, high agreement could be reached during daytime and for meteorologies with lower wind speeds. MUKLIMO_3 simulation runs that featured higher wind speeds, however, revealed that in ENVI-met's standard setting, where the wind field is updated in regular time intervals until a quasi-steady is reached, the forced wind speeds did not advance far into the ENVI-met model - the wind speed was reduced rapidly after entering the model area. When ENVI-met was run with a prognostic, continuous calculation of the wind flow, the model results showed much better results. While employing this continuous calculation of the wind flow was an adequate option to solve the rapid reduction of the wind speed in the smaller simplified model areas, the enormous increase of the simulation time due to the continuous calculation renders this option unfeasible for larger model areas. An alternative solution to this problem could be the introduction of "nudging". Nudging describes a method where, instead of the lateral boundary, the three-dimensional model grids are being forced by the parameters of the larger scale model. Future research should thus address the introduction of nudging into ENVI-met and the possibility of the new method to solve the reduction of the wind speed in the ENVI-met model area in coupled simulation runs with MUKLIMO_3.

Bibliography

Bruse, M. Mikroklima und thermischer Komfort in Städten. In *Presentation 7th DWD Klimatagung*, 2013.

Deutschländer, T., Koßmann, M., Steigerwald, T., and Namyslo, J. Verwendung von Klimaprojektionsdaten für die Stadtklimasimulation. In *Klimastatusbericht 2008*, number 12. Offenbach: Selbstverlag des Deutschen Wetterdienstes, 2008.

DWD. *User's Guide MUKLIMO_3 Thermodynamic Version*. Deutscher Wetterdienst - Department Climate and Environment Consultation, July 2015.

Früh, B., Becker, P., Deutschländer, T., Hessel, J.-D., Kossmann, M., Mieskes, I., Namyslo, J., Roos, M., Sievers, U., Steigerwald, T., Turau, H., and Wienert, U. Estimation of climate-change impacts on the urban heat load using an urban climate model and regional climate projections. *Journal of Applied Meteorology and Climatology*, 50:167–184, 2011a.

Früh, B., Koßmann, M., and Roos, M. Frankfurt am Main im Klimawandel. Eine Untersuchung zur städtischen Wärmebelastung. In *Berichte des Deutschen Wetterdienstes*, number 237. Offenbach: Selbstverlag des Deutschen Wetterdienstes, 2011b.

Huttner, S. Dynamische Kopplung von MUKLIMO_3 mit dem mikroskaligen Klimamodell ENVI-met. unpublished project report, 2011.

Huttner, S. *Further development and application of the 3D microclimate simulation ENVI-met*. Dissertation, Johannes Gutenberg-University Mainz, 2012.

Sievers, U. Verallgemeinerung der Stromfunktionsmethode auf drei Dimensionen. *Meteorologische Zeitschrift, Neue Folge*, 4(1):3–15, 1995.

Sievers, U. and Zdunkowski, W. G. A microscale urban climate model. *Contributions to Atmospheric Physics*, 59:3–15, 1986.

Simon, H. Anwendung eines mehrdimensionalen Interpolationsverfahrens mit einem mikroskaligen Klimamodell - ENVI-met. Diplomarbeit, Geographisches Institut der Universität Mainz, 2012.

von Storch, H., Güss, S., and Heimann, M. *Das Klimasystem und seine Modellierung.* Berlin, Heidelberg, New York: Springer-Verlag, 1999.

8 Conclusion

This dissertation aimed at further improving the ability to model urban microclimate with the microclimate model ENVI-met. In order to do so, a plant-as-object model, a BVOC model and an advanced multiple-node model were introduced into ENVI-met, and the coupling between the mesoscale model MUKLIMO_3 and ENVI-met was improved.

More specifically, in chapter 3, ENVI-met's vegetation model was advanced by the introduction of plants as individual organisms. In the past, plants in the microclimate model ENVI-met were only represented by a loose collection of grids cells with individual leaf area densities. Furthermore, no distinct root area that belonged to a plant could be digitized. Therefore a plant could and was not treated as a uniform object in the model, disallowing an analysis about the state of the plant as a whole. To overcome this limitation and to enable organism-based analyses that allow statements about a plant's vitality, the newly developed plant-as-object model treats plants as individual uniform organisms. All environment-plant interactions calculated at the individual leaf level are being aggregated and transferred back to the associated plant allowing the object-based analysis of a plant's water access and vitality. Additionally, a three-dimensional root model was introduced that allows the calculation of an object-based water supply for each plant organism. Making use of these advancements, evaluations of the plant parameters as aggregated clusters of leaf area density and root area density can now be performed.

To evaluate these new implementations, two sets of proof-of-concept simulations were conducted. In the first set of proof-of-concept simulation, the effect and the importance of different tree geometries onto the aggregated plant parameters such as water access and average leaf temperature were examined. The proof-of-concept simulations showed that, as was expected, larger trees with their more advantageous

surface-area-to-volume ratio can withstand more environmental stress than smaller trees. The second set of proof-of-concept simulations examined the effects of different microclimates onto the plant organism parameters. The simulation results showed that ENVI-met is capable of modeling the strong interactions of plants and local climates in the same ways that would be expected on theoretical grounds.

To further test the new implementations, the plant-as-object model was evaluated against measurement data in a case study (see chapter 4). In this study, two of the organism-based model outputs, transpiration and leaf temperature, were evaluated through comparison with measured (sap-flow derived) transpiration and leaf temperatures of shaded leaves of two trees in an urban environment. Since the availability of photosynthetic active radiation plays a key role in a plant's transpiration, the model was tested in different meteorological conditions which featured different levels of cloud cover. The comparison of the simulation results with the measurement data showed a very high agreement between the two. Apart from a generally high agreement in the absolute values, the vegetation model of ENVI-met was also capable of simulating short-term variations in transpiration that were caused by minor environmental changes such as local cloud cover. Small differences arose as the model estimated a slight water stress for one of trees in the less clouded simulation periods that was not visible in the measurement data. The study showed that with the newly implemented plant-as-object model ENVI-met is able to simulate transpiration and leaf temperatures of trees in complex urban environments very accurately.

In chapter 5, a BVOC emission model and chemistry model, more specifically an isoprene emission and chemistry model that models the additional forming potential of tropospheric ozone were implemented into the microclimate model ENVI-met. The implemented isoprene emission model is based on the work of Guenther et al. (1993) and the advancements in Guenther et al. (1999) and Guenther et al. (2006). To validate the implementation, several proof-of-concept simulations were conducted

and the resulting isoprene emission patterns were analyzed at the individual leaf level as well as at the aggregated organism level using the plant-as-object model (see chapter 3). The proof-of-concept simulations showed plausible model results and the isoprene emission values obtained from the model matched empirical values found in the literature very well.

Based on the isoprene emission model, the chemical reactions of isoprene that lead to the formation of tropospheric ozone were introduced into ENVI-met's chemistry model. Since higher concentrations of isoprene do not immediately increase the ozone formation, a number of intermediate reactions also had to be implemented. The validity of the advancements of the chemistry model was tested in several proof-of-concept simulations that compared the results of simulations based on the advanced dispersion and chemistry model - including the isoprene-induced reactions - to those of simulations based on the initial, basic dispersion and chemistry model - including only the reactions of NO, NO_2 and O_3. In a larger number of proof-of-concept simulations that examined the effects of different meteorological conditions as well as different chemical concentration levels of reactants, the validity of the implementation of the isoprene-induced reactions was tested. The comparison of the isoprene-including and the isoprene-excluding scenarios yielded results conforming to the theoretical expectations, validating the model advancements.

Chapter 6 describes the development of ENVI-met's advanced multiple-node wall and roof model. Since buildings play an important role in the urban microclimate, the accurate simulation of the processes at their walls and roofs are of great importance. Furthermore, the simulation of indoor temperatures allows an estimation of the indoor climate as well as on the energy demand to regulate the same. Using the new implementations, more complex walls and roofs can now be digitized, consisting of up to three different materials. Together with the possibility to divide buildings into separate building zones that are treated as confined spaces of air volumes, the indoor temperature can now be roughly estimated for separate rooms / flats. To

validate the multiple-node model, first a proof-of-concept simulation was conducted that examined the surface temperature and indoor climate evolution depending on different building materials. The model results showed that ENVI-met produces plausible results for the effects of different building materials on both the outside surface temperature as well as the indoor air temperature. In a second validation of the multiple-node model, the simulation results for the surface temperature were tested against measured surface temperature values provided by the Fraunhofer Institute for Building Physics Holzkirchen. The model was run under significantly different meteorological conditions in four simulation periods of several consecutive days. The evaluation of the simulated surface temperatures against the measured surface temperatures showed exceptionally high agreements between the modeled and the measured data under all meteorological conditions, corroborating the high accuracy of ENVI-met's wall and roof model. Overall, the results demonstrated that with the advancements of the multiple-node model ENVI-met is capable of precisely simulating building physics processes in complex urban environments.

The possibility to run coupled simulations of ENVI-met with the larger scale model MUKLIMO_3 was presented in chapter 7. In a previous research project (Huttner, 2011), an interactive user interface was developed that allowed offline coupling between the two models MUKLIMO_3 and ENVI-met. The application of the coupling, however, showed substantial discrepancies between the two models with respect to the near-surface air temperatures (Bruse, 2013; Simon, 2012). In the present study, the causes of these discrepancies were examined and several modifications were applied to improve the coupling process and consequently the agreement between the two models. Although a number of structural deficits in the coupling could be mitigated and new implementations were made, a significant improvement without the continuous calculation of the wind flow could only be reached in simplified model areas. In more complex environments where a prognostic, continuous calculation of the wind flow is no feasible option due to the enormous increase of the simula-

tion time, the coupled simulation runs still show substantial, although less strong, discrepancies in the near-ground air temperature between the two models. A possible solution to this problem could be the introduction of "nudging", where instead of the lateral boundary, the three-dimensional model grids are being forced by the parameters of the larger scale model.

By introducing the plant-as-object model, the BVOC model and the advanced multiple-node model, substantial advancements were thus achieved with regard to the modeling of urban microclimate. In addition, by improving the coupling of ENVI-met with the mesoscale model MUKLIMO_3, the boundary conditions driving the urban microclimate simulations can now be generated more accurately. The advancements presented here therefore constitute an important step in the modeling of urban microclimates.

Yet, further development and research are still needed: As far as the plant-as-object model is concerned, more measurements are needed to evaluate the model. In addition, the implementation of a topological structure to digitize the geometry of trees would be beneficial since the exact replication of the geometry of the plants plays an important role in organism-based analyses. Furthermore, differences in the physiology of plants such as special abilities to retain water or regulated transpiration as well as different metabolism types such as CAM-plants (Crassulacean Acid Metabolism) need to be implemented in the model. Based on the newly developed plant-as-object model, this could enable ENVI-met to simulate the effects of different plants on the local microclimate and vice versa in even more detail in the future.

While the BVOC model has proven itself to produce plausible results in a large number of proof-of-concept simulations, it still needs to be evaluated against actual measurement data. Additionally, ENVI-met's database needs to be updated to include more isoprene-related data such as the basal isoprene emission rate and the average leaf weight of different species.

The very promising evaluation results for the advanced multiple-node wall and roof model showed that with the new implementations ENVI-met is capable to accurately simulate the facade-atmosphere interactions. The comparison with the measurement data showed that ENVI-met can reliably model the outside facade temperature under various meteorological conditions and in a complex environment. To evaluate the inner nodes and the indoor air temperature modeling, more evaluation studies are however needed. Furthermore, it should be possible to use ENVI-met's highly accurate simulation data to couple the model results with building physics models such as WUFI Plus (Wärme Und Feuchte Instationär) developed by the Fraunhofer Institute for Building Physics Holzkirchen. Using coupled simulation runs, ENVI-met could be used to generate realistic boundary conditions accounting for the local microclimate around the building structure for the building physics model WUFI Plus. This would result in a more precise climate input for the simulation of the heat and moisture transiency and the indoor climate of the building physics model WUFI Plus.

Since the improvements of the coupling of ENVI-met and MUKLIMO_3 did not yield satisfying results in larger, more complex model areas where the continuous calculation of the wind flow is no feasible option due to the extraordinary increase of simulation time, more work is needed. So far, the most promising option seems to be the introduction of "nudging" into ENVI-met to couple the two models.

Beyond the topics of the dissertation, future development of ENVI-met should address possibilities to reduce the simulation time and to simulate larger model areas in high resolution (≤ 2.5 meters). This could be reached by a decomposition of the model area in several parts that are then simulated simultaneously on several computers. This option could speed up simulation time and increase the model areas immensely; however, it would require a lot of communication of the different simulations due to the interactions and inter-dependencies among the split-up model areas. The development of a communication module that transfers the current state

of one simulation to the others and that synchronizes the prognostic calculations for all simulations would require a fundamental restructuring of the model.

A second, more easily developed improvement could be the temporary suspension of a simulation that could be restarted by the user. To accomplish such a "pause" function, ENVI-met would need to save all current simulation data after it has been suspended. When restarting the simulation all saved data values need to be loaded into the main memory again and the simulation could be continued. The benefit of such a "pause" function would be that simulations that failed due to instabilities would not need to be restarted from the beginning, but rather from the last stable state of the simulation. Furthermore, paused simulations could be transferred to a faster, more powerful computer which would speed up the simulation time. The development of such a feature would require intensive work to implement saving and loading routines for all data fields, but no structural complications should arise. An alternative to save the state of a simulation could be to run ENVI-met in a virtual sandbox which can be saved to the hard drive and restarted on a different computer and / or time.

Bibliography

Bruse, M. Mikroklima und thermischer Komfort in Städten. In *Presentation 7th DWD Klimatagung*, 2013.

Guenther, A., Baugh, B., Brasseur, G., Greenberg, J., Harley, P., Klinger, L., Serca, D., and Vierling, L. Isoprene emission estimates and uncertainties for the central African EXPRESSO study domain. *Journal of Geophysical Research*, 104(23): 30625–30639, 1999.

Guenther, A., Karl, T., Harley, P., Wiedinmeyer, C., Palmer, P. I., and Geron, C. Estimates of global terrestrial isoprene emissions using MEGAN (Model of Emission of Gases and Aerosols from Nature). *Atmospheric Chemistry and Physics*, 6: 3181–3210, 2006.

Guenther, A. B., Zimmermann, P. R., and Harley, P. C. Isoprene and Monoterpene Emission Rate Variability: Model Evaluations and Sensitivity Analyses. *Journal of Geophysical Research*, 98(7):12609–12617, 1993.

Huttner, S. Dynamische Kopplung von MUKLIMO_3 mit dem mikroskaligen Klimamodell ENVI-met. unpublished project report, 2011.

Simon, H. Anwendung eines mehrdimensionalen Interpolationsverfahrens mit einem mikroskaligen Klimamodell - ENVI-met. Diplomarbeit, Geographisches Institut der Universität Mainz, 2012.